Analysis of Frequency-Dependent Anisotropy in VSP Data

Sonja Maultzsch
Diplom in Geophysics 2001
Technische Universität Berlin, Germany

Thesis submitted in fulfilment of
the requirements for the degree of
Doctor of Philosophy

School of GeoSciences
University of Edinburgh
2005

Declaration

I declare that this thesis has been composed solely by myself and that it has not been submitted, either in whole or in part, in any previous application for a degree. Except where otherwise acknowledged, the work presented is entirely my own.

Sonja Maultzsch
March, 2005

Abstract

The use of seismic anisotropy for the characterization of fracture systems in the subsurface is based upon equivalent medium theories that describe the average elastic response of a fractured material in the long wavelength limit. Traditional equivalent medium models predict a seismic response that is independent of frequency and insensitive to the size of the fractures. Recent observations from seismic data challenge these assumptions.

The interpretation of attenuation and velocity dispersion in laboratory data acquired in the kHz to GHz frequency range is based on the concept of squirt flow in porous fluid-saturated rock. A number of studies have also found effects of dispersion in the seismic frequency band, particularly in connection with fracture zones. However, these observations have been lacking quantitative explanation in terms of petrophysical processes, and with regard to wave-induced fluid motion in porous rock seismic data are generally assumed to represent the low frequency limit. Recent work on equivalent medium theories for fractured rock address these issues by incorporating wave-induced fluid motion into the modelling, which predicts seismic anisotropy to depend on frequency.

I analyse VSP data from five different sedimentary basins that contain naturally fractured hydrocarbon reservoirs. I design processing techniques to investigate whether frequency-dependent anisotropy can be detected in the seismic frequency band. I find broad evidence in support of the concept. Three different attributes are extracted from the data that give evidence of anisotropic dispersion: P-wave attenuation anisotropy, the frequency dependence of the time delay between split shear waves, and attenuation of the slow shear wave compared to the fast one.

The measured effects correlate with information on the presence of fractures in the reservoirs of the respective oil and gas fields. For one of the data sets where no anisotropic dispersion is detected, fracture-induced anisotropy is very weak

and dominated by polar anisotropy. The observations can be explained by a squirt-flow model for fractured rock. The sensitivity of the modelled response to fluid type and fracture length scales is consistent with the real data results and geological evidence.

It may not always be possible to detect frequency-dependent anisotropy in real data depending on data quality and the symmetry of the equivalent anisotropic medium. Nevertheless, the quantitative evidence of anisotropic dispersion from the majority of the VSPs and the correlation with the presence of fractures in the subsurface suggest that it is worthwhile considering these effects in analyses of seismic anisotropy.

Acknowledgements

With great respect I wish to express my gratitude to my supervisors Dr. Mark Chapman, Prof. Enru Liu and Prof. Xiang-Yang Li for their guidance and enthusiastic support throughout an exciting time of research. I have benefited a great deal from many stimulating discussions and very much enjoyed the years of fruitful and inspiring work. I hope that this can be continued in some form in the future. I am also grateful to Dr. Roger Scrutton for providing continuous help and support at the University.

I would like to thank the sponsors of the Edinburgh Anisotropy Project for supporting the research group and providing data sets I worked on. I am particularly grateful to a number of people who put a lot of effort into making data sets for this research available: These are Jerry Beaudoin (BP) and Sue Fowler (BP) for the Clair data, Heloise Lynn (Lynn Inc.) for the Bluebell data, Ernie Majer (LBL) for the Sanjuan data and Chris Thompson (ChevronTexaco) for the Rangely data. I also wish to thank David Taylor for providing a new version of the modelling software ANISEIS that was needed for this thesis. Furthermore, I am thankful to John Queen, Tom Daley, Rodney Johnston, Mosab Nasser, Wenjie Dong, Shiyu Xu, Michael Schoenberg, Roger Clark and Steve Horne, who have helped me with constructive discussions throughout this work.

A special thank you goes to Magnus H. for proof reading parts of this thesis and sorting out all the linux problems. I am grateful to Bärbel T., Andy D., Shaggy D., Fabio M., Serafeim V., Jinghua Z. and Lifeng W. for countless enjoyable days in the office. I would also like to thank all my friends in Edinburgh; it has been an unforgettable time filled with many great activities. A special thanks goes to Fahad A.-K. for wonderful days sharing a flat, enjoying the Edinburgh Festival and for sharing thoughts. I am very thankful to Guy H. for constant encouragement and lovely refreshing walks across Blackford Hill during stressful

times.
Finally, I wish to express my deep gratitude to my parents and my sister Janina for their continuous understanding and support.

To my family

Contents

List of Tables

List of Figures

Notations and Conventions

The Einstein summation convention, i.e. summation over repeated indices, applies throughout this thesis.

I will also adopt the notation:

$$u_{i,j} = \frac{\partial u_i}{\partial x_j}.$$

Furthermore, I use the convention

$$\dot{f} = \frac{\partial f}{\partial t}$$

for time variables t.

List of Symbols

Symbol	Meaning	Page Introduced
σ_{ij}	stress tensor	9
ϵ_{ij}	strain tensor	9
c_{ijkl}	stiffness tensor	9
s_{ijkl}	compliance tensor	23
u_i	displacement	10
ω	angular frequency	10
f	frequency	36
k	wave number	11
ρ	density	10
v	phase velocity	10
v_{P}	P-wave velocity	38
v_{S}	S-wave velocity	38
φ	azimuth	18
λ	Lamé parameter	12
μ	shear modulus	12
k_f	fluid bulk modulus	25
η	fluid viscosity	26
κ	permeability	26
Φ_p	porosity	35
ε_c	crack density	35
ε_f	fracture density	35
a_f	fracture radius	35
r	aspect ratio	35
ς	grain size	34
ν	Poisson's ratio	35
τ_m	grain scale relaxation time	35
τ_f	fracture-related relaxation time	35
Q	quality factor	50
α	spatial attenuation coefficient	50
A	amplitude	51
b	spectral ratio slope	51
R^2	R^2-value	65
E_{RMS}	root mean square error	67

Chapter 1

Introduction

Natural fracture systems are common geological features in the Earth's crust, and their characterization is of great importance for an assessment of subsurface reservoir properties. In outcrops, fractures are often found to follow a somewhat ordered pattern as shown in the photographs of Fig. 1.1. It is generally believed that such ordered patterns with an alignment of fractures related to the tectonic history and the current stress field are also present in the subsurface and affect the propagation of seismic waves (e.g. Teufel *et al.*, 1984; Helbig, 1984; Crampin, 1987; Queen and Rizer, 1990; Lorenz *et al.*, 1996; Lynn, 1996; Zatsepin and Crampin, 1997; Cosgrove, 1998; Thomsen, 2002).

During the past two decades there has been growing interest in the use of seismic anisotropy to identify and characterize subsurface fracture systems. A number of techniques have been developed to estimate an average fracture orientation and fracture intensity from measurements of seismic anisotropy. These include the analysis of shear-wave splitting, the directional dependence of NMO velocities or traveltimes and the azimuthal variation of AVO gradients (e.g. Crampin, 1985; Alford, 1986; Queen and Rizer, 1990; Ikelle, 1997; Li, 1999; Lynn *et al.*, 1999; Bakulin *et al.*, 2000a,b,c; Gray and Head, 2000; Winterstein *et al.*, 2001; Thomsen, 2002).

The link between seismic anisotropy and the characteristics of fracture systems in the subsurface is established through equivalent medium theory. In the long wavelength limit the heterogeneous fractured rock can be represented as an equivalent homogeneous medium. If the heterogeneities, or fractures, are aligned the average elastic properties of the equivalent medium are anisotropic. Conventional

(a) (b)

Figure 1.1: Examples of fracture patterns found in outcrops. a) Granite surface (Preikestolen, southern Norway). b) Sandstone formation (Beinn Eighe, Scotland).

equivalent medium theories share the assumption that the elastic response is independent of frequency as long as the seismic wavelength significantly exceeds length and spacing of the fractures. The most commonly used models are those of Hudson (1981) and Thomsen (1995), which agree for dry rock but predict quite different behaviour for fluid saturated rock. In the Thomsen (1995) model, fluid is allowed to flow between compliant fractures and stiffer equant pores in the surrounding matrix as seismic waves pass through the medium. The model assumes that the pressure always has sufficient time to equilibrate. As a result of the fluid squirt the magnitude of anisotropy is increased. In the Hudson (1981) model, in contrast, the fractures are isolated with respect to fluid flow.

A common feature of these traditional equivalent medium models is the insensitivity of the elastic response to the fracture size. The same elastic constants

are predicted for a medium containing many small cracks as for a material with a few large fractures. For this reason the terms "cracks" and "fractures" have been widely used as synonyms. In order to assess reservoir properties, however, it is important to distinguish between the two, because macro-fractures are much better flow conduits than microcracks.

Experiments carried out on rock samples in the laboratory and the comparison of these with sonic log and seismic data have given evidence of velocity dispersion and attenuation (e.g. Toksöz *et al.*, 1979; Spencer, 1981; Tittmann *et al.*, 1981; Murphy, 1985; Winkler, 1985, 1986; Jones, 1986; Sams *et al.*, 1997; Sothcott *et al.*, 2000). More specifically, it has been found that velocity dispersion and attenuation are higher for fluid saturated rock than for dry rock, and that the effect decreases as effective stress increases and microcracks close (Gardner *et al.*, 1964; Toksöz *et al.*, 1979; Winkler and Nur, 1979; Winkler *et al.*, 1979; Johnston, 1981; Spencer, 1981). These results suggest that it is important to consider the pore microstructure and fluid saturation in a rock physics model that describes the elastic properties of a medium.

A common framework for a theoretical description of the deformation of fluid-saturated porous rock is the Biot-Gassmann theory of poroelasticity (Gassmann, 1951; Biot, 1956). The theory models viscous and inertial interaction between the fluid and the solid as a function of frequency and reduces to Gassmann's equations for fluid substitution in the zero frequency limit. An experimental verification of the existence of a third body wave, which is predicted by the theory, is regarded as a validation of the Biot mechanism (Plona, 1980). Klimentos and McCann (1988) showed that in natural rocks this wave is rapidly attenuated due to the presence of clay. The pore geometry is not considered explicitly in Biot's theory, and it tends to underestimate the magnitude of velocity dispersion and attenuation seen in laboratory data (e.g. Winkler, 1985; Wang and Nur, 1990; Mavko and Jizba, 1991).

The pore microstructure plays an important role for the concept of fluid squirt between stiff and compliant parts of the pore space, which can explain much larger magnitudes of attenuation and dispersion. This mechanism has been the basis for the derivation of a number of models (O'Connell and Budiansky, 1977; Johnston *et al.*, 1979; Mavko and Jizba, 1991; Dvorkin and Nur, 1993; Dvorkin *et al.*, 1995; Endres and Knight, 1997; Chapman *et al.*, 2002). The comprehen-

sive work of Endres and Knight (1997) highlights the importance of considering differences both in pore geometry as well as in the orientation of low aspect-ratio pores in a theoretical description of squirt-flow effects. Based on laboratory and well log data, the characteristic squirt-flow frequency associated with the pore geometry on the grain scale is believed to lie between the sonic and ultrasonic frequency bands (e.g. Mason *et al.*, 1978; Toksöz *et al.*, 1979; Nur and Winkler, 1980; Tittmann *et al.*, 1981; Winkler, 1986; Mavko and Jizba, 1991; Brown and Seifert, 1997; Sams *et al.*, 1997). Therefore, the seismic frequency band is often regarded as representing the low frequency limit. However, a number of recent observations from field data suggest that this assumption can be questioned.

High magnitudes of attenuation that are comparable to the values measured in the laboratory have also been found in VSP data (e.g. Hauge, 1981; Stainsby and Worthington, 1985; De *et al.*, 1994; Hackert *et al.*, 2001). These could not be modelled with scattering from thin layers alone, and other interpretations have remained mostly qualitative. In particular, there are a number of studies that reveal effects of attenuation and velocity dispersion in conjunction with fracture zones (Bates *et al.*, 1995; Chen, 1995; Clark *et al.*, 2001; van der Kolk *et al.*, 2001; Parra *et al.*, 2002; Lynn, 2004). Moreover, the results of van der Kolk *et al.* (2001) suggest a sensitivity of the effects to the fluid type. If squirt flow associated with the microstructure of the pore space is causing dispersion measured on rock samples in the laboratory, it seems logical to consider the same mechanism on a larger scale for field data where fractures constitute parts of the heterogeneous pore space. The question arises whether fracture-related squirt flow would be associated with a lower characteristic frequency that could explain attenuation and velocity dispersion in the seismic frequency range. Moreover, if the fractures are aligned these effects should depend on the propagation direction of the seismic wave, so that attributes that measure the anisotropy in the data vary with frequency.

As mentioned earlier, traditional equivalent medium theories for fractured rock do not consider a dependence of the elastic response on frequency. A number of frequency-dependent models have been developed in recent years that incorporate effects of wave-induced fluid motion (Hudson *et al.*, 1996; van der Kolk *et al.*, 2001; Chapman, 2003; Gurevich *et al.*, 2003). The model of Chapman (2003) describes squirt flow associated with both the grain scale where the pore

space consists of microcracks and equant pores, as well as on a larger scale that involves aligned fractures. It can explain attenuation and velocity dispersion at seismic frequencies and predicts that these effects are linked to the fluid type and the size of the fractures.

Equivalent medium models are applicable as long as the seismic wavelength significantly exceeds the scale associated with the heterogeneities of the medium. For ordered heterogeneities with sizes and spacings comparable to the seismic wavelength, anisotropic dispersion due to scattering of the wavefield has been addressed in a number of recent studies (Shapiro and Hubral, 1995; Werner and Shapiro, 1999; Chesnokov *et al.*, 2001; Daley *et al.*, 2002; Nihei *et al.*, 2002; Willis *et al.*, 2004; Liu *et al.*, 2004). It is not known, however, whether scattering or the fluid-flow mechanism is dominant at seismic frequencies and whether the two effects could be distinguished in real data.

The main focus of studies on frequency-dependent anisotropy to this point has been the development of theoretical models or numerical forward modelling. The objective of this thesis is to establish whether frequency-dependent anisotropy exists in real data, and whether such an effect is associated with the presence of fractures. For this purpose appropriate techniques have to be developed that can identify frequency-dependent anisotropy in seismic data. If anisotropic dispersion is found in the seismic frequency band, the question arises as to what characteristics it shows and how these observations can be related to theoretical models. I compare the real data results with synthetic studies based on a squirt-flow model to investigate whether the observations are consistent with a theoretical framework. The model suggests a link between frequency-dependent anisotropy and the saturating fluid as well as the fracture size. I assess whether the data indicate such a link. If frequency-dependent anisotropy is detected in field data and the causes are understood it has the potential to be used as an additional tool for fracture characterization and to improve the estimation of fracture properties.

I begin my thesis with a review of wave propagation in anisotropic media and describe common methods of using seismic anisotropy for the detection of fractures in the subsurface.

In Chapter 3 I proceed with a review of rock physics models. I begin with a discussion of traditional equivalent medium theory for fractured rock. This is followed by a review of poroelastic models and the concept of squirt flow. I discuss evi-

dence of velocity dispersion and attenuation both from laboratory and from field data that highlights the importance of considering wave-induced fluid motion. These observations inspired the development of frequency-dependent equivalent medium theories for fractured rock, which is the subject of the remainder of the chapter. I perform a calibration of the model, which I use throughout this thesis, and discuss its predictions in more detail.

One of the attributes of frequency-dependent anisotropy, which I analyse, is anisotropy of P-wave attenuation. Techniques for such an analysis have first to be developed. In Chapter 4 I begin with a review of the definition of Q and methods of measuring attenuation in an isotropic case. I then demonstrate with synthetic studies how attenuation anisotropy can be detected and analysed quantitatively. Moreover, I show that these measurements can be used to derive fracture properties based on a rock physics model.

In Chapter 5 I apply the methods developed in Chapter 4 to field data. I analyse a walkaround VSP and a multi-azimuth walkaway VSP. In both cases I find a systematic variation in P-wave attenuation with azimuth. Only the second data set provides sufficient constraints to perform forward modelling and interpret the observations in relation to fracturing in the reservoir.

The focus of Chapter 6 is the frequency dependence of shear-wave anisotropy. I describe the analysis of frequency-dependent shear-wave splitting in a near-offset VSP. The data show a systematic change in the magnitude of anisotropy with frequency in the fractured reservoir. I use the results to invert for fracture length and fracture density based on a squirt-flow model and compare the derived fracture size to independent borehole data.

In Chapter 7 I discuss the analysis of shear-wave splitting in a 3D VSP. I find that the effect of fracture-induced anisotropy in this data set is very small compared to the effect of thin-layer anisotropy. Furthermore, I cannot detect any dependence of the measured anisotropy on frequency. I discuss some of the limitations of the analysis with respect to data quality and the symmetry of the equivalent anisotropic medium.

In Chapter 8 I conclude with a study of a data set that consists of a walkaround and an offset VSP. I analyse both P- and S-wave attributes. The main finding is the presence of differential attenuation between split converted waves in the fractured reservoir. The P-wave attributes support this result, although they are

not conclusive by themselves due to instability of the source wavelet. I confirm with synthetic modelling that the difference in attenuation between split shear waves can be explained by squirt flow between fractures and the matrix porosity. Finally, I summarize the main results of this thesis and discuss their implications for future work.

All data sets analysed in this thesis are necessarily 'legacy' data sets whose experimental design I could not control. The acquisition geometries are therefore not always ideal for the purpose of the study. Nevertheless, for the majority of the data sets *a priori* information about the presence of fractures in the subsurface is available and previous measurements of azimuthal anisotropy have been published.

Chapter 2

Review of seismic anisotropy and fracture detection

2.1 Introduction

In this chapter I review some of the theoretical fundamentals of seismic wave propagation in anisotropic media. Possible causes of different types of seismic anisotropy in the subsurface are summarized. The main focus of this thesis lies in the study of fracture-related anisotropy. I review the basic concepts of methods that are currently used to derive fracture characteristics from seismic anisotropy.

2.2 Fundamentals of wave propagation in anisotropic media

Seismic anisotropy is the dependence of the elastic properties of a medium on direction. Mathematically this is described through the stiffness tensor c_{ijkl}, which relates stress σ_{ij} to strain ϵ_{ij} in Hooke's Law:

$$\sigma_{ij} = c_{ijkl}\,\epsilon_{kl}. \tag{2.1}$$

c_{ijkl} is a fourth rank tensor with 81 components. However, due to the symmetry of the stress and the strain tensor as well as energy constraints the number of independent elastic constants reduces to 21 for the most general anisotropic case

(Aki and Richards, 2002, pp. 21-23). This allows the stiffness tensor to be condensed into a symmetric 6 by 6 matrix notation referred to as the Voigt notation, where the following scheme for conversion of the indices is used: $11 \rightarrow 1$; $22 \rightarrow 2$; $33 \rightarrow 3$; $32 \rightarrow 4$; $31 \rightarrow 5$; $21 \rightarrow 6$.
Combining Hooke's law with Newton's second law leads to the elastodynamic wave equation relating stiffness to displacement **u**:

$$c_{ijkl} u_{k,lj} = \rho \ddot{u}_i. \tag{2.2}$$

ρ is the density of the material. Assuming a plane wave solution of the form $u_k = U_k \exp[i\omega(t - p_j x_j)]$ to Eq. 2.2 where **U** is the polarization vector, $\mathbf{p} = \mathbf{n}/v$ is the slowness vector and ω is the angular frequency yields the following eigenvalue problem:

$$(\Gamma_{ik} - \rho v^2 \delta_{ik}) U_k = 0 \qquad \text{with} \quad \Gamma_{ik} = c_{ijkl} n_j n_l. \tag{2.3}$$

n is the unit vector normal to the wavefront and v is the phase velocity. Eq. 2.3 is commonly referred to as the Kelvin-Christoffel equation with the Christoffel matrix Γ_{ik} (Tsvankin, 2001, pp. 3-4).
A solution of the eigenvalue problem yields three eigenvalues and corresponding eigenvectors. The eigenvalues are equal to ρv^2 and thus give the phase velocities, whereas the eigenvectors are the corresponding polarization vectors **U**. These are always mutually orthogonal, because the Christoffel matrix Γ_{ik} is real and symmetric. It follows that for any given propagation direction **n** there exist three body waves in a general anisotropic medium: a quasi-compressional wave (qP) and two quasi-shear waves (qS1 and qS2). The term "quasi" is used to emphasize that the polarization vectors are not necessarily parallel and normal to the propagation direction as they would be in isotropic media. The existence of two shear waves with different velocities and polarizations gives rise to the concept of shear-wave splitting, which will be described in more detail in section 2.4.
As a consequence of the angular velocity variation in anisotropic media phase and group velocity vectors are not identical. Fig. 2.1 illustrates the phenomenon. The group velocity vector $\mathbf{V_g}$ determines the propagation of energy along a ray and is normal to the slowness surface, whereas the phase velocity vector is always normal to the wavefront (Musgrave, 1970; Helbig, 1994). In its most general form, the

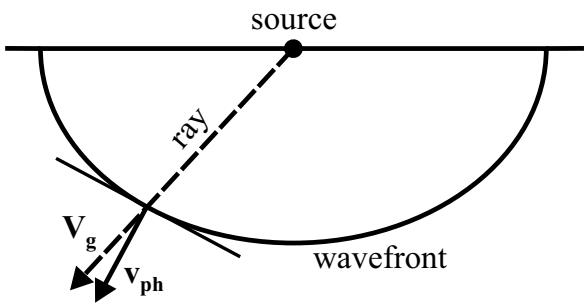

Figure 2.1: Group velocity vector $\mathbf{V_g}$ and phase velocity vector $\mathbf{v_{ph}}$ in an anisotropic medium. The former points into the source-receiver direction, while the latter is normal to the wavefront.

relationship between group and phase velocity is given by (e.g. Berryman, 1979)

$$\mathbf{V_g} = \mathrm{grad}^{\mathbf{k}}(kv) = \frac{\partial(kv)}{\partial k_1}\mathbf{i_1} + \frac{\partial(kv)}{\partial k_2}\mathbf{i_2} + \frac{\partial(kv)}{\partial k_3}\mathbf{i_3}. \tag{2.4}$$

$\mathbf{k}$ is the wave vector, which is parallel to the phase velocity vector, and $\mathbf{i_{1,2,3}}$ are unit vectors aligned with the coordinate system. It can be further derived that the projection of the group velocity vector onto the phase or slowness direction is equal to the phase velocity (Tsvankin, 2001, pp. 7):

$$(\mathbf{V_g} \cdot \mathbf{n}) = v. \tag{2.5}$$

The equation shows that the magnitude of the group velocity is always greater than or equal to the phase velocity for a given direction of wave propagation.

2.3 Symmetry systems

The symmetry of a medium is reflected in the structure of the stiffness tensor c_{ijkl} and the number of its independent components. This in turn determines the spatial pattern of velocities, polarizations and amplitudes of elastic waves travelling through the medium (Crampin, 1981). Techniques for measuring seismic anisotropy in field data are based upon identifying the symmetry of a material in these attributes.

Isotropy represents the highest possible symmetry where there are only two in-

dependent elastic constants, namely the Lamé parameters λ and μ. At the lower end of the spectrum of symmetry classes are triclinic media, which contain no rotational symmetry except the trivial one of 180°. Here the full set of 21 stiffness components is required to describe the medium. In between these end members, there are three symmetry systems that are commonly identified in the subsurface and thus are particularly important for seismic applications: hexagonal, orthorhombic and monoclinic symmetry.

Media with hexagonal symmetry are described by 5 independent stiffness constants. They posses a single axis of rotational symmetry, so that the plane normal to this axis is a plane of isotropy. Therefore hexagonal media are also called *transversely isotropic* or TI. The properties of elastic waves travelling through such media depend on the angle between the propagation direction and the symmetry axis. If the symmetry axis is vertical the medium is called VTI and the stiffness tensor has the following form:

$$\begin{pmatrix} c_{11} & c_{11}-2c_{66} & c_{13} & 0 & 0 & 0 \\ c_{11}-2c_{66} & c_{11} & c_{13} & 0 & 0 & 0 \\ c_{13} & c_{13} & c_{33} & 0 & 0 & 0 \\ 0 & 0 & 0 & c_{44} & 0 & 0 \\ 0 & 0 & 0 & 0 & c_{44} & 0 \\ 0 & 0 & 0 & 0 & 0 & c_{66} \end{pmatrix}.$$

Common causes for VTI anisotropy in the subsurface are thin horizontal bedding or the preferential alignment of minerals and grains during deposition. The latter is well documented for shales, in which plate-shaped clay particles are horizontally aligned (e.g. White *et al.*, 1983; Slater *et al.*, 1993; Miller *et al.*, 2000; Wang, 2002). Fine horizontal layering on a scale much smaller than the seismic wavelength is present in many sedimentary basins and has long been recognized to be the source of VTI anisotropy observed in field data (Backus, 1962; Thomsen, 1986; Helbig, 1994).

Another important case of transverse isotropy is represented by HTI media where the symmetry axis lies in the horizontal plane. Taking x_1 as the direction of the

symmetry axis, the stiffness tensor has the form:

$$\begin{pmatrix} c_{11} & c_{13} & c_{13} & 0 & 0 & 0 \\ c_{13} & c_{33} & c_{33}-2c_{44} & 0 & 0 & 0 \\ c_{13} & c_{33}-2c_{44} & c_{33} & 0 & 0 & 0 \\ 0 & 0 & 0 & c_{44} & 0 & 0 \\ 0 & 0 & 0 & 0 & c_{66} & 0 \\ 0 & 0 & 0 & 0 & 0 & c_{66} \end{pmatrix}.$$

Materials containing aligned vertical fractures or cracks that are rotationally invariant about their normals exhibit HTI symmetry (*see* Chapter 3 for corresponding petrophysical models). The strike of open vertical fractures or cracks at depth can often be related to the direction of maximum horizontal compressive stress (Crampin, 1987; Lorenz *et al.*, 1996; Lynn, 1996; Zatsepin and Crampin, 1997; Cosgrove, 1998). Therefore, a non-uniform horizontal stress regime is also regarded as one of the common causes of HTI anisotropy (Helbig, 1984; Crampin, 1985; Crampin and Lovell, 1991; Thomsen, 2002). VTI and HTI symmetry are also referred to as polar and azimuthal anisotropy.

In the case of orthorhombic symmetry the stiffness tensor contains 9 independent elastic constants. An orthorhombic medium has three mutually orthogonal symmetry planes. A common cause of this form of anisotropy in sedimentary basins is a combination of thin layering and vertical aligned fractures (i.e. VTI and HTI) (Bush and Crampin, 1991; Wild and Crampin, 1991; Bakulin *et al.*, 2000b). Moreover, materials containing two orthogonal sets of aligned fractures are orthorhombic (Bakulin *et al.*, 2000b). A medium with only one set of aligned fractures can also become orthorhombic, if the fractures are elongated along a particular direction (Hudson, 1994).

Monoclinic media are described by 13 independent stiffness components. They contain a single plane of mirror symmetry. Materials containing two or more non-orthogonal sets of aligned fractures may be represented as monoclinic media (Bakulin *et al.*, 2000c). The large number of independent parameters, which is required to characterize this symmetry system, poses a problem for identifying monoclinic anisotropy from seismic data. Therefore, hexagonal and orthorhombic symmetry systems are the main focus of seismic applications.

2.4 Shear-wave splitting

In anisotropic media two quasi-shear waves exist with distinct velocities and polarizations for a given propagation direction. When a shear wave enters an anisotropic zone it splits into two quasi-shear modes (subsequently called S1$\hat{=}fast$ and S2$\hat{=}slow$) that have fixed polarizations and velocities according to the propagation direction of the wave. The difference in the velocities of the two modes leads to a time delay between the modes that increases with path length. This is referred to as shear-wave splitting. The detection of this phenomenon in field data is used to gain insight into the anisotropy of the rock.

Each anisotropic symmetry system has a characteristic spatial pattern of S1 and S2 polarizations and of the time delay per unit pathlength. Fig. 2.2 shows an example of S1 polarizations and time delays for a VTI and an HTI medium as equal area projections of a hemisphere of propagation directions. If a medium is HTI due to the presence of vertical aligned fractures, the S1 polarization for propagation directions close to the fracture plane is parallel to the strike of the fractures. The time delay reaches a maximum for vertical propagation. In the VTI case the S1 polarization reflects the radial symmetry around the vertical axis and the time delay reaches its maximum for horizontal propagation. Fig. 2.2 also demonstrates that there are propagation directions for which the time delay between the two shear waves is zero and the S1 polarization changes abruptly. These are so-called shear-wave singularities where the two qS modes have the same wave speeds (Crampin, 1991). They can therefore only be observed as a single mode polarized in the plane normal to the qP polarization. It has been suggested that the detection of these singularities in field data is useful to constrain an interpretation in terms of the symmetry of the anisotropic material (e.g. Bush and Crampin, 1991).

For lower symmetry than hexagonal the spatial pattern of shear-wave splitting becomes more complicated. Wild and Crampin (1991) model these patterns for a number of orthorhombic models that are combinations of VTI and HTI materials. They find that the shear-wave behaviour is very sensitive to the relative magnitudes of polar and azimuthal anisotropy. Liu *et al.* (1993a) study a range of models containing two vertical fracture sets striking at different angles. They conclude that with the limited spatial coverage of standard field data it will be

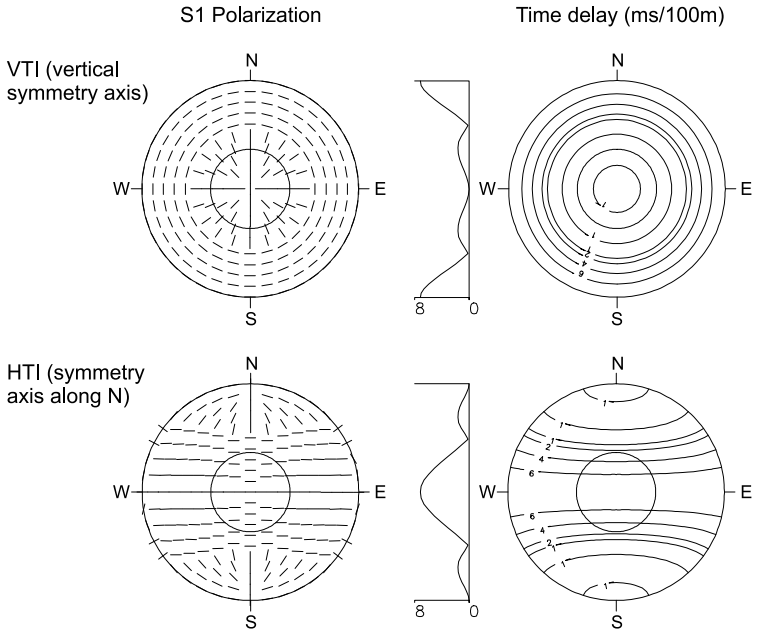

Figure 2.2: S1 polarizations and time delay as equal area projections of a hemisphere of propagation directions for VTI and HTI media.

difficult to distinguish between these models and an HTI material containing only one fracture set that represents an average of the original two sets. The analysis of shear-wave splitting has therefore found the widest application in the study of transversely isotropic materials. The standard technique of shear-wave splitting analysis will now be summarized.

The objective of shear-wave splitting analysis is to determine the azimuths of the S1 and S2 polarizations and the time delay between the split shear waves. In a field experiment with two orthogonal horizontal sources and receivers the source and receiver components are not necessarily aligned with the azimuths of the S1 and S2 polarizations. The process that finds these azimuths and separates S1 and S2 by rotating the data into the "natural" coordinate system is called Alford rotation (Alford, 1986). The time delay between S1 and S2 is subsequently found by cross-correlating the rotated traces. Assuming a homogeneous medium between sources and receivers and independently propagating pure modes, the linear model underlying the Alford rotation is given by the following equation:

$$\mathbf{D}(t) = [\mathbf{R}^T(\theta_{\mathrm{G}})\mathbf{\Lambda}(t; t_f, t_s)\mathbf{R}(\theta_{\mathrm{S}})] * \mathbf{S}(t). \tag{2.6}$$

with

$$\mathbf{D}(t) = \begin{pmatrix} d_{xx} & d_{xy} \\ d_{yx} & d_{yy} \end{pmatrix}, \qquad \mathbf{S}(t) = \begin{pmatrix} s_x & 0 \\ 0 & s_y \end{pmatrix},$$
$$\mathbf{R}(\theta) = \begin{pmatrix} \cos\theta & \sin\theta \\ -\sin\theta & \cos\theta \end{pmatrix}, \qquad \mathbf{\Lambda}(t; t_f, t_s) = \begin{pmatrix} \lambda_f & 0 \\ 0 & \lambda_s \end{pmatrix}.$$

$\mathbf{D}(t)$ is the 4-component data matrix, i.e. the displacement recorded at the two horizontal geophone components. The matrix of the two horizontal sources is $\mathbf{S}(t)$. The application of the rotation matrix $\mathbf{R}(\theta)$ describes rotation of the source vectors into the polarization directions of S1 and S2 and then back again into the geophone directions. The operator $\mathbf{\Lambda}(t; t_f, t_s)$ extrapolates the S1 and S2 wave modes from the source to the receiver where they have arrival times t_f and t_s. If the data are rotated into the coordinate system of the S1 and S2 polarizations the off-diagonal energy should become zero. A solution of Eq. 2.6 therefore finds the angles θ_{G} and θ_{S} that minimize the off-diagonal components of the matrix

$$\mathbf{\Lambda}(t; t_f, t_s) * \mathbf{S}(t) = \mathbf{R}(\theta_{\mathrm{G}})\mathbf{D}(t)\mathbf{R}^T(\theta_{\mathrm{S}}). \tag{2.7}$$

Various techniques have been developed to perform this process. Early methods were based on the assumption that sources and geophones are aligned, i.e. $\theta_{\mathrm{G}} = \theta_{\mathrm{S}}$. They determine the optimum angle by scanning through a range of θ-values and performing numerical rotation of the recorded data matrix, which is computationally intensive (Alford, 1986; Thomsen, 1988). Zeng and MacBeth (1993) derived efficient algebraic solutions, which also allow the condition that sources and geophones are aligned to be relaxed. Another technique that can determine source and geophone angles independently and is fast by making use of linear transforms has been suggested by Li and Crampin (1993). Finally, Dellinger *et al.* (2001) developed a generalized Alford rotation for the case that the S1 and S2 polarizations measured at the two horizontal receiver components are not orthogonal, again by utilizing the linear transforms of Li and Crampin (1993).
Layer stripping and propagator matrix approaches have been suggested to handle the case where the azimuths of S1 and S2 polarizations change with depth (Nicoletis *et al.*, 1988; Lefeuvre and Mandal, 1991; Winterstein and Meadows,

1991). Layer stripping involves successively removing the effects of anisotropy from the data starting from the top layer, which is followed by an analysis of shear-wave splitting for the interval immediately below. In a propagator matrix technique shear-wave splitting parameters are estimated between adjacent recording levels. The displacement field at level i acts as a source for the recorded displacement field at level $i + 1$. The medium is only assumed to be uniformly anisotropic between the two levels. Zeng and MacBeth (1993) showed that the propagator matrix approach can also be used if the shear waves are only excited by one source direction. The authors derive an algebraic solution of the problem in the frequency domain under the assumption that the two shear waves have equal amplitude spectra. I use their algorithm to estimate the S1 polarization and time delay of split converted waves in VSP data studied in Chapter 8. The other data sets analysed for shear-wave splitting in this thesis (Chapters 6 and 7) have two orthogonal source components and did not appear to require any layer stripping. The techniques of Zeng and MacBeth (1993) and Li and Crampin (1993) generally gave consistent results.

2.5 Methods of fracture detection

As outlined in section 2.3 the most simple model relating fractures to seismic anisotropy is a material containing a set of vertical aligned fractures, which as a result is azimuthally anisotropic with a horizontal axis of symmetry (HTI). Although this may be a simplified representation of the real rock in many cases, the nature of seismic field data with a limited signal-to-noise ratio and limited spatial coverage often does not justify an interpretation in terms of lower symmetries. Therefore, methods of fracture detection from seismic anisotropy and their application in practice are generally based on the assumption of the HTI model.

Seismic attributes that are commonly analysed for the detection of fractures are shear-wave splitting, the azimuthal variation of traveltimes or NMO velocities, and the variation of reflected amplitudes with offset and azimuth (AVOAZ). As discussed in the previous section, the analysis of shear-wave splitting yields the polarization azimuth of the leading shear wave and the time delay between the

split shear waves. For near-vertical propagation the S1 polarization is parallel to the fracture strike, whereas the increase in time delay with depth is a measure of the magnitude of azimuthal anisotropy. Shear-wave splitting analysis for fracture detection using Alford rotation is commonly performed on 9-component near-offset VSP data (e.g. Crampin, 1985; Queen and Rizer, 1990; Lynn *et al.*, 1999; Winterstein *et al.*, 2001). If only P-wave sources are used, multi-azimuth VSP or surface seismic data provide means of analysing converted-wave splitting for fracture detection (e.g. Gaiser, 2000; Horne, 2003). Here the energy ratio of the transverse to radial component as a function of azimuth indicates the symmetry directions since in the symmetry planes only the shear wave polarized parallel to the plane will be excited. After rotating the data into the symmetry directions, the time delay can be determined, so that the analysis again yields the fracture strike and a measure of the magnitude of azimuthal anisotropy.
The normal moveout in azimuthally anisotropic media describes an ellipse in the horizontal plane to the same approximation that it is hyperbolic in time (Grechka and Tsvankin, 1998):

$$\frac{1}{v^2_{\mathrm{NMO}}(\varphi)} = \left(\frac{\cos(\varphi-\varphi_0)}{v_{max}}\right)^2 + \left(\frac{\sin(\varphi-\varphi_0)}{v_{min}}\right)^2 . \tag{2.8}$$

φ is the azimuthal angle, v_{max} and v_{min} are the maximum and minimum NMO velocities and φ_0 is the azimuth of the major axis of the ellipse. This can equally be written in terms of traveltimes t:

$$t^2(\varphi) = t^2_{max}\cos^2(\varphi-\tilde{\varphi}_0) + t^2_{min}\sin^2(\varphi-\tilde{\varphi}_0) \tag{2.9}$$

with $\tilde{\varphi}_0 = \varphi_0 - \pi/2$. If a fractured medium is HTI, then φ_0 and $\tilde{\varphi}_0$ are the fracture strike and fracture normal directions, respectively. For weak anisotropy Eq. 2.9 can be written as

$$t(\varphi) = C_1 + C_2\cos[2(\varphi-\tilde{\varphi}_0)] \tag{2.10}$$

with $C_1 = \frac{1}{2}(t_{max}+t_{min})$ and $C_2 = \frac{1}{2}(t_{max}-t_{min})$. Li (1999) shows that starting from a fourth-order moveout equation and making the weak anisotropy assumption the difference in traveltime between two orthogonal survey lines also shows a $\cos(2\varphi)$-variation with azimuth, where the amplitude of the variation

is related to the offset and the magnitude of anisotropy. Thus, the above equations provide a number of tools to derive fracture strike and magnitude of azimuthal anisotropy from NMO velocities and traveltimes in multi-azimuth VSP and reflection seismic data.

Methods of analysing reflected amplitudes for fracture detection are based upon the fact that for azimuthally anisotropic media the reflection coefficient does not only vary with incidence angle but also with azimuth. Retaining only second-order terms in incidence angle θ, the P-wave reflection coefficient R_{PP} can be approximated by (e.g. Rüger and Tsvankin, 1997; Ikelle, 1997; Thomsen, 2002):

$$R_{\mathrm{PP}}(\theta,\varphi) = I + G(\varphi)\sin^2\theta \qquad \text{with} \quad G(\varphi) = A' + B'\cos[2(\varphi-\varphi_0)], \quad (2.11)$$

or for a fixed incidence angle θ_0

$$R_{\mathrm{PP}}(\theta_0,\varphi) = A + B\cos[2(\varphi-\varphi_0)]. \quad (2.12)$$

I is the reflection coefficient at normal incidence or AVO intercept, G is the AVO gradient, and A, B, A' and B' are constants. Both the AVO gradient and the reflected amplitude at a fixed incidence angle vary as a $\cos(2\varphi)$-function with azimuth. Again, these two attributes are inverted to find the symmetry directions of an HTI medium and the magnitude of anisotropy from multi-azimuth reflection data.

Although numerous case studies of AVOAZ analysis can be found in the literature (e.g., Pérez *et al.*, 1999; Lynn *et al.*, 1999; Gray and Head, 2000; Liu, 2003; Hall and Kendall, 2003) it remains questionable whether equating the azimuthal variation in reflected amplitudes with the azimuthal variation of the reflection coefficient is a valid concept. The amplitudes are also influenced by transmission through the rock above the reflector, and effects such as transmission coefficients, geometric spreading and attenuation in anisotropic rock can equally lead to azimuthal amplitude variation. It has been suggested that especially attenuation is an important factor to be considered (Horne and MacBeth, 1997; MacBeth, 1999; Maultzsch *et al.*, 2003b; Chapman and Liu, 2003). The lack of attention to this effect in the past is partly due to the difficulty of describing attenuation anisotropy with an adequate rock physics model. This aspect will be discussed in

more detail in the next chapter. In this thesis I measure attenuation anisotropy in multi-azimuth VSP data sets from arrivals transmitted through fractured rock. The attenuation can then be used as an additional attribute for the characterization of fractures.
The methods of fracture detection from seismic data discussed in this section all yield the orientation of the symmetry planes, i.e. fracture strike and fracture normal, and a measure of the magnitude of anisotropy. The latter is often identified with the fracture intensity, which is a rather qualitative parameter. Only through an appropriate rock physics model it can be related to quantitative fracture properties. The basic concepts of various models with their merits and limitations are discussed in the next chapter.

2.6 Summary

Anisotropic symmetry systems are reflected in the structure of the stiffness tensor, from which the variation of the elastic response with propagation direction of the waves can be derived. The use of seismic anisotropy for fracture characterization is commonly based on a model of vertical parallel fractures in the subsurface, so that the medium has hexagonal symmetry and the elastic properties change as a function of azimuth. The symmetry directions and the magnitude of anisotropy can be derived from shear-wave splitting and the azimuthal variation of velocities and amplitudes. Petrophysical models are required to interpret these further in terms of fracture parameters.

Chapter 3

Review of equivalent medium theory and poroelastic models

3.1 Introduction

I begin this chapter with a review of equivalent medium theories for fractured rock that are commonly used for the interpretation of seismic anisotropy. The models assume that the elastic response is independent of frequency, and there are considerable differences in the predicted anisotropy between models for fluid-saturated fractures. Laboratory data from the past 25 years have given strong evidence of dispersion related to the microstructure of the porosity. I review poroelastic theories and squirt flow models that have been used to explain these effects. A few recent observations suggest that, at seismic frequencies, fractures may play an equally important role in connection with velocity dispersion and attenuation. I discuss the basic concepts of models for fractured rock that include effects of wave-induced fluid motion, frequency and porosity other than the fractures. A squirt-flow model for fractured media, which I use throughout this thesis, is reviewed in detail.

3.2 Equivalent medium theory for fractured media

A medium containing a uniform distribution of heterogeneities can be represented as an equivalent homogeneous medium for wavelengths much longer than the scale associated with the heterogeneities. If the heterogeneities are orientated along preferred directions the resulting effective medium is anisotropic. Equivalent medium theories for materials containing aligned fractures as heterogeneities can therefore establish the link between seismic anisotropy and fracture characteristics, so that fracture properties may be derived from measurements of anisotropy parameters. For analytical solutions to the equivalent medium problem the heterogeneities have to be approximated by simple geometric shapes. Fractures and cracks are commonly modelled as ellipsoids or flat disks ("penny-shaped"). Based on Eshelby's (1957) derivation of the elastic response of an ellipsoidal inclusion embedded in an infinite elastic solid, a number of equivalent medium models for rock containing isolated fractures have been developed (e.g. O'Connell and Budiansky, 1974; Berryman, 1980; Hudson, 1981; Nishizawa, 1982). For a dilute concentration of fractures there is reasonable agreement between these models.
The model of Hudson (1981) is widely used in the interpretation of seismic anisotropy. Its derivation is based upon the analysis of the mean wavefield in an elastic solid containing penny-shaped cracks using scattering theory. The effective elastic tensor $\mathbf{c}$ is given as

$$\mathbf{c} = \mathbf{c^{(0)}} + \epsilon\, \mathbf{c^{(1)}} + \epsilon^2\, \mathbf{c^{(2)}}, \tag{3.1}$$

where $\mathbf{c^{(0)}}$ is the isotropic stiffness tensor of the background medium, $\mathbf{c^{(1)}}$ are the first-order corrections due to the presence of the cracks and $\mathbf{c^{(2)}}$ accounts for crack-crack interaction. ϵ is the crack density, which is defined as the number N of cracks per unit volume times the cube of the crack radius a:

$$\epsilon = N \cdot a^3. \tag{3.2}$$

The first-order correction $\mathbf{c^{(1)}}$ is a function of the elastic parameters of the uncracked solid and the response of the isolated, single crack to normal and shear

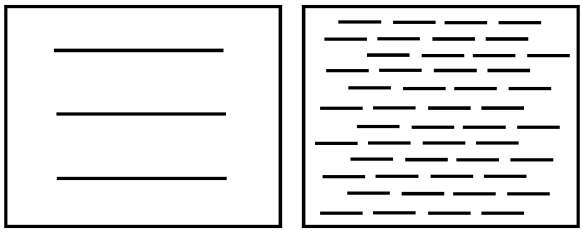

Figure 3.1: The same crack density can be caused by a few large fractures as shown on the left or many small cracks as shown on the right.

traction, respectively. These in turn depend on the crack aspect ratio and the elastic moduli of the material filling the cracks.

In seismic applications the model is used to derive the crack density ϵ, or a relative change in crack density from place to place, from the measured magnitude of azimuthal anisotropy. In terms of a quantitative characterization of fractures, however, the crack density provides only limited information. From Eq. 3.2 it becomes clear that the same crack density can be caused by only a few large fractures or many small microcracks, as demonstrated in Fig. 3.1. With regard to the flow of fluids in the rock and production from a reservoir these two models would have very different properties. Therefore it is of great interest to find a link between parameters such as the fracture size or the fracture volume and seismic anisotropy, which the model of Hudson (1981) and similar models cannot provide.

Another commonly used equivalent medium theory for fractured materials is the linear slip model of Schoenberg (1980), which follows a different approach to the Hudson (1981) model. Here the fractures are modelled as planes of weakness with linear-slip boundary conditions, and the elastic constants are therefore not derived in terms of microstructural parameters. The stiffness tensor of the effective medium is obtained by adding excess compliances $\mathbf{s_f}$ for the fractures to the background compliances $\mathbf{s_b}$ of the host rock and taking the inverse:

$$\mathbf{s} = \mathbf{s_b} + \mathbf{s_f} \qquad \text{and} \qquad \mathbf{c} = \mathbf{s^{-1}}. \tag{3.3}$$

This approach is particularly useful for deriving elastic constants for media of lower symmetry than hexagonal, such as materials containing more than one set

of aligned fractures (Schoenberg and Douma, 1988; Sayers and Kachanov, 1991; Schoenberg and Sayers, 1995; Schoenberg and Helbig, 1997; Sayers, 2002). For each additional fracture set the respective excess compliance can simply be added. Due to rotational invariance about the fracture normal the compliance tensor $\mathbf{s_f}$ contains only two independent elements: the normal and tangential fracture compliances Z_N and Z_T, respectively. Since the effective elastic tensor of the Schoenberg (1980) model is equivalent in form to the effective elastic tensor of microstructural models such as Hudson's (1981), Z_N and Z_T can equally be expressed in terms of microstructural parameters. Liu *et al.* (2000) have derived these expressions for a number of different fracture models; their analysis again demonstrates that an interpretation of measured seismic anisotropy in terms of actual fracture properties using these models is limited.

Both the linear slip model of Schoenberg (1980) and the inclusion-based model of Hudson (1981) are frequency-independent equivalent medium theories, and the fractures or cracks in the models are isolated with respect to flow. Any porosity other than the crack or fracture porosity is not considered in these models.

Mukerji and Mavko (1994) and Thomsen (1995) recognized that the exchange of fluid between compliant parts of the pore space such as fractures or cracks and stiffer more equant pores in the surrounding matrix can have a strong influence on the predicted anisotropy of the rock. Thomsen (1995) developed a model where fluid moves between aligned fractures and equant pores in the matrix, so that pressure is always equalized throughout the pore space. It can thus be regarded as a low frequency limit. Due to the fluid squirt, fluid-filled fractures are much more compliant than in the isolated case, so that the magnitude of anisotropy is considerably increased. Thomsen (1995) found much better agreement between his low-frequency model and laboratory measurements of Rathore *et al.* (1995) on samples containing aligned cracks in a porous matrix, than between the isolated crack model of Hudson (1981) and the data.

In a fracture model where fluid is allowed to flow along wave-induced pressure gradients, fractures are effectively isolated with respect to flow if pressure relaxation takes much longer than the time frame given by the wave period. The unrelaxed state therefore represents the high frequency limit. The low frequency limit, in contrast, is the state where pressure throughout the pore space always has sufficient time to equilibrate. The traditional equivalent medium theories for

fractured rock described in this section can therefore be regarded as representing either high or low frequency limits, bearing in mind that wavelengths still have to be larger than the scale associated with the fractures. For a given seismic experiment, however, it may not be straightforward to judge which model would be more appropriate. Furthermore, there is the need for a model that can also handle the frequency range in between the low and high limits, as there are a number of observations from seismic data that cannot be explained by frequency-independent behaviour (*see* Section 3.4).
Effects of wave-induced fluid motion in isotropic porous rock have been studied for many years, mostly in connection with laboratory data. The main results of these efforts are discussed in the following section, whereas attempts to model the effects in anisotropic fractured rock are the subject of Sections 3.5 and 3.6.

3.3 Poroelasticity and squirt flow

Theories of poroelasticity describe the deformation of a porous and permeable material that is saturated with a fluid. The most widely accepted model is the Biot-Gassmann theory of poroelasticity (Gassmann, 1951; Biot, 1956). Gassmann (1951) derived simple expressions for the bulk and shear moduli of a saturated isotropic rock as a function of dry rock parameters and the fluid bulk modulus:

$$\begin{aligned} \frac{k_{\rm sat}}{k_0 - k_{\rm sat}} &= \frac{k_{\rm dry}}{k_0 - k_{\rm dry}} + \frac{k_f}{\phi(k_0 - k_f)}, \\ \mu_{\rm sat} &= \mu_{\rm dry}. \end{aligned} \tag{3.4}$$

$k_{\rm sat}$ and $\mu_{\rm sat}$ are the effective bulk and shear moduli of the saturated rock, $k_{\rm dry}$ and $\mu_{\rm dry}$ are the effective bulk and shear moduli of the dry rock frame, k_0 is the bulk modulus of the mineral material making up the rock, k_f is the fluid bulk modulus and ϕ is the porosity. An extension of Gassmann's relations for anisotropic rock has been given by Brown and Korringa (1975). The theory assumes that the porosity in the rock is completely connected and that pressure is always equalized throughout the pore space during deformation. It is therefore thought to be valid in the static limit or for very low frequencies. Based on laboratory measurements in the frequency range of a few hundred Hz to a few

kHz that could be reasonably well matched with Gassmann's relations, it is often stated that seismic frequencies can be regarded as the low-frequency limit (e.g. Murphy, 1984, 1985; Wang and Nur, 1992; Mavko and Mukerji, 1995; Nolen-Hoeksema, 2000). Nevertheless, recent observations suggest that this may not always be true (*see* Section 3.4). Furthermore, many studies have shown that particularly at higher frequencies the Gassmann predictions often underestimate measured velocities and only appear to work better at high values of effective stress where microcracks are closed (e.g. King, 1966; Coyner and Cheng, 1984; Murphy, 1985; Winkler, 1986; Mavko and Jizba, 1991; Wang, 1992). This observation led to the development of a range of dynamic theories.

Biot (1956) considered viscous and inertial interaction between the fluid and the solid and derived a theory to predict saturated velocities as a function of frequency from dry rock parameters. The model reduces to Gassmann's equations in the low-frequency limit. The critical frequency f_c where transition from a low-frequency regime to a high-frequency regime occurs is given by $f_c = \frac{\phi\eta}{2\pi\rho_f\kappa}$, where η is the fluid viscosity, ρ_f is the fluid density and κ is the permeability of the rock. Values for f_c are high and generally lie between 50 kHz and 1 GHz (Bourbié *et al.*, 1987; Mavko *et al.*, 1998). Biot's theory predicts the existence of a third body wave, the "slow" P-wave, which has been observed experimentally (Plona, 1980; Klimentos and McCann, 1988; Kelder and Smeulders, 1997). Although this is generally considered as a validation of the theory, it has been found that the model significantly underestimates velocity dispersion and attenuation measured in laboratory data (King, 1966; Winkler, 1985, 1986; Han, 1986; Wang and Nur, 1990; Mavko and Jizba, 1991). Furthermore, the proportionality between f_c and η leads to the prediction that velocities decrease with increasing viscosity of the pore fluid. This is in contradiction to experimental results (e.g. Geertsma, 1961; Winkler, 1985; Jones, 1986). It therefore appears that the Biot mechanism, describing the "drag" of the fluid due to movement of the solid, cannot account fully for poroelastic effects seen in data.

A process that is not considered in Biot's theory but is very powerful in explaining large magnitudes of velocity dispersion and attenuation is squirt flow. In general we can expect the pore space of a rock to be heterogeneous. Due to different geometries and orientations of the pores, a passing elastic wave induces pressure gradients that can be away from the propagation direction of the wave. Fluid then

flows along these gradients, i.e. it is squirted out of the more compliant parts of the pore space into the stiffer parts of the pore space during compression and flows back again during dilatation. Velocities and attenuation generally depend on the frequency of the elastic wave in relation to the time that is needed to equalize the pressure. The characteristic frequency associated with the squirt-flow mechanism is inversely proportional to viscosity, in contrast to the Biot frequency. Thus, squirt flow predicts an increase in velocity with increasing viscosity of the pore fluid, which is in agreement with experimental results.

Mavko and Jizba (1991) included the concept of squirt flow in a model that predicts the high-frequency saturated moduli from dry rock properties without explicitly describing the microstructure. They found reasonable agreement of the modelled velocities with laboratory data. The theory has been extended by Dvorkin *et al.* (1995) for all frequencies. The model does not include the Biot mechanism. A fundamental prediction of the model is proportionality between the dispersion in shear modulus and the dispersion in bulk modulus.

In addition to these theories, other models have been developed that explicitly consider microstructural aspects of the pore space. O'Connell and Budiansky (1977) derived a squirt flow model for media containing randomly oriented cracks of small aspect ratio. Because the same pressure would be introduced in each crack under hydrostatic stress, there is no dispersion in the bulk modulus, but only in the shear modulus. However, this result will not hold in the case where equant pores and cracks of different aspect ratio are present, which would be a more realistic representation of a rock's pore space. Furthermore, O'Connell and Budiansky (1977) argue that the bulk modulus of the saturated rock is equal to the bulk modulus of the mineral material making up the rock, which is only consistent with Gassmann's relations in the limit of zero porosity. Johnston *et al.* (1979) derived a model for squirt flow between thin cracks and spherical pores, where in contrast to O'Connell and Budiansky's (1977) results there is no dispersion in the absence of pores. It therefore does not consider squirt flow between cracks of different orientation.

Endres and Knight (1997) presented a comprehensive study of calculating the magnitude of dispersion between the low and high frequency limits as a function of the aspect ratio distribution. The low-frequency moduli are consistent with Gassmann's relations, and the overall results address limitations of previous

models. Their main findings are as follows: If only spherical pores are present neither bulk compression nor shear will introduce any pressure gradients and therefore there is no dispersion at all. In the presence of cracks and pores both the bulk and the shear modulus are dispersive, and there is squirt flow between cracks and pores as well as between cracks of different orientation. If the rock contains only cracks of a constant aspect ratio there is dispersion in the shear modulus due to different orientations of cracks, but not in the bulk modulus. This is in contrast to the theories of Mavko and Jizba (1991) and Dvorkin *et al.* (1995) which predicted the dispersion in shear modulus to be proportional to the dispersion in bulk modulus. Endres and Knight (1997) confirm their findings with experimental data. With regard to the models of O'Connell and Budiansky (1977) and Johnston *et al.* (1979), the results of Endres and Knight (1997) demonstrate the importance of considering both the difference in pore geometry as well as the orientation of low aspect ratio pores for the derivation of squirt flow models.

A poroelastic model for the entire frequency range that retains the fundamental results of Endres and Knight (1997) has been developed by Chapman (2001). It is consistent with Gassmann's relations at zero frequency and predicts the existence of the slow Biot wave. The porosity in the model consists of cracks and spherical pores that are placed on the vertices of a random lattice. Local flow is then considered between nearest neighbours. Chapman (2001) finds that the model can explain experimental data from Sothcott *et al.* (2000), where velocities were measured as a function of frequency, fluid saturation and effective stress.

The theories discussed in this section consider effects of pore structure and fluid flow on the grain scale, and the significance of these effects has been recognized through a considerable number of laboratory studies. With regard to seismic data, however, there can be additional pore space heterogeneity due to the presence of fractures that are much larger than the grain scale. An accurate model should therefore take account of these different scales and any resulting effects of dispersion.

3.4 Observations of velocity dispersion and attenuation

Many laboratory experiments have given evidence of velocity dispersion and attenuation at the kHz to MHz frequency range. It is generally observed that attenuation is larger in fully saturated rock than in fully dry rock, and that it decreases with increasing effective stress where microcracks close (Gardner *et al.*, 1964; Toksöz *et al.*, 1979; Winkler and Nur, 1979; Johnston and Toksöz, 1980; Johnston, 1981; Spencer, 1981; Tittmann *et al.*, 1981; Winkler, 1986). Therefore it is widely accepted that fluid flow and the microstructure of the pore space play an important role in explaining these observations, despite the differences in actual theoretical models pointed out in the last section. Peaks in attenuation have been observed from frequencies around a few kHz (Nur and Winkler, 1980; Tittmann *et al.*, 1981; Winkler, 1986) up to ultrasonic frequencies (Mason *et al.*, 1978; Toksöz *et al.*, 1979). Sams *et al.* (1997) compared velocities and attenuation measured in saturated sedimentary rock from VSP, crosshole, sonic and laboratory data and found a peak in attenuation in the sonic frequency range (8-24 kHz). Similar magnitudes of velocity dispersion between VSP and sonic data have been reported by Stewart *et al.* (1984) and Brown and Seifert (1997). All these studies suggest that characteristic frequencies for squirt flow associated with the pore microstructure lie somewhere between the sonic and ultrasonic range. In consequence it is often concluded that seismic frequencies represent the low frequency limit, but a number of studies have shown contradictory evidence.
Fig. 3.2 shows data from Spencer (1981) who observed attenuation peaks around 500 Hz for saturated sandstone and at 10-20 Hz for saturated limestone, whereas the dry samples showed no attenuation. Kan *et al.* (1983) and Raikes and White (1984) found evidence of frequency-dependent attenuation in wideband VSP data (10-375 Hz). Furthermore, there are numerous VSP studies that report similar magnitudes of attenuation in situ as has been measured in the laboratory at the attenuation peaks (e.g. Hauge, 1981; Stainsby and Worthington, 1985; De *et al.*, 1994). These could not be explained by scattering due to thin layers and were attributed to intrinsic attenuation, but an interpretation in terms of rock physical properties is less clear.

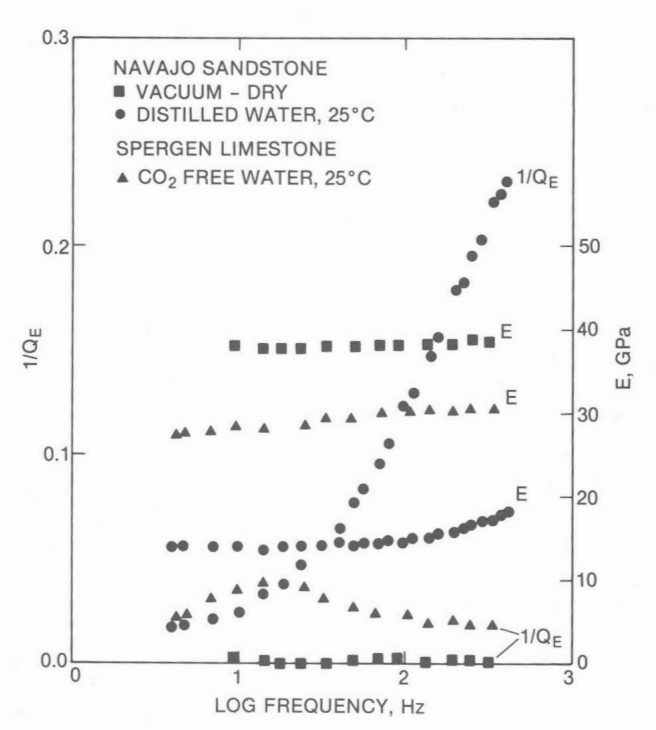

Figure 3.2: Attenuation Q_E^{-1} and Young's modulus E as a function of frequency for dry and saturated rock measured by Spencer (1981). The saturated samples show attenuation peaks below sonic frequencies, whereas no attenuation is detected for dry rock. (*From Johnston (1981).*)

As mentioned earlier, on the scale of seismic wavelengths there may be additional pore space heterogeneity due to the presence of fractures. How this affects velocity dispersion and anisotropy measured in the field, however, is not well understood. Again there is evidence of anisotropic attenuation from laboratory experiments (e.g. Johnston, 1981). Lockner *et al.* (1977) measured attenuation anisotropy in saturated rock under differential stress where microcracks close in certain directions, so that the rock becomes anisotropic. It therefore seems logical to assume that similar effects could occur on a larger scale when fractures are present.

In recent years there have been some observations of dispersive effects in connection with anisotropy and fracturing from seismic data. Systematic azimuthal variations of transmitted P- and S-wave amplitudes in walkaround VSP data that correlated with observed velocity anisotropy have been reported by Liu *et al.* (1993b) and Horne and MacBeth (1997). Modelling results showed that the observations could in principle be explained by anisotropic attenuation. Chen (1995)

studied seismic anisotropy in 9-component reflection data from a fractured tight gas reservoir. Through analysis of the spectral content of the data he found high attenuation in regions of high anisotropy that were interpreted as fracture zones. Clark *et al.* (2001) measured P-wave attenuation as a function of azimuth from 3D reflection seismic data. The results showed a systematic azimuthal variation in attenuation that indicated the same symmetries as previous AVOAZ studies. Furthermore, the azimuth of maximum attenuation matched the azimuth of lowest NMO velocities. Bates *et al.* (1995) and Liu *et al.* (2003) measured shear-wave splitting in VSP data from a fractured tight gas reservoir and found that the time delay between split shear waves changes with frequency. van der Kolk *et al.* (2001) analysed 3D seismic data from a fractured carbonate reservoir and reported a large increase in shear-wave splitting together with attenuation of higher frequencies in a region that coincided with the gas-oil contact. Particularly interesting in this example is the role of the fluid, since the shear-wave splitting and attenuation anomaly is only observed where gas replaces oil in the reservoir. Under the assumption of seismic frequencies representing the low-frequency limit, however, vertically propagating shear waves should not be affected by the fluid if the fractures are vertical.

Observations of this kind have not received much attention in the past, reflecting the limitations of traditional equivalent medium theories for fractured rock that were outlined in Section 3.2. Only recently have there been advances on the theoretical aspect of incorporating effects of matrix porosity, fluid flow and frequency into fracture models. This will be discussed in the remainder of this chapter.

3.5 Dispersive equivalent medium theory for fractured media

A number of dispersive equivalent medium theories that consider fluid motion in rock containing aligned fractures and predict elastic constants as a function of frequency have been developed recently. Hudson *et al.* (1996) considered the cases of flow between cracks ("interconnected cracks") and flow between cracks and smaller equant pores. The resulting expressions for the stiffness constants are of similar form as in the earlier isolated crack model of Hudson (1981), except that

the response of the crack to normal traction entering the first-order corrections is now frequency dependent. Theoretical predictions of the models were studied in great detail by Pointer *et al.* (2000). The equant porosity model predicts significant attenuation anisotropy at seismic frequencies for a range of rock properties commonly encountered in sedimentary rock (Pointer *et al.*, 2000; Maultzsch *et al.*, 2003b). At zero frequency, however, the model reduces to the result given by Hudson (1981) for dry cracks, which is in contradiction to Gassmann's formulae. It can therefore not be assumed that the model is valid over the entire frequency range, but it is unclear what the exact limits would be. Gurevich *et al.* (2003) suggested circumventing the problem by first computing zero-frequency saturated stiffnesses from the dry ones using Brown and Korringa's (1975) equations and then applying an empirical frequency correction based on the dispersion relation of the Hudson *et al.* (1996) equant porosity model. Another unsatisfactory and related aspect of the model is that no account is taken of the mechanical effect of the porosity. The equant porosity enters the model only through the frequency-dependent term in the response of the crack to normal traction.

In the interconnected crack model Hudson *et al.* (1996) considered fluid flow along mechanically "invisible" pathways between aligned cracks. The flow then only occurs on a wavelength scale and in the direction of wave propagation. The mechanism becomes more important as the wavelength and thus the distance between peaks and troughs of the stress field decreases. At seismic wavelengths this form of global flow as predicted by the model only causes significant velocity dispersion and attenuation if the permeability is very high, i.e. $\gg 1$ D (Tod and Liu, 2002; Maultzsch *et al.*, 2003b). It is however questionable whether in such a case it is still realistic to model the fluid pathways as mechanically invisible if they permit flow over tens of metres within the time scale associated with the seismic wave period.

A further equivalent medium theory describing velocity dispersion in fluid saturated rock with aligned fractures has been suggested by van der Kolk *et al.* (2001) (the BOSK model). The authors combine the model of O'Connell and Budiansky (1977) for squirt flow between randomly oriented cracks with results of Sayers and Kachanov (1991) to orient the cracks in one plane. They find that the BOSK model can in principle explain the shear-wave anisotropy and attenuation anomaly mentioned in the previous section, which they observed over a fractured

carbonate reservoir. The petrophysical interpretation of the model, however, is difficult, because the squirt flow in the original theory of O'Connell and Budiansky (1977) is only caused by the difference in orientation of the cracks. The actual flow mechanism leading to dispersion in the BOSK model, where the cracks are aligned, is therefore not clear (Hudson and Crampin, 2003).

Chapman (2003) has extended the earlier poroelastic model of Chapman (2001) and Chapman *et al.* (2002), which was mentioned in Section 3.4, to include aligned fractures on a scale larger than the grain scale. In contrast to the other fracture models discussed in this section, it explicitly considers two different scales of pore space: the grain scale where squirt flow occurs between microcracks and equant pores and between differently oriented microcracks, as well as a larger scale where squirt flow takes place between fractures and the porosity in the surrounding matrix. Moreover, the model is still a full poroelastic theory in the absence of fractures where it simply returns to the earlier microstructural model of Chapman (2001). This in principle allows the theory to be tested and calibrated against laboratory data on samples that do not contain large fractures. In the high frequency limit the model is consistent with the equivalent medium theory of Hudson (1981) for rock containing isolated fractures. At zero frequency the model agrees with the anisotropic Gassmann equations of Brown and Korringa (1975).

Similarly to the equant porosity model of Hudson *et al.* (1996) and the BOSK model of van der Kolk *et al.* (2001), the theory predicts that frequency-dependent anisotropy can be significant in the seismic frequency range, so that observations such as the examples given in Section 3.4 could potentially be explained. Compared to the other theories the model of Chapman (2003) appears to have the advantage that it takes account of the mechanical effect of the porosity, describes the squirt flow process explicitly considering two scales of pore space heterogeneity and that it is correct in its frequency limits. Since I will use the model throughout this thesis, it is worthwhile to discuss it in more detail in the following section. I will also perform a calibration of the model against published laboratory data.

3.6 The model of Chapman, 2003

3.6.1 Basic concepts of the model

The poroelastic equivalent medium theory of Chapman (2003) models the pore space of a rock as a lattice configuration of spherical pores, randomly oriented ellipsoidal microcracks and aligned ellipsoidal fractures. The size of the pores and microcracks is identified with the grain size, whereas the fractures are allowed to be larger as long as size and spacing remain smaller than the seismic wavelength. Since the fractures are aligned along a preferred direction and are rotationally invariant about their normals the resulting effective medium is of hexagonal symmetry (or transversely isotropic).

Pair-wise fluid exchange takes place between adjacent elements of pore space due to wave-induced pressure gradients. It should be noted that the pore space is fully saturated with one type of fluid and effects of partial saturation are not considered. Based on D'Arcy's law for fluid filtration in a permeable material the mass flow between adjacent voids a and b is described as follows:

$$\partial_t m_a = \frac{\rho_0 \kappa \varsigma}{\eta}(p_b - p_a). \tag{3.5}$$

m_a is the fluid mass in element a, ρ_0 is the fluid density, η is the fluid viscosity, κ is the permeability, ς is the grain size and p_i is the pressure in the ith element. Some assumptions have to be made about the number of connections between the voids. The fractures are larger than the microcracks and pores, and thus will have more adjacent voids, with which fluid is exchanged. To ensure that there is some spacing between the fractures it is assumed that each pore or microcrack is connected to at most one fracture, and that fractures are not connected to each other. It follows that the number of microcracks and pores must vastly exceed the number of fractures.

Based on Eq. 3.5 Chapman (2003) now derives expressions for the expected mass flow out of an individual fracture, microcrack and pore in terms of expected pressure gradients. Furthermore, the mass in each element of pore space is written as a function of inclusion pressure and applied stress. Chapman (2003) then solves for the time-variant pressure in each type of inclusion in terms of the imposed stress field. The derivation ensures that mass is conserved throughout the pore

space. Finally, the effective elastic constants are calculated using Eshelby's (1957) interaction energy approach for a material with embedded inclusions, where stress and strain inside the inclusions are calculated from the derived time-dependent pressures. The resulting formulas for the elastic constants are given explicitly in Chapman (2003).

The effective stiffness tensor of the model is of the form:

$$\mathbf{c} = \mathbf{c^{(0)}} - \Phi_p \mathbf{c^{(1)}} - \epsilon_c \mathbf{c^{(2)}} - \epsilon_f \mathbf{c^{(3)}}. \tag{3.6}$$

$\mathbf{c^{(0)}}$ is the isotropic elastic tensor of the mineral material making up the rock with Lamé constants λ and μ; $\mathbf{c^{(1)}}$, $\mathbf{c^{(2)}}$ and $\mathbf{c^{(3)}}$ are the contributions from pores, microcracks and fractures, respectively, multiplied by the porosity Φ_p, the crack density ϵ_c and the fracture density ϵ_f. These contributions are functions of the Lamé parameters, fluid and fracture properties, frequency and relaxation times associated with the squirt flow. The fact that two scales of pore space are considered in the modelling of fluid exchange leads to the existence of two such relaxation times (or characteristic frequencies). Fluid flow between microcracks and pores is associated with the traditional squirt-flow frequency $f_m^c = 1/\tau_m$, which experiments suggest lies between the sonic and ultrasonic range (Murphy, 1985; Winkler, 1986; Lucet and Zinszner, 1992; Sothcott *et al.*, 2000, *see* Section 3.4). τ_m is given by

$$\tau_m = \frac{c_v \eta (1 + K_c)}{\sigma_c \kappa \varsigma c_1}, \tag{3.7}$$

where c_v is the volume of an individual crack and c_1 is the number of connections to other voids. $\sigma_c = \frac{\pi \mu r}{2(1-\nu)}$ is the critical stress and $K_c = \sigma_c / k_f$ with r being the aspect ratio of the cracks, ν Poisson's ratio of the matrix and k_f the fluid bulk modulus. The flow in and out of fractures is characterized by a lower frequency or larger time scale constant τ_f, which depends on the size of the fractures. With increasing fracture radius the ratio of surface area to volume decreases. Therefore, more volume of fluid has to move through a constant element of surface area to equilibrate the pressure, which requires more time. The two time-scale parameters are related to each other by the expression

$$\tau_f = \frac{a_f}{\varsigma} \tau_m, \tag{3.8}$$

where a_f is the fracture radius. It is the larger relaxation time τ_f which leads to velocity dispersion and attenuation in the seismic frequency range. In consequence, the anisotropy caused by the alignment of the fractures is frequency dependent.

3.6.2 Parameterization

The effective stiffness tensor of the Chapman (2003) model depends on the following parameters: the Lamé parameters λ and μ of the mineral grains, the density of the rock ρ, the porosity Φ_p, the crack density ϵ_c, the fracture density ϵ_f, the aspect ratio r of fractures and cracks, the fracture radius a_f, the fluid bulk modulus k_f, and the relaxation time τ_m. For practical applications it is desirable to reduce the number of free parameters to those that can be directly measured from physical properties of the rock or otherwise inverted from data.
The interaction energy approach of Eshelby (1957), which is used in deriving the effective elastic tensor of the Chapman (2003) model, is only valid for dilute concentrations of inclusions. The model is therefore formally restricted to low porosity, and the use of the grain moduli λ and μ in the calculation of the fracture correction is expected to result in substantial errors if the porosity is high. Furthermore, it is unsatisfactory for a user having to specify moduli that cannot be obtained from measured velocities. To circumvent this problem, Chapman *et al.* (2003) suggest a slightly modified version, which is based on similar ideas to the self-consistent scheme (Zimmerman, 1991) where the effect of the inclusions is evaluated as a function of the as yet unknown effective stiffness tensor of the porous material. Chapman *et al.* (2003) propose to use Lamé parameters λ° and μ° for the corrections that are derived from the velocities V_P° and V_S° of the unfractured porous rock. Additionally, $\mathbf{c^{(0)}}(\Lambda, \mathrm{M})$ is required to be defined in such a way that the measured isotropic velocities are obtained by applying the crack and pore correction at a reference frequency f_0. Therefore, we must have

$$\begin{aligned} \Lambda &= \lambda^\circ + \Phi_{c,p}(\lambda^\circ, \mu^\circ, f_0), \\ \mathrm{M} &= \mu^\circ + \Phi_{c,p}(\lambda^\circ, \mu^\circ, f_0), \end{aligned} \tag{3.9}$$

with $\mu^\circ = \rho(V_\mathrm{S}^\circ)^2$; $\lambda^\circ = \rho(V_\mathrm{P}^\circ)^2 - 2\mu^\circ$. Eq. 3.6 is then written as

$$\mathbf{c}(f) = \mathbf{c^{(0)}}(\Lambda, \mathrm{M}) - \Phi_p \mathbf{c^{(1)}}(\lambda^\circ, \mu^\circ, f) - \epsilon_c \mathbf{c^{(2)}}(\lambda^\circ, \mu^\circ, f) - \epsilon_f \mathbf{c^{(3)}}(\lambda^\circ, \mu^\circ, f), \quad (3.10)$$

where f is the frequency. Now the corrections for microcracks, pores and fractures, which describe the frequency dependence and anisotropy of the material, will be calculated with physical properties obtained from measured velocities rather than being fitted to the data. The use of measured velocities for the definition of the Lamé parameters instead of grain moduli is also common practice in the application of other equivalent medium theories, such as the models of Hudson *et al.* (1996).

Chapman *et al.* (2003) show that in cases of high porosity the model can be further simplified by setting the microcrack density ϵ_c to zero. The influence of the parameter is negligible for modelling the effect of fractures if the spherical porosity is significantly larger than the crack porosity. This is the case for most clastic reservoir rocks found in sedimentary basins, and therefore the number of variables can be further reduced in these applications. However, the assumption of negligible microcrack porosity compared to equant porosity may not hold for fractured carbonate reservoir rocks.

Another parameter that has to be specified in the model, but is usually unknown, is the aspect ratio r of the cracks and fractures. It enters the calculations through the term $1 + K_c = 1 + \frac{\pi\mu r}{2k_f(1-\nu)}$. We can see that for fluid fill and small aspect ratios $K_c \ll 1$, so that the effective elastic constants will be insensitive to the exact value of r as long as it is small enough. Since the cracks and fractures in the model represent the flat, compliant part of the pore space in contrast to stiffer, high aspect-ratio pores, it is reasonable to assume r to be small.

The parameter that is most difficult to determine is the relaxation time τ_m. Estimates can be obtained by calibrating the model against published laboratory data, which I will describe in the following section. For applications to field data the calibrated value then has to be corrected according to changes in fluid and rock properties (Maultzsch *et al.*, 2003a).

3.6.3 Calibration with laboratory data

The laboratory data of Rathore *et al.* (1995) have found wide application in the past to test equivalent medium theories for fractured rock (Thomsen, 1995; Hudson *et al.*, 2001). Rathore *et al.* (1995) performed velocity measurements on synthetic porous sandstone samples that contained aligned fractures of known geometry. The samples were manufactured by embedding thin metal discs into a sand-epoxy matrix, which were chemically leached out later on. P- and S-wave velocities were measured as a function of angle from the fracture normal at a frequency of 100 kHz.

Rathore *et al.* (1995), Thomsen (1995) and Hudson *et al.* (2001) used the data to test equivalent medium models and discuss their differences. Rathore *et al.* (1995) and Thomsen (1995) found that for fluid-saturated samples the data are well matched by the Thomsen equant porosity model where pressure in the pore space is always relaxed and anisotropy is increased due to the fluid squirt from fractures into matrix porosity. While the Hudson (1981) model for isolated fractures gives a poor fit, the data were satisfactorily matched with the equant porosity model of Hudson *et al.* (1996) if the matrix wave speeds were themselves fitted to the data and not taken from measured velocities (Hudson *et al.*, 2001).

I now test the Chapman (2003) model against the data, which also yields a value for the relaxation time τ_m. All relevant parameters are given in Table 3.1. The only free variable in the modelling is the relaxation time. I seek the value of τ_m that minimizes the misfit between data and model. Fig. 3.3 shows the error curve as a function of τ_m. There is a minimum at $\tau_m = 0.27\mu$s. This value is used

v_{P}	2678 m/s
v_{S}	1384 m/s
ρ	1712 kg/m^3
f	100 kHz
ϵ_f	0.1
a_f	2.75 mm
r	0.0036
Φ_p	34.6%
k_f	2.16 GPa

Table 3.1: Parameters of the Rathore experiment.

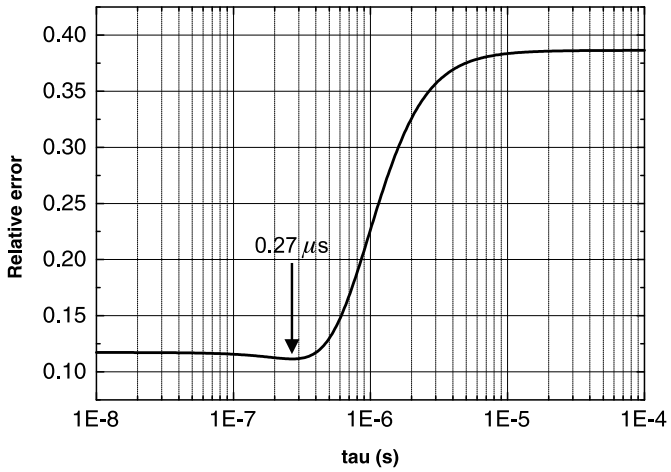

Figure 3.3: Relative RMS error between measured and modelled velocities as a function of τ_m. There is a minimum at $\tau_m = 0.27\mu$s.

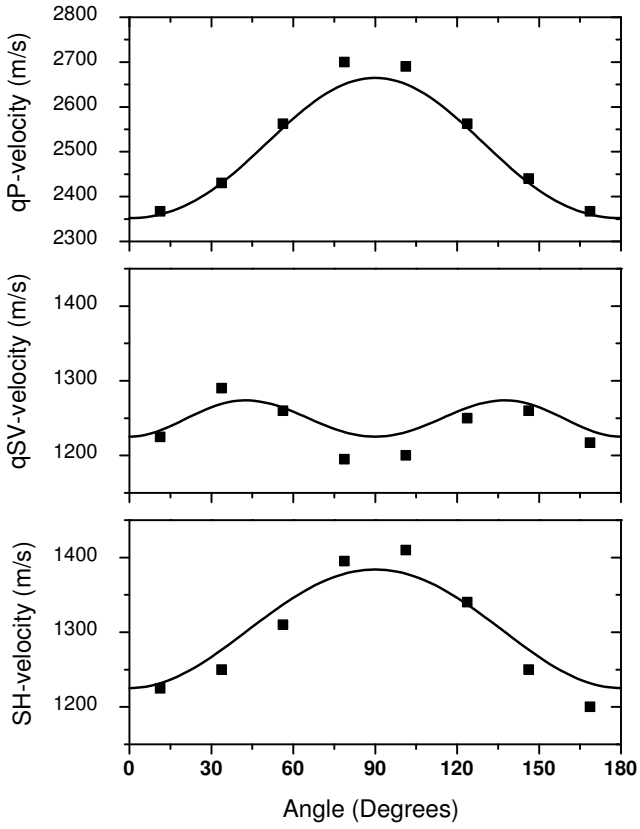

Figure 3.4: Modelled velocities for the optimum τ_m-value in comparison with the data of Rathore *et al.* (1995) (squares).

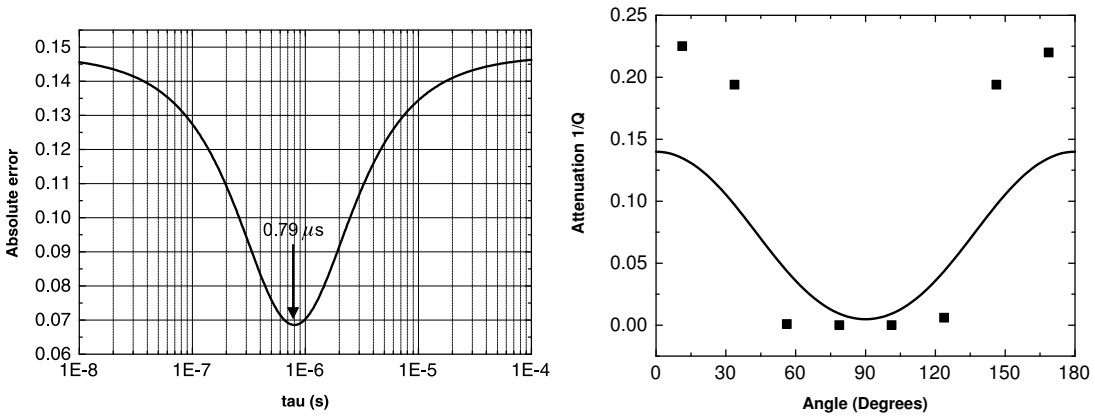

(a) (b)

Figure 3.5: Fit to the attenuation data reported by Thomsen (1995). a) Error curve, b) Modelled and measured values.

to compute P- and S-wave velocities as a function of angle, which are displayed together with the data from Rathore *et al.* (1995) in Fig. 3.4. The modelled velocities match the data well. The error curve in Fig. 3.3 supports the findings of Rathore *et al.* (1995) and Thomsen (1995) that the data can be better explained by a low frequency model (small τ_m) with perfect fluid communication than by a high frequency model (high τ_m) where fractures are isolated with respect to flow. The misfit for the optimum τ_m value is not significantly smaller than for the low frequency limit. Therefore, I also attempt to model the attenuation data which were reported by Thomsen (1995). Fig. 3.5 shows the corresponding error curve and optimum model values in comparison with the data points. In this case the error function has a distinct minimum, which is near the value obtained for the velocity modelling. This result constrains the estimate for τ_m against the lower frequency limit. A perfect numerical match with the attenuation data cannot be expected, because scattering effects are likely to play a role as well (Hudson *et al.*, 2001).

The value of 0.27 μs for τ_m is obtained for the specific rock and fluid properties of the samples used in the Rathore experiments. Chapman (2001) obtained a value of 20 μs from calibrating the unfractured poroelastic model against resonant bar data from Sothcott *et al.* (2000). I will now compare the two estimates by applying

corrections to the second one to match fluid and rock properties of the Rathore experiment.

Sothcott *et al.* (2000) measured velocities on porous sandstone samples under 10-40 MPa effective stress. The porosity of the rock was 22.7% and the density 2288 kg/m^3. The samples were brine-saturated with a fluid bulk modulus of 2.91 GPa. From Eq. 3.7 we see that

$$\tau_m \propto \eta \left(\frac{1}{\sigma_c} + \frac{1}{k_f} \right) \qquad \text{and} \qquad \tau_m \propto \frac{1}{\kappa}. \tag{3.11}$$

Since the samples in the Rathore experiment were saturated with water, there is very little change in viscosity and fluid bulk modulus. There are, however, differences in the elastic parameters of the rock matrix. The first proportionality in Eq. 3.11 yields a factor of 0.069 to 0.087 for 10 to 40 MPa effective stress, by which τ_m has to be corrected. With respect to the dependence of τ_m on permeability the difficulty occurs that explicit permeability values are not known in either experiment. However, the porosities are given in both cases, and I propose to infer the change in permeability from the porosity change. For this purpose I use an extended form of the Kozeny-Carman relationship given by Mavko and Nur (1997), which considers the existence of a percolation threshold. It can explain experimentally observed changes in permeability with porosity over a wide range of porosity values, whereas the original form of the Kozeny-Carman relation contains an additional free parameter that is porosity-dependent. Mavko and Nur (1997) give the equation

$$\kappa = B \frac{(\Phi - \Phi_c)^3}{(1 + \Phi_c - \Phi)^2} d^2, \tag{3.12}$$

where B is a geometric factor, d is the characteristic grain dimension and Φ_c is the percolation porosity. The latter parameter is usually of the order of 1-3% (Mavko and Nur, 1997), and I assume B and d to be the same in both cases. Taking $\Phi_c = 2\%$, Eq. 3.12 gives an increase in permeability by a factor of 5.41 between the sandstone used in Sothcott's (2000) experiment and the Rathore *et al.* (1995) samples. The resulting value of τ_m inferred from Sothcott's data for the Rathore experiment varies between 0.26 μs and 0.32 μs for effective stresses of 10 to 40 MPa. These results are consistent with the result of numerically fitting

the Chapman (2003) model to the data of Rathore *et al.* (1995), which gave a value of 0.27 μs for τ_m. If the relaxation time has to be defined for an application of the model to field data, the same procedure of correcting the calibrated values according to changes in fluid and rock properties can be followed.

3.6.4 Predictions of the model

In order to show some numerical predictions of the model I choose a set of parameters given in Table 3.2. In the absence of fractures the model predicts P- and S-wave velocity dispersion associated with the relaxation time τ_m that represents the traditional squirt-flow frequency. If, however, fractures are present, there is velocity dispersion at a lower frequency associated with the relaxation time τ_f for the flow in and out of fractures. Since the fractures are aligned, velocities and the dispersion also depend on propagation direction. The corresponding P- and S-wave dispersion curves are shown in Fig. 3.6. In the anisotropic case the qP-wave travelling in the fracture plane shows no dispersion, while the velocity of the qP-wave travelling normal to the fractures is strongly frequency dependent. Similarly, the pure shear wave (SH), which is polarized in the fracture plane, is frequency independent, whereas the quasi-shear wave (qSV) shows velocity dispersion. Hence, the magnitude of anisotropy varies with frequency, and it is largest in the low-frequency limit while it decreases towards higher frequencies. The velocity dispersion at seismic frequencies in the fractured rock is associated with a peak in attenuation, as shown in Fig. 3.7 for qP-waves travelling at 60°

v_{P}	4780 m/s
v_{S}	2750 m/s
ρ	2300 kg/m^3
f	40 Hz
ϵ_c	0.1
ϵ_f	0.05
a_f	20 cm
r	0.0001
Φ_p	0.10
k_f	2.25 GPa
τ_m	20 μs

Table 3.2: Parameters that were used in the modelling.

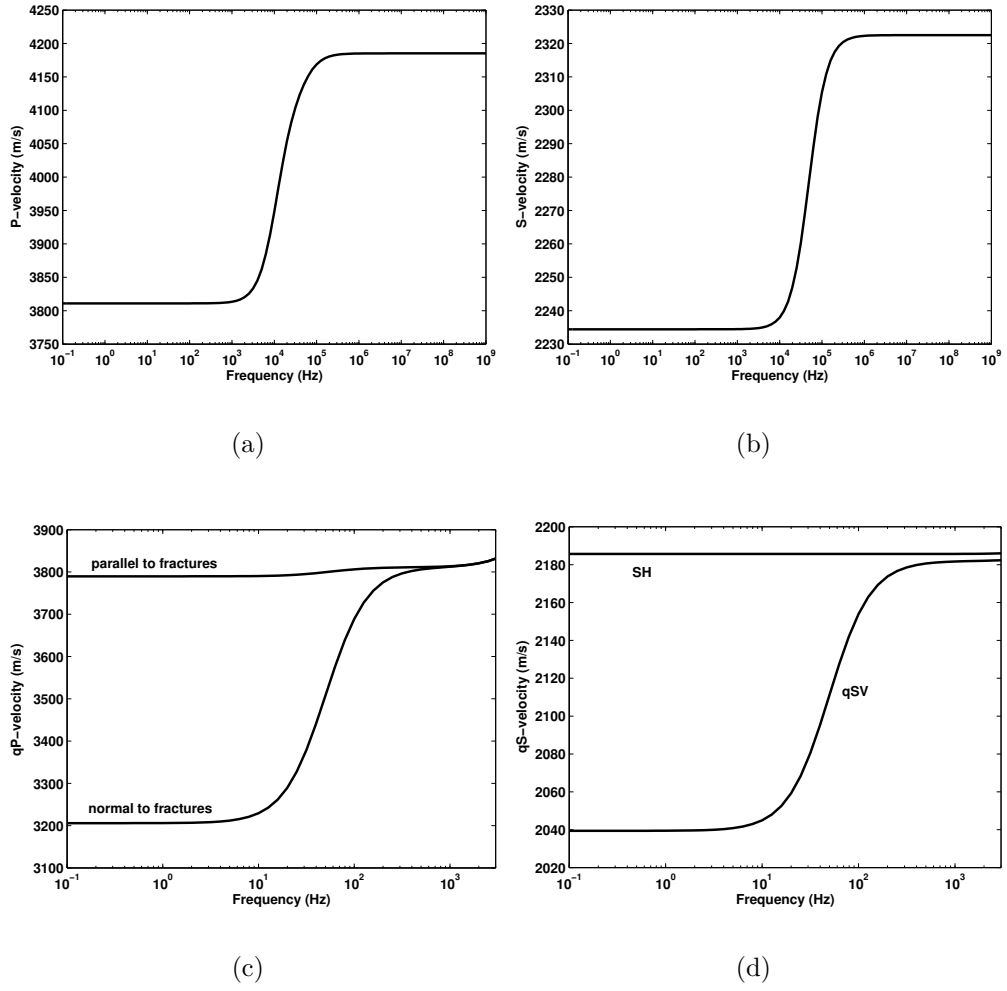

Figure 3.6: P- and S-wave velocity dispersion: a,b) In the absence of fractures; c,d) In the presence of fractures. The anisotropy caused by the fractures is frequency dependent showing a decrease in magnitude with increasing frequency.

from the fracture normal. The angular variation of the three body-wave velocities at a frequency of 40 Hz is displayed in Fig. 3.8. The qP-wave velocity shows a $\cos(2\theta)$-variation, where θ is the angle from the fracture normal. In contrast, theories for isolated fractures such as the model of Hudson (1981) predict a $\cos(4\theta)$-variation for fluid filled fractures, which causes the poor match between these models and the Rathore data (Thomsen, 1995).

Since τ_f is a function of the fracture size, the frequency range in which anisotropy changes with frequency also depends on this parameter. Fig. 3.9 shows the percentage shear-wave anisotropy, defined as $100 \cdot (v_{\mathrm{SH}} - v_{\mathrm{SV}})/v_{\mathrm{SH}}$, as a function

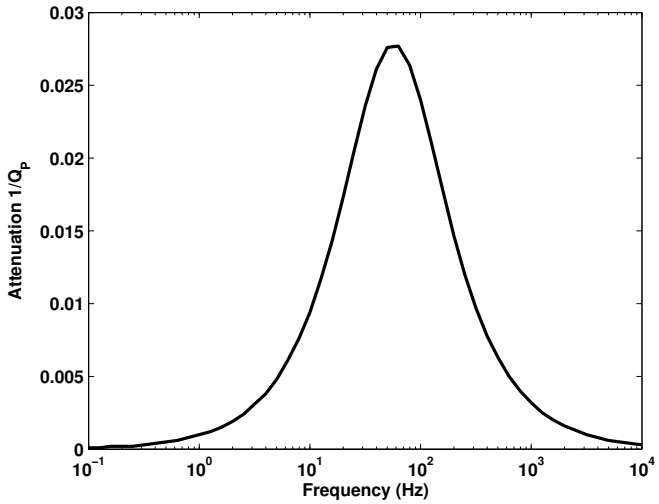

Figure 3.7: Attenuation of qP-waves travelling at an angle of 60° from the fracture normal. There is a peak in attenuation in the seismic frequency range where maximum velocity dispersion occurs.

of frequency for various fracture sizes. The shear waves are travelling at an angle of 60° from the fracture normal. The equant porosity is 10% in Fig. 3.9a and 0% in Fig. 3.9b. For a given fracture size the magnitude of shear-wave anisotropy decreases with increasing frequency. The characteristic frequency associated with the effect decreases with increasing size of the fractures and can lie in the seismic frequency range. From Fig. 3.9 we may say that if frequency-

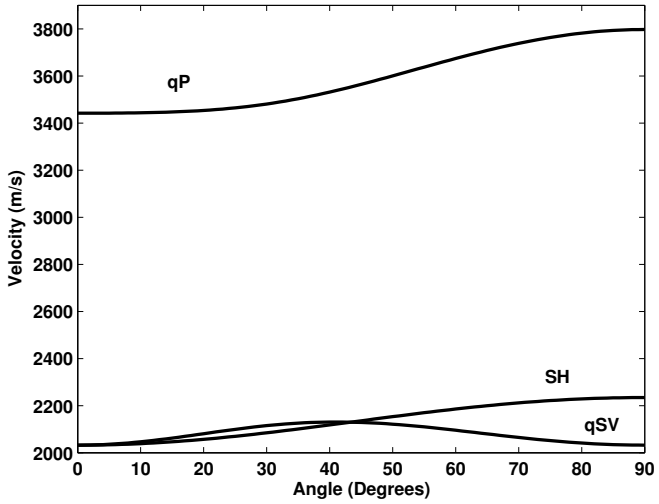

Figure 3.8: Variation of body-wave velocities as a function of angle from the fracture normal.

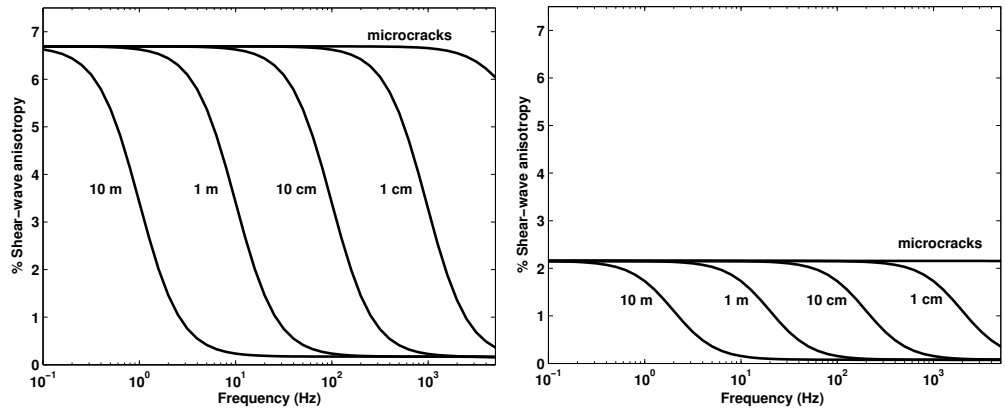

(a) (b)

Figure 3.9: Percent shear-wave splitting as a function of frequency and fracture radius, a) with 10% porosity, b) at zero porosity. The anisotropy decreases with increasing frequency, and the larger the fractures, the lower is the frequency range where the change occurs. The equant porosity is a key factor in determining the magnitude of the change in anisotropy.

dependent anisotropy can be measured from data the model provides means to derive an average fracture size. The equant porosity has a strong influence on the magnitude of anisotropy at the lower frequency end and therefore on the

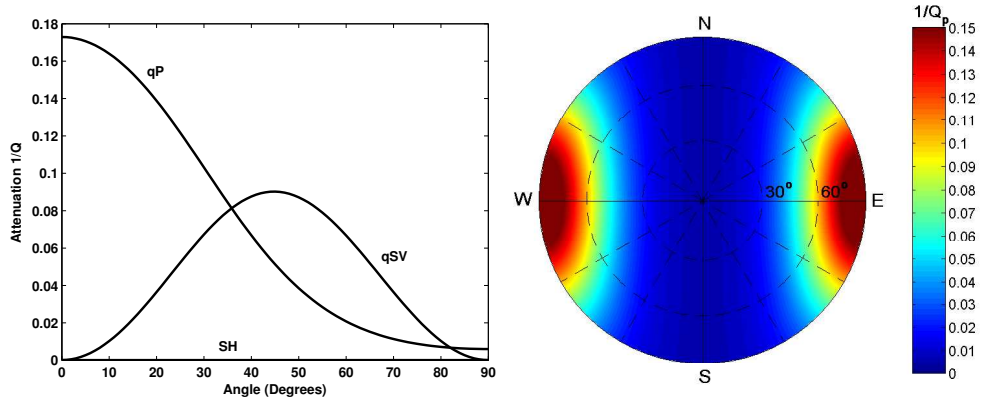

(a) (b)

Figure 3.10: a) Attenuation of the three body waves as a function of angle from the fracture normal at a frequency of 40 Hz. b) qP-wave attenuation as an equal-area projection of propagation directions onto the horizontal plane. The fracture strike is N-S. Attenuation is maximum in the direction normal to the fractures, and it increases with polar angle.

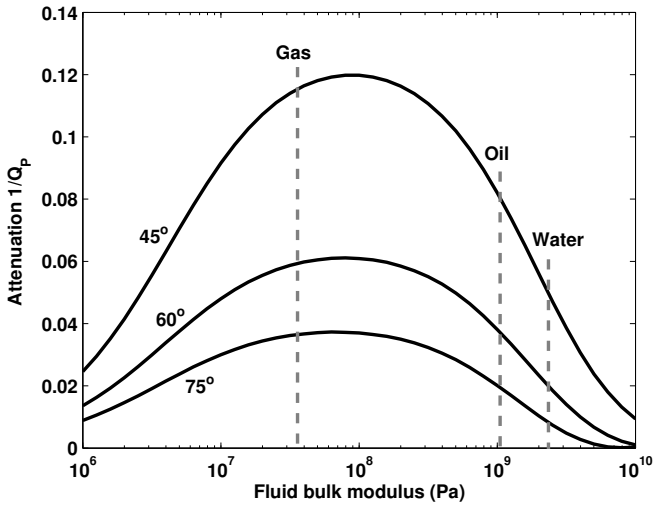

Figure 3.11: qP-wave attenuation at various angles from the fracture normal as a function of fluid bulk modulus.

magnitude of dispersion. If the fluid can flow from the fractures into equant pores in the matrix, the fractures are much more compliant and the magnitude of anisotropy is increased. This agrees with the results of Thomsen (1995).

As a consequence of the flow in and out of fractures, which causes anisotropic velocity dispersion, the attenuation is anisotropic as well. Fig. 3.10a shows the angular variation in attenuation of the three body waves at a frequency of 40 Hz. Both the qP- and the qSV-wave are strongly attenuated away from the fracture plane, whereas the pure shear-wave shows no attenuation. The qP attenuation is displayed as an equal-area projection of propagation directions onto the horizontal plane in Fig. 3.10b. The fractures in the example strike N-S. The attenuation is largest in the direction normal to the fractures, and it also increases with polar angle. If these spatial patterns can be seen in field data, attenuation may serve as an additional attribute for the characterization of fractures.

The magnitude of attenuation anisotropy also depends on the fluid bulk modulus. Fig. 3.11 shows the qP-wave attenuation for several propagation directions from the fracture normal as a function of fluid bulk modulus. In the limits of zero bulk modulus and for very stiff fluids attenuation vanishes. For the bulk moduli of water or brine, which lie around 2 GPa, attenuation and its angular variation are still rather small. The effect is considerably increased towards lower fluid bulk moduli (e.g. oil and gas). For gas saturation with fluid bulk moduli around 25

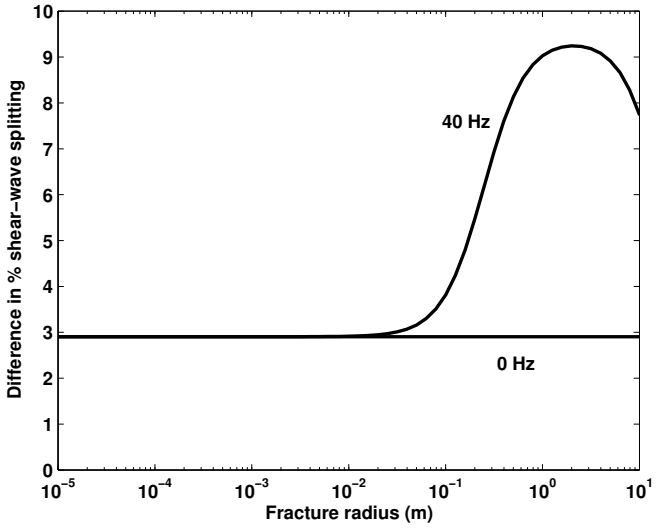

Figure 3.12: Difference in percentage shear-wave anisotropy between gas and brine saturation as a function of fracture size for two different frequencies. In the static limit fluid substitution has very little effect on the shear-wave anisotropy, but at some finite frequency and for a certain fracture size shear-wave splitting is very sensitive to the fluid.

MPa the magnitude of attenuation anisotropy is particularly high.

The dynamic fluid substitution effect is further demonstrated in Fig. 3.12. Here the difference in percentage shear-wave anisotropy between gas and brine saturation is plotted as a function of fracture size for frequencies of 0 Hz and 40 Hz. The shear waves are propagating at an angle of 60° from the fracture normal. At zero frequency the change in shear-wave anisotropy due to fluid substitution is very small, but at a higher frequency there is a particular range of fracture sizes where fluid substitution has a significant effect. The dynamic fluid substitution effect reported by van der Kolk *et al.* (2001) may potentially be explained by this behaviour.

3.7 Summary

Traditional equivalent medium theories for fractured rock are independent of frequency and only require the wavelength to be much larger than the scale associated with the fracturing. The models of Hudson (1981) and Thomsen (1995) represent high and low frequency limits, respectively, and are considerably different in their predictions of anisotropy for fluid saturated rock.

Wave-induced fluid motion in the pore space of isotropic rock due to heterogeneity of the pore microstructure has been described by a number of poroelastic models. The comprehensive results of Endres and Knight (1997) give a general framework for the dispersion in shear and bulk modulus as a function of the distribution of compliant and stiff porosity. The poroelastic model of Chapman (2001) follows this framework and it includes the entire frequency range from low to high frequency limits.

The concept of fluid squirt causing significant velocity dispersion and attenuation has been supported by many observations from laboratory data. These suggest that the characteristic squirt-flow frequency lies between the sonic and ultrasonic frequency bands. Recent observations from seismic data indicate that it may be important to consider fractures in the squirt flow process, which may have an effect at seismic frequencies. In particular, this would cause anisotropy to be frequency dependent if the fractures are aligned.

A number of theories have been brought forward to address this issue and to extend the traditional high and low frequency models to the entire frequency range. The model of Chapman (2003) appears to have some advantages compared to other theories in that it models the microstructure of the porosity explicitly and that the fractures can be removed from the model, still leaving a poroelastic theory describing squirt flow on the grain scale. It agrees with the traditional frequency-independent equivalent medium theories in its frequency limits. The model predicts anisotropic velocity dispersion and attenuation in the seismic frequency range. The characteristic frequency is dependent on the fracture size, and the fluid bulk modulus has a strong influence on the magnitude of attenuation anisotropy. Furthermore, the theory can model dynamic fluid substitution effects such as observed by van der Kolk *et al.* (2001) in seismic data. After testing and calibrating the model against published laboratory data and reducing the number of unknown parameters, it is brought into a form where it can be used in applications to seismic field data.

Chapter 4

Anisotropy of P-wave attenuation in VSP data: Synthetic studies

4.1 Introduction

Laboratory measurements of high attenuation and velocity dispersion at low effective stress, which I have discussed in the previous chapter, the Rathore *et al.* (1995) data from synthetic fractured sandstone, and observations of attenuation from seismic data associated with fracture zones suggest that fractures play an important role in attenuation mechanisms. If fractures are aligned, so that the rock is anisotropic, fracture-related attenuation should be anisotropic as well. In order to investigate whether such an effect exists at seismic frequencies, appropriate techniques have to be designed to detect and quantify attenuation anisotropy from field data. For that purpose I carry out synthetic studies based on the frequency-dependent equivalent medium model of Chapman (2003). In this chapter I begin with a review of the definition of attenuation parameters and of methods to measure attenuation from seismic data with a focus on VSP data. I then discuss the analysis of attenuation anisotropy from synthetic VSP data. I demonstrate its use as an attribute for the characterization of fractures based on equivalent medium theory.

4.2 Definition of Q

The most common measure of attenuation is the dimensionless quality factor Q, which is an intrinsic property of a material (Aki and Richards, 2002, pp.161-177). It describes the ratio of stored to dissipated energy, so that attenuation is high if Q is low. In a dissipative medium stress and strain are out of phase and the elastic moduli relating the two can be represented by complex variables. Attenuation $1/Q$ is then defined as (Mavko *et al.*, 1998):

$$\frac{1}{Q} = \frac{1}{2\pi} \frac{\Delta W}{W_{max}} = \frac{M_I}{M_R} = \tan\varphi. \tag{4.1}$$

ΔW is the strain energy loss per cycle, W_{max} is the energy at maximum strain, M_I and M_R are the imaginary and real parts, respectively, of the complex elastic modulus M^*, and φ is the phase delay between stress and strain. The complex modulus also appears in the wave equation, so that attenuation of a propagating elastic wave is mathematically described by a complex phase velocity $v^* = \sqrt{M^*/\rho}$, or equivalently by a complex wave number $k^* = k - i\alpha$ where α is the spatial attenuation coefficient in units of inverse length (Aki and Richards, 2002). The displacement of a plane wave $u(x,t)$ is then given by:

$$u(x,t) = u_0 e^{i(\omega t - k^* x)} = u_0 e^{-\alpha x} e^{i(\omega t - kx)}, \tag{4.2}$$

where u_0 is an initial amplitude. The attenuation coefficient α thus describes the exponential amplitude decay with distance x. Using the definition of Eq. 4.1, $1/Q$ can now be related to the phase velocity and the attenuation coefficient:

$$\begin{aligned} \frac{1}{Q} &= \frac{M_I}{M_R} = \frac{2 v_I v_R}{v_R^2 - v_I^2} = \frac{\alpha v}{\pi f - \frac{\alpha^2 v^2}{4\pi f}}, \\ \text{with } v^* &= v_R + i v_I \quad \text{and} \quad v = \frac{\omega}{k}. \end{aligned} \tag{4.3}$$

Geophysical studies of attenuation in the Earth's crust have shown that rocks are generally low-loss materials, i.e. $M_I \ll M_R$ and $v_I \ll v_R$ (Knopoff, 1964; Toksöz and Johnston, 1981; Mavko *et al.*, 1998; Aki and Richards, 2002). Therefore, the

relations in Eq. 4.3 can be simplified to

$$\frac{1}{Q} \approx 2\frac{v_I}{v_R} = \frac{\alpha v}{\pi f}. \tag{4.4}$$

In general, Q, α, k and v are functions of frequency. Causality requires that the real and imaginary parts of the complex modulus, or equivalently, the complex wave number are Hilbert transform pairs (Aki and Richards, 2002, *see* Appendix A.2). Thus, there always is a specific relationship between velocity dispersion and attenuation. For seismic applications Q and v are normally assumed to be constant over the narrow frequency band of investigation, so that α becomes a linear function of frequency (McDonald *et al.*, 1958; Tullos and Reid, 1969; Hamilton, 1972; Newman and Worthington, 1982).

4.3 Spectral ratio method

The spectral ratio method is the most widely used technique to measure attenuation from seismic data (Johnston, 1981; Hauge, 1981; Pujol and Smithson, 1991; Liu *et al.*, 1993b; Dasgupta and Clark, 1998; Hackert *et al.*, 2001). It uses the logarithmic ratio of the amplitude spectra A_0 and A_1 of two signals recorded at distances x_0 and x_1. With Eq. 4.2 the spectral ratio is given by

$$\ln\frac{A_1}{A_0} = \ln\frac{G_1}{G_0} - (a_1x_1 - a_0x_0)f \quad \text{with} \quad a = \frac{\pi}{Qv}. \tag{4.5}$$

G is a parameter describing amplitude losses that are assumed to be frequency independent, such as geometric spreading and transmission coefficients. Assuming also frequency independent Q and v, the spectral ratio $\ln A_0/A_1$ is a linear function of frequency with the slope $b = a_0x_0 - a_1x_1$. If the two signals have travelled partially along the same raypath such that $x_1 = x_0 + \Delta x$, then

$$b = -\frac{\pi\Delta x}{Qv} = -\frac{\pi\Delta t}{Q} \tag{4.6}$$

with $\Delta t = \Delta x/v$. An absolute value of Q for the interval Δx can then be derived from the slope of the spectral ratios and the traveltime difference between the two arrivals. This is commonly used to measure Q as a function of depth from

zero-offset VSP data or sonic logs (e.g. Hauge, 1981; Raikes and White, 1984; Stainsby and Worthington, 1985; Pujol and Smithson, 1991; Tonn, 1991; Hackert *et al.*, 2001; Reid *et al.*, 2001).

The Q factor as defined in the previous section is an intrinsic property of a homogeneous medium. Any method of measuring attenuation from seismic data faces the difficulty that frequency-dependent amplitude losses are also produced by scattering from heterogeneities, such as thin layers. The two effects can generally not be separated (e.g. Schoenberger and Levin, 1978; Spencer *et al.*, 1982; Pujol and Smithson, 1991). Attenuation due to multiple scattering of a layered sequence at normal incidence has been studied in detail by O'Doherty and Anstey (1971) and Schoenberger and Levin (1974, 1978). This particularly affects measurements of Q from near-offset VSPs. To estimate the contribution of the scattering effect to the overall attenuation authors have suggested computing synthetic seismograms without intrinsic Q for a reflectivity series derived from well logs (Schoenberger and Levin, 1978; Hauge, 1981; Brown and Seifert, 1997; Hackert *et al.*, 2001). The scattering attenuation is then measured from the synthetic data. At larger offsets, however, scattering from heterogeneities other than layering would have to be considered as well.

The spectral ratio method is very sensitive to the effect of scattering (Spencer *et al.*, 1982; Sams and Goldberg, 1990; Pujol and Smithson, 1991). The interference pattern created by multiple scattering and reflections from interfaces within a wavelength of the receiver can produce strong local variations and notches in the spectrum of a pulse. This causes large oscillations in the computed spectral ratios, as shown schematically in Fig. 4.1. The overall linear trend, from which Q is derived, then depends crucially on the chosen frequency bandwidth, over which a straight line is fitted to the data. A wider frequency range will reduce the sensitivity of the result to local oscillations, but this is often compromised by the narrow bandwidth of significant energy contained in seismic data. The sensitivity of the spectral ratio method to interference effects also has important implications for the spatial resolution of the method, if applied to zero-offset VSP data. This issue has been studied by Spencer *et al.* (1982), who found that the receiver separation has to be more than twice the dominant wavelength for the measured Q to represent attenuation in the interval between the receivers, rather than the difference in local interference effects at the receivers.

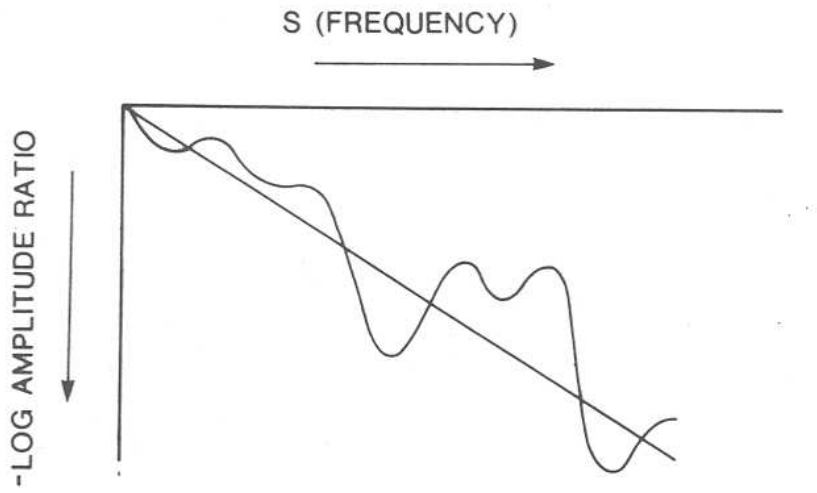

Figure 4.1: Schematic diagram of the spectral ratio as a function of frequency. The oscillations are introduced by multiple scattering and local reflections. (*From* Spencer *et al.* (1982).)

Another parameter that can influence the result of attenuation measurements with the spectral ratio method is the time window that is used to extract an arrival from a seismic trace (Sams and Goldberg, 1990; Pujol and Smithson, 1991). Windowing is applied to obtain a local spectrum of a particular arrival. Narrowing the time window to minimize the effect of secondary arrivals, however, decreases resolution in the frequency domain (*see* Appendix A). Furthermore, it is desirable to reduce leakage in the frequency domain, which depends on the type of window function that is used (Appendix A.3). The trade-off between time and frequency resolution has to be considered carefully in an application of the spectral ratio method.
Other factors that may affect Q estimates are instability of the source pulse, differences in receiver coupling, the presence of strong noise and processing artefacts. Due to these reasons Q estimates have sometimes been found to be very unreliable, particularly for data with a low signal-to-noise ratio (e.g. Raikes and White, 1984; Goldberg *et al.*, 1985; Sams and Goldberg, 1990). Significant discrepancies between Q values obtained with different methods are reported for a number of studies (Cheng *et al.*, 1982; Engelhard *et al.*, 1984; Goldberg *et al.*, 1985; De *et al.*, 1994). Furthermore, local distortions of amplitudes and the shape of the spectra can result in negative Q values, which are non-physical (De *et al.*, 1994; Dasios *et al.*, 2001). The general difficulty lies in the fact that many

mechanisms affecting the spectral content of an arrival operate at the same time and are superposed, whereas methods of measuring Q are based solely on the effects of intrinsic attenuation.

The data analysis described in the following chapter aims to detect changes in Q with propagation direction that may be associated with fracturing. I intend to investigate whether the data show any systematic variation in Q with azimuth at non-zero offset and whether this azimuthal variation, if present, changes with polar angle (*see* Chapter 3, Section 3.6). To circumvent some of the uncertainties associated with measuring absolute Q values I estimate only differences in attenuation as a function of azimuth. For multi-azimuth VSP geometries where sources are placed at constant offsets around the well I compute spectral ratios between a reference pulse at a chosen azimuth and the arrivals from all other azimuths. The arrivals do not share partly the same raypath, but assuming lateral homogeneity they travel nearly equal distances. For traveltimes $t_i = x_i/v_i$ along the ith azimuth and assuming Q and v to be frequency independent over the bandwidth of seismic data, the slope b from Eq. 4.5 is then

$$b = -\pi \left(\frac{t_1}{Q_1} - \frac{t_0}{Q_0} \right) \approx -\pi \bar{t} \left(\frac{1}{Q_1} - \frac{1}{Q_0} \right), \tag{4.7}$$

where $\bar{t}$ is an average traveltime for all azimuths. I therefore measure the change in attenuation $\Delta 1/Q = \frac{1}{Q_0} - \frac{1}{Q_1}$ with azimuth, rather than estimating absolute values of Q and comparing them for different propagation directions. The method has the advantage that azimuthally invariant factors, such as multiple scattering from thin horizontal layers or the bias introduced by windowing and the selection of a frequency range for the linear regression, do not affect the results. Hence, I expect relative anisotropic attenuation to be easier to measure than an absolute isotropic Q.

As demonstrated in Section 3.6 of the previous chapter, frequency-dependent anisotropy due to squirt flow in fractured rock is characterized both by the variation of $1/Q$ with propagation direction at a given frequency, as well as the dependence of $1/Q$ on frequency itself. The latter would be difficult to measure accurately from seismic data alone, where the usable frequency bandwidth is usually less than 100 Hz. Determining only the spatial change of $1/Q$ at the peak frequency of a seismic pulse therefore appears to be a more appropriate approach.

As for the traveltimes and NMO velocities in a weakly anisotropic HTI medium, the variation in $\Delta 1/Q$ with azimuth φ at a constant offset can be described by a $\cos(2\varphi)$-function (*see* Chapter 2, Section 2.5):

$$\Delta 1/Q = C_1 + C_2 \cos[2(\varphi - \varphi_0)]. \tag{4.8}$$

Here, C_1 is an arbitrary constant, since no absolute value of $1/Q$ is determined. C_2 is the magnitude of azimuthal variation and φ_0 is the symmetry direction, in which attenuation is smallest. If multi-azimuth data are also acquired at different offsets, then the change in C_2 with offset indicates whether the magnitude of attenuation anisotropy varies with polar angle.

4.4 Instantaneous frequency method

Dasios *et al.* (2001) suggested measuring attenuation through the shift in instantaneous frequencies between two arrivals. The authors found that the method is less sensitive to processing parameters and local variations in the spectra than the spectral ratio method. The definitions of instantaneous attributes are given in Appendix A.2. In this section I therefore only review Dasios *et al.*'s (2001) technique of analysing attenuation.

Barnes (1991) has shown that for a constant phase wavelet the instantaneous frequency at the peak of the pulse envelope is equal to the centre frequency f_c of the Fourier amplitude spectrum $A(f)$, which is defined as the amplitude-weighted mean of all frequencies:

$$f_c = \frac{\int_0^\infty f A(f) df}{\int_0^\infty A(f) df}. \tag{4.9}$$

This is approximately true for any wavelet (Saha, 1987). Furthermore, Barnes (1993) demonstrated that the average of the instantaneous frequencies of a signal over time, weighted by the envelope squared, is equal to the centre frequency of the signal's Fourier power spectrum. Since the centre frequency decays due to attenuation of a pulse, a decrease in instantaneous frequency can also be related to attenuation (Toksöz and Johnston, 1981; Barnes, 1991; Engelhard, 1986, 1996).

Based on these concepts Dasios *et al.* (2001) compute instantaneous frequencies at the peak of the pulse envelope as a weighted average over a short time window, where the weights are the envelope squared. The Q between a reference pulse and another arrival is then determined by attenuating the reference pulse, until the instantaneous frequencies of the two signals are matched.
Dasios *et al.* (2001) include a damping factor in the computation of the instantaneous frequencies in order to reduce the influence of low-amplitude noise. For an analytic signal $z(t) = x(t) + iy(t)$ the damped instantaneous frequency f_I is given by (*see* Appendix A.2):

$$f_I(t) = \frac{1}{2\pi} \frac{x(t)\dot{y}(t) - y(t)\dot{x}(t)}{x^2(t) + y^2(t) + \varepsilon^2}, \tag{4.10}$$

where ε is the damping factor. The mean instantaneous frequency $f_w(t_p)$ at the peak of the envelope $|z(t_p)|$ is then computed as:

$$f_w(t_p) = \frac{\int_{t_p-T}^{t_p+T} f_I(t)|z(t)|^2 dt}{\int_{t_p-T}^{t_p+T} |z(t)|^2 dt}, \tag{4.11}$$

where $2T$ is the length of the time window, over which f_I is averaged. For the attenuation of the reference pulse Dasios *et al.* (2001) use the following attenuation operator that is defined in the frequency domain (Aki and Richards, 2002, p. 175):

$$A(\omega) = \exp\left[-\frac{i\omega}{\pi}\hat{t}\ln\left(\frac{\omega}{\omega_r}\right)\right]\exp\left(-\frac{\omega}{2}\hat{t}\right) \quad \text{with} \quad \hat{t} = \int \frac{dx}{Q(x)v(x)}. \tag{4.12}$$

ω_r is a reference frequency at the upper limit of the amplitude spectrum of the reference pulse. $\hat{t}$, which measures the attenuation accumulated along the distance x, is updated until the instantaneous frequency of the reference pulse matches the instantaneous frequency of the arrival that is analysed.
Dasios *et al.* (2001) tested the method on sonic log data and compared the results to Q values derived from spectral ratios. They found that overall the results agreed well, but that the instantaneous frequency method is more stable in the presence of noise and interfering arrivals.

4.5 S-transform and spectral colour display

A spectral colour display can be used to visualize spatial changes in the spectral content of arrivals. It serves as a qualitative assessment of the effect of attenuation anisotropy, rather than yielding quantitative measurements of Q. Theophanis and Queen (2000) propose a colour representation that mimics human vision, such that properties of the pixel colour can be intuitively related to properties of the localized spectrum of an event. I now summarize their technique.

In Appendix A I discuss various time-frequency representations that have been developed in order to analyse the local spectral content of transient signals. The resolution in time and in frequency depends on the particular type of transform and is fundamentally limited by the Heisenberg uncertainty principle (Appendix A.3). The S-transform is a time-frequency representation that aims to optimize resolution in both domains by combining elements of the wavelet transform and the windowed Fourier transform (Stockwell *et al.*, 1996; Chu, 1996; Theophanis and Queen, 2000). The S-transform of a time series $h(t)$ at frequency f and time τ is defined as (Stockwell *et al.*, 1996):

$$S(f,\tau) = \int_{-\infty}^{\infty} h(t) \frac{|f|}{\sqrt{2\pi}} e^{-\frac{(\tau-t)^2 f^2}{2}} e^{-i2\pi f t} dt. \tag{4.13}$$

Theophanis and Queen (2000) derive the spectral colour display from the S-transform of a signal. Each localized spectrum obtained with the S-transform is represented by a colour pixel. The pixel colour, defined by an RGB triplet, is formed by placing the spectrum over the frequency band of visible light, so that low frequencies are identified as red and high frequencies as blue. Fig. 4.2 illustrates the technique. First, the bandwidth of the localized spectrum is divided into six equal parts, represented by the six basic colours red, yellow, green, cyan, blue and magenta. Their corresponding RGB values are shown in the top table of Fig. 4.2. The RGB triplet representing the spectrum is then computed as a weighted sum of the RGB triplets $(RGB)_n$ of the six basic colours, where the weights are the average spectral power $\bar{P}_n$ in the corresponding frequency band:

$$RGB_{pixel} = \sum_{n=1}^{6} (RGB)_n \bar{P}_n. \tag{4.14}$$

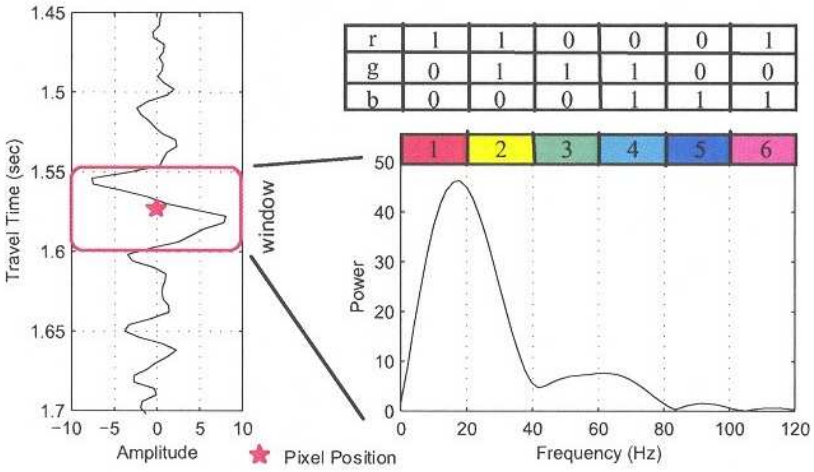

Figure 4.2: Representation of a localized spectrum by a colour pixel. The spectrum is devided into six equal frequency bands, each representing one of the six basic colours from red to magenta. The pixel colour is computed as a weighted sum of the six basic colours, where the weights are the average power over the corresponding frequency band. (*From* Theophanis and Queen (2000).)

When the pixels have been computed for every time sample along each trace, they are normalized by the maximum RGB value of the entire image, and the resulting image is displayed.

Instead of representing a colour as a combination of red, green and blue an alternative system can be used that has the three attributes hue, luminosity and saturation (HLS). The HLS system can be illustrated as a double hexagonal cone as shown in Fig. 4.3 with the six basic colours plus black and white placed at the vertices. A colour is then represented in a cylindrical coordinate system with hue being the azimuthal angle, luminosity the vertical axis and saturation the radius. By using this system it is more intuitive how the pixel colour computed with Eq. 4.14 represents characteristics of the local spectrum: hue is a measure of the centre frequency, luminosity corresponds to the overall power, and saturation is a measure of the bandwidth where high saturation of a particular colour is caused by a narrow bandwidth of the spectrum. An example of the spectral colour display for synthetic data that illustrates these aspects will be given in the next section.

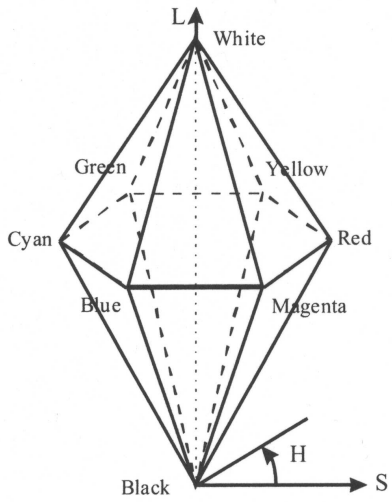

Figure 4.3: Representation of the HLS system as a double hexagonal cone in a cylindrical coordinate system.

4.6 Synthetic VSP studies

In this section I demonstrate the application of some of the methods described in the previous section with synthetic VSP data. The models contain a frequency-dependent anisotropic material, the elastic constants of which are computed according to the model of Chapman (2003). I show how the change in attenuation as a function of azimuth at different offsets is measured from the synthetic traces, and how this attribute can be used to invert for fracture parameters. I also demonstrate possible applications of the spectral colour display.

4.6.1 Models and VSP geometry

I use two different models for the synthetic studies. The first model *(model 1)* is simply a halfspace of a frequency-dependent anisotropic material, while the second model *(model 2)* contains three isotropic layers above the anisotropic halfspace. Parameters of the anisotropic dispersive material and the properties of the three overburden layers of model 2 are given in Table 4.1. The model parameters are roughly based on well log data from the Clair field, which will be discussed in the next chapter. The fractures in both models are vertical and strike N-S. Fracture size and relaxation time τ_m of the fractured material are chosen in such a way

Fractured medium properties	
v_{P}	4064 m/s
v_{S}	2345 m/s
ρ	2450 kg/m^3
ϵ_f	0.05
a_f	0.01 m
r	0.0001
Φ_p	10%
k_f	1.25 GPa
τ_m	$6 \cdot 10^{-4}$ s

Overburden of model 2	
Layer 1	
v_{P}	1500 m/s
v_{S}	0 m/s
ρ	1000 kg/m^3
depth	137 m
Layer 2	
v_{P}	2300 m/s
v_{S}	1330 m/s
ρ	2200 kg/m^3
depth	1625 m
Layer 3	
v_{P}	3580 m/s
v_{S}	1905 m/s
ρ	2450 kg/m^3
depth	1780 m

Table 4.1: Parameters of the frequency dependent fractured material in model 1 and 2 *(left)* and properties of the overburden layers in model 2 *(right)*.

that attenuation reaches its maximum in the seismic frequency range. Fig. 4.4 shows the P-wave attenuation $1/Q$ of the medium as a function of frequency at a propagation direction of 45^o from the fracture normal. The attenuation peaks around 30 Hz.

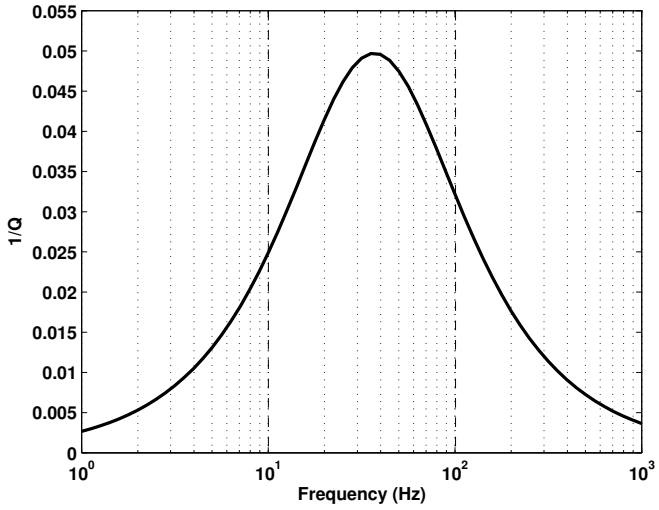

Figure 4.4: P-wave attenuation $1/Q$ as a function of frequency for the dispersive fractured material of models 1 and 2. Attenuation peaks around 30 Hz.

I generate synthetic traces according to multi-azimuth walkaway VSP geometries. For model 1 a receiver is placed at a depth of 1000 m and source offsets range from 0 m to 1000 m with an increment of 50 m. The walkaway lines extend along azimuths from 0^o to 90^o (measured clockwise from N) in increments of 15^o. In model 2 the receiver depth is 1900 m, and the sources have a spacing of 100 m between offsets of 0 m and 2000 m. Here, walkaway lines are only modelled every 45^o from North.

The synthetic seismograms are generated with the modelling package ANISEIS (Taylor, 2001), which uses the reflectivity method. The most recent version of the software allows the elastic constants of a material to be frequency-dependent. The source wavelet used in the computation of the seismograms is a Ricker wavelet

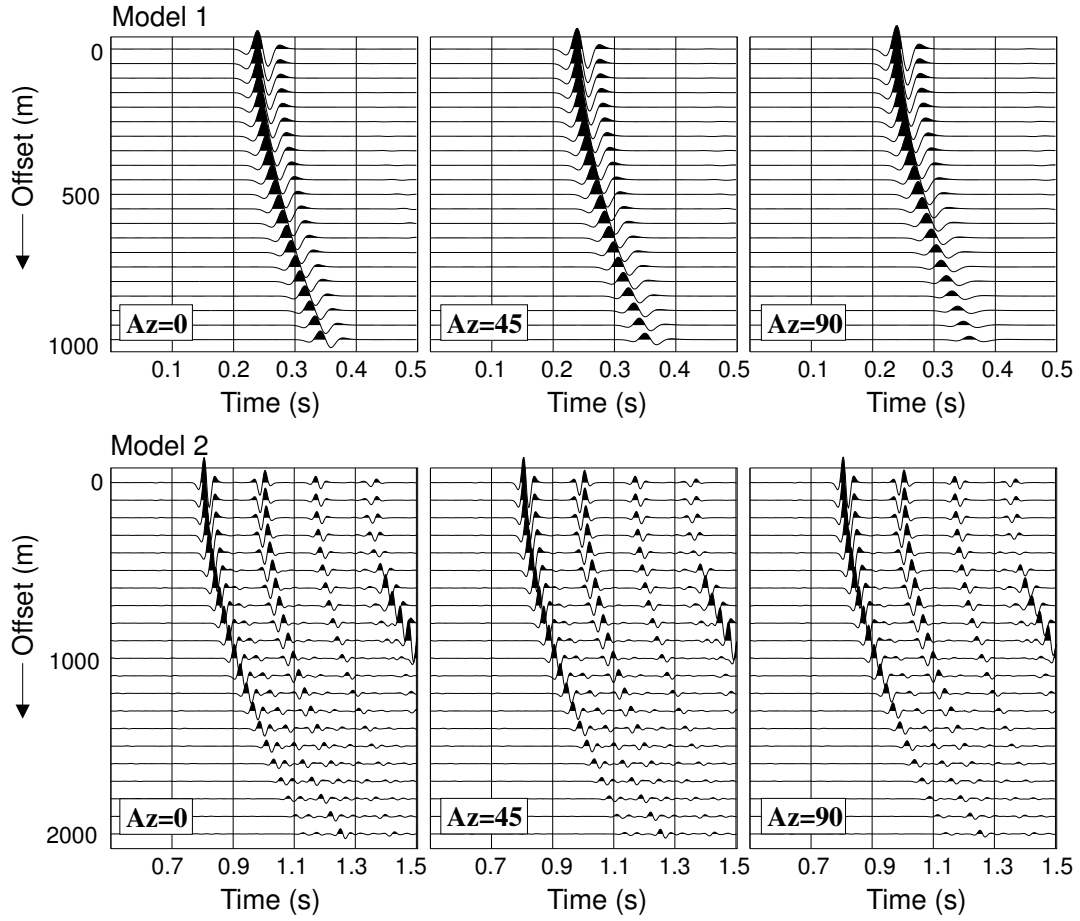

Figure 4.5: Synthetic traces (vertical component) of walkaway lines at different azimuths for model 1 and 2. The effect of attenuation anisotropy can easily be seen at large offsets.

with a peak frequency of 20 Hz. Trace lengths are 2 s and the sample rate is 2 ms.

The vertical component of the synthetic seismograms of walkaway lines along azimuths of 0^o, 45^o and 90^o for models 1 and 2 are displayed in Fig. 4.5. At far offsets the amplitudes are increasingly dimmed towards the direction normal to the fractures (azimuth of 90^o) and the shape of the wavelet changes. This shows the effect of attenuation anisotropy as described by the model of Chapman (2003) wih an increase in $1/Q$ as a function of azimuth towards the fracture normal and with polar angle at azimuths away from the fracture strike.

4.6.2 Analysis of attenuation anisotropy

I use the spectral ratio method to demonstrate how the azimuthal variation in attenuation can be measured from the synthetic data. I choose a reference azimuth and compute the spectral ratios of the windowed first arrivals at each offset between all other azimuths and the reference azimuth. The reference azimuth is 0^o in the analyses shown in this section.

The windowing is performed with a Blackman window function, which reduces leakage in the frequency domain (Pujol and Smithson, 1991, *see* Appendix A.2). I also use this type of window function in the real data studies described in the next chapter. The choice of window width becomes important for the analysis of the model 2 data, where it is desirable to narrow the window around the first arrivals, so that any energy from secondary arrivals is not included in the computation of the Fourier spectrum. From Fig. 4.5 we can see that particularly at far offsets the direct-arrival energy is not well separated in time from other events. On the other hand decreasing the length of the time window causes a loss in frequency resolution (Appendix A). I set the window width to 160 ms for the model 2 data and to 200 ms for the model 1 data. With a sample rate of 2 ms this means that in the case of model 2 the spacing of independent data points in the frequency domain is 6.25 Hz, whereas it is 5 Hz for model 1.

Fig. 4.6 shows examples of the windowed trace data, amplitude spectra and spectral ratios for both models. From the amplitude spectra and spectral ratios it is obvious that high frequencies become increasingly attenuated towards an azimuth of 90^o, i.e. normal to the fracture strike. The effect of interference with

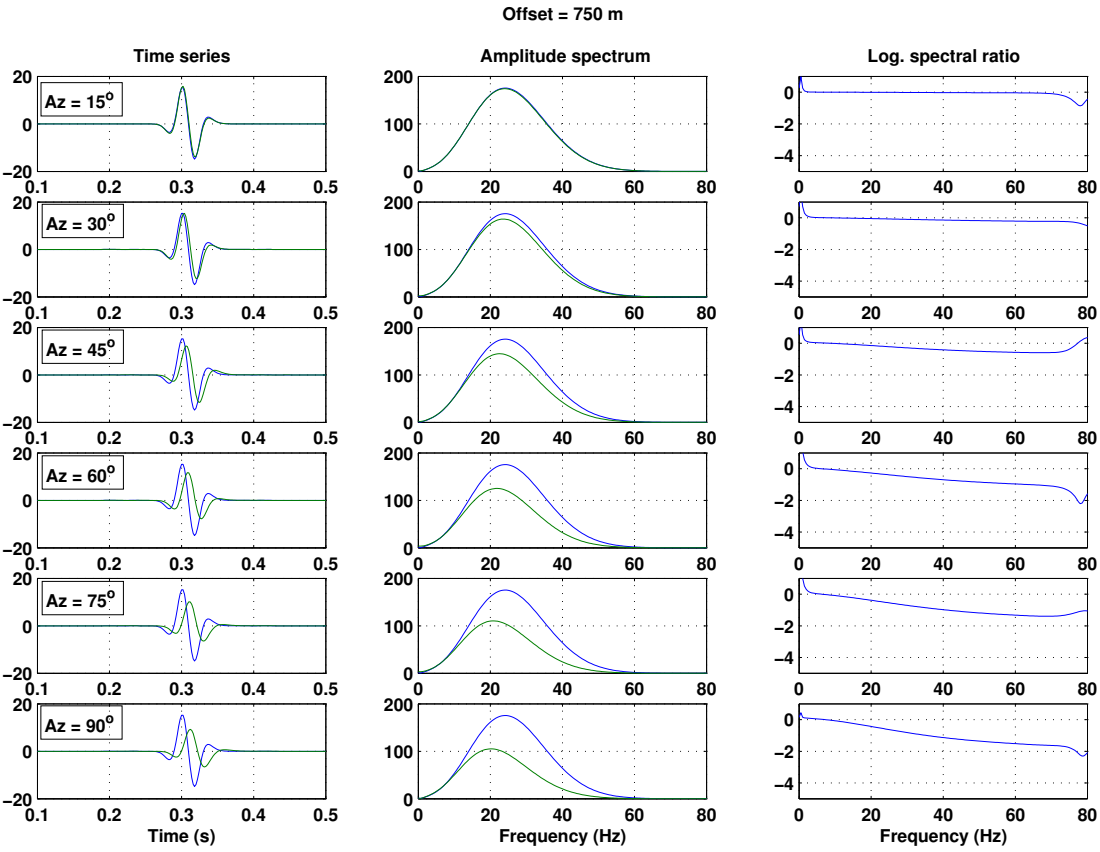

(a)

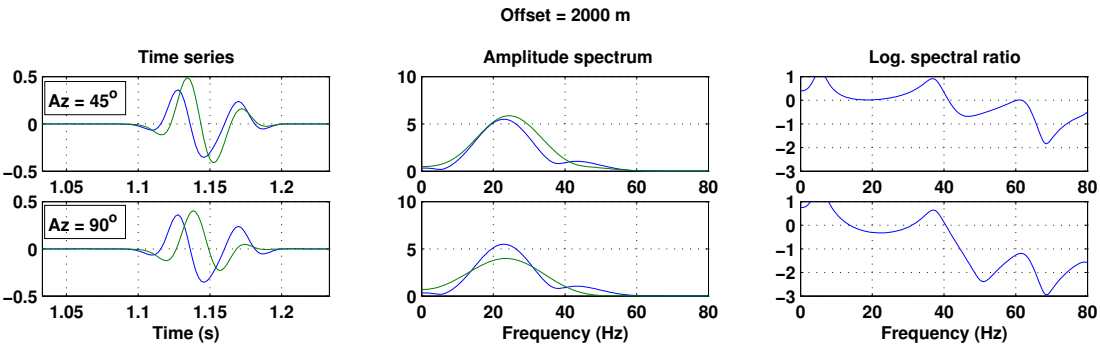

(b)

Figure 4.6: Examples of windowed direct arrivals, amplitude spectra and spectral ratios. a) Model 1; b) model 2. The wavelet and amplitude spectrum of the reference trace are displayed in blue.

other arrivals is apparent in the model 2 data, where it causes large variations in the spectral ratios at particular frequencies. It becomes clear that in these cases the slope of a line fitted to the data depends strongly on the frequency bandwidth, over which the fit is performed. The results will be more stable against local oscillations in the spectral ratios, if the frequency band is wide, but the choice is limited by the bandwidth of the data itself. I use a frequency range of 10-50 Hz for the linear regression to the spectral ratios in the case of model 1 and 10-60 Hz in the case of model 2.

Figs. 4.7 and 4.8 show the linear regression to the spectral ratios for both models with corresponding R^2 values. For N data points y_i and fitted values $\hat{y}_i$, R^2 is

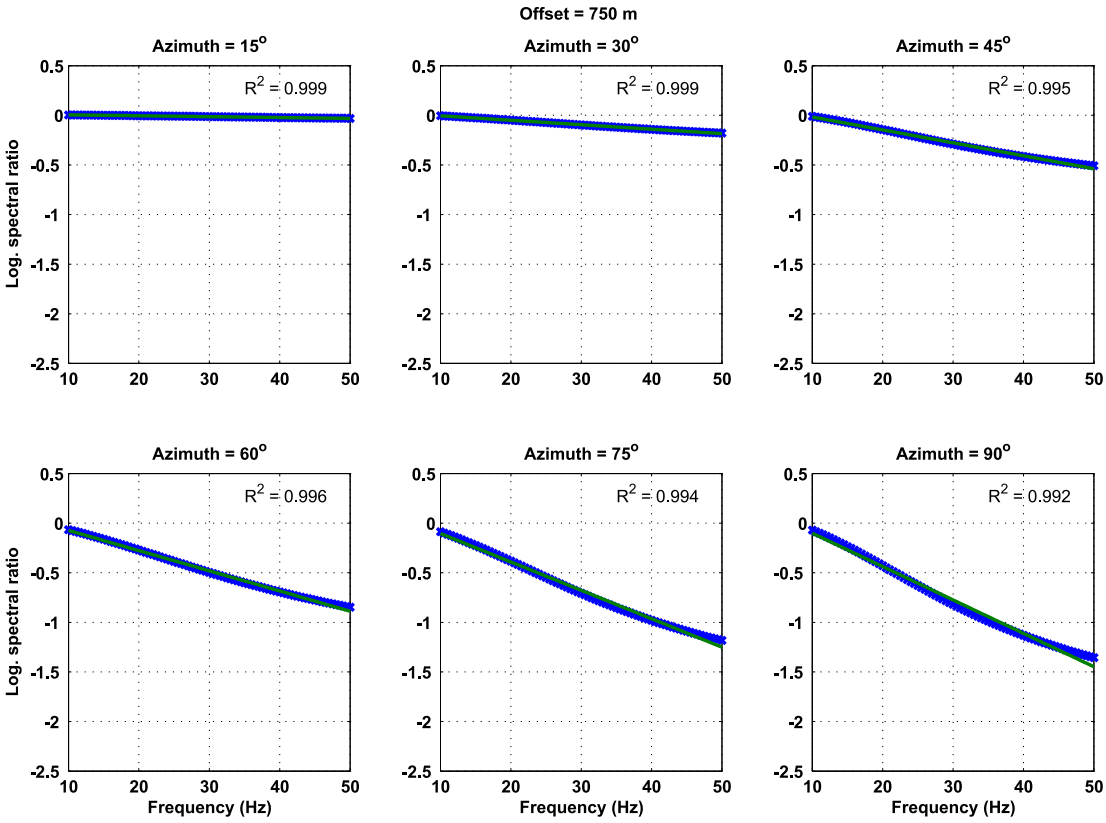

Figure 4.7: Linear regression to the spectral ratios of the model 1 data. Although Q depends on frequency in the model, the spectral ratios are well approximated by a straight line over the narrow frequency band contained in the data.

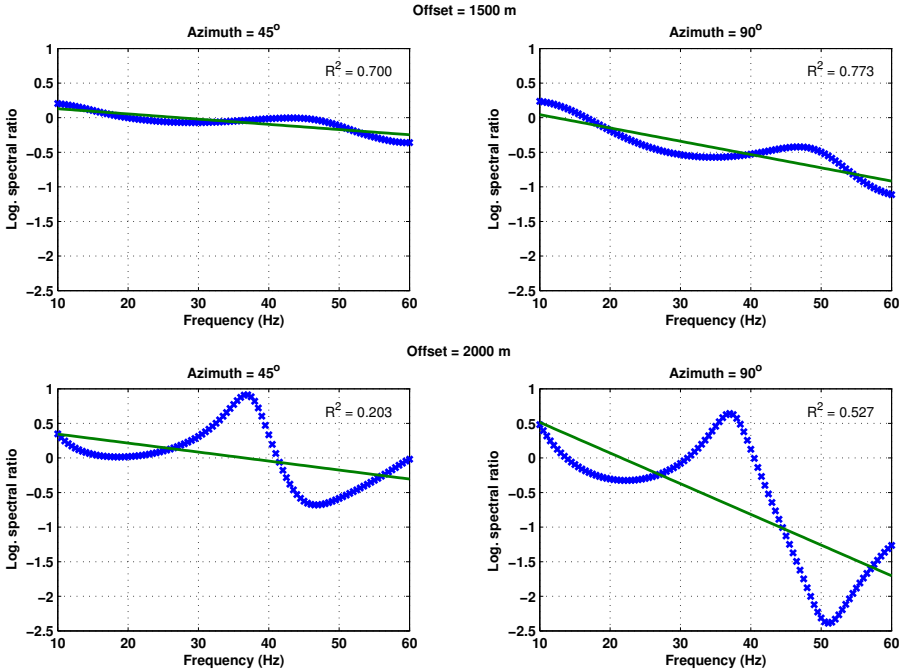

Figure 4.8: Linear fit to the spectral ratios of the model 2 data at two different offsets. The interference effects that cause the spikes in the spectral ratios are stronger at far offsets.

defined as:

$$R^2 = 1 - \frac{\sum_{i=1}^{N}(y_i - \hat{y}_i)^2}{\sum_{i=1}^{N}(y_i - \bar{y})^2}, \tag{4.15}$$

where $\bar{y}$ is the mean of y_i. For a perfect fit $R^2 = 1$. The excellent fit to the spectral ratios in Fig. 4.7 demonstrates that, although Q is a function of frequency in the models, a linear approximation to the spectral ratios over this narrow bandwidth is still appropriate. In comparison with Fig. 4.8 we can see that the effects of noise, such as interference from reflections, mode conversions and multiple scattering, are much stronger than the effects of the frequency dependence of Q. This also means that the method would not allow an accurate measurement of Q as a function of frequency. The absolute values of the slopes of the lines fitted to the spectral ratios in Figs. 4.7 and 4.8 increase towards an azimuth of 90^o, showing an increase in attenuation $1/Q$ compared to the reference azimuth. The change in attenuation $\Delta 1/Q$ as a function of azimuth is computed according to Eq. 4.7.

In principle, errors of the derived $\Delta 1/Q$ values can be estimated from the variances

of the slopes. The variance of the inverted slope b of a linear regression of data y_i measured at x_i is given by (Snedecor and Cochran, 1989, pp. 158-159):

$$\mathrm{var}\{b\} = \frac{\mathrm{var}\{y\}}{\sum_{i=1}^{N}(x_i - \bar{x})^2} \tag{4.16}$$

White (1992) points out that for the spectral ratio analysis it is important to include only the independent data points of the amplitude spectrum, which are defined by the size of the time window (Appendix A.3). However, there are

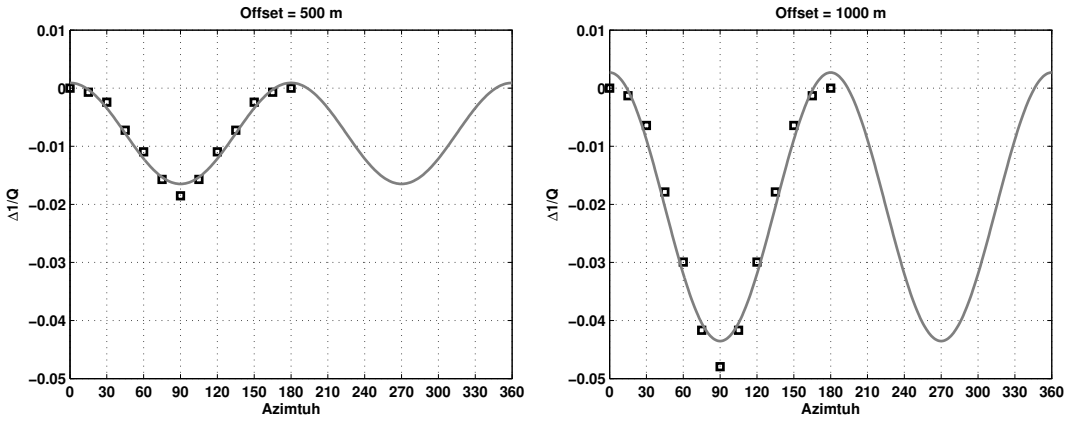

(a)

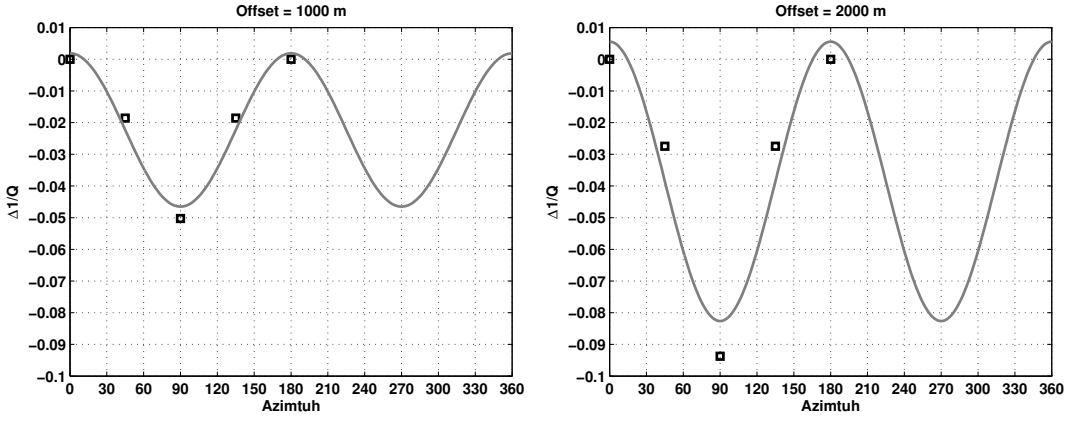

(b)

Figure 4.9: Least squares fit to $\Delta 1/Q$ as a function of azimuth. a) Model 1; b) model 2.

other uncertainties involved in attenuation measurements from spectral ratios, as discussed in Section 4.3, which are difficult to quantify.

I finally perform a least-squares fit of the $\cos(2\varphi)$-function given in Eq. 4.8 to the measured values of $\Delta 1/Q$ at every offset. Fig. 4.9 shows examples of the data points and fitted function at different offsets. The inverted parameters C_2 and φ_0 and the errors of the fit are displayed in Figs. 4.10 and 4.11. C_2 is the magnitude of azimuthal variation and φ_0 is the azimuth of minimum attenuation. The RMS error is defined as:

$$E_{RMS} = \sqrt{\frac{1}{N}\sum_{i=1}^{N}(\hat{y}_i - y_i)^2}. \tag{4.17}$$

I normalize the RMS error by C_2 to reflect the fact that the azimuthal fit to the data is only meaningful if the amplitude of azimuthal variation is significant.

As expected, C_2 increases with offset. For both models φ_0 is constant at 0^o, which is the fracture strike direction. Errors are slightly larger at near offsets, where the azimuthal variation in $1/Q$ is small. For model 2 the errors introduced by interference effects become again apparent at far offets, where C_2 does not

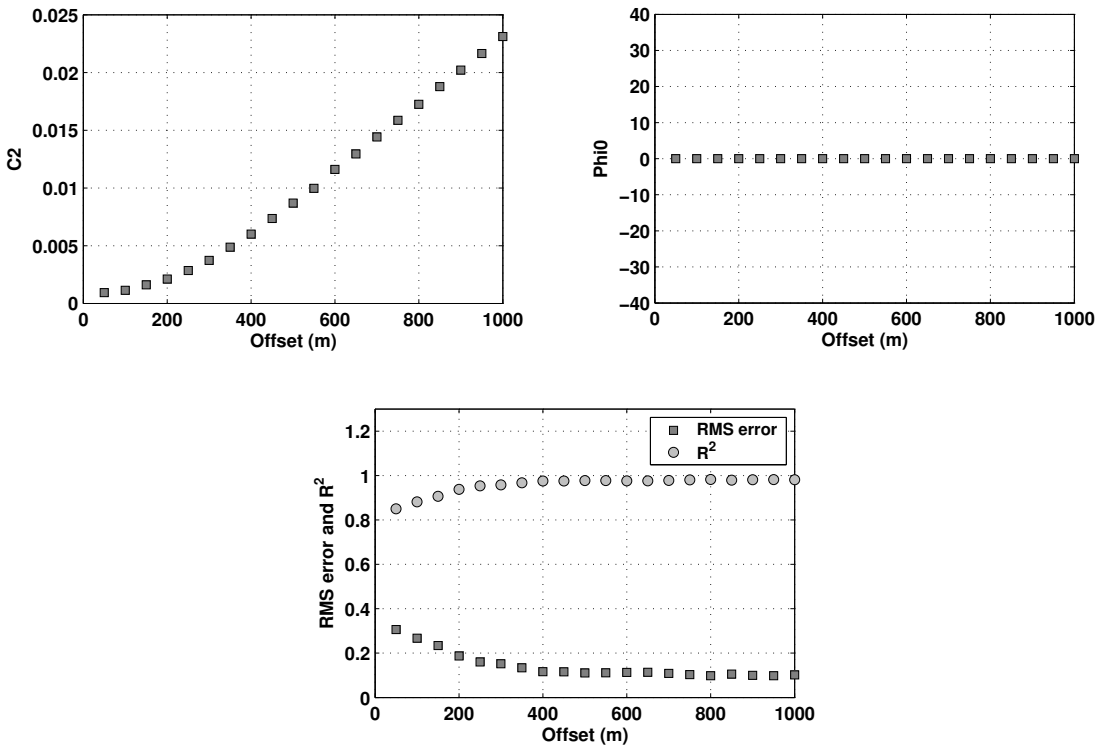

Figure 4.10: Inverted parameters and errors of the azimuthal fit to $\Delta 1/Q$ for model 1.

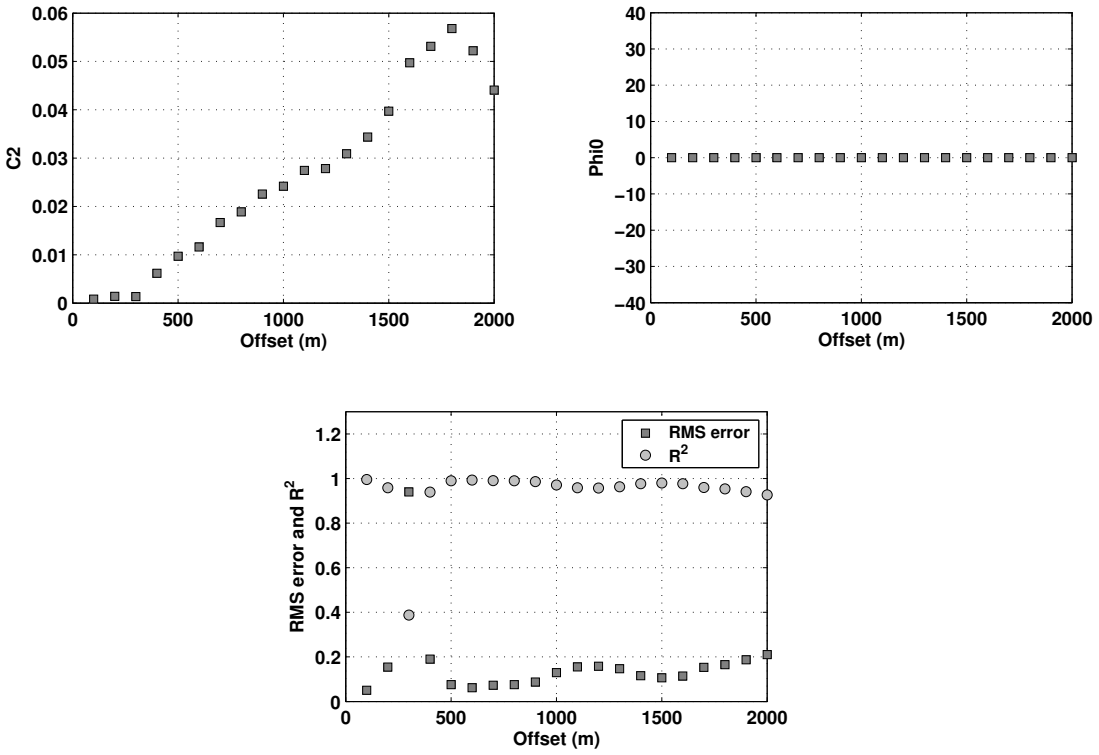

Figure 4.11: Inverted parameters and errors of the azimuthal fit to $\Delta 1/Q$ for model 2.

show a steady increase. Overall, however, the errors are small and the azimuthal variation in attenuation is detected with the correct symmetry.

If the measured variation in $\Delta 1/Q$ is to be used to invert for fracture parameters, it is also important that the absolute values of C_2 are correct. I test this by adding the measured values of $\Delta 1/Q$ at each azimuth and offset to the input $1/Q$ of the fracture strike direction and comparing the results to the input values of $1/Q$ at the peak frequency of 20 Hz. This comparison is shown in Fig. 4.12 for two walkaway lines of model 2. Overall there is a good match between model values and measured data. Some scatter around the theoretical curve, however, can be seen again at mid to far offsets, which is due to the interference effects mentioned above.

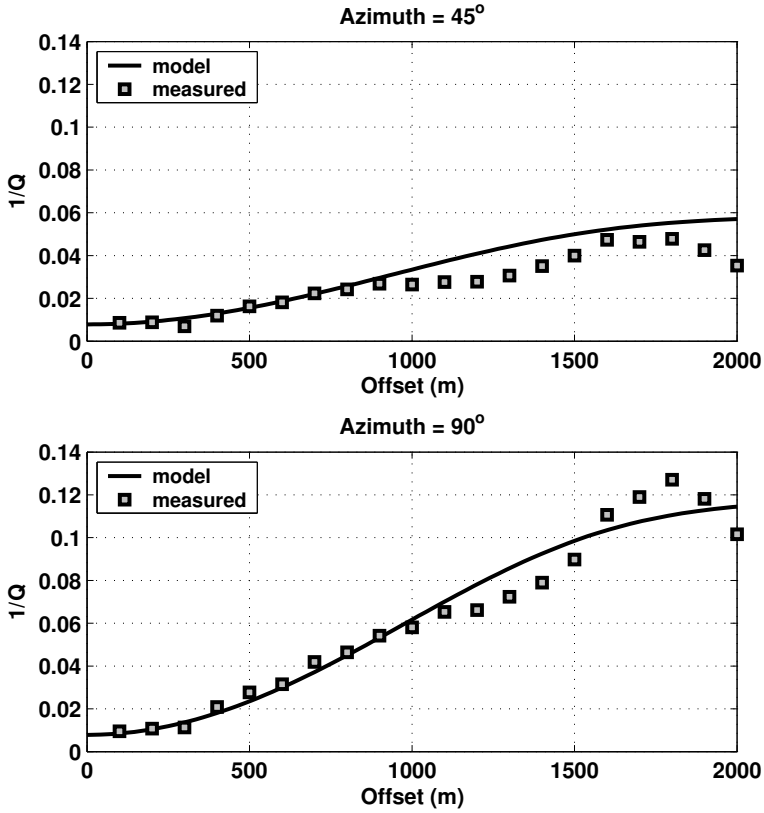

Figure 4.12: Comparison of $1/Q$ input into the model with measured values for two walkaway lines of model 2.

4.6.3 Inversion for fracture density and size

In Section 3.6 of Chapter 3 I discussed how a value for the relaxation time τ_m of the model of Chapman (2003) can be derived from the calibration against laboratory data. The model can then be used to invert for fracture density and fracture radius from measurements of the frequency dependence of anisotropy. Here, I examine how the attenuation anisotropy derived from the synthetic data can be used for such an inversion. I restrict the analysis to model 2, which represents a more realistic case.

Fig. 4.13 displays the RMS error between predicted and measured values of $\Delta 1/Q$ for all offsets and azimuths plotted as a function of fracture density and fracture radius. The white dot shows the values $\varepsilon_f = 0.05$ and $a_f = 0.01$ m that were input into the model. It is obvious that the inversion is not unique. This is due to the fact that I only measure $\Delta 1/Q$ at the peak frequency of the

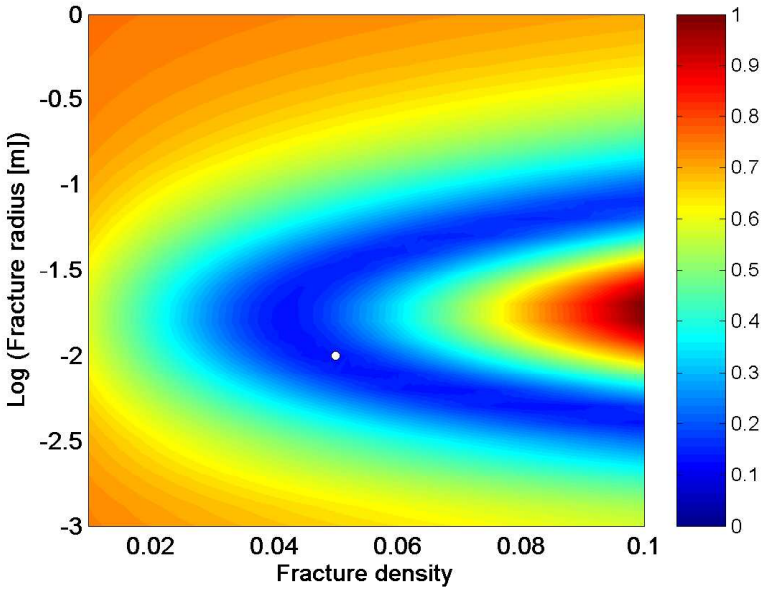

Figure 4.13: Inversion for fracture density and size from the measured values of $\Delta 1/Q$ at all offsets and azimuths. The correct fracture parameters are indicated by the white dot. The inversion is not unique, because attenuation is only measured at one frequency.

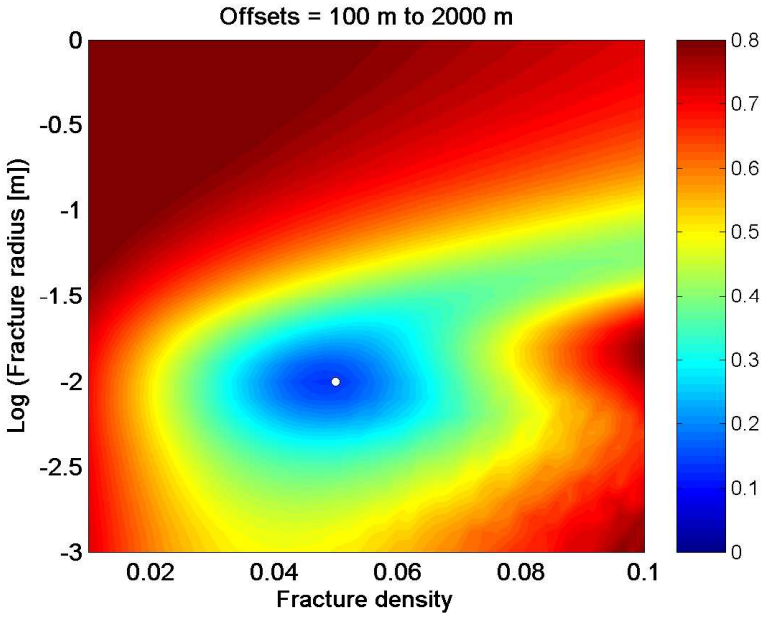

Figure 4.14: Error function for simultaneously fitting the model to the azimuthal variation in $1/Q$ and to the azimuthal variation in traveltimes. There is now a confined minimum around the correct values of the fracture parameters.

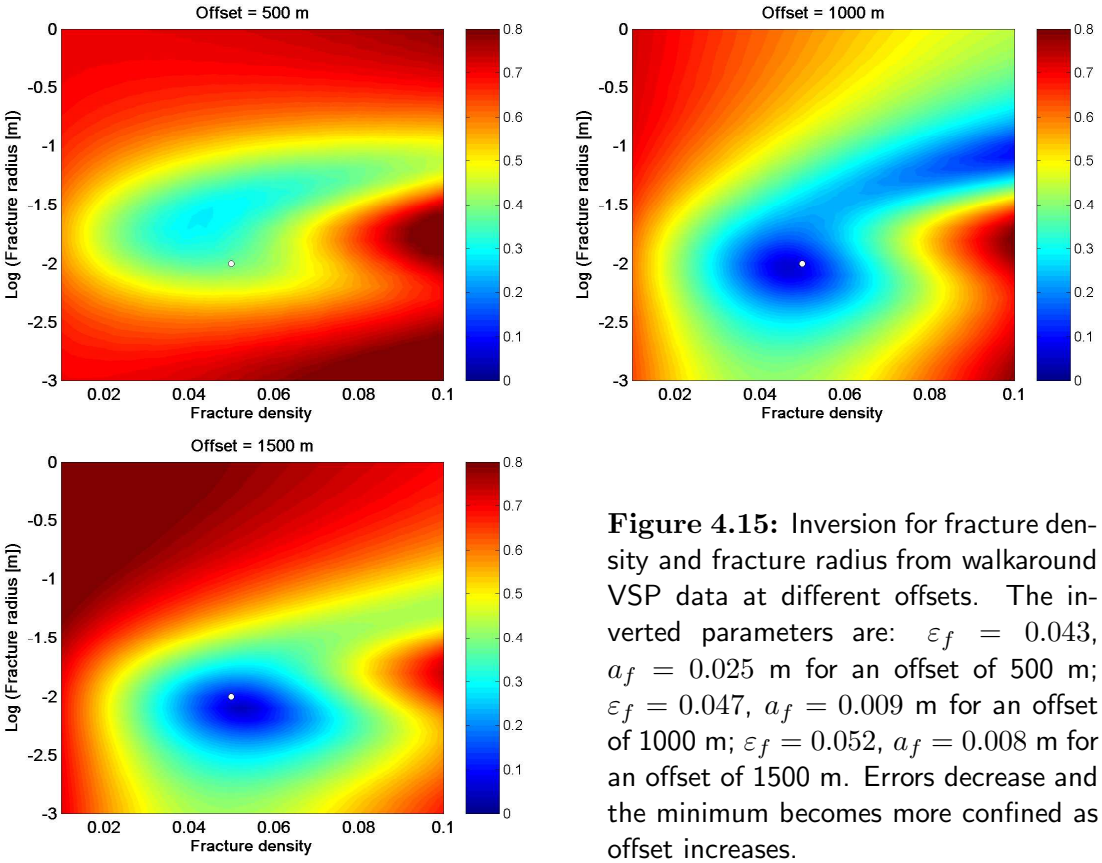

Figure 4.15: Inversion for fracture density and fracture radius from walkaround VSP data at different offsets. The inverted parameters are: $\varepsilon_f = 0.043$, $a_f = 0.025$ m for an offset of 500 m; $\varepsilon_f = 0.047$, $a_f = 0.009$ m for an offset of 1000 m; $\varepsilon_f = 0.052$, $a_f = 0.008$ m for an offset of 1500 m. Errors decrease and the minimum becomes more confined as offset increases.

wavelet and not its variation with frequency. Nevertheless, the problem can be overcome by incorporating another anisotropic attribute into the inversion, such as the azimuthal variation in traveltimes.

Fig. 4.14 shows the RMS error of jointly fitting the model to $\Delta 1/Q$ and the magnitude of the azimuthal variation in picked traveltimes. I use raytracing to compute the predicted traveltimes of each model. There is now a confined minimum around the correct fracture parameters. The inverted fracture density and fracture radius are 0.048 and 0.01 m, respectively. The shape of the error function indicates that the minimum is related to a log-normal distribution of fracture sizes, and a derived fracture radius from real data therefore represents the mean of the log of fracture sizes.

For walkaround VSP geometries only data points from one particular offset are available. The results of inverting for fracture density and size from walkaround data at offsets of 500 m, 1000 m, and 1500 m are shown in Fig. 4.15. At near offsets the azimuthal variation in both attributes is small, so that uncertainty

in the inversion is larger than at far offsets. It is particularly affected by the traveltimes where the differences with azimuth only exceed the sample rate of 2 ms beyond an offset of 500 m. Therefore, the error function in Fig. 4.15 for a walkaround VSP at 500 m offset has a rather broad minimum, and the inverted parameter values are further away from the true values than in the other figures. As offset increases, the minimum becomes more confined, and the error at the minimum decreases. Despite the sensitivity of the inversion to the offset at which the measurement is taken, the plots show that overall the derived fracture radius is well constrained and errors in the inverted values are significantly less than an order of magnitude. This demonstrates the potential merits of using attenuation anisotropy as an additional seismic attribute for the characterization of fractures. Although larger offsets increase stability in the inversion, it should be kept in mind that the measurement of $\Delta 1/Q$ becomes less accurate at far offsets, as demonstrated in the previous section. Furthermore, the analysis assumes homogeneity in each layer accross an area spanned by the walkaway lines. This assumption is more likely to be violated at far offsets. In practice, the analysis of field data will benefit from a large number of data points, so that effects of noise are reduced. In particular, a dense sampling in azimuth will increase confidence in the inversion.

4.6.4 Application of the spectral colour display

In order to demonstrate potential applications of the spectral colour display I use the synthetic walkaround VSP data of model 1 at an offset of 1000 m. In Appendix B I show how the effects of frequency dependent anisotropy are revealed by the S-transform of the data. In this section I use the local spectra obtained with the S-transform in Appendix B and demonstrate the visualization of spatial changes in average spectral properties represented by the spectral colour.
For each trace of the walkaround VSP data set I compute the spectral colour pixels as a function of time as described in Section 4.5. I then normalize the entire image by the maximum values. In order to visualize changes with azimuth, I plot each trace of colour pixels along a segment at the azimuth of the corresponding source location with time increasing radially from the centre of the plot. The resulting image is shown in Fig. 4.16. The bright ellipse is the direct-arrival energy.

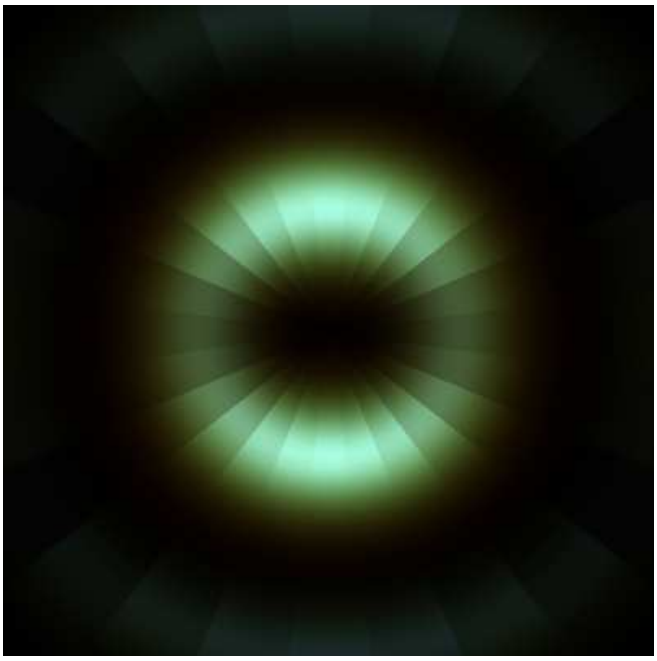

Figure 4.16: Spectral colour display of the walkaround data of model 1 at an offset of 1000 m. Time is increasing radially from the centre of the image. The dimming towards the E-W direction shows the effect of attenuation normal to the fracture strike.

The fact that it forms an ellipse in the horizontal plane reflects the traveltime anisotropy of the HTI medium, where the short axis of the ellipse is parallel to the fracture strike direction (*see* Chapter 2, Section 2.5). The effect of attenuation anisotropy is visualized by the dimming of the image towards the fracture normal direction together with a slight change in colour and saturation.

As explained in Section 4.5 the pixel colours can be represented in the HLS system where the three attributes luminosity, hue and saturation are measures of the overall power, centre frequency and bandwidth, respectively. We can therefore look at the effects of attenuation on these three attributes separately. Fig. 4.17 displays the luminosity, hue and saturation of the image of Fig. 4.16 as filled contour plots. The interval of the contour lines is 0.1. The luminosity reaches maximum values along the fracture strike (N-S) and decreases towards an azimuth perpendicular to the fractures. Attenuation in the E-W direction significantly reduces the overall spectral power of the signal. Hue has lower values at an azimuth of 90^o, which corresponds to a shift in colour towards red (*see* Fig. 4.3), indicating a decrease in centre frequency. Saturation is slightly increased in the direction of the fracture normals, reflecting a decrease in frequency bandwidth of the signal.

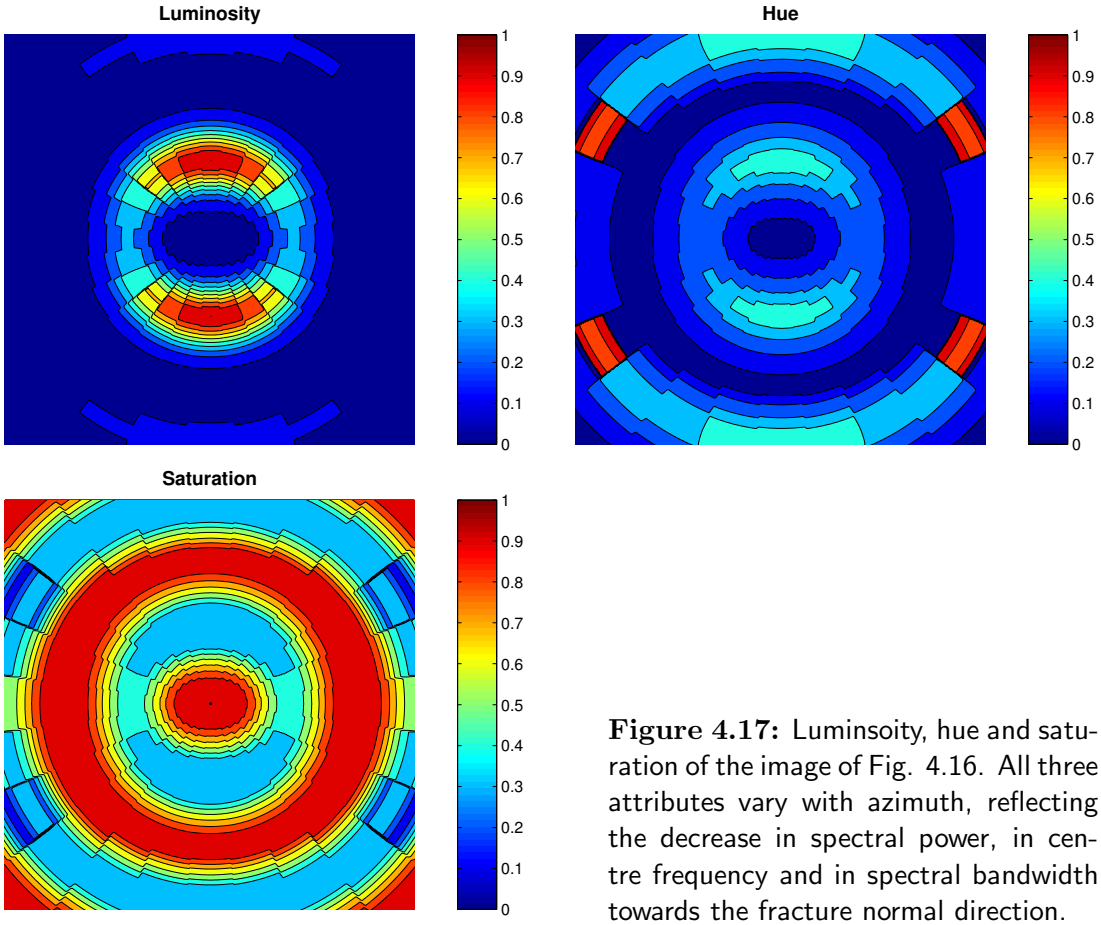

Figure 4.17: Luminsoity, hue and saturation of the image of Fig. 4.16. All three attributes vary with azimuth, reflecting the decrease in spectral power, in centre frequency and in spectral bandwidth towards the fracture normal direction.

For a particular dataset it may be the case that the effect of attenuation is more pronounced in one of the three attributes displayed in Fig. 4.17. The synthetic data analysed here clearly show the largest azimuthal variation in luminosity. We can create a colour image that reflects only this effect by setting hue and saturation to a constant value. The resulting image is displayed in Fig. 4.18.

The technique therefore offers various possibilities of visualizing effects of attenuation anisotropy that produce changes in different attributes of the spectrum. Since the spectral colour attributes are obtained by averaging over the spectrum, this may be particularly useful in field data cases where issues such as source instability prevent the use of quantitative techniques, which are much more sensitive to the particular shape of the spectrum.

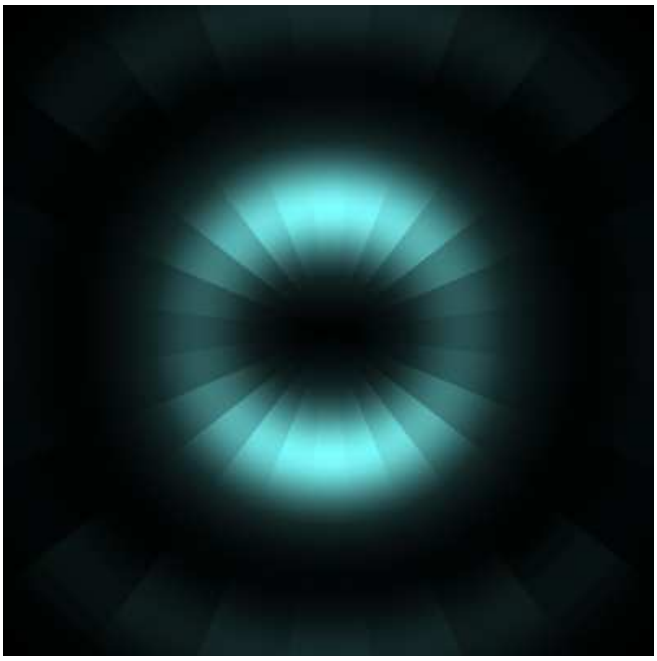

Figure 4.18: Spectral colour display of Fig. 4.16 with constant hue and saturation.

4.7 Summary

If frequency-dependent anisotropy exists and causes P-wave attenuation anisotropy at seismic frequencies, adequate techniques are needed to detect such an effect from seismic data. I have demonstrated with simple synthetic VSP data that the traditional spectral ratio method can be used to measure the change in attenuation as a function of azimuth. The technique correctly detects the symmetry and magnitude of azimuthal variation in $1/Q$ at different offsets, if the effect is present in the synthetic data.

Alternatively attenuation can be measured through the shift in instantaneous frequencies, which may be more stable in field data cases. Therefore, confidence in any field data results can be increased by using two independent methods to derive the change in $1/Q$ as a function of propagation direction.

I have demonstrated how the changes in average spectral characteristics with propagation direction can be visualized and qualitatively assessed using a spectral colour display. The spectral colour represents localized spectra obtained with a time-frequency transform of the data.

The model of Chapman (2003) provides a way to relate the attenuation anisotropy

to fracture properties. The synthetic studies have shown that an inversion for fracture parameters is well constrained by the difference in attenuation between azimuths together with measurements of velocity anisotropy. This demonstrates that attenuation anisotropy, if found in field data, could be a very useful tool to characterize fractures in the subsurface.

The application of the techniques to field data to detect potential anisotropy in attenuation is the subject of the next chapter.

Chapter 5

Anisotropy of P-wave attenuation in VSP data: Field data

5.1 Introduction

In this chapter I analyse the direct P-wave arrivals from two different multi-azimuth VSP data sets to investigate whether there are any systematic changes in attenuation as a function of azimuth. The first data set is a walkaround VSP from an oil field in California, the second one is a 3-arm walkaway VSP from an oil field in the North Sea. In both cases it is known that fractures are present in the subsurface, and anisotropy has previously been measured from the data using shear-wave splitting or P-wave traveltimes and polarizations. With the attenuation analysis of this chapter I intend to determine whether the anisotropy is also frequency dependent. I apply the methods discussed in the previous chapter.

5.2 Analysis of walkaround VSP data, Railroad Gap oil field

5.2.1 Geological setting and VSP geometry

The Railroad Gap oil field is located about 60 km west of Bakersfield in the southwest San Joaquin basin of California. The structure of the field is a doubly-

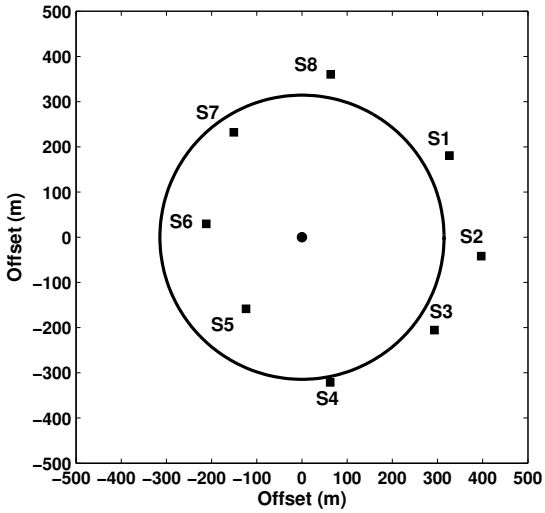

Figure 5.1: Map of source locations relative to the well.

plunging anticline trending NW-SE (McWilliams, 2001). Its axis is parallel to the San Andreas fault that runs approximately 16 km southwest of the field. Although crustal shortening has taken place in a NE-SW direction, there is also evidence of significant NE-oriented faulting and fracturing in the basin from satellite and aircraft imagery (Montgomery and Morea, 2001).

The main reservoir unit in the field is the Antelope Shale, which is a siliceous shale largely composed of the skeletal remains of diatoms (McWilliams, 2001; Montgomery and Morea, 2001). It is characterized by high porosities ($\geq$ 30%) but extremely low matrix permeabilities ($<$ 1 mD). Permeability is increased locally due to the presence of thin sand beds and natural fractures (Montgomery and Morea, 2001). Distribution and orientation of the fractures, however, are unknown (Winterstein and Meadows, 1991). Overlying the reservoir is a 950 m thick shallow marine sandstone formation, followed by 450 m of conglomerates and poorly sorted sands in the near surface (Montgomery and Morea, 2001). The top of the Antelope Shale is at a depth of about 1300 m in the VSP area (Winterstein and Meadows, 1991).

The walkaround VSP data were acquired with one 3-component receiver deployed in the borehole at a depth of 1675 m and eight source points located around the well at an average offset of 314 m. Fig. 5.1 is a plot of the source locations relative to the well. A multi-component source was used, but only the P-wave data were available for this analysis. Traces were recorded up to 6 s with a sample rate of

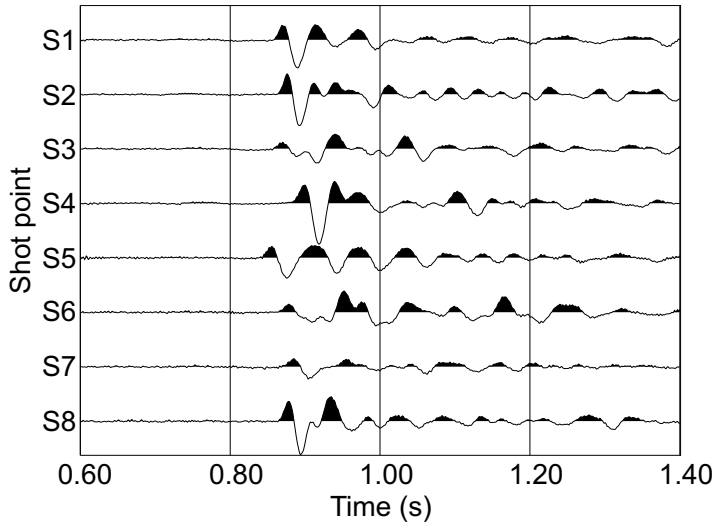

Figure 5.2: Trace data of the walkaround VSP.

1 ms.

The shear-wave data of a near-offset VSP acquired in the same well have been analysed by Winterstein and Meadows (1991). The authors found that significant shear-wave splitting occurs in the overburden and in the reservoir, and that the azimuth of the fast shear-wave polarization changes considerably with depth.

5.2.2 Attenuation analysis

Fig. 5.2 shows the traces of the walkaround VSP after rotation into the direction of maximum first-arrival energy. Horne and MacBeth (1997) analysed the amplitudes of the direct P-wave arrivals of these data and found a strong systematic variation with azimuth. The authors discussed several possible causes of the observed amplitude variation in this and five other data sets. These were the geophone response, source radiation pattern, structure and topography, transmission coefficients and attenuation. They concluded that only anisotropic attenuation has the potential to explain their findings, but the magnitude of the observed amplitude variation at seismic frequencies could not be explained by rock physics models available at the time.

Here I want to take the analysis further and investigate, whether the data actually show azimuthal anisotropy in attenuation, so that not only the peak amplitude

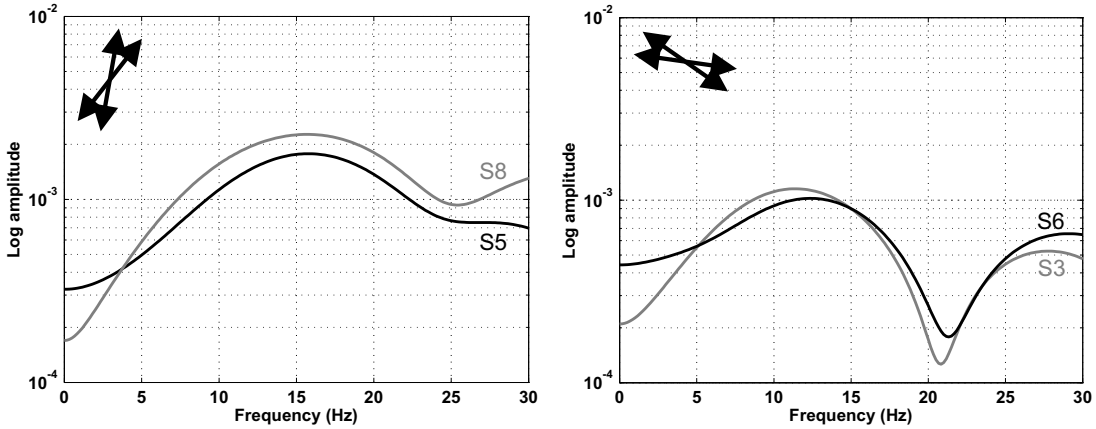

(a) (b)

Figure 5.3: Amplitude spectra of direct P-wave arrivals recorded along orthogonal azimuths.

changes, but also the frequency content. I use the spectral ratio method to measure attenuation as a function of azimuth as described in Chapter 4.

Fig. 5.3 displays the amplitude spectra of the direct P-wave arrivals in four of the traces corresponding to orthogonal directions. Sources 8 and 5 have an average azimuth of N28^{o}E and N152^{o}W, whereas sources 6 and 3 are located at an average azimuth of N111.5^{o}E and N68.5^{o}W. The spectra among each pair of arrivals are very similar, but there is considerable difference between the two directions. The signals from sources 3 and 6 are clearly attenuated compared to the arrivals from sources 5 and 8. This indicates that there is a distinct azimuthal change in the spectral signature of the direct P-wave arrivals.

As discussed in the previous chapter the measured spectral ratios can be influenced by the width of the time window that is applied to the trace data. To ensure that any detected azimuthal variation is not due to a particular choice of window I perform the analysis for different window sizes between 250 ms and 500 ms as well as without any windowing. I also vary the frequency bandwidth, over which a linear regression to the spectral ratios is performed, since it is another sensitive parameter in the analysis. The smallest bandwidth is 5 Hz to 15 Hz, the largest is 5 Hz to 25 Hz. Finally, I choose different traces as the reference trace, to which all other spectra are compared.

Figs. 5.4 to 5.6 show examples of computed spectral ratios and fitted straight

lines for window widths of 250 ms, 400 ms, and no windowing, respectively. Different frequency ranges are also used. The reference trace is S8 at 10^o from N. By comparing the diagrams we can see that independently of window size and chosen frequency range there is a consistent relative change in the slopes of the spectral ratios with azimuth.

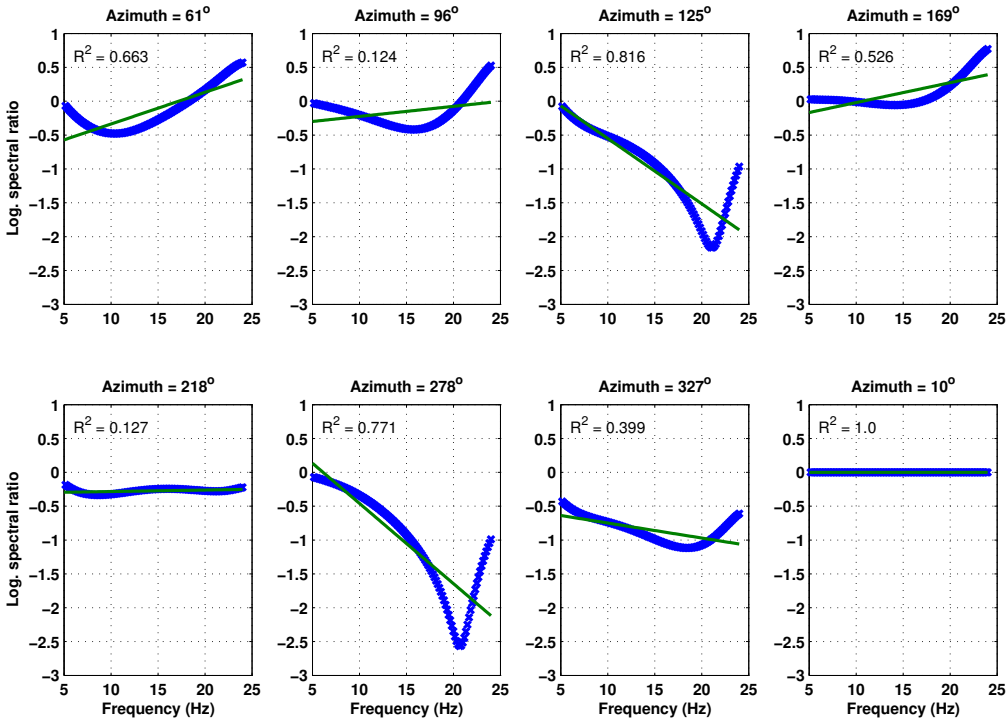

Figure 5.4: Linear regression to the spectral ratios. The width of the time window is 250 ms.

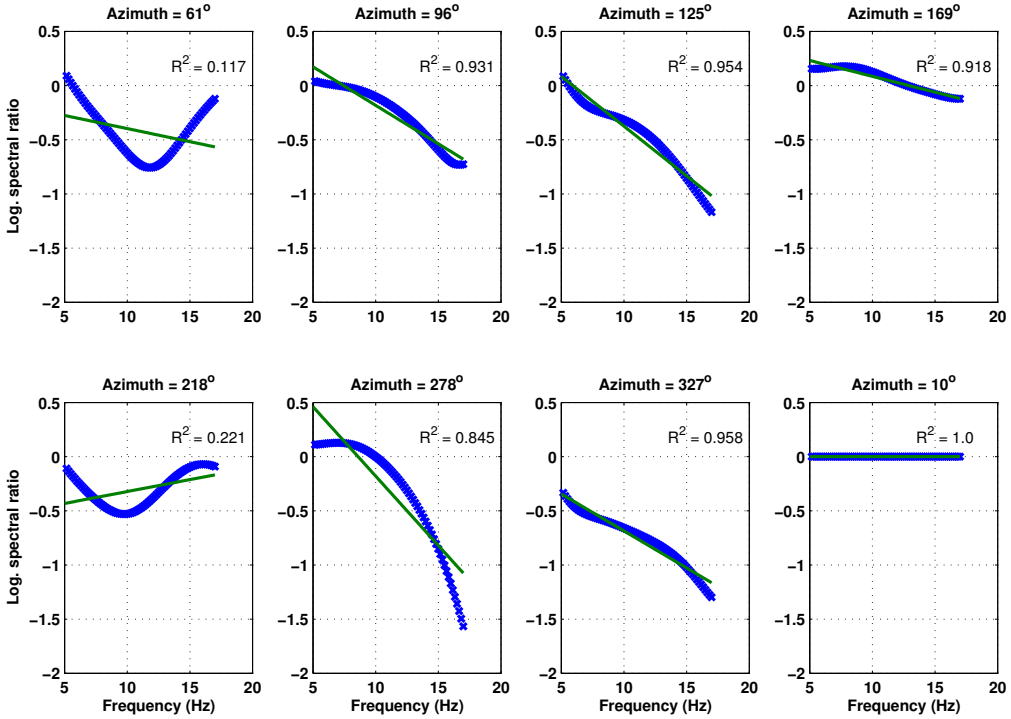

Figure 5.5: Spectral ratios and fitted straight lines for a 400 ms time window.

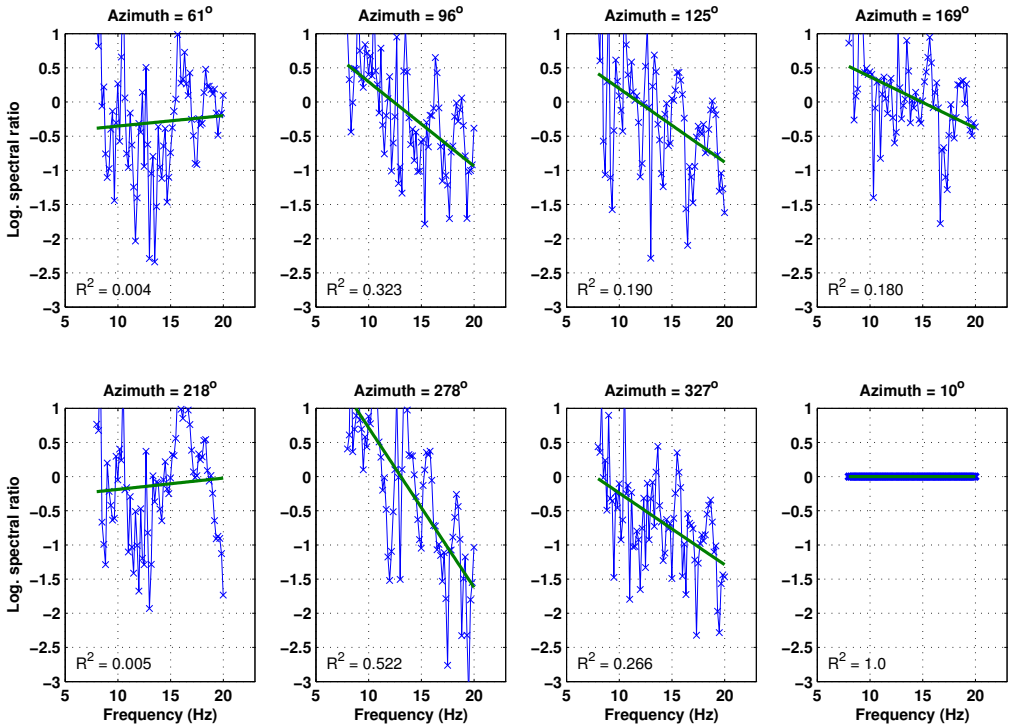

Figure 5.6: Linear regression to spectral ratios obtained without any windowing of the trace data.

As in the synthetic studies of Chapter 4 I compute $\Delta 1/Q$ from Eq. 4.7 using the average first-arrival time. I then fit the $\cos(2\varphi)$-function of Eq. 4.8 to the data. Fig. 5.7 shows examples of the measured $\Delta 1/Q$ and fitted function for a 300 ms time window, no windowing, and a window width of 250 ms with S3 as the reference trace instead of S8. The mean values of $\Delta 1/Q$ measured for the different frequency ranges (*squares*) are plotted, whereas the standard deviations are displayed as error bars. All three Figures show a systematic variation in $\Delta 1/Q$ with azimuth with similar symmetry directions and magnitudes. It should be

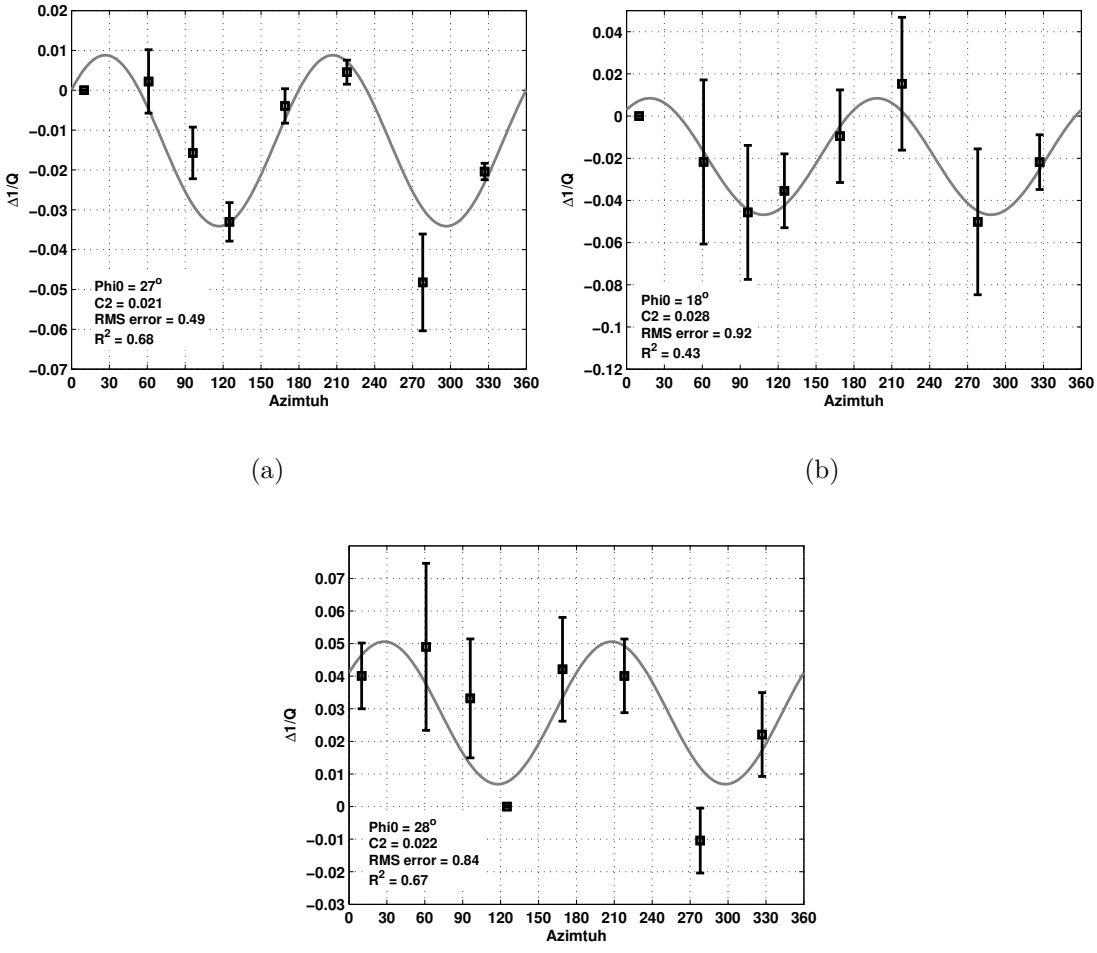

(a) (b)

(c)

Figure 5.7: Azimuthal fit to $\Delta 1/Q$ obtained for different time windows and reference traces. a) Window width = 300 ms, reference trace = S8; b) no windowing, reference trace = S8; c) Window width = 250 ms, reference trace = S3. The symmetry and magnitude of the azimuthal variation in $\Delta 1/Q$ is similar among all cases.

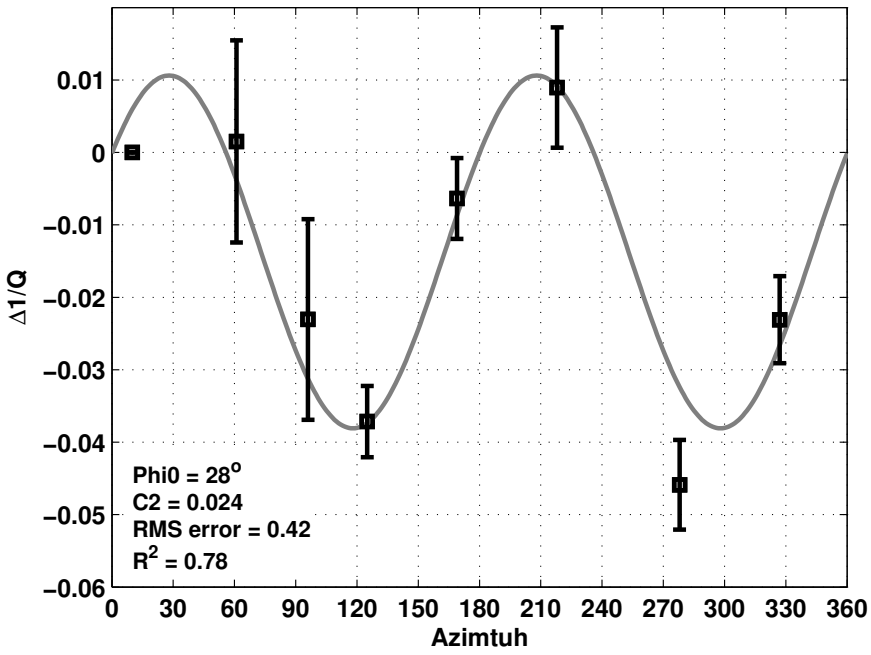

Figure 5.8: Combining the values of $\Delta 1/Q$ obtained for all processing parameters. The inverted azimuth of minimum attenuation is N28^{o}E.

noted that each set of data points contained in the average plotted in the Figures follows this azimuthal variation (*see* Figs. 5.4 to 5.6). Combining all the data obtained for the range of processing parameters yields the azimuthal variation of $\Delta 1/Q$ displayed in Fig. 5.8. The inverted azimuth of minimum attenuation is N28^{o}E, and the difference in $1/Q$ between the symmetry azimuths is 0.048.

5.2.3 Discussion and conclusions

An interpretation of the measured attenuation anisotropy in terms of rock properties is limited due to the fact that only one receiver depth was used in the experiment. Therefore, any changes of the effect with depth are not revealed, and it remains unknown whether the attenuation only occurs in a certain depth interval. I can assess, however, whether the derived symmetry directions correlate with the symmetry directions of other anisotropic attributes and the results of fracture studies that have been conducted in the field or the area.

Fig. 5.9 shows the shear-wave splitting results of Winterstein and Meadows (1991) that were obtained from a multi-component near offset VSP acquired in the same well as the walkaround VSP. Significant shear-wave splitting occurs at almost all

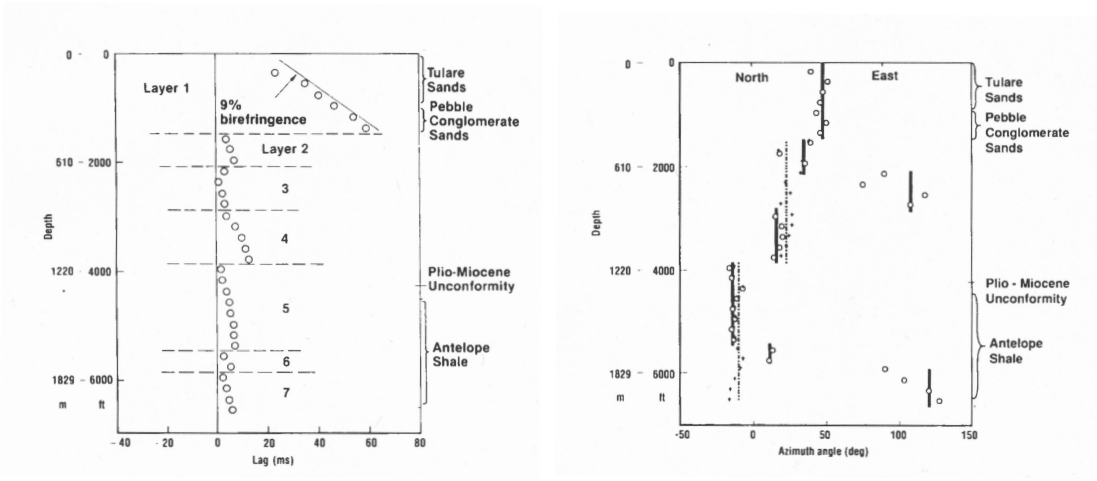

(a) (b)

Figure 5.9: Shear-wave splitting results of Winterstein and Meadows (1991) from a near-offset VSP acquired in the same well. a) Time delay; b) polarization azimuth of the fast shear wave.

depths, and there are considerable changes in the polarization direction of the fast shear wave with depth. Rose diagrams of the S1 polarization azimuths are displayed in Fig. 5.10. For Fig. 5.10b the time delays per depth unit were used as weights. The largest shear-wave anisotropy with a time delay of 15 ms per 100 m is found in the near-surface sands and conglomerates down to a depth of 400 m. Winterstein and Meadows (1991) interpret the near-surface anisotropy in terms of small aspect-ratio pore throats that close perpendicular to the direction of maximum horizontal stress, which is oriented NE in the basin normal to the San Andreas fault (Zoback *et al.*, 1987). The authors also note that the rocks are dry down to a depth of 200 m.

The azimuth of minimum attenuation of N28^{o}E agrees both with an average of the S1 polarizations over depth as well as with the dominant S1 polarization of N25^{o}E in the 800 m thick sandstone unit between the base of the conglomerates and the unconformity above the reservoir. If it represents an average symmetry direction of the entire depth interval, it is however not dominated by the near-surface anisotropy, as the shear-wave splitting data might suggest. Considering that the rocks in the near-surface are dry, this means that the attenuation anisotropy, which I have found in the data, does not reflect the dry-rock anisotropy of the

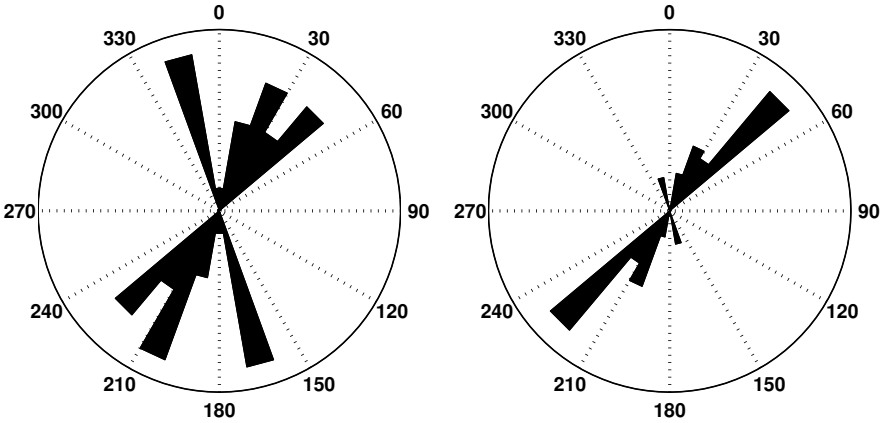

(a) (b)

Figure 5.10: Rose diagrams of the polarization azimuths of the fast shear waves derived by Winterstein and Meadows (1991). a) Raw data; b) weighted with the time delay per depth interval.

upper few hundred metres, but rather correlates with the shear-wave anisotropy in the fluid-filled rock section.

Hackert *et al.* (2001) and Parra *et al.* (2002) studied attenuation from sonic log and cross-well data in the Antelope Shale formation in a nearby oil field. They found a zone of high attenuation ($Q \approx 20$) in the upper part of the formation for horizontally propagating waves along a NW-SE direction, correlating with a low horizontal velocity in the same direction and fracture zones found in cores. Parra *et al.* (2002) modelled the observations in terms of fluid motion in partially saturated fractures based on the model of Dvorkin and Nur (1993). Although the data analysed by Hackert *et al.* (2001) and Parra *et al.* (2002) were not recorded at different azimuths, it is an observation of velocity and attenuation anisotropy between the vertical and the horizontal propagation directions that would also agree with an azimuthally anisotropic interpretation. The fact that high attenuation occurs along a NW-SE azimuth agrees well with the azimuth of maximum attenuation of N62^{o}W, which I found in the Railroad Gap walkaround VSP data.

I now use the model of Chapman (2003) to investigate whether the magnitude of the observed attenuation anisotropy can in principle be explained by a squirt-flow mechanism between aligned vertical fractures and the matrix porosity. The

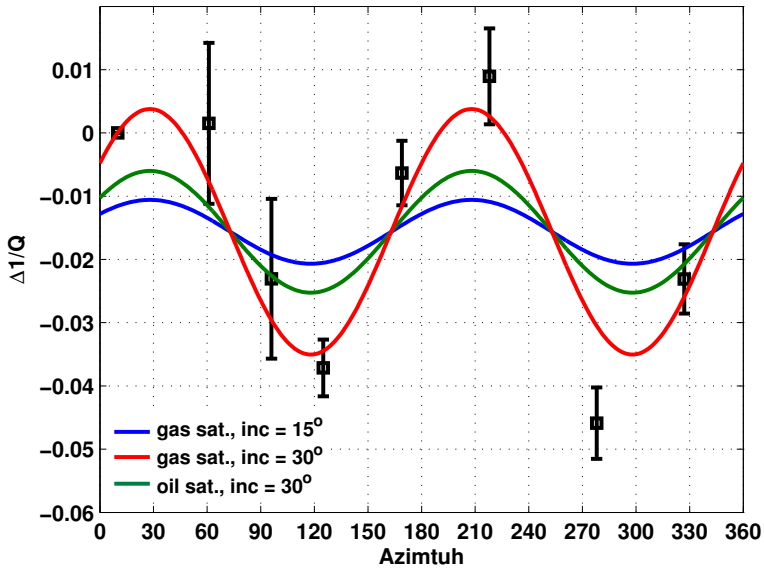

Figure 5.11: Azimuthal variation in $\Delta 1/Q$ predicted by the model of Chapman (2003) for different fluid saturation and incidence angles together with the data from the Railroad Gap walkaround VSP.

average source offset of 314 m in the walkaround VSP data is rather small compared to the receiver depth of 1675 m, so that incidence angles are only around 10^o-15^o. From Fig. 3.10 in Chapter 3 we can see that the azimuthal variation in $1/Q$ described by the model is very small for these polar angles under the assumption that the fractures are vertical. Fig. 5.11 shows the data together with modelled curves for different fluid saturations and incidence angles. In the modelling I assume $\omega\tau_f = 1$ to simulate a measurement at the characteristic frequency associated with the fracture-induced squirt flow where attenuation peaks. I choose a porosity of 30% (*see* Section 5.2.1) and set the fracture density to 0.1. For gas saturation, the magnitude of attenuation anisotropy that is seen in the data can only be modelled for an incidence angle of 30^o. At an incidence angle of 15^o the azimuthal variation in $1/Q$ predicted by the model is much smaller. For oil saturation even larger incidence angles than 30^o would be required to explain the observed magnitude of attenuation anisotropy.

It is possible that scattering attenuation contributes significantly to the measured attenuation values. However, it would have to vary azimuthally in the same fashion as the squirt-flow related attenuation to increase the magnitude of azimuthal anisotropy in $1/Q$. An increased azimuthal variation in attenuation

at small incidence angles could also be expected if the fractures are not modelled as perfectly vertical but with a distribution of dips around the vertical, or if their surfaces are corrugated instead of planar (Brown *et al.*, 2000; Bakulin *et al.*, 2000c; Sayers, 2002). However, these possible explanations remain speculative, because the nature and distribution of fractures around the VSP well is unknown. Despite the uncertainty in explaining the magnitude of the measured effect and the limitations in any conclusive interpretation due to the lack of data, it is a clear observation of azimuthal anisotropy in P-wave attenuation that is consistent in its symmetry with shear-wave anisotropy measured in the same well.

5.3 Analysis of VSP data from the Clair field

In this section I analyse P-wave attenuation in marine multi-azimuth walkaway VSP data from the Clair field in the North Sea. The data are acquired in the overburden and in the fractured reservoir, so that an interpretation of the results is more constrained than for the VSP data studied in the previous section. I first measure attenuation as a function of azimuth independently at each recording depth and then determine a zero-offset Q for the reservoir section between the two depth levels before concluding with a discussion of the results.

5.3.1 Geological background

The Clair field is located on the UK Continental Shelf about 75 km west of Shetland. A schematic cross-section of the field is shown in Fig. 5.12. The structure is formed by a NE-SW trending pre-Cambrian basement ridge (Coney *et al.*, 1993). Overlying the basement is the Clair group, which is a sequence of Devonian and Carboniferous continental red beds roughly 700 m thick. These are overlain by a thick unit of Cretaceous tight mudstones. Oil was discovered in both the basement rocks and the clastics of the Clair group (Coney *et al.*, 1993). The latter were deposited in fluviatile, aeolian and lacustrine environments with marginal marine sediments at the top (Allen and Mange-Rajetzky, 1992). As a consequence of the large spectrum in depositional environments the reservoir

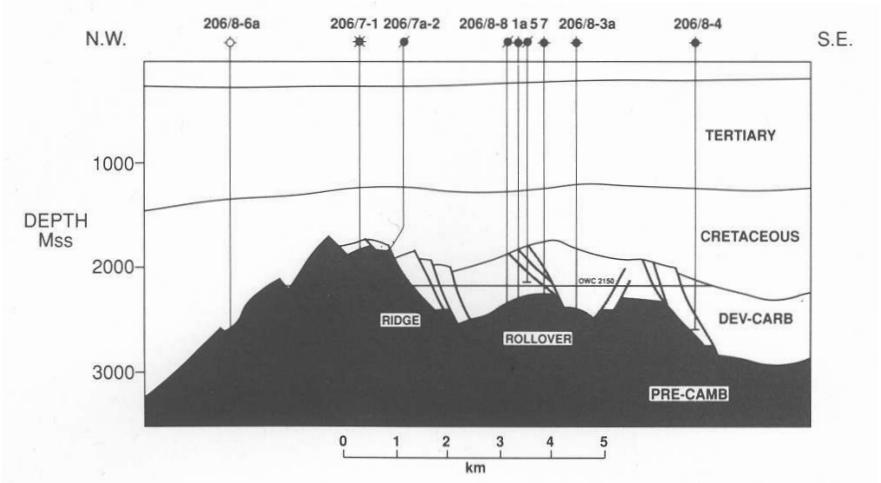

Figure 5.12: Schematic cross-section of the Clair field. (*From* Coney *et al.* (1993).)

quality is extremely variable. Although the porosity is fairly constant at 12% to 15%, the permeability varies between 5 mD and 360 mD in the lithological units of the Clair group (Coney *et al.*, 1993). It has been recognized that natural open fractures play an important role in locally enhancing the permeability in the reservoir, and a number of studies have been conducted to characterize the fracture system (Coney *et al.*, 1993; Wijnands, 1997; Horne *et al.*, 1998; Smith and McGarrity, 2001).

Coney *et al.* (1993) discuss a structural model for the basement faulting that was derived from 3D seismic data, well data and aeromagnetometry. It contains a set of NNE-SSW striking regional faults and a secondary set of faults trending NE-SW to ENE-WSW. It is believed that these faults partly continue upwards into the Clair group (Coney *et al.*, 1993). Furthermore, the 3D seismic data revealed a set of late Cretaceous NNW-SSE trending faults in the Clair group. Data from cores show that high fracture densities are associated with faulting and are confined to certain lithological units of the Clair group.

Wijnands (1997), Horne *et al.* (1998) and Smith and McGarrity (2001) discuss the analysis of azimuthal anisotropy in the 3-arm walkaway VSP data that is investigated for P-wave attenuation effects in the remainder of this chapter. The results of traveltime and polarization inversion revealed a larger magnitude of azimuthal anisotropy in the reservoir than in the overburden. The fast direction obtained from both analyses was found to be consistent at N120^{o}E for the overburden and at N100^{o}E for the interval from the surface to 400 m below the reservoir top.

5.3.2 VSP geometry and data pre-processing

Three walkaway VSP lines were acquired in well 206/8-9Y, which is located in the central area of the Clair field. The azimuths of the lines were N1^{o}E, N46^{o}E and N136^{o}E. Each of the walkaway lines was about 4 km long and centred at the wellbore. The downhole tool consisted of an array of five 3-component receivers that were 15 m apart. It was deployed at two different depths in the borehole: 65 m above the base Cretaceous with vertical receiver depths of 1486 m to 1535 m, and in the reservoir at vertical depths of 1850 m to 1906 m.

The source locations for both tool settings are shown in Fig. 5.13. The average

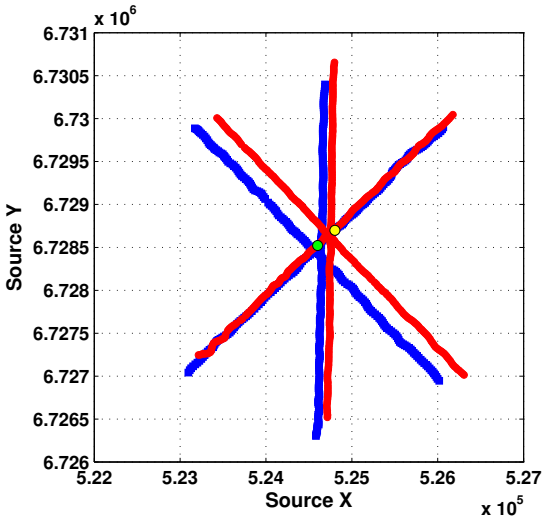

Figure 5.13: Source locations of the Clair field walkaway VSP data. Source points for the data recorded at the lower tool setting are displayed in blue, the ones for the upper tool setting in red. The yellow and green dots show the x- and y-coordinates of the shallow and deep receiver settings, respectively.

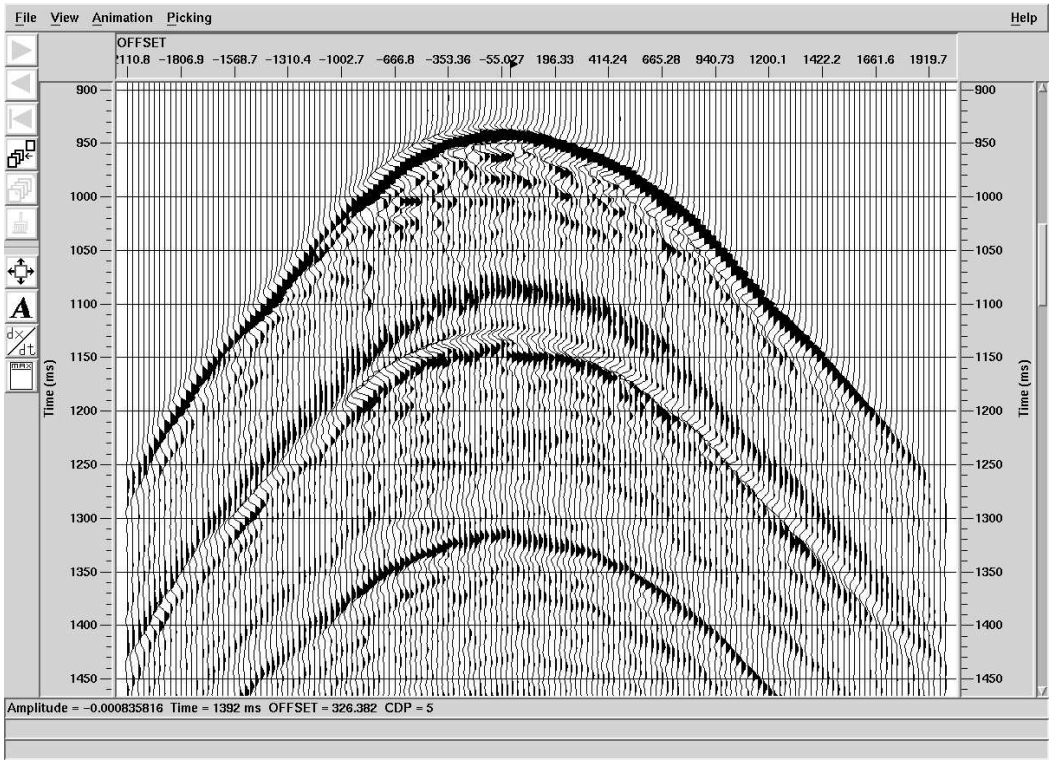

Figure 5.14: Common receiver gather of a walkaway line after rotation onto one receiver component, extraction of the downgoing wavefield and source-signature deconvolution.

spacing is about 25 m, but source intervals are not constant along the lines. The source was a cluster of three airguns suspended at 4.5 m below sea level. The data were recorded with a sample rate of 1 ms, and the trace length is 4 s.
I have rotated the 3-component data into the direction where the first-arrival energy becomes maximized in one component. I picked the first break times on the rotated data and separated up- and downgoing wavefields using a τ-p domain dip filter. Care is taken that the process preserves amplitudes. The attenuation measurements are performed on the first arrivals of the downgoing wavefield. I also used the hydrophone recordings to perform source-signature deconvolution. However, I found that this step did not affect the results of the attenuation analysis, which I carried out both on the deconvolved as well as on the original data. An example of a common receiver gather after rotation, wavefield separation and source-signature deconvolution is shown in Fig. 5.14.

5.3.3 Attenuation anisotropy in the overburden and the reservoir

In this section I analyse attenuation as a function of azimuth at constant offsets as described in Chapter 4 for each tool setting. Compared to the Railroad Gap VSP analysed in the previous section the acquisition geometry of the Clair field VSP has the advantage that data are recorded in the fractured reservoir as well as at the base of the essentially unfractured overburden layers. A comparison of attenuation measurements for the two depth levels provides better constraints for a potential interpretation of results. On the other hand, there are only data points at three different azimuths per 180^o interval in the Clair VSP. (The remaining three can be regarded as a second measurement of the first three in this analysis.) The number of independent data points is just sufficient to constrain the azimuthal inversion of $\Delta 1/Q$, which estimates two parameters. Nevertheless, the data set contains roughly 80 different source offsets that serve as additional constraints in the analysis. If attenuation anisotropy is present it should show a pattern that is consistent with offset. Furthermore, I seek to increase confidence in the analysis by applying both the spectral ratio method and the instantaneous frequency method as two independent techniques.

In the subsequent paragraphs I describe the attenuation measurements from this data set, which consist of the following steps:

- Estimation of $\Delta 1/Q$ between a reference azimuth and all other azimuths at each offset and for both tool settings using the spectral ratio and the instantaneous frequency method, respectively.
- Fitting a $\cos(2\varphi)$-function to the resulting data points of $\Delta 1/Q$ for each offset and both recording levels.
- Display of the inverted symmetry azimuth φ_0 and magnitude of azimuthal variation C_2 as well as the inversion errors as a function of offset. This allows an assessment as to whether there is any systematic spatial pattern in the attenuation data. The results from both methods and from both recording depths are compared.
- Further assessment of errors by computing confidence bounds of the inverted parameters, weights for the derived symmetry azimuths, and by varying offset bin sizes.
- Summarizing the results over the entire offset range in rose diagrams of φ_0, which provides a direct comparison of the attenuation signature between the two receiver depths.

I begin with estimating $\Delta 1/Q$ as a function of azimuth using the spectral ratio method. I window the first arrivals by applying a time window of a length of 100 ms. This is a relatively narrow window, but we can see from Fig. 5.14 that longer time windows would include strong energy from secondary arrivals. Fig. 5.15 shows an example of the windowed pulses, amplitude spectra and spectral ratios at all six azimuths for the lower tool setting. The reference azimuth is N46^{o}E. Since the difference in raypath length between the top and the bottom receiver of the tool is less than a wavelength, there is little difference in the spectra across the five receivers of the tool and I compute the average spectrum. Furthermore, I average the spectra over offset bins of 50 m. Offset binning is required, because the source spacing is not constant across the survey. Both the spectra corresponding to single offsets *(thin lines)* and the averaged spectra *(bold lines)* are displayed in Fig. 5.15. We can see that their differences are very small compared to the

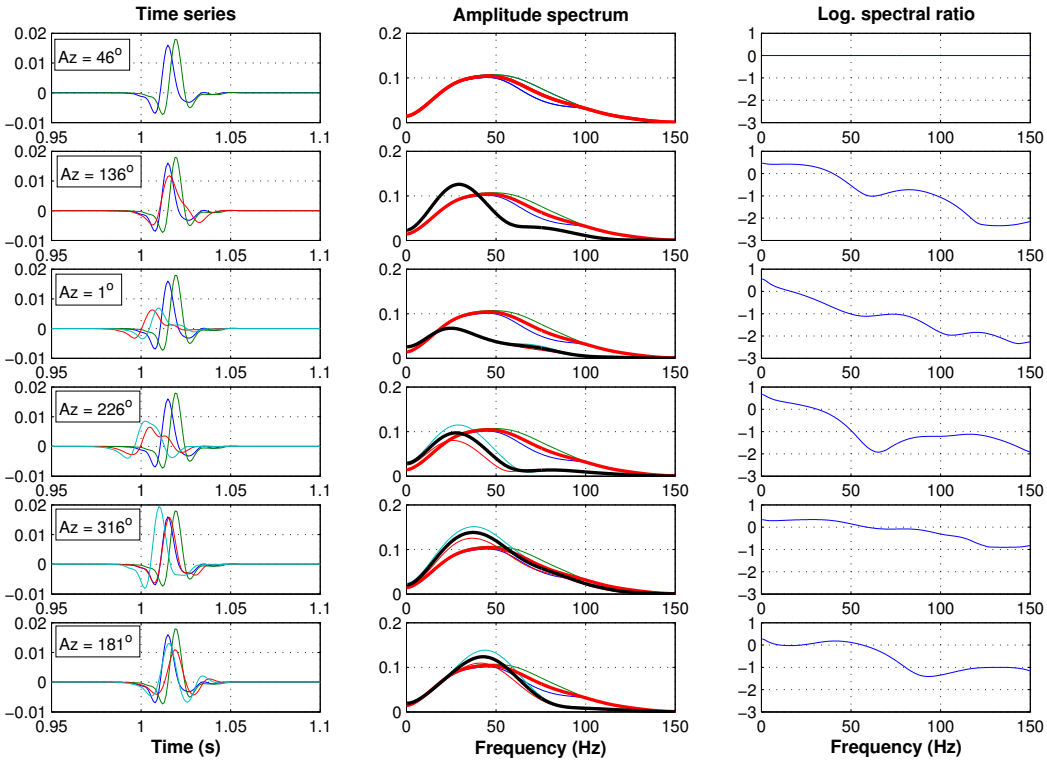

Figure 5.15: Example of first arrivals, spectra and spectral ratios as a function of azimuth at a constant offset. The reference azimuth is 46^o. Spectra are averaged over all five receiver levels and offset bins of 50 m. The resulting spectrum at each azimuth is shown in black, whereas the spectrum of the reference signal is shown in red. The thin lines are the the spectra corresponding to different offsets that are averaged. The windowed first arrivals at these offsets together with the first arrivals of the reference azimuth are also shown. We can see that at some azimuths the signal is strongly attenuated and the waveform is very different from the reference pulse.

changes that occur between azimuths. At some azimuths the high frequencies are clearly attenuated and the waveforms are very different from the reference pulse. This results in steep slopes of the logarithmic spectral ratios.

I choose a frequency bandwidth of 20 Hz to 120 Hz for the linear regression to the spectral ratios. Slopes of the lines where the R^2-value of the fit is smaller than 0.5 are excluded from further analysis. Values of $\Delta 1/Q$ are computed from the slopes using the average first-arrival time for each offset. They are therefore attributed to the entire depth interval from the surface to the receiver tool.

I also use the instantaneous frequency method to estimate $\Delta 1/Q$ as a function of azimuth. Fig. 5.16 shows the instantaneous frequencies computed as described in Chapter 4 for all azimuths and each receiver setting. Each graph in Fig. 5.16

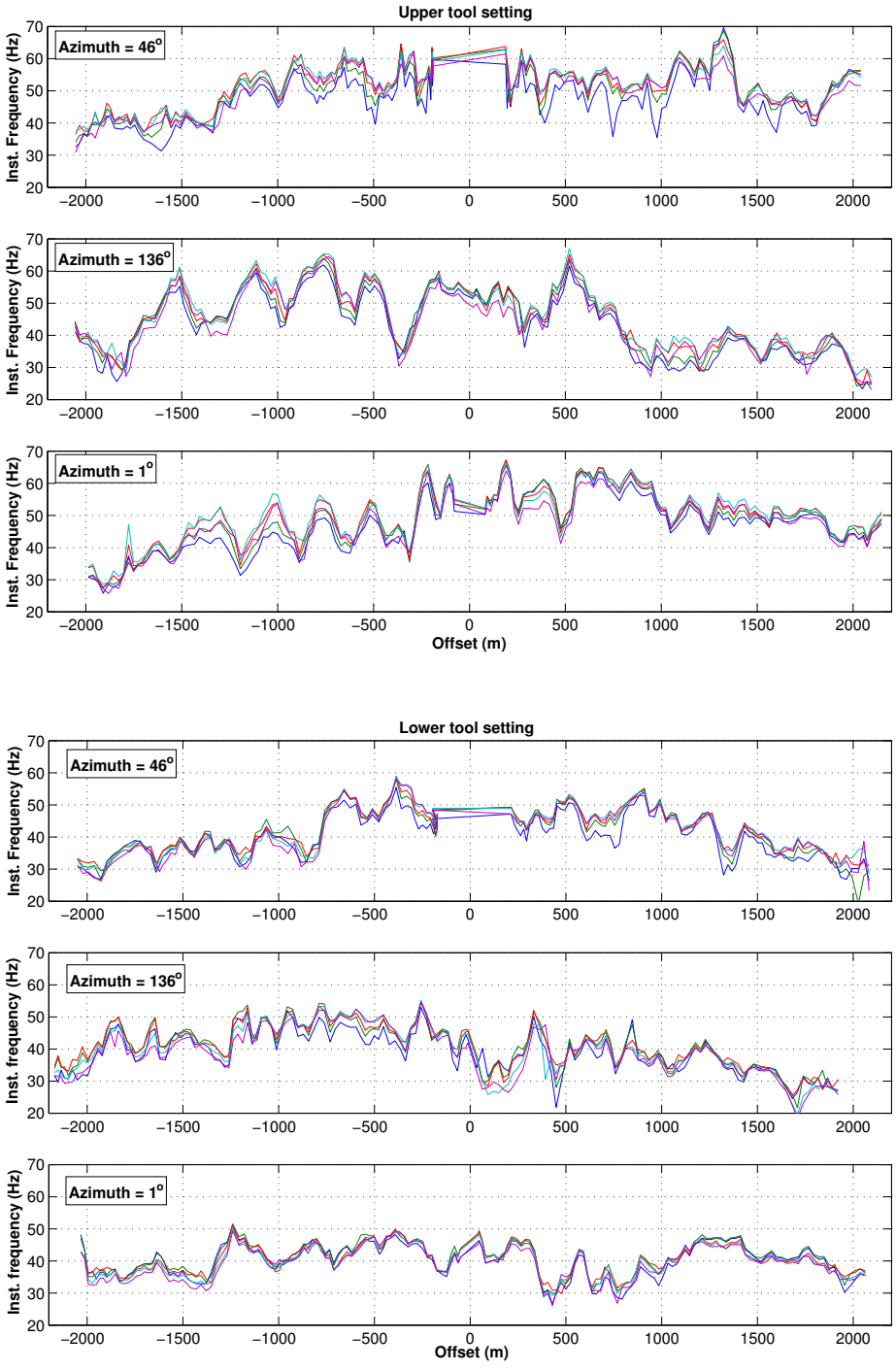

Figure 5.16: Instantaneous frequencies computed at the peak of the amplitude envelope for the upper and the lower tool setting. Despite large local variations along each walkaway line, the instantaneous frequencies are generally lower at the deeper tool setting than at the shallow setting.

contains the values obtained for all five receivers along the tool. I averaged the instantaneous frequencies over a 7-sample time window, applying the envelope squared as weights. It is obvious from Fig. 5.16 that there are strong local variations in the values along each walkaway line. Nevertheless, the instantaneous frequencies are generally lower at the deeper tool setting than at the shallow setting. This indicates that the arrivals recorded in the reservoir are attenuated compared to the arrivals recorded in the overburden.

To compute the change in $1/Q$ between azimuths I again average over the five receiver levels and over offset bins of 50 m. The computation is performed by attenuating the reference pulse as described in Chapter 4. I use a reference frequency of 150 Hz in the attenuation operator of Eq. 4.12, which is at the upper end of the frequency bandwidth contained in the data (*see* Fig. 5.15).

The next step of the analysis consists of fitting the $\cos(2\varphi)$-function given in Eq. 4.8 to the measured values of $\Delta 1/Q$ at each offset and assessing whether there is any significant azimuthal variation for either tool setting. In addition to computing RMS errors and R^2 values of each fit I perform this analysis for several offset bin sizes. If the data show a pattern that is consistent with offset, averaging over larger offset bins will effectively smooth the results. If, however, random variations in the data are fitted, increasing the offset bin size will not

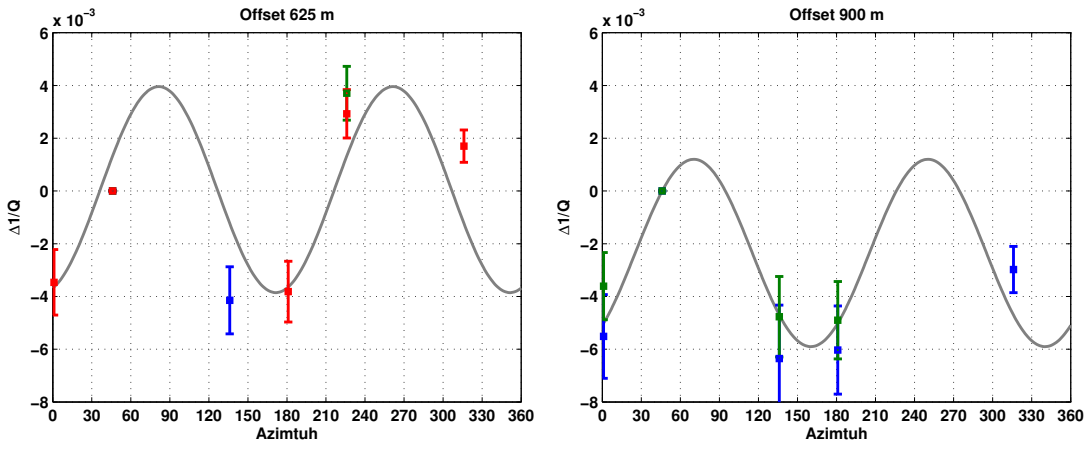

(a) (b)

Figure 5.17: Examples of azimuthal fit to $\Delta 1/Q$ obtained with the spectral ratio method for the lower tool setting at different offsets.

increase stability in the inversion.

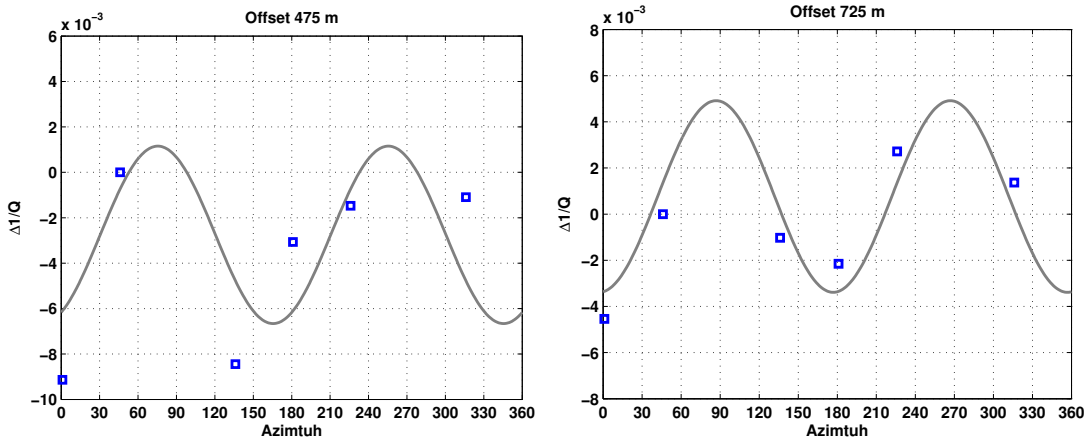

(a) (b)

Figure 5.18: Examples of $\Delta 1/Q$ obtained with the instantaneous frequency method for the lower tool setting as a function of azimuth. The data and azimuthal fit are shown for different offsets.

Figs. 5.17 and 5.18 show examples of the data and azimuthal fit from the lower tool setting for different offsets. Fig. 5.17 displays data obtained with the spectral ratio method, while Fig. 5.18 shows results of the instantaneous frequency method. For the spectral ratio results the offset bin size is increased to 150 m in Fig. 5.17a and to 100 m in Fig. 5.17b. The error bars are derived from the variance of the inverted spectral ratio slope defined in Eq. 4.16.

The fitted functions in Figs. 5.17 and 5.18 all show a very similar symmetry direction with an azimuth of minimum attenuation around 90^o. This symmetry is indeed found at many of the offsets for the lower tool setting, which can be seen in Figs. 5.19 and 5.20. The Figures show the inverted parameters C_2 and φ_0 as a function of offset, as well as the RMS errors and R^2 values of the fit. RMS errors are again normalized by the magnitude of azimuthal variation C_2. Fig. 5.19 corresponds to the data obtained with the spectral ratio method, while Fig. 5.20 displays the results for the instantaneous frequency method. Both Figures show that most values of the inverted symmetry azimuth φ_0 lie between 80^o and 100^o. However, they switch to 0^o (or 180^o) in the instantaneous frequency results beyond an offset of 1000 m. The magnitude of azimuthal variation in $\Delta 1/Q$, C_2, is very scattered at near- to mid-offsets in the spectral ratio results, but shows

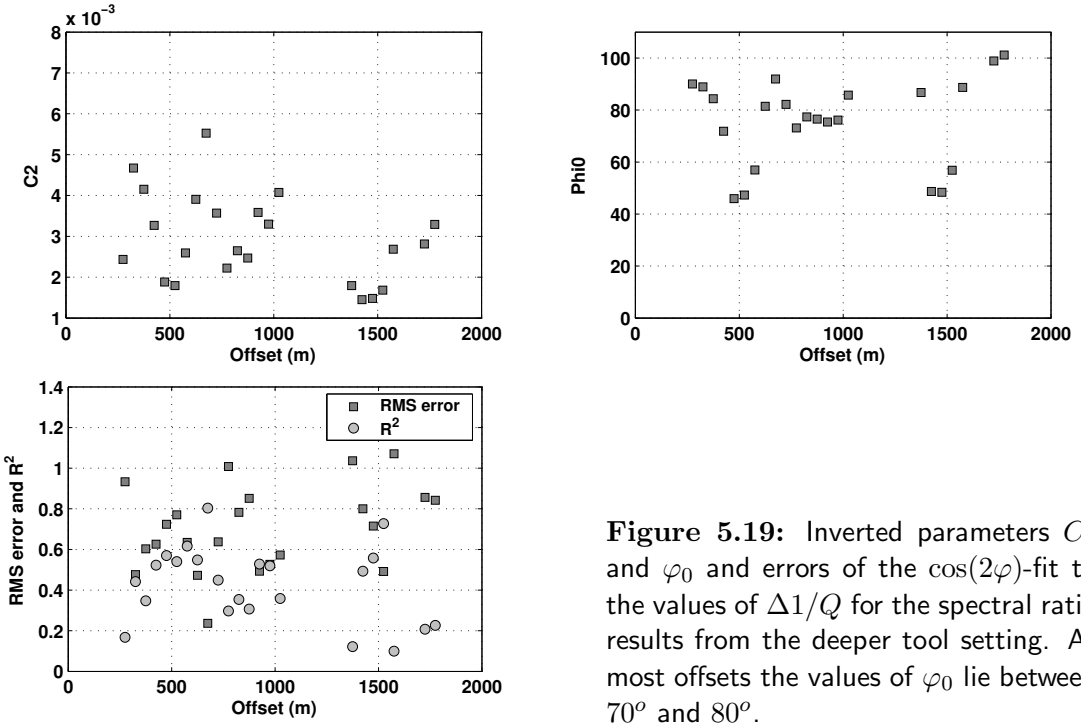

Figure 5.19: Inverted parameters C_2 and φ_0 and errors of the $\cos(2\varphi)$-fit to the values of $\Delta 1/Q$ for the spectral ratio results from the deeper tool setting. At most offsets the values of φ_0 lie between 70^o and 80^o.

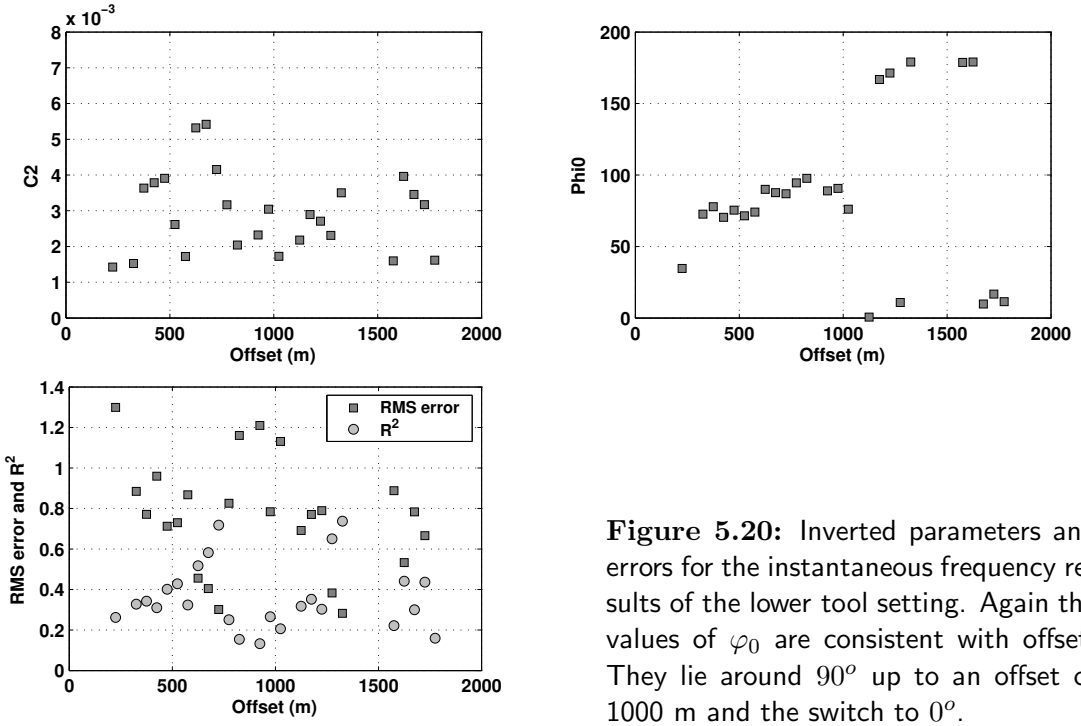

Figure 5.20: Inverted parameters and errors for the instantaneous frequency results of the lower tool setting. Again the values of φ_0 are consistent with offset. They lie around 90^o up to an offset of 1000 m and the switch to 0^o.

some increase at far offsets. In the instantaneous frequency results C_2 somewhat increases at near offsets, although this is not very clear. Beyond an offset of about 700 m the parameter does not show any systematic variation. The errors

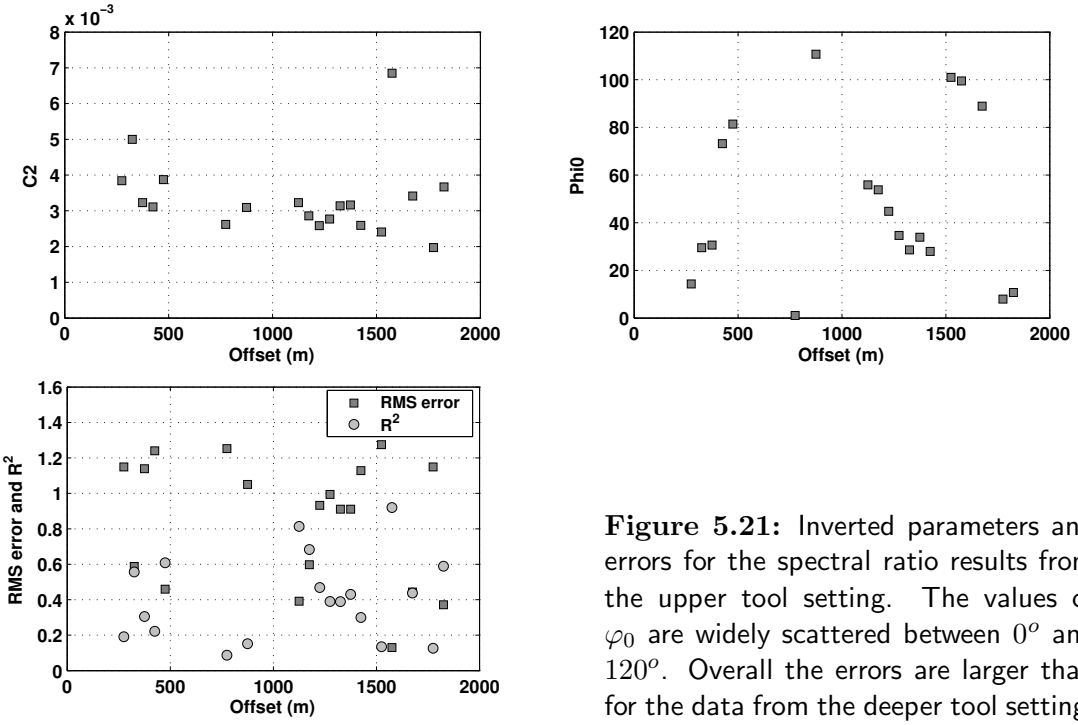

Figure 5.21: Inverted parameters and errors for the spectral ratio results from the upper tool setting. The values of φ_0 are widely scattered between 0^o and 120^o. Overall the errors are larger than for the data from the deeper tool setting.

are generally large, and for both methods there is a significant fraction of data points where the R^2 values are below 0.5.

The inverted parameters of the azimuthal fit for the shallow tool setting are shown in Figs. 5.21 and 5.22, corresponding to the spectral ratio and the instantaneous frequency results, respectively. Here, there appears to be no consistent symmetry in the data and the angles φ_0 are widely scattered between 0^o and 120^o. The errors of the fit are even higher than in the results for the deeper tool setting. This indicates that the attenuation data measured at the reservoir depth may show a systematic pattern that is not present in the data measured in the overburden. I investigate this further by assessing errors and the significance of inverted parameters in different ways.

Uncertainty bounds of C_2 and φ_0 can be determined from the shape of the error function around the minimum. Fig. 5.23 shows examples of contour plots of the error function corresponding to the $\cos(2\varphi)$-fit with the inverted parameters shown as a black dot. Contour lines are drawn at 5-80% increased RMS errors measured relative to the minimum error in 5% intervals. In Fig. 5.23a there is a confined minimum from which the error function increases steeply, especially in the directions of lower and higher azimuthal angles φ_0. In contrast, Fig.

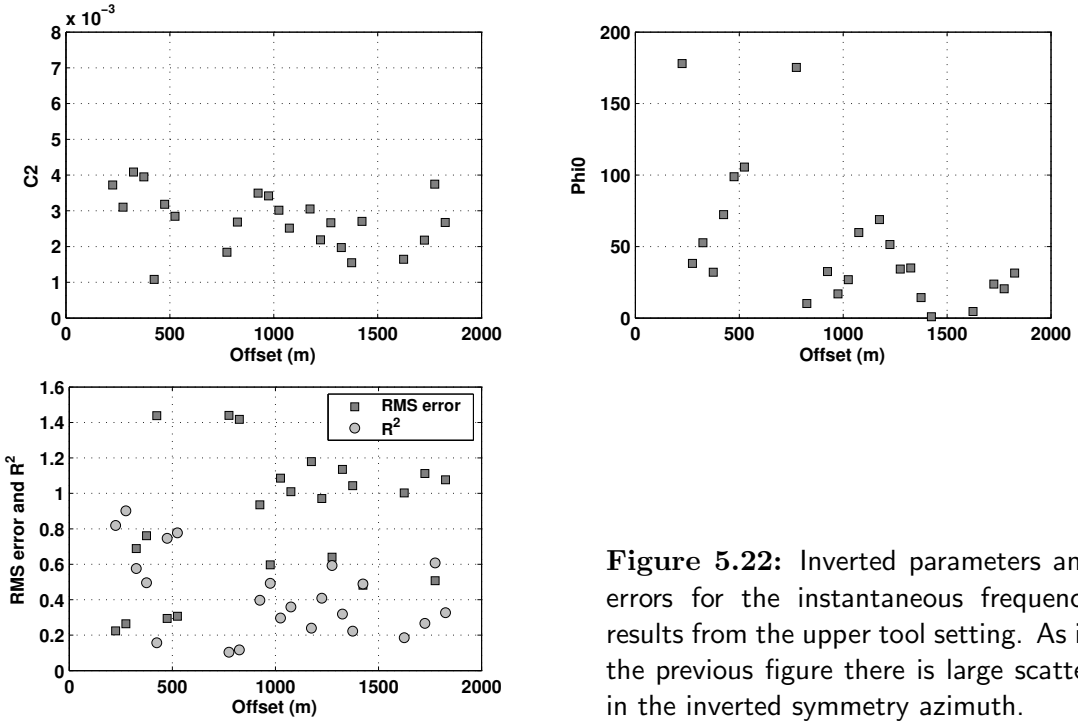

Figure 5.22: Inverted parameters and errors for the instantaneous frequency results from the upper tool setting. As in the previous figure there is large scatter in the inverted symmetry azimuth.

5.23b displays an example where the error function does not contain a confined minimum, so that the inversion for C_2 and φ_0 is not constrained and a $\cos(2\varphi)$-fit to the data is not meaningful. I derive uncertainty bounds of C_2 and φ_0 as the

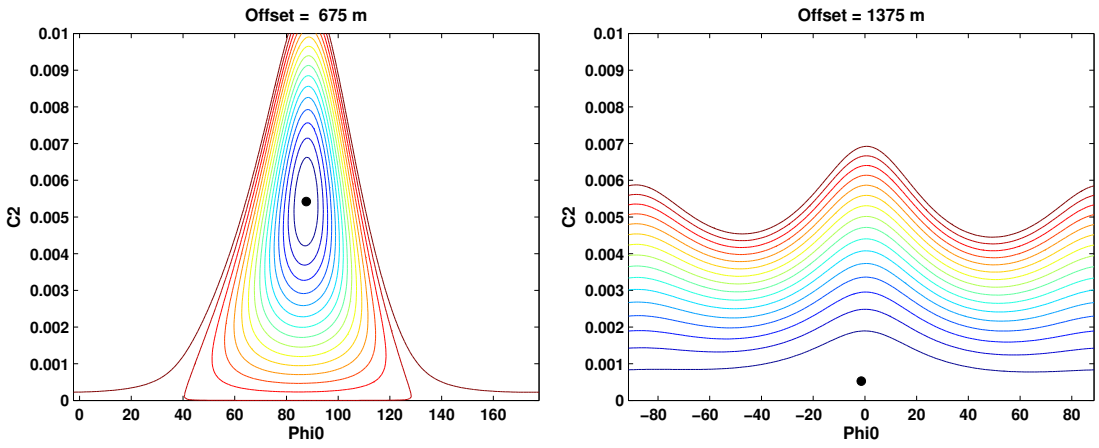

(a) (b)

Figure 5.23: Contour plots of the error function with contours at intervals of 5% increases from the minimum RMS error. Example from the deeper tool setting. In a) there is a confined minimum, whereas in b) the inversion is not constrained.

maximum distance of the minimum from the 5% contour line in the directions of both parameters.

Furthermore, the estimated symmetry direction φ_0 is only meaningful, if the magnitude of the measured azimuthal variation is significant. If, however, C_2 is close to zero, the angle φ_0 is arbitrary and should not have any weight in an interpretation of the results. I therefore compute the product of C_2 and R^2 as a measure of the significance of the results, which is related to both the magnitude of the inferred azimuthal variation, as well as to the error of the fit. The inverted parameters with uncertainty bounds and the weights $C_2 \cdot R^2$ are displayed as a function of offset for the lower and the upper tool setting, respectively, in Figs. 5.24 to 5.27. Figs. 5.24 and 5.26 correspond to the spectral ratio results, whereas Figs. 5.25 and 5.27 show the instantaneous frequency results. Again the difference between the upper and the lower tool setting becomes apparent. For the measurement in the reservoir the uncertainty bounds of the inverted parameters are narrower than for the data from the overburden. The symmetry azimuth φ_0 is consistent with offset in the data from the lower tool setting, whereas it shows

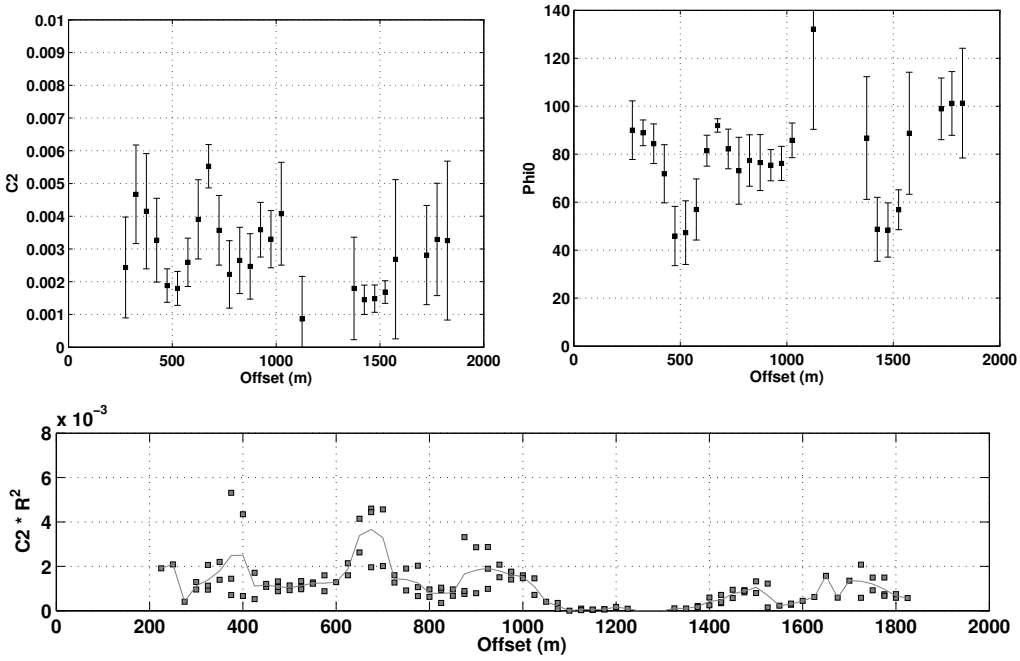

Figure 5.24: Inverted parameters with uncertainty bounds for the spectral ratio results of the lower tool setting and $C_2 \cdot R^2$ as a measure for the significance of the measured azimuthal variation in $\Delta 1/Q$.

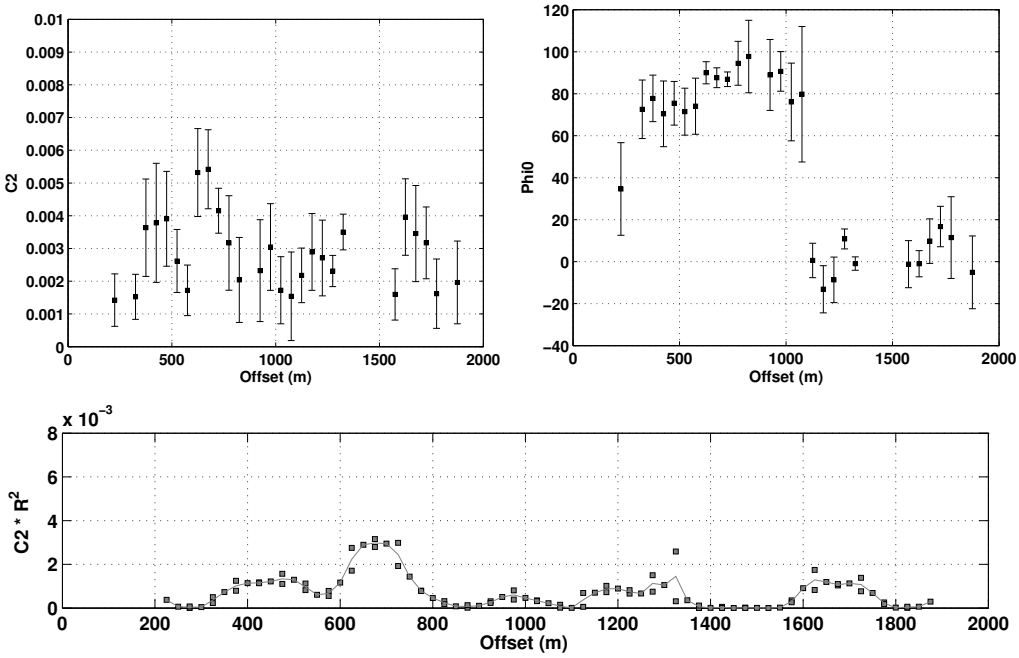

Figure 5.25: Inverted parameters with uncertainty bounds and weights for the instantaneous frequency results of the lower tool setting. There is an increase in the weights $C_2 \cdot R^2$ at near- to mid-offsets.

large scatter in the results from the upper tool setting.

The weights $C_2 \cdot R^2$ are computed for all offset bin sizes, for which the fit was performed, and displayed as squares. The line shows the average value at each offset. For the instantaneous frequency results of the lower tool setting (Fig. 5.25) the weights show an increase with offset up to offsets around 700 m. This may also be present, but is less clear in the spectral ratio results of the deeper receiver setting. An increase in the magnitude of the azimuthal variation of $\Delta 1/Q$ together with a decrease in errors is a pattern that is expected if attenuation anisotropy as modelled in the synthetic studies of Chapter 4 is present. The weights for the shallow tool setting exhibit no such systematic variation with offset. They are close to zero for large fractions of the data and only show random strong increases in the spectral ratio results (Fig. 5.26) for particular offset bin sizes.

The effect of changing offset bin sizes is demonstrated in Fig. 5.28. Figs. 5.28a and b show φ_0 inverted from the data of the deeper tool setting for offset bins of 150 m and 250 m, respectively. The corresponding results of the shallow tool setting are displayed in Figs. 5.28c and d. For the lower tool setting an averaging

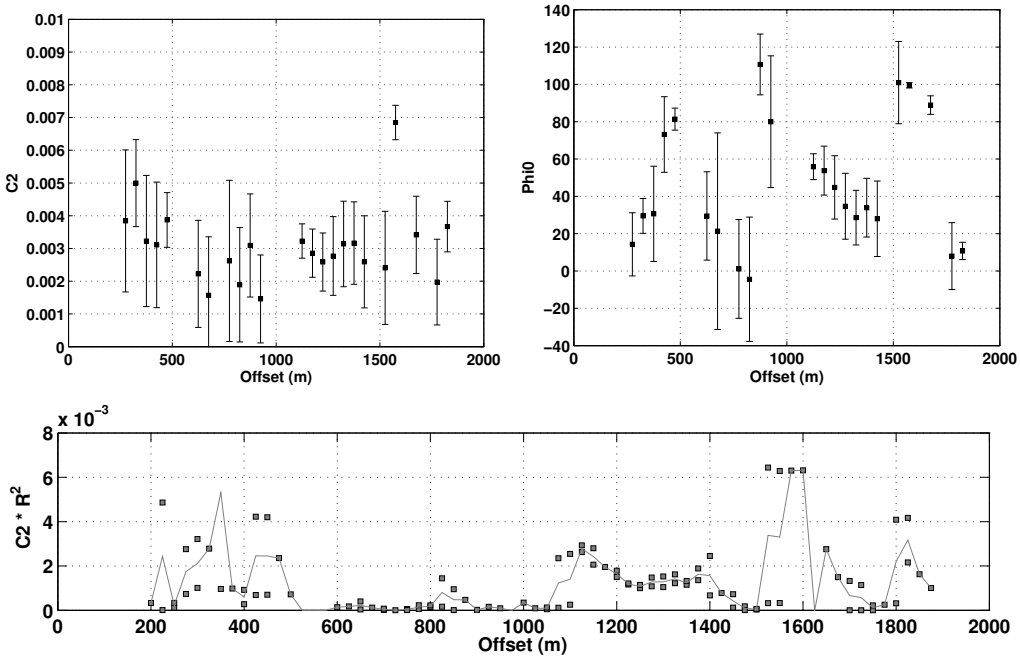

Figure 5.26: C_2 and φ_0 with uncertainty bounds and computed weights for the spectral ratio results of the upper tool setting. The errors are larger than for the lower tool setting.

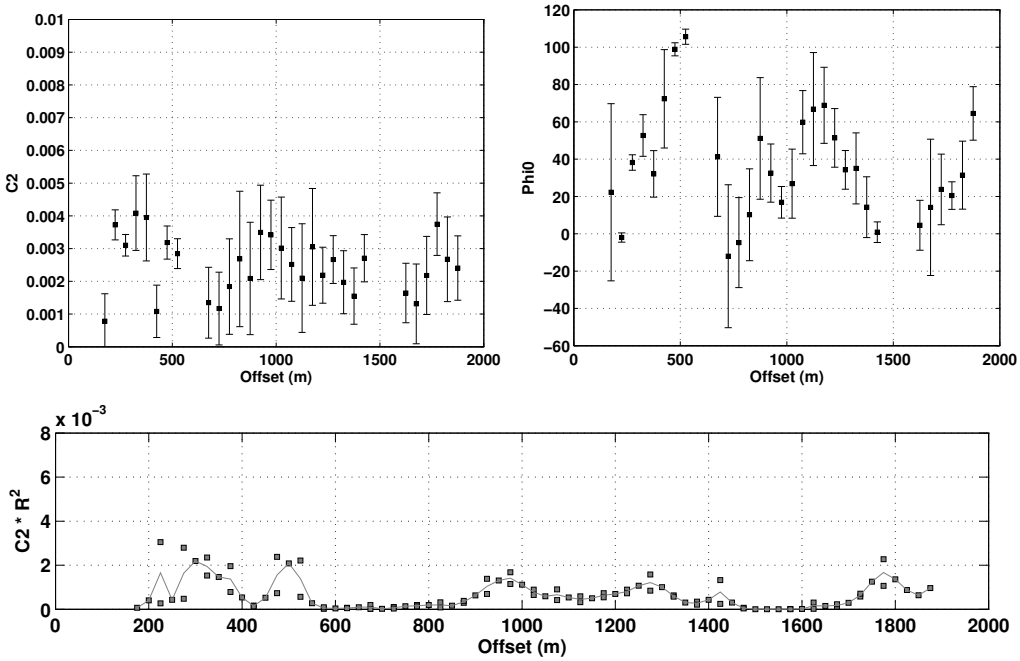

Figure 5.27: Inverted parameters with uncertainty bounds and weights for the instantaneous frequency results of the upper tool setting. The weights are effectively zero for a large fraction of the data points.

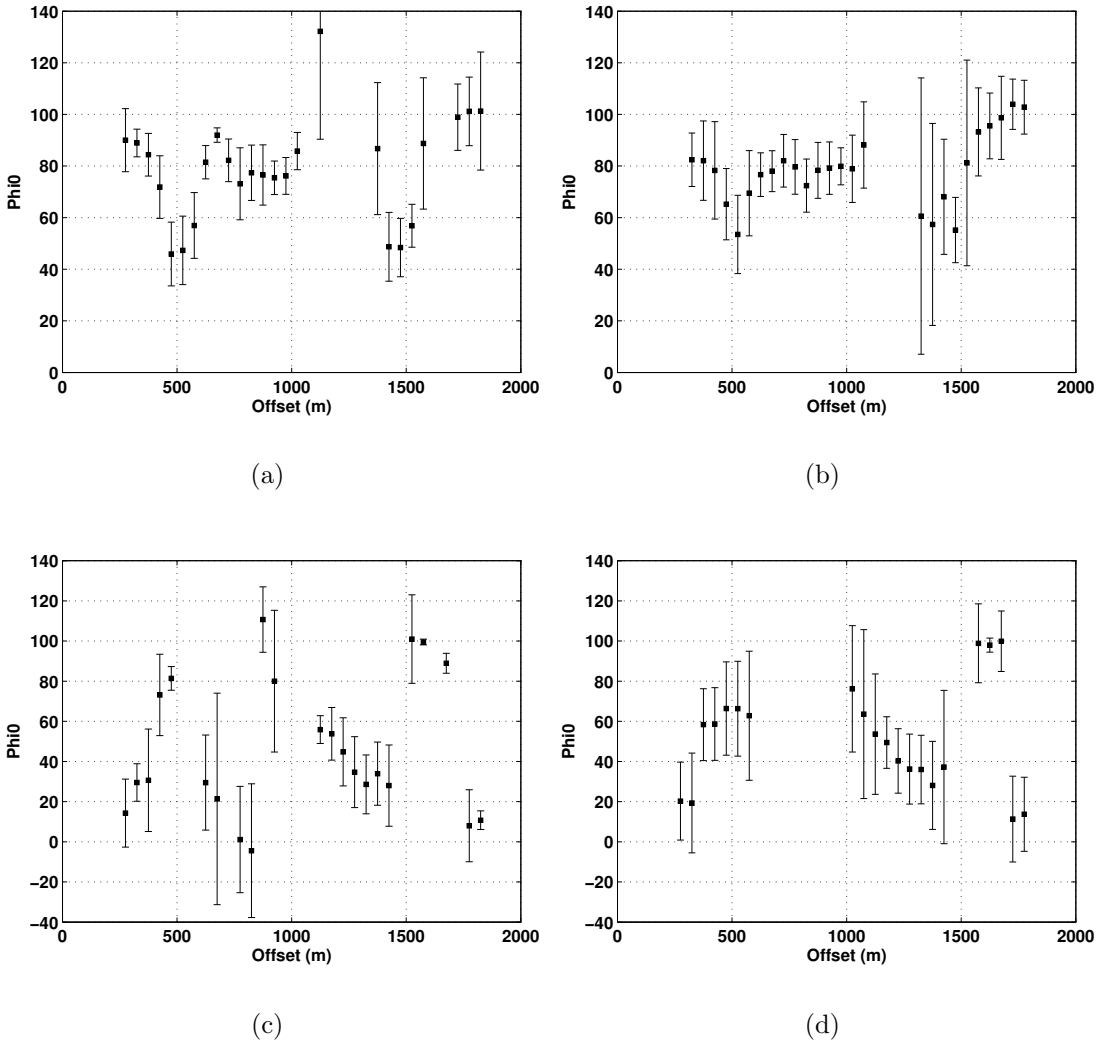

Figure 5.28: Effect of offset binning. a) Lower setting, offset bins of 150 m; b) lower setting, offset bins of 250 m; c) upper setting, offset bins of 150 m; d) upper setting, offset bins of 250 m. The results from the deeper receiver setting are smoothed by averaging over larger offset bins. For the results of the shallow setting an increase in offset bin size increases instability of the inversion over a range of offsets and does not reduce the scatter in the results.

over larger offset bins smoothes the results, so that the scatter in the inverted symmetry azimuths is reduced. For the upper tool setting, however, increasing the size of the offset bins has the effect that the inversion becomes instable between offsets of 500 m to 1000 m, and the remaining data points are still scattered over an azimuth range of 100^o.

A good visualization of all these results combined is obtained by rose diagrams

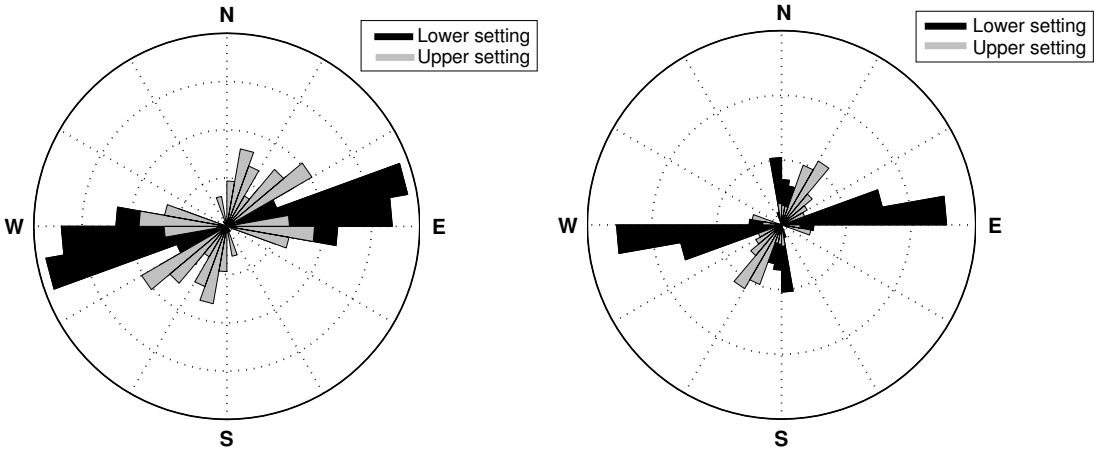

Figure 5.29: Rose diagrams of the inverted azimuth of minimum attenuation φ_0. a) Spectral ratio results, b) instantaneous frequency results. The values of $C_2 \cdot R^2$ were used as weights. The data recorded in the reservoir show significant azimuthal variation in $\Delta 1/Q$ with a clear dominant azimuth of φ_0 close to E-W. In comparison, the attenuation anisotropy measured in the data from the overburden is small and the symmetry directions are widely scattered.

of the inverted symmetry azimuths φ_0 where the values $C_2 \cdot R^2$ are used as weights. These are shown in Fig. 5.29 for the spectral ratio and the instantaneous frequency results, respectively. The results for the upper and lower tool setting are displayed in the same diagram, which allows a direct comparison of the measured patterns. Both analysis methods reveal azimuthal variation in $\Delta 1/Q$ with a dominant direction of minimum attenuation at N80-90^{o}E for the data recorded in the reservoir. The data recorded above the reservoir top, in contrast, show no dominant symmetry in $\Delta 1/Q$. The values of φ_0 are spread over a wide azimuth range and they have small weights compared to the results from the deeper tool setting. Therefore, the $\cos(2\varphi)$-fit to the attenuation data from the overburden appears to be fitting noise rather than a meaningful signal.

5.3.4 Zero-offset attenuation in the reservoir

I compute spectral ratios between the deeper and the shallow tool setting at each offset and azimuth to derive a zero-offset Q-value for the reservoir. The approach is adapted from the method of Dasgupta and Clark (1998) who measured zero-offset attenuation between reflectors from surface seismic data. The authors suggested fitting a straight line to the slopes of the spectral ratios as a function of offset squared, the intercept of which yields the true value of Q at zero offset. The spectral ratios are computed between the reflection of interest and the source wavelet and therefore reflect cumulative attenuation along the raypath from the surface down to the reflector. Interval Q-values are then derived for successive layers starting from the first reflector in a layer-stripping fashion. I now investigate whether a similar approach of measuring zero-offset Q can be followed if spectral ratios are formed between data recorded at two different depth levels in a walkaway VSP.

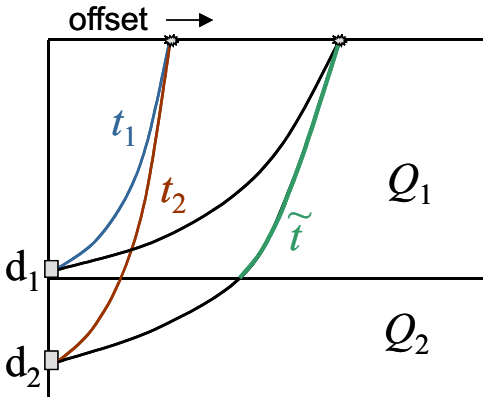

Figure 5.30: Raypaths involved in the analysis of offset VSP data for attenuation between two receiver depths.

Fig. 5.30 is a schematic diagram of the raypaths from sources at different offsets to receivers at depths d_1 and d_2. The slope of the spectral ratios b between arrivals recorded at d_2 and d_1 at any offset is given by

$$b = \pi \left[\frac{t_1}{Q_1} - \left(\frac{\tilde{t}}{Q_1} + \frac{t_2 - \tilde{t}}{Q_2} \right) \right]. \tag{5.1}$$

t_1 is the traveltime to the receiver at depth d_1, t_2 is the traveltime to the receiver at d_2, and $\tilde{t}$ is the traveltime in the upper medium along raypaths to the lower receiver. Deriving Q_2 from the spectral ratio slopes would therefore require Q_1 and $\tilde{t}$ to be known. However, this is normally not the case. Using the traveltime difference $\Delta t(x) = t_2(x) - t_1(x)$ as in near-offset VSP data yields an apparent quality factor Q_a that decreases with offset x due to the decrease in Δt and reduces to Q_2 at zero offset:

$$b = -\pi \frac{\Delta t(x)}{Q_a(x)} \qquad \text{with} \quad Q_a(0) = Q_2. \tag{5.2}$$

If the traveltime differences Δt become very small at large offsets the values of the apparent quality factor Q_a can fall below the minimum of 2π for the true physical Q. The slope b as a function of offset squared can be approximated by a straight line if the terms containing Q_1 in Eq. 5.1 are negligible compared to the term containing Q_2. This requires $Q_2 \ll Q_1$, so that

$$b \approx -\pi \frac{t_2 - \tilde{t}}{Q_2}. \tag{5.3}$$

$t_2 - \tilde{t} = \Delta\hat{t}$ is the traveltime in the lower medium. Approximating $\Delta\hat{t}$ with a two-term Taylor series expansion around $x = 0$ gives $\Delta\hat{t}(x) = \Delta\hat{t}(0) + Cx^2$ where C is a constant. Eq. 5.3 then becomes

$$b \approx -\frac{\pi}{Q_2}(\Delta\hat{t}(0) + Cx^2) = -\frac{\pi}{Q_2}(\Delta t(0) + Cx^2). \tag{5.4}$$

This is a linear function of offset squared, and Q_2 can be derived from its intercept and the traveltime difference at zero offset.

Fig. 5.31 shows forward modelling examples of b and Q_a as a function of offset for a high and a low contrast in Q, respectively. The parameters are $Q_1 = 100$ and $Q_2 = 20$ for Fig. 5.31a, whereas $Q_1 = 50$ and $Q_2 = 35$ for Fig. 5.31b. The depths are $d_1 = 1500$ m and $d_2 = 1900$ m in both cases with velocities of $v_1 = 2104$ m/s and $v_2 = 2340$ m/s. For a high contrast in Q the slope b decreases with offset and the linear approximation of $b(x^2)$ is valid. Q_a also decreases with offset. For a lower contrast in Q, however, Fig. 5.31b demonstrates that the linear approximation of $b(x^2)$ breaks down. In this case the shape of the curves

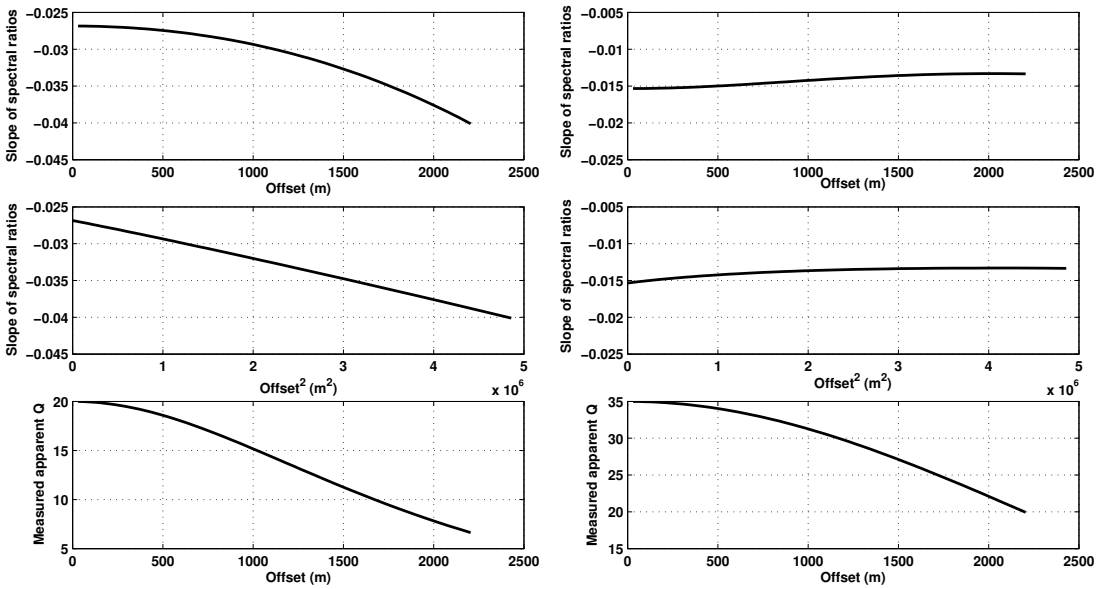

Figure 5.31: Forward modelling examples for a large and a small contrast in Q, respectively. a) $Q_1 = 100$, $Q_2 = 20$. The slopes of the spectral ratios decrease as a function of offset and approximate a straight line as a function of offset squared. The apparent attenuation Q_a also decreases with offset. b) $Q_1 = 50$ and $Q_2 = 35$. Here the slopes of the spectral ratios increase with offset and cannot be approximated by a straight line as a function of offset squared. However, the apparent Q still decreases with offset.

also depends on the traveltime structure. Nevertheless, Q_a still decreases with offset. Fig. 5.32 shows a case where Q_2 is anisotropic as described by the fracture model of Chapman (2003), so that Q_2 itself decreases with offset at azimuths away from the fracture strike. The slopes b and Q_a then show a larger decrease with offset, but the differences from the isotropic case are not of a larger magnitude than the variations introduced by changing the contrast in Q. I therefore do not consider this as a robust technique to detect anisotropy in Q.

Fig. 5.33 shows the slopes of the spectral ratios measured between the upper and lower tool settings of the Clair field VSP data as a function of offset squared and apparent quality factor Q_a as a function of offset. The slopes increase slightly with offset, indicating that the contrast in Q between overburden and reservoir is not as high as in the modelling example of Fig. 5.31. However, since the scatter in the data is large and it is not obvious in which way the slopes as a function of offset

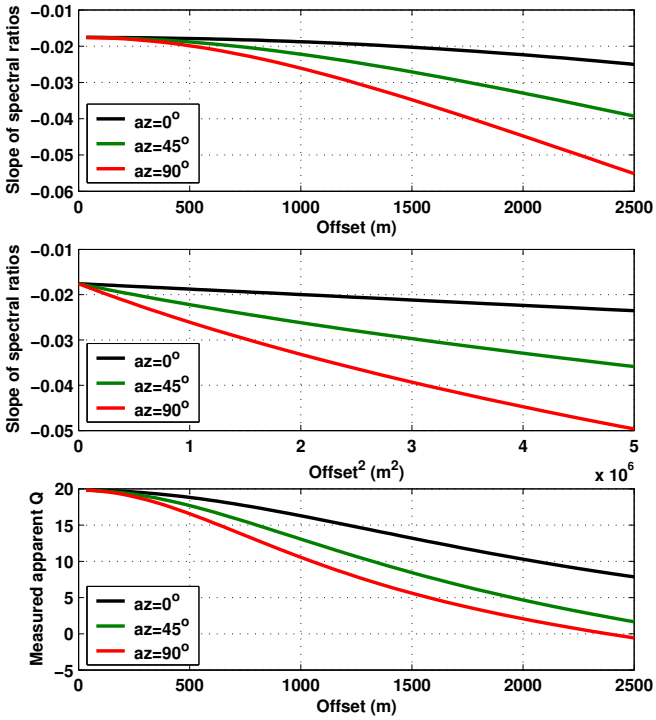

Figure 5.32: Spectral ratio slopes and Q_a for $Q_1 = 100$ and an anisotropic Q_2. Although the offset dependence of both parameters changes with azimuth, the sensitivity to the contrast in Q is much larger.

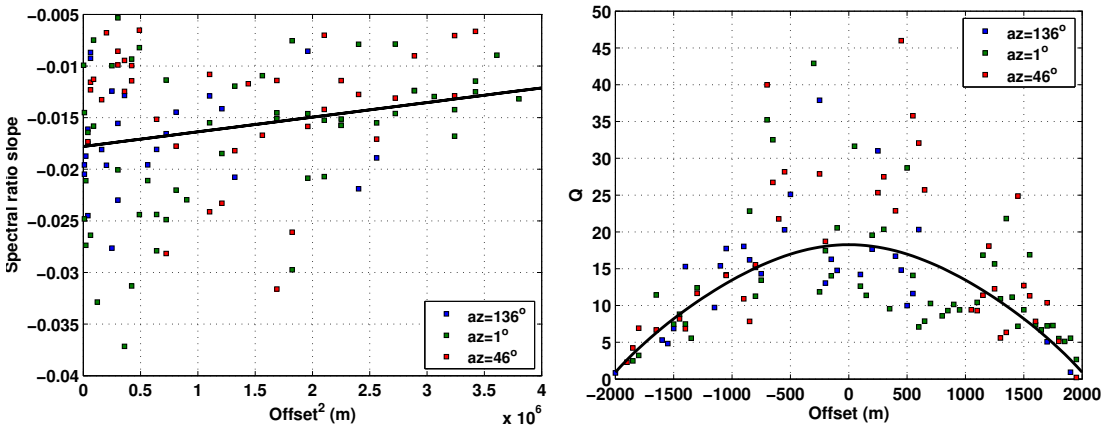

(a) (b)

Figure 5.33: a) Linear fit to the slopes of spectral ratios as a function of offset squared, b) Measured and fitted apparent Q as a function of offset. The zero offset Q value is 18.

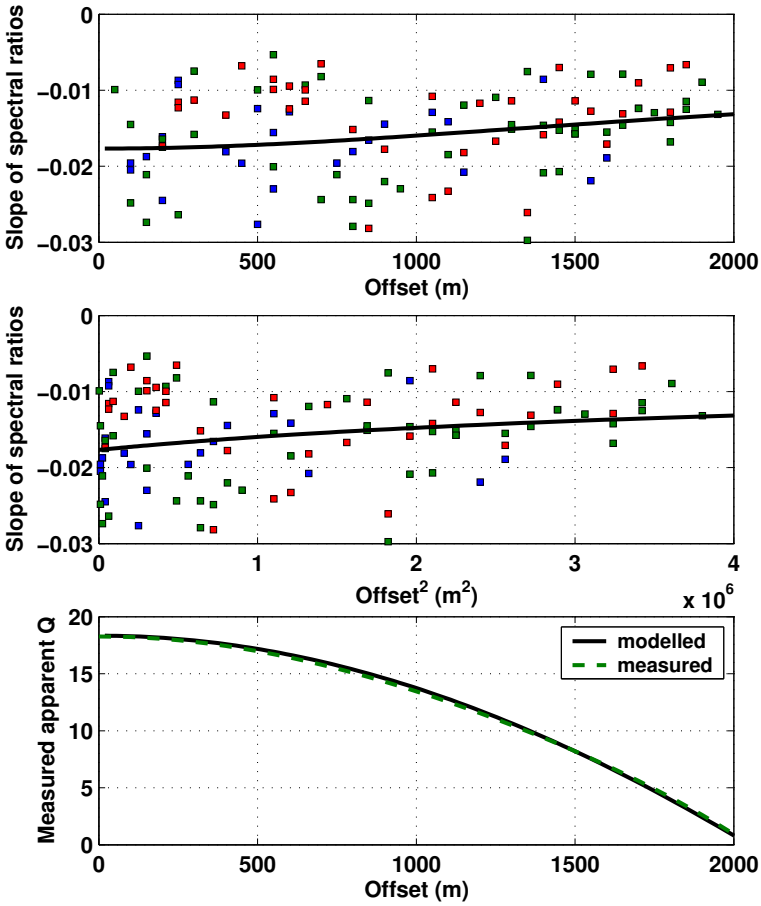

Figure 5.34: Modelling of the slope of the spectral ratios and apparent Q as a function of offset for $Q_1 = 35$ and $Q_2 = 18$. The colours of the datapoints correspond to the different azimuths as in Fig. 5.33.

squared depart from a straight line, I perform a linear fit as a first approximation. This is shown as the black line in Figs. 5.33a and b. It yields a zero-offset Q of 18 for the reservoir. The Q of the overburden cannot be determined directly, but using Eq. 5.1 I calculate lower and upper limits for Q_1 according to lower and upper limits of $\tilde{t}$, so that the traveltimes in either medium along raypaths to the lower receiver are always greater than the zero offset times. The calculation yields $24 \leq Q_1 \leq 40$. I choose a Q_1 of 35 to perform forward modelling, the results of which are shown in Fig. 5.34. I assume a simple two-layer model with velocities obtained from the NMO velocities to match the traveltimes t_1 and t_2. There is good agreement between modelled and measured data, and the modelled spectral ratio slope as a function of offset squared is close to a straight line.

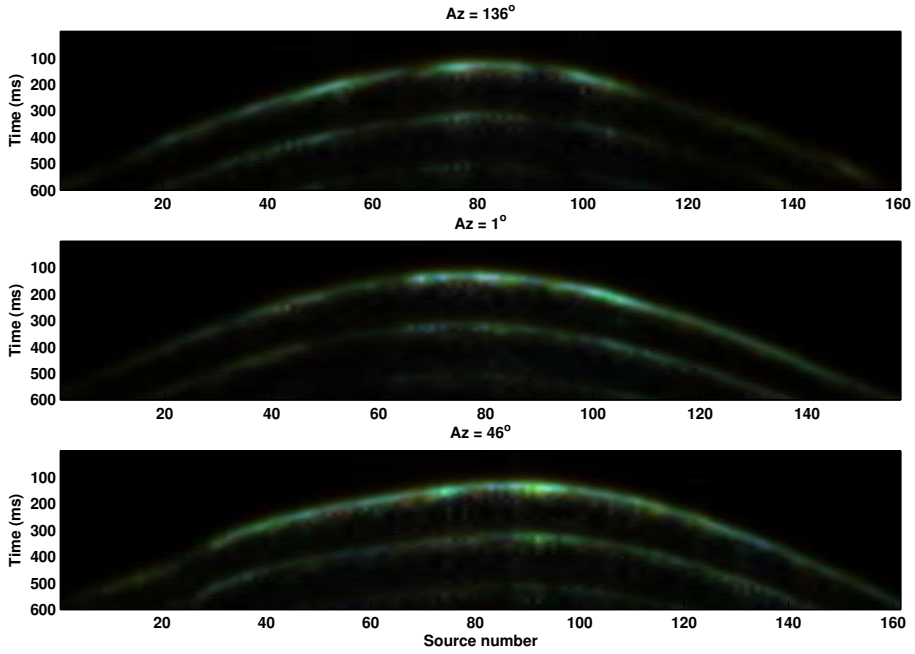

Figure 5.35: Spectral colour display of the walkaway VSP lines from the upper tool setting.

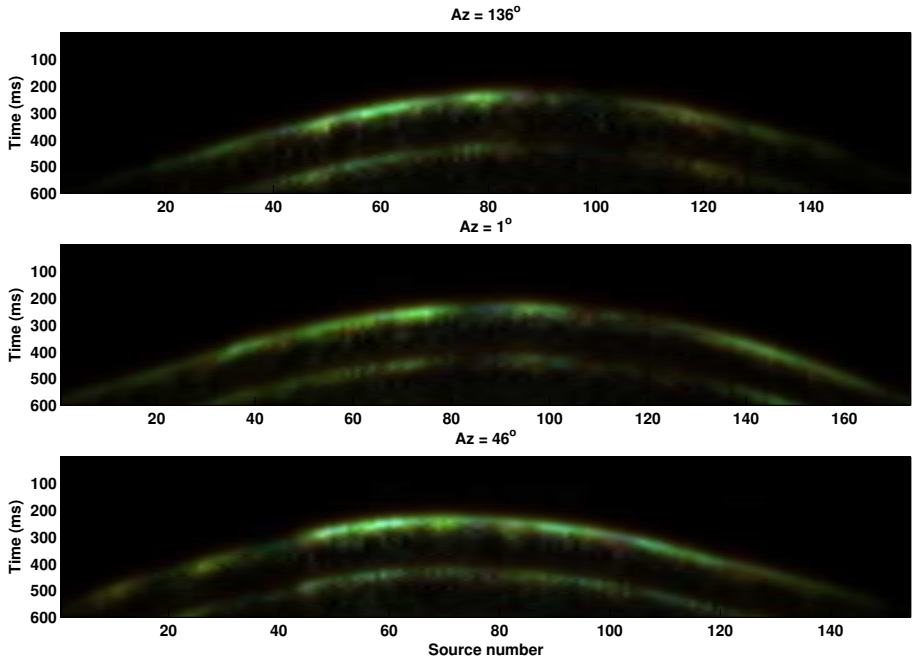

Figure 5.36: Spectral colour display of the walkaway VSP lines from the lower tool setting. Colours are shifted towards green compared to the upper tool setting, which means that centre frequencies are lower.

The result of $Q_1 = 35$ and $Q_2 = 18$ means that attenuation is significantly higher in the reservoir as it is in the overburden. Due to the reasons discussed above any anisotropy in attenuation cannot be determined by this analysis. From Fig. 5.33 it is also obvious that the scatter in the data is much larger than any azimuthal differences would be.

The effect of significant attenuation of the arrivals recorded in the reservoir compared to the arrivals recorded at the base of the overburden layers can also be visualized by the spectral colour display. This is shown in Figs. 5.35 and 5.36 for all walkaway lines and both receiver settings. For each tool setting the pixels are normalized individually by the maximum value of the corresponding image. Comparing the images for the upper and lower tool setting, a clear change in colour from predominantly blue to predominantly green can be seen, which represents a decrease in centre frequency. Furthermore the first arrivals at the lower tool setting are stretched in time compared to the arrivals recorded above the reservoir. This indicates that the frequency bandwidth is decreased due to attenuation in the reservoir. The results also confirm the observation of Fig. 5.16 of lower instantaneous frequencies measured at the deeper tool setting.

5.3.5 Discussion and conclusions

The zero-offset Q of 18 that I have derived for the reservoir interval down to the receiver depth of 1900 m means that attenuation is high in this section of the reservoir. The smallest Q values measured from seismic data that are reported in the literature for sedimentary rocks lie between 10 and 20 (e.g. Stainsby and Worthington, 1985; Dasgupta and Clark, 1998; Hackert *et al.*, 2001; Parra *et al.*, 2002). The increase in attenuation in the reservoir by a factor of two compared to the overburden coincides with a change in pore fluid from brine to oil, i.e. a reduction in fluid bulk modulus. As might be expected from Fig. 3.11, an increase in the magnitude of attenuation linked to a decrease in fluid bulk modulus would be observed if attenuation is related to squirt flow in the porous fractured rock.
The analysis of azimuthal anisotropy in attenuation at both receiver levels has revealed that only at the deeper tool setting is there a systematic azimuthal variation with a dominant direction of minimum attenuation at N80^o-90^{o}E. The data from the shallow tool setting show only small azimuthal variations with no consistent symmetry. The result is confirmed by two independent methods of measuring attenuation. Since the waves arriving at the deeper tool setting have also travelled through the overburden, I conclude that the observed differences in the attenuation pattern are caused by effects in the reservoir.
The symmetry directions of the attenuation anisotropy in the reservoir are in good agreement with the symmetry directions of other anisotropic attributes that have previously been derived from the data (Horne *et al.*, 1998; Smith and McGarrity,

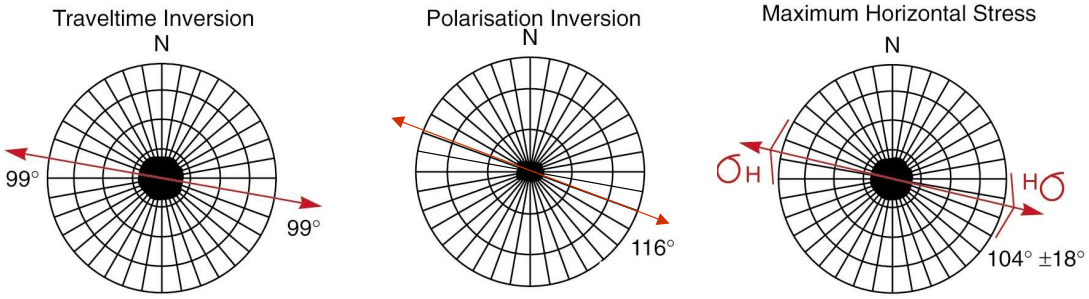

Figure 5.37: Fast direction obtained from the traveltime and polarization inversion by Horne *et al.* (1998) and orientation of maximum horizontal stress. (*From* Smith and McGarrity (2001).)

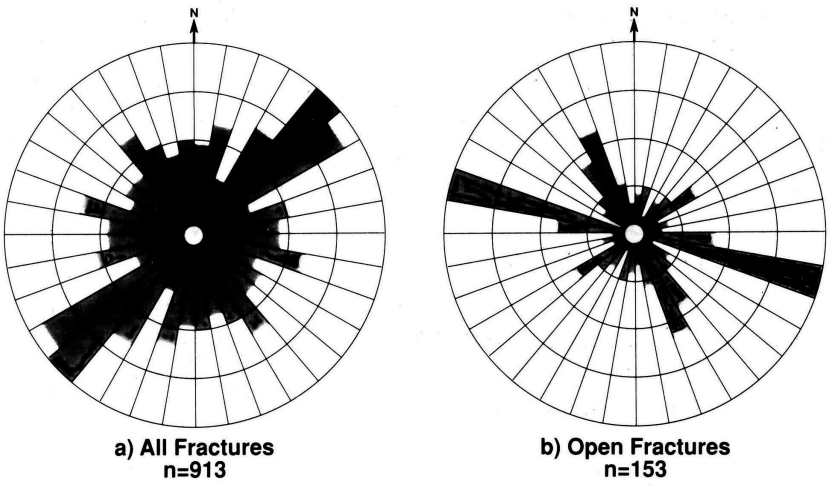

Figure 5.38: Fracture orientations mapped from cores and borehole image logs in well 206-8/8, which is close to the VSP well. The dominant strike of open fractures is different from the dominant strike of the entire fracture population, and it is in good agreement with the azimuth of minimum attenuation in the reservoir. (*From* Coney *et al.* (1993).)

2001). Fig. 5.37 shows the results of Horne *et al.* (1998) and Smith and McGarrity (2001). The azimuth of minimum attenuation of N80^o-90^{o}E is close to the fast direction determined from traveltime and polarization analysis as well as to the orientation of the maximum horizontal stress. Furthermore, the same orientation has been reported by Li *et al.* (2004) as the direction of the maximum converted-wave migration velocity derived from OBC data at the location of the VSP well. Fig. 5.38 shows the orientation of fractures mapped from cores and image logs in a nearby well presented by Coney *et al.* (1993). The rose diagrams demonstrate that the dominant strike of the entire fracture population is different from the dominant orientation of only open fractures. The E-W direction of minimum attenuation in the reservoir closely matches the strike of open fluid-filled fractures, which is N100^o-110^{o}E. These results suggest that the attenuation anisotropy, which I have measured in the VSP data, is related to the orientation of open fractures in the reservoir. Moreover, they support the hypothesis that fluid squirt is an important cause of the attenuation, which is only sensitive to open fluid-filled fractures.

The data recorded in the reservoir may also contain an increase in attenuation anisotropy with polar angle at near to mid offsets, although the values of C_2 are fairly scattered. In general, this pattern can be described by a squirt flow

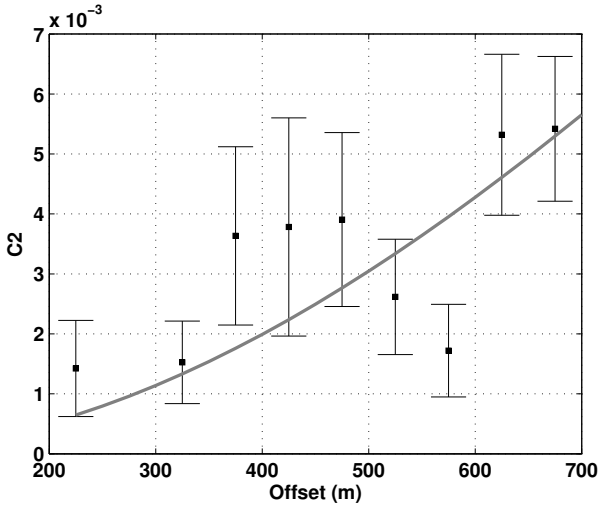

Model parameters	
v_P	3730 m/s
v_S	2102 m/s
ρ	2450 kg/m^3
f	50 Hz
ϵ_f	0.045
a_f	0.65 m
r	0.0001
Φ_p	15%
k_f	1.41 GPa
τ_m	10^{-5} s

Figure 5.39: Modelling the magnitude of azimuthal anisotropy in attenuation as a function of polar angle (or offset) with the model of Chapman (2003).

model for fractured rock. Fig. 5.39 shows the measured amplitude of azimuthal variation in $1/Q$ as a function of offset together with a curve computed with the model of Chapman (2003). The model parameters are given in the Table next to the diagram. The velocities, density and porosity are taken from well logs, the fluid bulk modulus is chosen to represent oil and τ_m is derived from the calibrated value as described in Section 3.6.3 of Chapter 3. I then determine the fracture size and density so that the model best fits the data in Fig. 5.39 and the velocity anisotropy of 6% reported by Horne *et al.* (1998). It should be noted though that the values of $\Delta 1/Q$ in section 5.3.3 were calculated using the arrival time at the receiver and therefore represent the entire depth interval from the surface to the receiver location. A proper inversion for fracture density and fracture size would require the knowledge of an accurate velocity model to determine correct magnitudes of attenuation and velocity anisotropy for only the reservoir interval.

If I relate the attenuation anisotropy observed in the reservoir at near to mid offsets to a squirt-flow mechanism in fractured porous rock the question arises as to why the effect cannot be observed at larger offsets where its magnitude should be even higher. A possible explanation is that heterogeneity becomes too large for far offsets and the assumption, that the rock mass between sources at all azimuths and the receiver can be represented as a stack of homogeneous layers, breaks down.

Furthermore, Wijnands (1997) suggests that the first arrivals at offsets beyond 1500 m may be refractions from a high velocity layer rather than direct arrivals. The author also mentions that raypaths from far-offset source locations could be severely distorted by a fault cutting through the base Cretaceous southeast of the well.

Whether the small azimuthal anisotropy in $1/Q$ with a N-S direction of minimum attenuation measured with the instantaneous frequency method at offsets beyond 1000 m is a meaningful signal, remains questionable. In the rose diagram of Fig. 5.29 this orientation is of similar weight as the data from the upper setting, which I interpret as noise, but it is much less scattered. I find the same switch to a N-S azimuth of minimum attenuation at far offsets in the spectral ratio results, if I decrease the bandwidth of the linear regression to the spectral ratios to 20-80 Hz. A larger bandwidth, however, yields generally more reliable values, as discussed in Chapter 4. Nevertheless, the N-S orientation would closely match the second dominant strike of open fractures seen in Fig. 5.38, as well as the strike of faults in the Clair group mapped from 3D seismic data (Coney *et al.*, 1993). If it is a meaningful signal, it therefore supports the interpretation of the near-offset data in terms of attenuation anisotropy in the reservoir being related to the orientation of open fluid filled-fractures.

5.4 Summary

I have measured azimuthal anisotropy of P-wave attenuation in two VSP data sets from different sedimentary basins. In both cases the symmetry azimuth where attenuation reaches its minimum can be related to the symmetries derived from traditional anisotropic attributes and to the orientation of fractures.

For the first data set, a walkaround VSP from the Railroad Gap oilfield in California, the lack of data prevents a more detailed interpretation of the results in terms of properties of different lithologic units between the surface and the receiver in the reservoir.

In the second data set, which is a 3-arm walkaway VSP from the Clair field in the North Sea, data were acquired close to the reservoir top and within the fractured reservoir. By comparing results from the two receiver depths the analysis reveals

that attenuation in the reservoir, where oil substituting brine as a pore fluid leads to a decrease in fluid bulk modulus, is significantly larger than in the overburden. It also shows that attenuation is anisotropic in the fractured reservoir, whereas the overburden data reveal no such pattern. The azimuth of minimum attenuation closely matches the strike of open fluid-filled fractures mapped in a nearby well. The data indicate an increase in azimuthal attenuation anisotropy together with a decrease in errors at near to mid offsets. The results can be described by a squirt-flow model, which relates the measured attenuation anisotropy to wave-induced fluid motion in the fractured porous rock.

Chapter 6

Frequency-dependent shear-wave splitting in VSP data from the Bluebell-Altamont field

6.1 Introduction

In this chapter I analyse shear-wave splitting in a multi-component VSP for different frequency bands. In the previous chapter I have found that P-wave anisotropy measured in field data can be frequency dependent. Here I investigate the possible frequency dependence of shear-wave anisotropy. The methodology consists of bandpass filtering the data followed by an Alford rotation to measure polarization angles and time delays as a function of frequency. Based on the squirt-flow model of Chapman (2003) I use the results to estimate fracture parameters. Finally, I carry out forward modelling to test whether the observations can be reproduced with synthetic data.

6.2 Geological background and VSP geometry

The Bluebell-Altamont field is a naturally fractured oil and tight gas field in the Uinta basin in northeast Utah. The Uinta basin is an E-W trending asymmetric basin with a steep northern and a gently dipping southern flank (Narr and Currie, 1982; Montgomery and Morgan, 1998). The Bluebell-Altamont field is located

near the northern margin of the basin.

Gas is produced from the marginal lacustrine sandstones of the Upper Green River formation at depths of 6500 ft (1980 m) to 8550 ft (2600 m), whereas oil was found in deeper reservoirs of the underlying Wasatch formation (Montgomery and Morgan, 1998; Lynn *et al.*, 1999). The top of the Upper Green River formation forms an E-W trending anticline, and gas is trapped in pinchouts of the sand bodies, which are encased by lacustrine tight shales and carbonates (Bates *et al.*, 1995). The sandstones have porosities of 7-10% and very small matrix permeabilities that lie below 1 mD. It has been recognized that production in the Bluebell-Altamont field is largely controlled by fracturing in the reservoirs, and that an understanding of orientation, size and concentration of the fractures is vital to improve recovery (Narr and Currie, 1982; Bates *et al.*, 1995; Montgomery and Morgan, 1998; Lynn *et al.*, 1999).

The VSP data have been acquired as part of a comprehensive study funded by the US Department of Energy to characterize fractures in the tight gas reservoirs of the Upper Green River formation (Bates *et al.*, 1995; Lynn *et al.*, 1999). The research project also included analysis of surface seismic P- and S-wave data, of cores and FMI logs, and studies of fractures in outcrops. The VSP is a near-offset

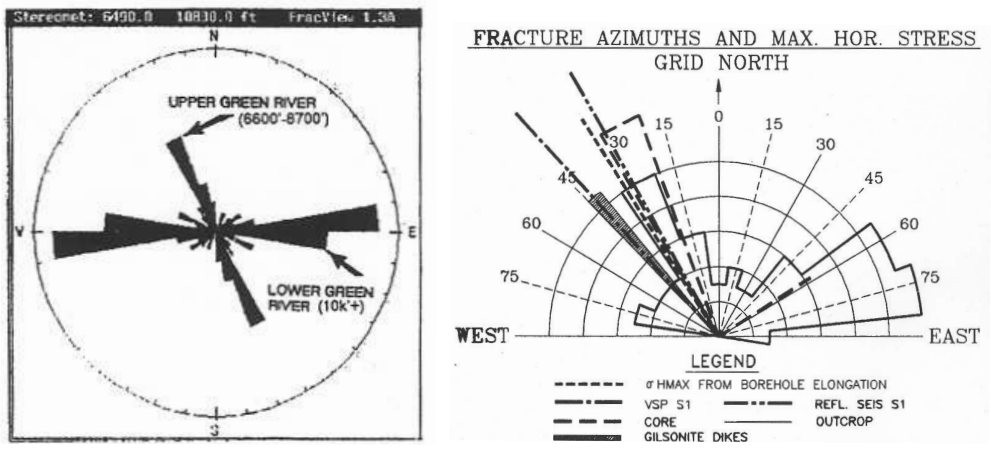

(a) (b)

Figure 6.1: Results from Lynn *et al.* (1999). a) Fracture orientations mapped from FMI data. b) Outcrop fracture orientations and horizontal stress directions compared with results of analysing seismic anisotropy.

VSP with the source located 550 ft (170 m) west of the well. A three-component source consisting of two orthogonal horizontal vibrators and a vertical vibrator was used. Three-component receivers were deployed in the borehole at depths of 2800 ft (850 m) to 8650 ft (2640 m) with a spacing of 50 ft (15 m). The Upper Green River formation extends from 6687 ft (2038 m) to 8591 ft (2619 m) at the location of the VSP well (Bates *et al.*, 1995).

Bates *et al.* (1995) and Lynn *et al.* (1999) present results of analysing shear-wave splitting from the direct arrivals recorded in the horizontal components of the VSP data. The authors found that significant shear-wave splitting occurs in the near surface and at the reservoir level, where the time delay between the split shear waves increases sharply with depth. The derived polarization azimuth of the fast shear wave is N43^{o}W for all recording levels. This orientation agrees well with the results of shear-wave splitting and azimuthal P-wave AVO analysis from the surface seismic data given by Bates *et al.* (1995) and Lynn *et al.* (1999). Furthermore, the authors show that the observed azimuthal anisotropy is well supported by fracture orientations inferred from geological data and by the orientation of the stress field. This is summarized in Fig. 6.1.

Fractures mapped from Upper Green River outcrops are predominantly vertical and show two dominant strike directions: NW-SE and ENE-WSW (Bates *et al.*, 1995). The same two fracture orientations are found in FMI data from the Upper and Lower Green River formations, respectively. NW-SE striking fractures are also observed in cores from the Upper Green River sandstones. The fractures mapped from FMI data and cores are sub-vertical to vertical and between 10 cm and a few metres long (Bates *et al.*, 1995). The NW-SE fracture strike is parallel to the in-situ maximum horizontal stress as well as to the palaeo stress direction indicated by gilsonite dikes that have formed due to natural hydrofracturing events (Bates *et al.*, 1995).

A more detailed inspection of the VSP data by Bates *et al.* (1995) and Liu *et al.* (2003) revealed that the magnitude of shear-wave anisotropy measured in the data changes with frequency. In the following sections I will repeat the analysis of frequency-dependent shear-wave splitting and present an interpretation of the effect in terms of the poroelastic model of Chapman (2003).

6.3 Shear-wave splitting analysis in different frequency bands

Shear-wave splitting is analysed by performing an Alford rotation of the four-component data corresponding to the two horizontal source and geophone components as described in Section 2.4 of Chapter 2. Fig. 6.2 shows the seismograms recorded in the reservoir interval before and after rotation. The strong energy in the off-diagonal components indicates that shear-wave splitting is present in the data. The rotation of the data into the natural coordinate system defined by the respective polarization azimuths of the fast and slow shear wave minimizes the energy in the off-diagonal components. The polarization angle of S1 is determined from the rotation angle, and the time delay between the split shear waves is measured by cross-correlating the rotated traces. The results of this analysis are shown in Fig. 6.3. The polarization angles of the fast shear waves are nearly

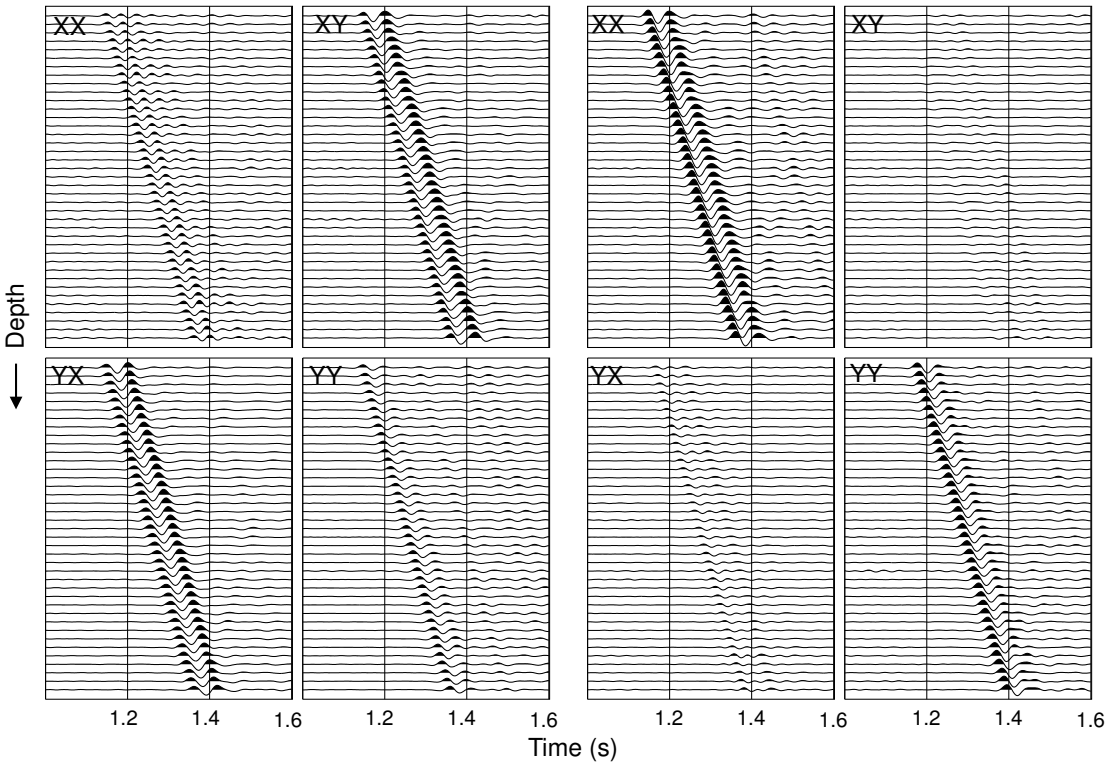

Figure 6.2: Four-component data recorded in the reservoir interval between 6700 ft and 8650 ft before and after Alford rotation. The first letter of the labels denotes the source orientation, the second letter the receiver orientation. The strong energy in the off-diagonal components, which is minimized by the rotation of the data, indicates shear-wave splitting.

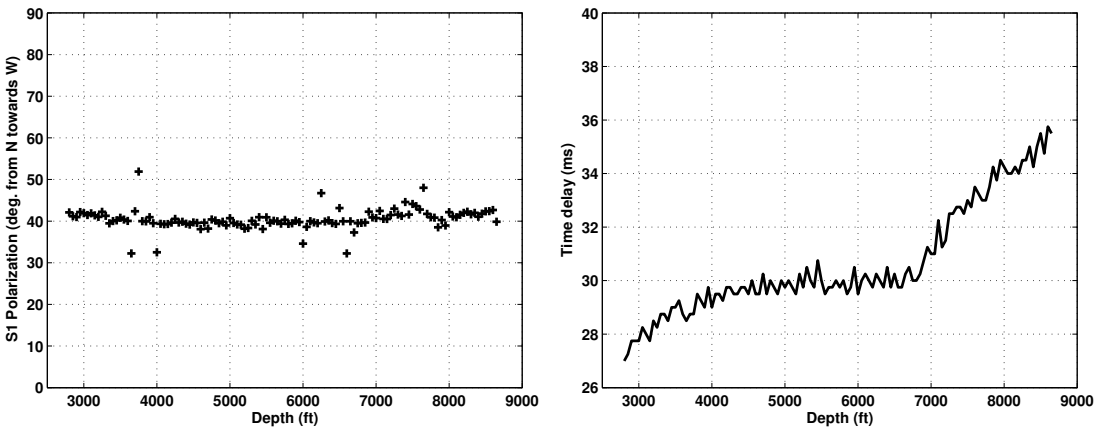

(a) (b)

Figure 6.3: a) S1 polarization azimuth; b) Time delay as a function of depth. The polarization of the fast shear wave is nearly constant with depth at N43^{o}W. The time delay between the split shear waves increases steeply in the reservoir.

constant with depth and have an average value of N43^{o}W in the reservoir. The time delay is 27 ms at the shallowest receivers, indicating that shear-wave splitting already occurs in the near surface above the recording levels. It increases slightly for another 500 ft but then remains nearly constant down to the top of the reservoir at 6700 ft. In the reservoir the time delay between the split shear waves rises again sharply, which indicates that the rock is azimuthally anisotropic.

Following the approach of Liu *et al.* (2003) I now filter the data into several frequency bands and repeat the rotation analysis for each of the filtered data sets. As shown in Fig. 6.4, which displays average spectra of the direct shear-wave arrivals recorded in the reservoir interval, the energy of the data is concentrated between 5 Hz and 35 Hz. The graph also indicates that on average the slow shear-wave arrivals are slightly attenuated compared to the fast shear-wave arrivals. For the filtering I use cosine-tapered zero phase bandpass filters with a passband of 10 Hz and a taper length of 5 Hz. The centre of the passband is moved between 9 Hz and 25 Hz in 1 Hz increments, so that the frequency range where the data contain significant energy is covered, but results are not biased by frequency components that have very small amplitudes.

Fig. 6.5 shows examples of the bandpass filtered traces. As discussed in Appendix A the decrease in frequency bandwidth causes a loss in time resolution.

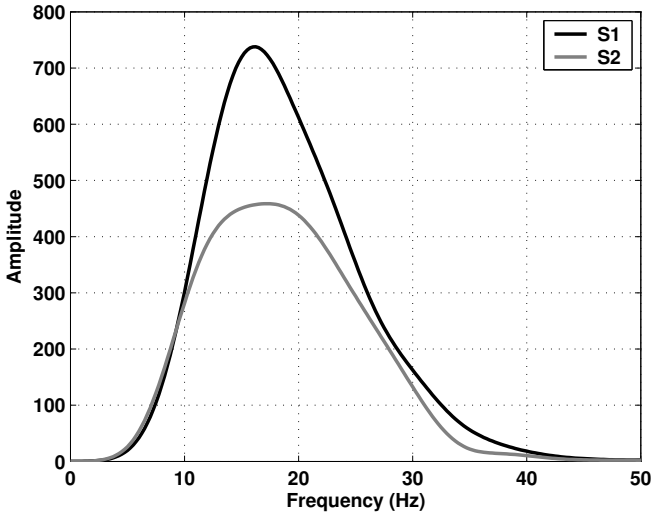

Figure 6.4: Average amplitude spectra of the direct shear-wave arrivals of the fast and slow component recorded in the reservoir interval.

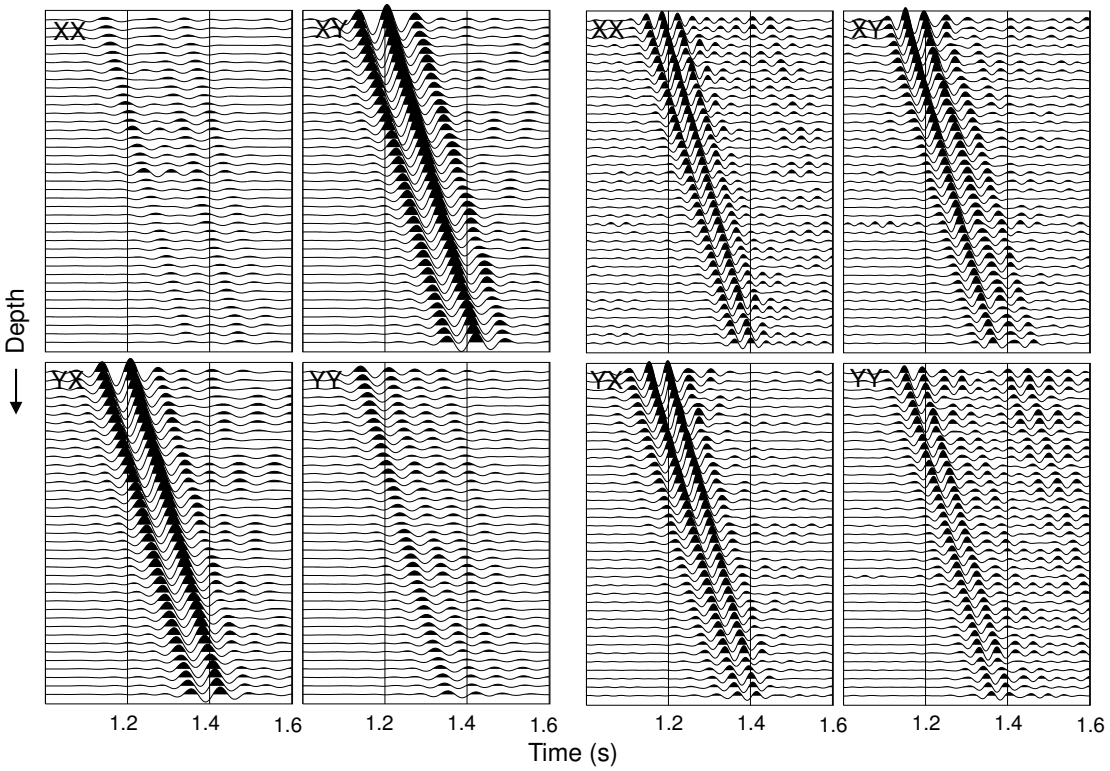

Figure 6.5: Four-component data filtered into frequency bands of 5-15 Hz (left) and 30-40 Hz (right). Although time resolution is reduced after bandpass filtering, the direct shear-wave arrival is still a distinct event, on which an Alford rotation can be performed.

The direct arrivals are spread in time compared to the unfiltered data in Fig. 6.2 and show considerable ringing. It would therefore not be possible to measure absolute arrival times accurately from the filtered traces. Time delays, however, are determined from a cross-correlation of the rotated traces, which avoids the difficulty of estimating absolute arrival times. Furthermore, there is no strong multiple energy following the direct arrivals that could interfere with the event after bandpass filtering and affect the time delay measurements.

Fig. 6.6 shows the derived time delays for four different frequency bands as a function of depth. It is obvious that already at the shallowest receiver the time delays are larger for low frequencies than for high frequencies. The separation remains constant over the depth interval between 3800 ft and the top of the reservoir at 6700 ft. In the reservoir, however, the time delay rises more sharply for lower frequency bands than for high frequency bands. This can be seen more clearly in Fig. 6.7b which displays the measured time delays with fitted straight lines for the reservoir interval below 6700 ft. The S1 polarization azimuth in contrast, which is displayed in Fig. 6.7a for the four different frequency bands, does not show any systematic variation with frequency. The increase in time delay per

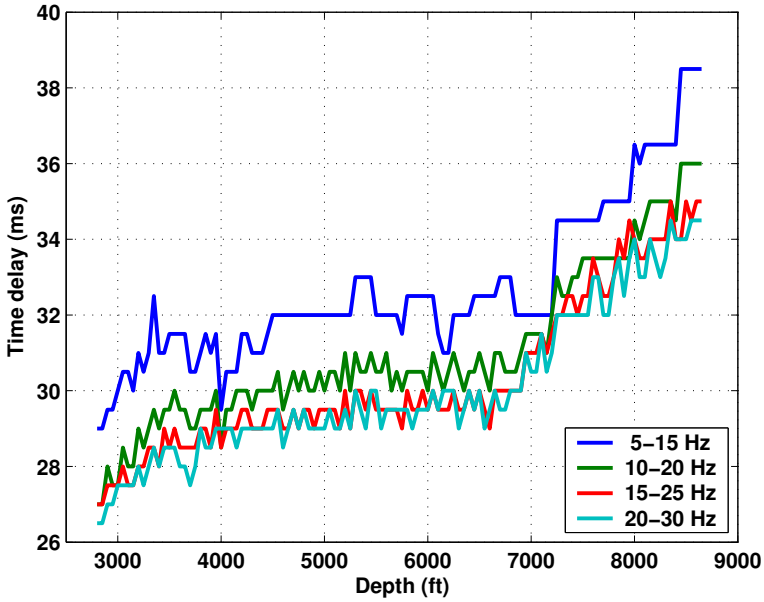

Figure 6.6: Time delay as a function of depth for four different frequency bands. The time delays are larger for low frequencies than for high frequencies, and in the reservoir they also increase more steeply for the lower frequency bands.

depth interval is a measure of the magnitude of shear-wave anisotropy. Thus, the data reveal a systematic decrease in the magnitude of azimuthal anisotropy with increasing frequency. Such a behaviour is described by the squirt-flow model of Chapman (2003) as discussed in Section 3.6 of Chapter 3. In the following section I demonstrate how the model can be used to invert for fracture parameters from the frequency-dependent time delay data.

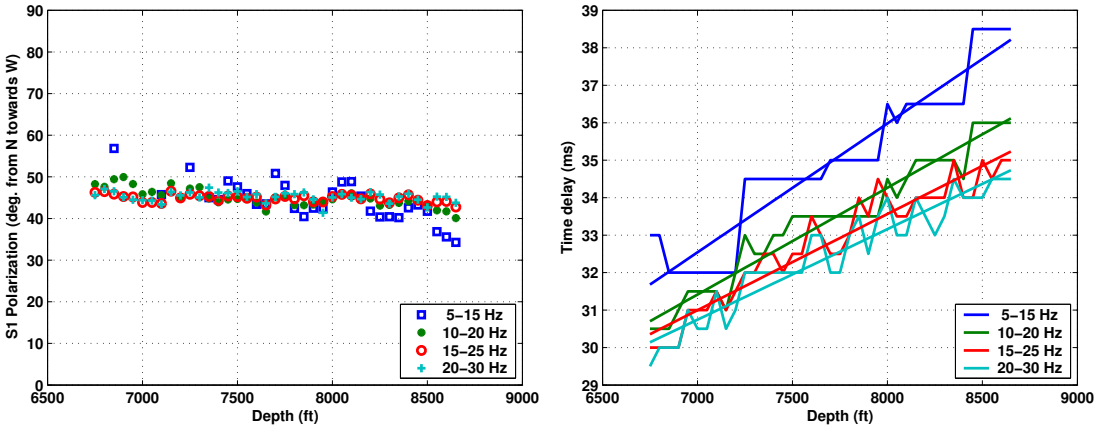

(a) (b)

Figure 6.7: a) S1 polarization azimuth; b) Time delay in the reservoir interval for different frequency bands. The S1 polarization lies around N43^{o}W for all frequencies, but the time delay shows a systematic variation with frequency.

6.4 Inversion for fracture density and size

In order to use the model of Chapman (2003) to invert for fracture properties from the data all other rock and fluid parameters that appear in the model have to be specified. Table 6.1 lists the given parameters of the Upper Green River sandstone. The P-wave velocity and density are obtained from well logs presented by Bates *et al.* (1995). I derive the S-wave velocity from the arrival times of the fast shear wave in the VSP data. Bates *et al.* (1995) report an average porosity of 9.4% for the Upper Green River formation measured from cores and thin sections. The pore fluid is natural gas, and I therefore set the fluid bulk modulus to 25 MPa.

Another parameter that has to be specified is the relaxation time τ_m associated

v_{P}	4877 m/s
v_{S}	2575 m/s
ρ	2600 kg/m^3
Φ_p	9.4%
k_f	25 MPa

Table 6.1: Rock properties of the Upper Green River formation.

with the squirt flow on the grain scale. In Section 3.6.3 of Chapter 3 I have shown how the value of τ_m obtained from the calibration of the model against laboratory data can be corrected in order to match other fluid and rock properties. The change in τ_m due to a difference in permeabilities was inferred from the porosity change. I now follow the same approach to obtain a value of τ_m for the Upper Green River sandstone. The laboratory experiments of Rathore *et al.* (1995) discussed in Section 3.6.3 were performed on water saturated high-porosity sandstone, whereas the Upper Green River formation is a gas saturated sandstone of low porosity. The change in τ_m is therefore mainly effected by the difference in fluid viscosity, fluid bulk modulus and permeability. From the decrease in permeability derived from the difference in porosities I obtain an increase in τ_m by a factor of 123. The first proportionality of τ_m given in Eq. 3.11, which contains the viscosity and fluid bulk modulus, yields a decrease in τ_m by a factor of 0.18. Thus, the correction of τ_m gives a value of 6 μs for the Upper Green River sandstone.

From the S1 polarization angles measured in the VSP data I infer an average fracture strike of N43^{o}W. I model the fractures as thin with an aspect ratio of 0.0001, so that the resulting elastic constants are not sensitive to the exact value of this parameter. The assumption is supported by observations of Bates *et al.* (1995) from borehole image logs and cores, who report average fracture apertures of 10 microns and fracture lengths on the decimetre to metre scale. Since incidence angles in the near-offset VSP are only around 5^o I tilt the fractures by 20^o from the vertical in order to model propagation directions of the waves where frequency-dependent effects would occur. In reality one would expect a distribution of fracture orientations around the vertical to be present as observed by Bates *et al.* (1995) and Lynn *et al.* (1999) in the field, which then produces the effect at small incidence angles.

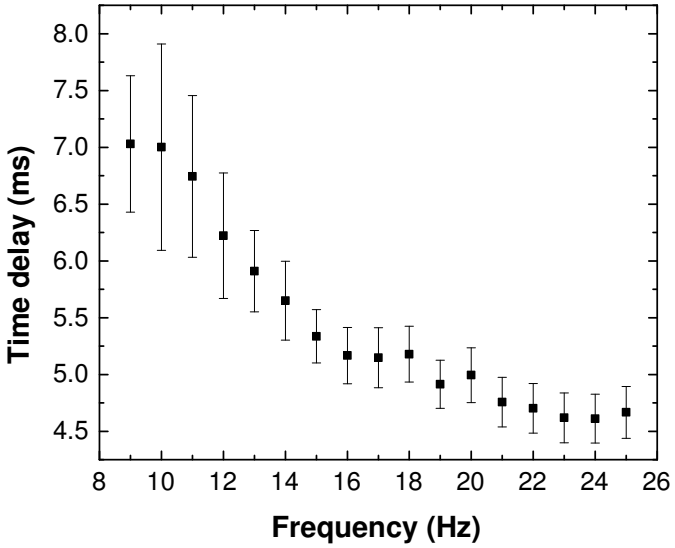

Figure 6.8: Measured increase in time delay over the reservoir interval as a function of frequency.

Now the only unknown parameters in the model of Chapman (2003) are the fracture density and the fracture radius. I estimate these properties by matching the observed change in time delay per depth interval with frequency. Fig. 6.8 shows the measured increase in time delay over the reservoir interval plotted as a function of the centre frequency of each of the analysed frequency bands. I compute the RMS error between these data points and the predicted values for each pair of fracture density and fracture radius.

The resulting error function is displayed in Fig. 6.9. There is a well-defined minimum around a fracture radius of 3 m and a fracture density of 3.5%. It is interesting to look at the shape of the error function in more detail. The bottom and top sections of the diagram represent the error functions that would be obtained by using the equivalent medium theories of Thomsen (1995) and Hudson (1981), respectively. As discussed in Chapter 3 neither of these frequency-independent models is sensitive to the fracture size, which becomes obvious from Fig. 6.9. Furthermore, the plot shows the range of fracture densities that could be inferred from the data by using frequency-independent equivalent medium theories. With the model of Thomsen (1995) one would obtain a fracture

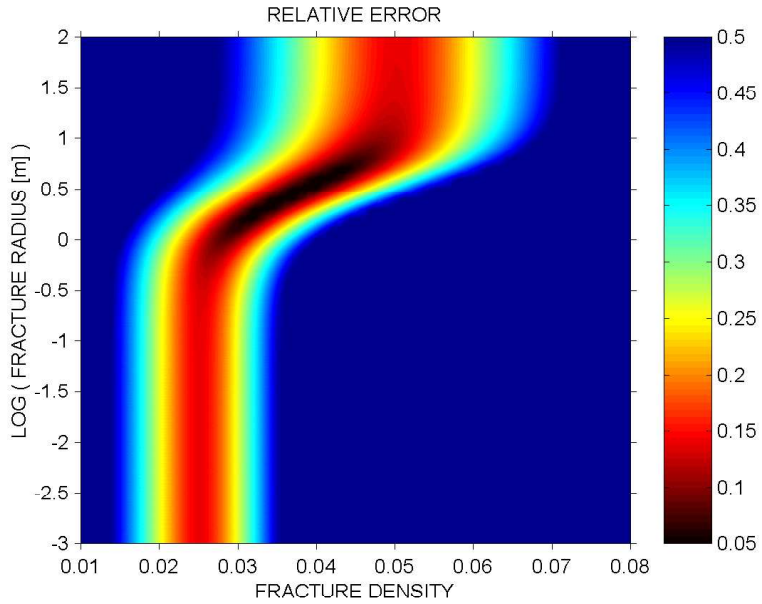

Figure 6.9: RMS error between measured and computed time delays accumulated over the reservoir interval as a function of frequency. Errors are normalized by the mean of the data values. There is a clear minimum around a fracture radius of 3 m and a fracture density of 0.035.

density of 2.5%, whereas the model of Hudson (1981) yields a fracture density of 5%. By incorporating frequency-dependent effects, however, the estimate of this parameter is much better constrained, and a value for the fracture size can be derived as well. In the following section I use the inverted fracture parameters to carry out forward modelling.

6.5 Synthetic modelling

I create a simple four-layer model that matches the main geological intervals in the field. The model parameters are given in Table 6.2. Again I take the P-wave velocities and densities from well logs and determine the S-wave velocities from the arrival times of the fast shear wave in the VSP data. For simplicity, I model the top layer as fractured but frequency independent. I use the model of Hudson (1981) to compute the elastic constants of a water-saturated fractured material with a fracture density of 0.045 in order to match the time delay of 27 ms measured at the shallowest receiver. The fracture strike is N43^{o}W as in the reservoir. The properties of the frequency-dependent anisotropic reservoir interval are given in

Depth (ft)	ρ (kg/m^3)	v_{P} (m/s)	v_{S} (m/s)	
2800	2200	2963	1363	Anisotropic
6687	2450	4000	2128	Isotropic
8591	2600	4877	2575	Anisotropic, frequency-dependent
Halfspace	2500	4382	2583	Isotropic

Table 6.2: Parameters of the model that is used to generate synthetic seismograms.

the previous section.

I use the same VSP geometry and acquisition parameters as in the real data. Synthetic seismograms are computed using the modelling package ANISEIS (Taylor, 2001). The synthetic four-component shear-wave data recorded in the reservoir interval are shown in Fig. 6.10 before and after Alford rotation. They are similar to the real data displayed in Fig. 6.2. I process the synthetic traces in the same way as the real data to analyse frequency-dependent shear-wave splitting. Fig. 6.11 shows the measured polarization angles of the fast shear wave for four

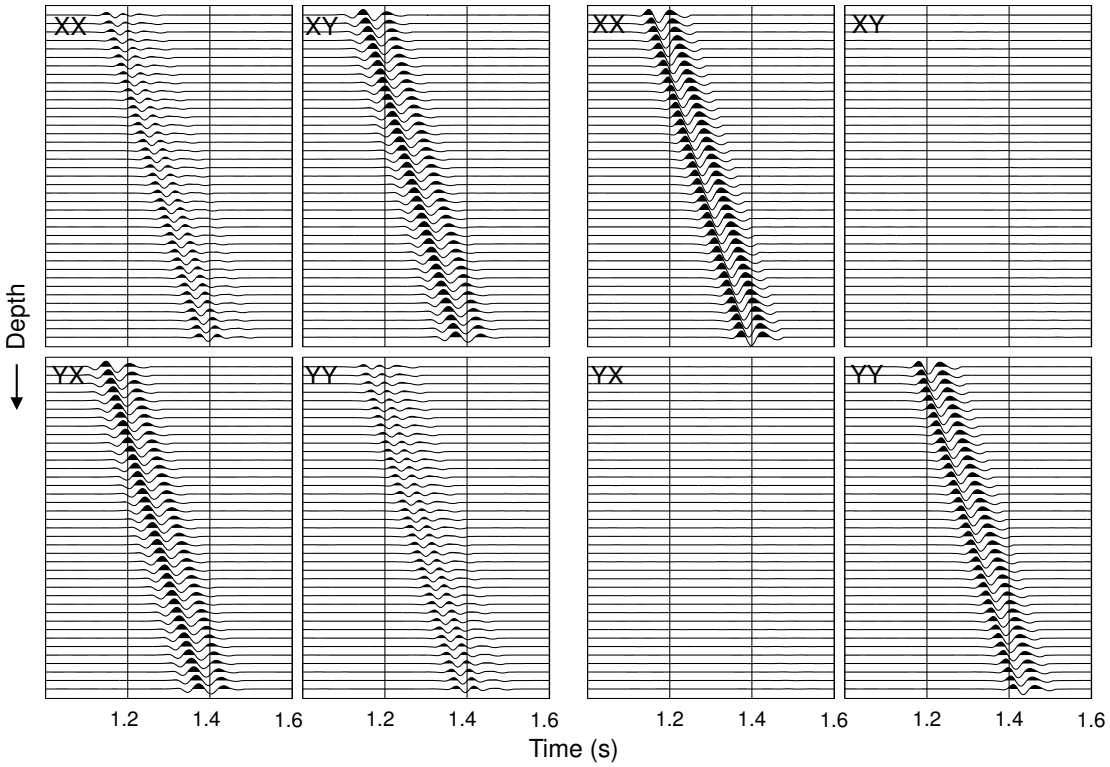

Figure 6.10: Four-component synthetic data corresponding to the reservoir interval before and after Alford rotation. The traces can be compared with the real data shown in Fig. 6.2.

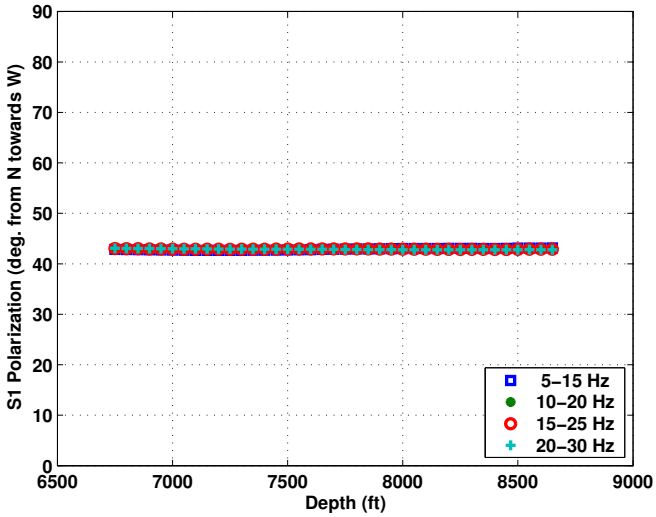

Figure 6.11: Polarization angles measured from the synthetic data for different frequency bands. The values are invariant with frequency and lie at N43^{o}W.

different frequency bands. As in the real data they are invariant with frequency and have a constant value of N43^{o}W, which is parallel to the fracture strike input into the model. The increase in time delay over the reservoir interval, however, varies with frequency in the same way as seen in the real data. From the time

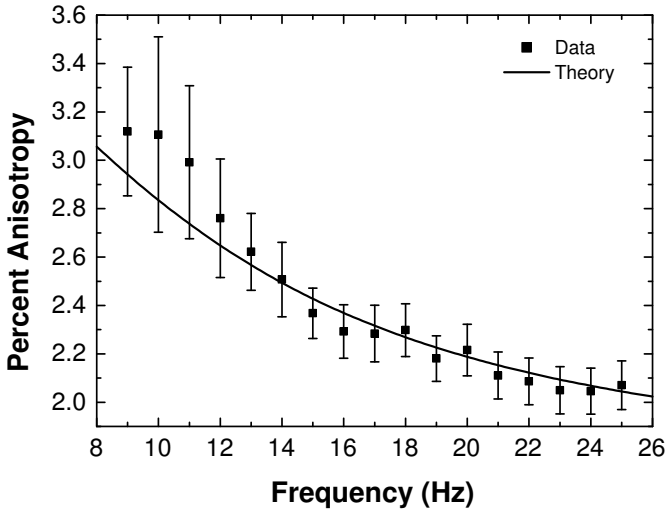

Figure 6.12: Measured and modelled percentage anisotropy as a function of frequency. The modelling results agree well with the real data.

delays I compute the percentage anisotropy given by $(v_{S1} - v_{S2})/v_{S2} = \Delta t/t_{S1}$, where Δt is the time delay accumulated between the top and the base of the reservoir and t_{S1} is the traveltime of the fast shear wave over that distance. The modelled values are compared to the real data results in Fig. 6.12. The curve obtained from the synthetic modelling reproduces the observations from the field data very well.

To ensure that the measured effect is not processing-induced I repeat the synthetic study for the case that the fractured third layer in the model is frequency independent. I use the model of Hudson (1981) to compute the elastic constants of the reservoir interval and leave all other parameters unchanged. Again I filter the data into different frequency bands and perform an Alford rotation to determine polarization angles and time delays. Fig. 6.13 displays the measured time delays for four different frequency bands resulting from the analysis. The values are invariant with frequency, which confirms that the effect observed in the real data is not an artefact produced by the way the data are processed.

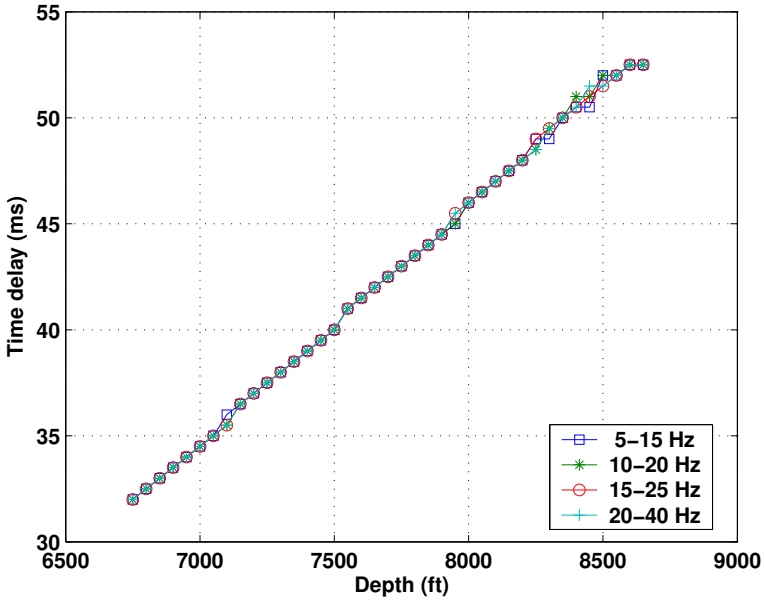

Figure 6.13: Time delays measured in different frequency bands for a model containing a frequency-independent fractured layer. The time delays are constant with frequency.

6.6 Discussion

The average fracture radius of 3 m, which I have obtained from the analysis of frequency-dependent shear-wave splitting, can be compared to independent borehole data. Bates *et al.* (1995) report fracture lengths on a scale of tens of centimetres to metres measured from cores and FMI logs. The average fracture size I have derived from the analysis of the VSP data is comparable in scale to these observations. This demonstrates that measurements of frequency-dependent anisotropy can be used to distinguish between the effects of micro-cracks and macro-fractures. Furthermore, it means that the measured frequency dependence of shear-wave splitting can be explained by a squirt flow mechanism as described in the poroelastic theory of Chapman (2003) with model parameters that match rock and fluid properties observed in the field.

Theoretical studies have shown that scattering of seismic waves due to ordered heterogeneities at wavelengths that are comparable to the size of the heterogeneities can also lead to frequency-dependent anisotropy (e.g. Shapiro and Hubral, 1995; Werner and Shapiro, 1999; Chesnokov *et al.*, 2001). Shapiro and Hubral (1995) demonstrated that frequency-dependent shear-wave splitting can occur at far offsets in finely layered media, if there is a specific ratio between wavelength and correlation length. The data set analysed in this chapter, however, is a near-offset VSP with nearly vertical propagation of the waves, for which the effect of thin layering does not lead to shear-wave splitting. Chesnokov *et al.* (2001) derived equations for scattering in media with ellipsoidal inclusions to model frequency-dependent anisotropy in fractured materials. In order to explain the effect measured in the Bluebell VSP data at seismic frequencies, the model would require fracture lengths on the scale of 200 m and fracture apertures of several metres. For fracture properties observed in the field, however, the effect described by the model of Chesnokov *et al.* (2001) would occur in a much higher frequency range. Modelling of the observed shear-wave behaviour based on wave-induced fluid motion has also been presented by Tod and Liu (2002) who used a layer-bounded fracture model based on Hudson *et al.* (1996). Here, rather high values (> 10 D) of the local permeability of the rock had to be assumed to explain the frequency-dependent effect in the seismic frequency range. It remains an open question as to whether these values are reasonable, since matrix permeabilities measured in

the field lie below 1 mD (Lynn *et al.*, 1999). Moreover, the authors argued for a non-monotonic relationship between frequency and the magnitude of anisotropy on the basis of a single data point obtained for the frequency band of 0-10 Hz. However, the data contain hardly any energy below 10 Hz (*see* Fig. 6.4), and therefore I do not consider the result for the 0-10 Hz passband to be reliable.
The technique of determining time delays from bandpass-filtered traces is tested on synthetic data in the previous section and also appears to be robust when applied to the field data. It should be noted, however, that the VSP from the Bluebell field is a data set of very high quality with a large signal-to-noise ratio. The direct shear-wave arrivals are very distinct events, and there is little multiple energy that could cause interference effects. Later in this thesis I will show that the technique fails if events of similar amplitude are closely spaced in time, which leads to interference of the energy after bandpass filtering.
The approach followed here may not be the only possible technique to analyse frequency-dependent shear-wave splitting. Liu *et al.* (2003) present results of analysing the same data set using a time-frequency transform. As I explain in Appendix A different types of these transforms have different resolution in the time-frequency plane. Therefore, certain transforms may be more robust in analysing the particular phenomenon of frequency-dependent time delays in this data set than others. Due to the fundamental trade-off between time and frequency resolution, however, neither of these methods will yield perfectly accurate values of the time delay at each frequency value (*see* Appendix A). Regardless of the applied technique one can only estimate an average time delay for an energy spread over a range of frequencies.

6.7 Conclusions

I have measured the frequency dependence of shear-wave anisotropy in a multi-component near-offset VSP from the Bluebell-Altamont field. In the reservoir the increase in time delay with depth decreases systematically as a function of frequency, while the polarization angles show no distinct frequency variation. This means that the magnitude of azimuthal anisotropy decreases as frequency increases.

I have modelled the measured effect with the poroelastic model of Chapman (2003), which describes frequency-dependent anisotropy due to squirt flow between fractures and matrix porosity. The only unknowns in the model are fracture density and fracture radius. Inverting for these parameters from the data yields an average fracture size that closely matches the length scales of fractures observed in the field. The analysis and modelling of the frequency-dependent behaviour therefore serves as a tool to differentiate between the effect of microcracks and fractures that are much larger than the grain scale but still smaller than the wavelength. The latter are regarded as flow units in subsurface reservoirs and have a strong influence on the permeability. A frequency-independent approach using static models would not allow to discriminate between these different length scales.

The VSP data show that a separation of time delays with frequency already occurs in the near surface. Since rock and fluid properties are unknown for that interval, I have not included the frequency dependence of the near-surface anisotropy in the analysis. Nevertheless, it is only in the reservoir that the separation in time delays with frequency changes again. Natural gas, which is the saturating fluid in the reservoir, has a low bulk modulus, for which the squirt-flow model of Chapman (2003) predicts a large magnitude of the frequency-dependent effect. Since the data set is a near-offset VSP with nearly vertical incidence, scattering due to thin layering cannot explain the frequency-dependent shear-wave anisotropy. Scattering from fractures would require fracture sizes to be on the order of the seismic wavelength, i.e. several tens to hundreds of metres. For these reasons I conclude that the squirt-flow mechanism is more likely to be the dominant cause of the observed frequency-dependent anisotropy.

Chapter 7

Influence of polar anisotropy in VSP data from the San Juan Basin

7.1 Introduction

In this chapter I analyse shear-wave splitting in a multi-component 3D VSP data set from the San Juan basin. The objective is to apply the method of measuring frequency-dependent shear-wave anisotropy used in the previous chapter to this data set, which comprises many more source offsets and azimuths. The shear-wave splitting measurements reveal that azimuthal anisotropy in the data is much weaker than polar anisotropy. This poses questions as to whether frequency-dependent effects related to fracturing could be detected in such a case.

7.2 Geological setting

The San Juan Basin in northwest New Mexico is one of the largest tight gas reservoirs in the United States. The structure of the basin is a broad syncline with a NW-SE trending axis (Whitehead, 1993). The lithology is characterized by a succession of shale- and sandstone sequences with coal being present in the shallow sandstone intervals. Gas has been produced from several fractured sandstone formations: the Mesaverde Group, the Dakota sandstone and the Pictured Cliffs

sandstone. More recently, the development of coal-bed methane in the shallower Fruitland formation has also added to the gas production in the basin (Whitehead, 1993).

Lorenz and Cooper (2003) present a tectonic model of the basin, which they relate to fractures observed in the Mesaverde and Dakota sandstones in outcrops and cores. A set of vertical extension fractures striking N-S to NNE-SSW appear to be pervasive throughout most of the basin, which the authors attribute to shortening of the basin in this direction during Laramide orogeny. However, there is evidence of local variations from this general pattern, indicating maximum horizontal compressive stresses and associated fracture orientations in a NE-SW direction (e.g. Yale *et al.*, 1993; Bird, 1998). In addition, Lorenz and Cooper (2003) find multiple sets of younger fractures in the outcrops, mostly striking NE-SW and ESE-WNW.

The matrix permeabilities in the sandstone formations are less than 1 mD, so that flow in the reservoirs is largely controlled by the presence of natural open fractures. Therefore, there is great interest in evaluating the use of seismic data to extract additional fracture information. Majer *et al.* (2002) present results of FMI and surface seismic data analysis from the area in the basin where the VSP was acquired (*see* following section). The FMI logs showed only a few open fractures in the thinly layered sandstones of the Mesaverde Group. They were found to strike NE-SW, which is parallel to the maximum NMO velocity measured from 3D surface seismic data in the area. Faults in the reservoir had also been mapped from the 3D seismic data. A major set of NE trending faults and a secondary set of smaller faults striking NW were identified (Majer *et al.*, 2002).

7.3 VSP geometry

The area covered by the 9-component 3D VSP is situated in the northwest corner of the San Juan Basin close to a NE-trending basin bounding fault. Fig. 7.1 shows a map of the 53 source locations that were placed around the well. Source offsets vary between 285 ft (87 m) and 7440 ft (2268 m). Three-component receivers were deployed in the borehole between depths of 1150 ft (350 m) and 5200 ft (1585 m) with a 25 ft spacing for some of the VSPs or a 50 ft spacing otherwise.

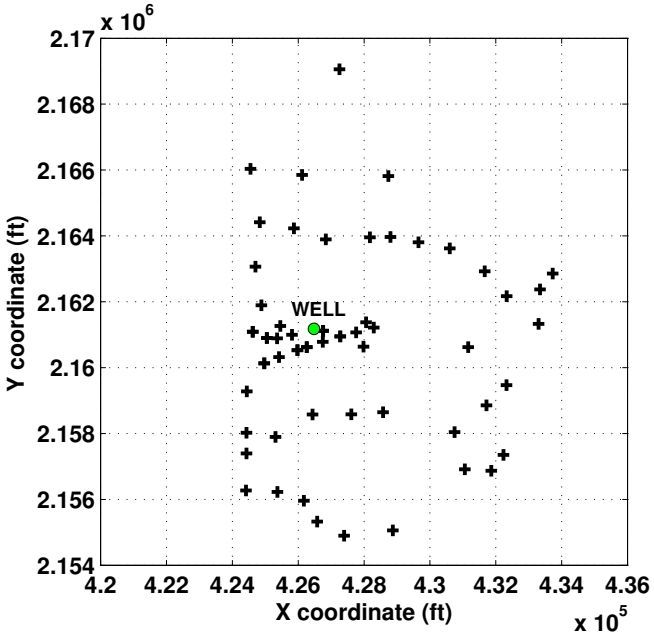

Figure 7.1: Map of source locations around the VSP well.

Three-component sources were used, consisting of two orthogonal horizontal and one vertical vibrator. The data were acquired with a sample rate of 2 ms.

Fig. 7.2 shows a velocity profile for the logged depth section that has been derived from well log and reflection seismic data (Daley *et al.*, 2002). The tops of major formations are indicated. The VSP begins above the coal-bearing Fruitland formation, passes through a thick interval of Lewis shale and covers the upper 1200 ft of the Mesaverde Group, which is the main reservoir unit.

In order to investigate whether frequency-dependent anisotropy is present in the data, I perform a shear-wave splitting analysis as explained in the previous chapter. The application of P-wave attenuation techniques used in Chapter 5 requires an acquisition geometry with a regular azimuthal coverage at constant offsets. Since the locations of sources in the San Juan VSP do not follow an ordered pattern and because four-component shear-wave data are available, the analysis of shear-wave splitting appears to be a more appropriate approach. In principle, the technique also allows detection of lateral changes because the data from every source location are processed independently. The P-wave attenuation analysis used in Chapter 5, in contrast, assumes lateral homogeneity.

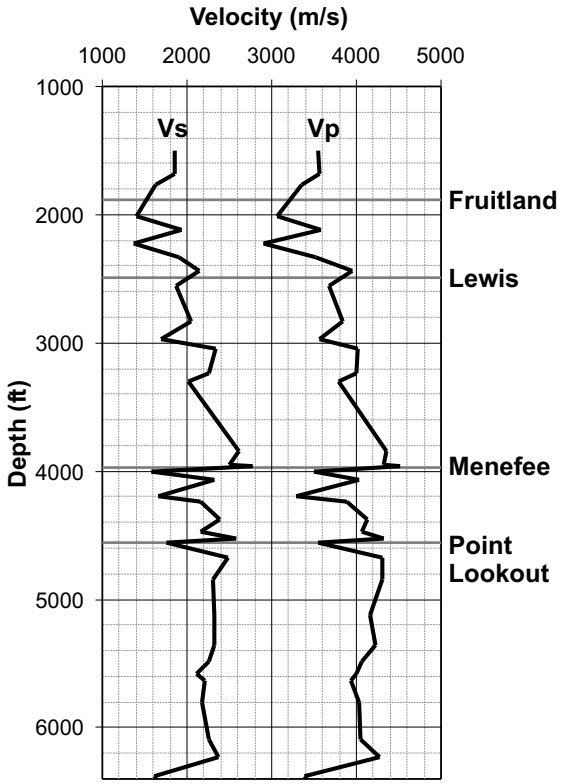

Figure 7.2: Velocity model derived from well log and reflection seismic data with tops of major formations. Menefee and Point Lookout are sandstones of the Mesaverde Group, which contains the main reservoir zones. The Lewis is a thick shale formation, whereas the layers above are again sandstones with coal being present in the Fruitland interval.

7.4 Shear-wave splitting analysis

Before measuring shear-wave splitting in different frequency bands of the data I analyse shear-wave anisotropy in the unfiltered VSPs to investigate how it changes with source offset and azimuth. For the VSP data sets studied in the previous two chapters it was known *a priori* that they show effects of significant azimuthal anisotropy. This is not the case for the San Juan VSP. In the following two sections I therefore carry out an analysis of shear-wave splitting in the data set and discuss an interpretation of the results in terms of anisotropic symmetry systems.

The four-component shear-wave data for one of the near-offset source locations are displayed in Fig. 7.3a. Again, polarization angles and time delays between the split shear waves are derived by performing an Alford rotation (*see* Chapter 2). As shown in Fig. 7.3b the process minimizes the energy in the off-diagonal

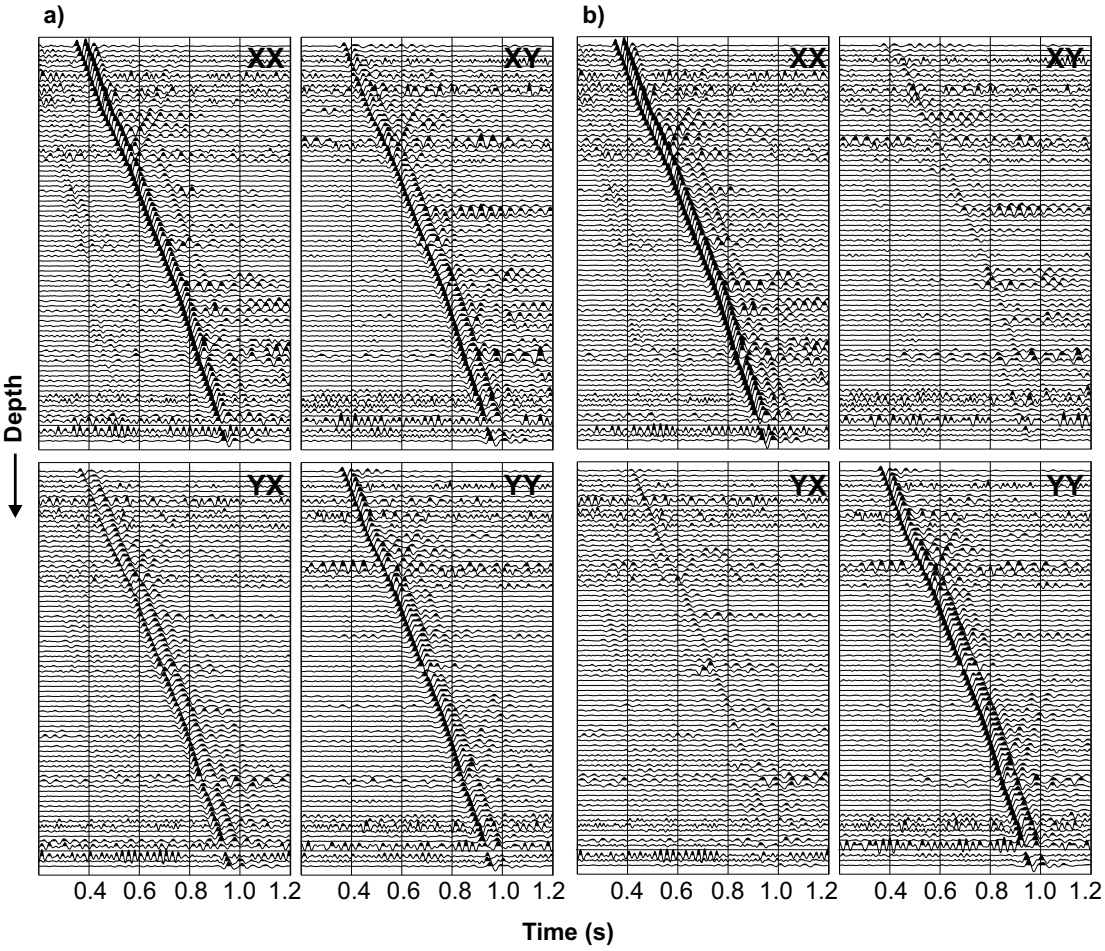

Figure 7.3: Four-component shear-wave data from a near-offset source location, a) before Alford rotation, b) after Alford rotation. The components are labelled according to source and receiver orientation, respectively. After rotation the energy in the off-diagonal components is minimized.

components and thereby rotates the data into the natural coordinate frame of the anisotropic system. At far offsets it is important to incorporate the vertical geophone component into the analysis, because it contains a large portion of the shear-wave energy. The seismograms displayed in Fig. 7.3 represent an example of the highest signal-to-noise ratio present in the data. Compared to the VSP from the Bluebell-Altamont field the noise level is higher in this data set (*see* Fig. 6.2). Especially at large source offsets, the signal-to-noise ratio is often very low as demonstrated in Fig. 7.4. Therefore, not all the data can be used for shear-wave splitting measurements. VSPs acquired at source offsets beyond 4700 ft had to be omitted from the analysis due to poor data quality.

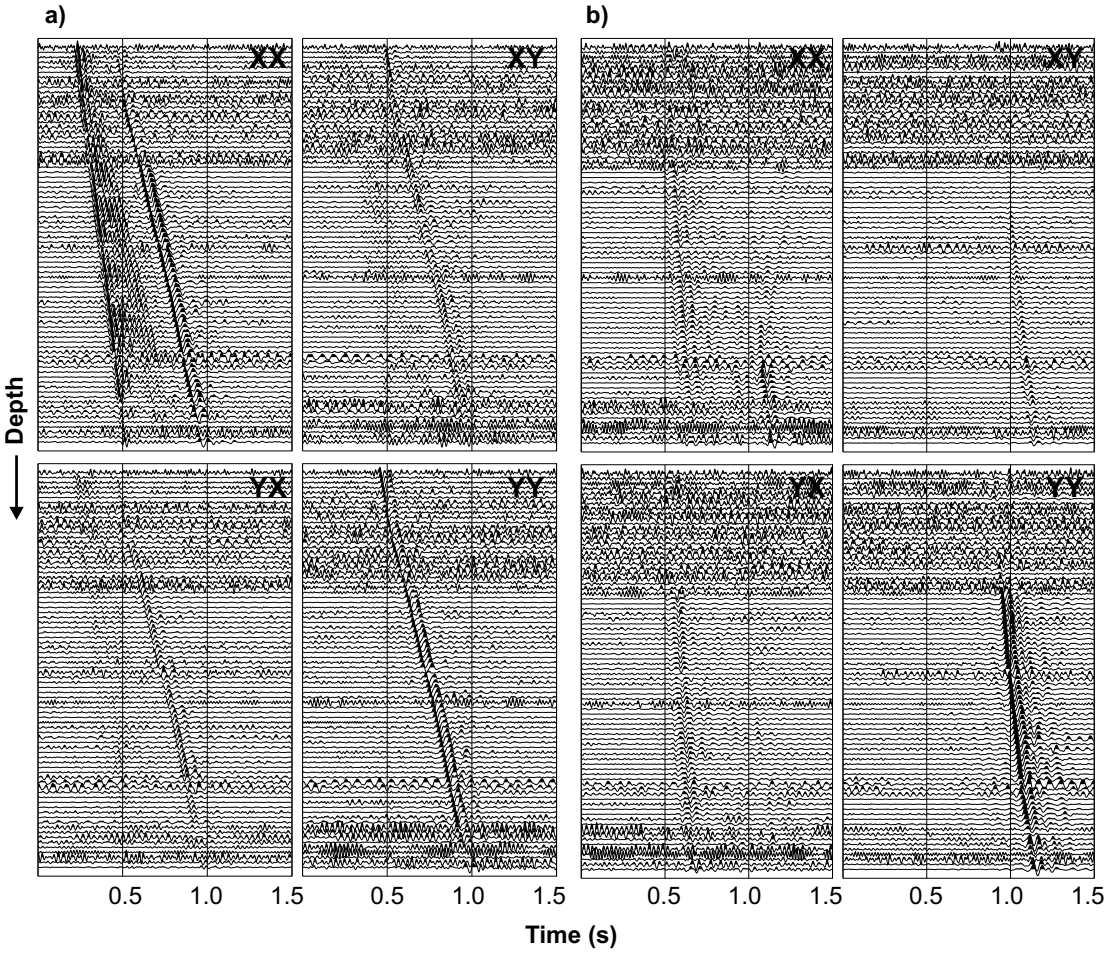

Figure 7.4: Data examples for larger source offsets where the level of noise is increased. a) Source 1001, offset = 1597 ft. b) Source 54, offset = 4687 ft.

Fig. 7.5 shows typical examples of analysis results from a near- and a far-offset source location. Polarization angles of the two shear waves and time delays are plotted as a function of depth. The displayed results are characteristic for the shear-wave splitting behaviour observed in the entire data set, which I will discuss in the following sections.

7.4.1 Shear-wave splitting pattern in the overburden

It can be seen from Fig. 7.5 that for the near-offset source the polarization azimuth of the fast shear wave is nearly constant below a depth of 2200 ft at N40-60^{o}E. The values have considerable scatter at shallower depths, which could be due to the small time delays that make the estimation of the S1 polarization more

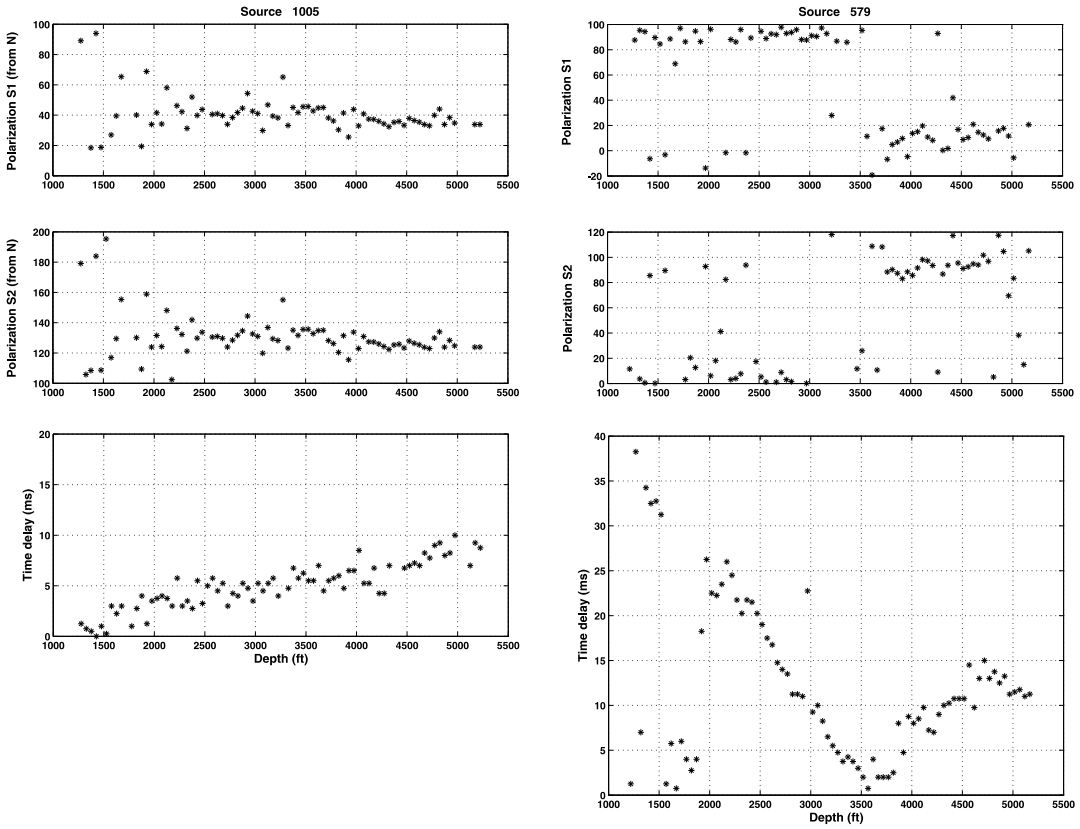

Figure 7.5: Characteristic examples of measured shear-wave splitting patterns for a) near offsets (source 1005: offset = 833 ft, azimuth = N106^{o}E), b) far offsets (source 579: offset = 2831 ft, azimuth = N156^{o}E). At far offsets the polarization angles displayed are measured relative to the source-well azimuth.

susceptible to error. In general, the time delay measured for near-offset sources shows a clear increase in the Fruitland formation down to the top of the Lewis shale at 2500 ft. Values vary between 5 and 15 ms, depending on the location of the source. In the Lewis shale, between 2500 ft and 4000 ft, the time delay remains constant.

The far-offset data show a different shear-wave splitting pattern as a function of depth. Here, the time delays have high values of up to 30 ms at the shallowest receivers, then decrease down to zero around an offset-to-depth ratio of one, followed by a large increase of up to 26 ms over the remaining depth interval. The polarization of the fast shear wave in the far-offset data is perpendicular to

the source-well azimuth at shallow depths. At the depth where the time delay reaches zero, the S1-polarization flips to 0-20^o from the source-well direction.

7.4.2 Shear-wave splitting pattern in the reservoir

As in the overburden, the polarization of the fast shear wave in the reservoir measured for near-offset sources follows a preferred orientation of N55^{o}E. The magnitude of shear-wave anisotropy, however, is rather small with time delays of 2-3 ms over an interval of 1200 ft. For far-offset source locations (or higher incidence angles) the polarization of the fast shear wave lies within 20^o of the source-well azimuth. The time delays measured over the reservoir interval are much larger than for near offsets and reach up to 13 ms. Only for far-offset sources northwest and southeast of the well do the data not show a significant increase in time delay in the reservoir (*see* also Fig. 7.10). The larger time delays at far offsets cannot simply be explained by the change in propagation pathlength. The maximum increase between zero offset and the largest offset used in the analysis (4687 ft) is a factor of 1.35 for the raypath from the reservoir top to the deepest receiver.

The results of the shear-wave splitting analysis from the entire data set for the reservoir interval below 4000 ft are summarized in Fig. 7.6. For each shotpoint, a line is drawn parallel to the measured polarization of the fast shear wave, with the length of the line being proportional to the increase in time delay over the reservoir interval. The plot represents an equal area projection of a hemisphere of propagation directions, assuming straight rays down to the reservoir depth. For shotpoints not shown in the figure the data quality is not sufficient to give reliable shear-wave splitting estimates.

Overall, the shear-wave splitting data displayed in Fig. 7.6 show a symmetric pattern. The near-offset pattern resembles that of an HTI medium containing vertical fractures aligned around N55^{o}E. The far-offset pattern, however, would be expected in a VTI medium. This indicates that at least a combination of the two symmetry systems will be necessary to explain the observed shear-wave behaviour.

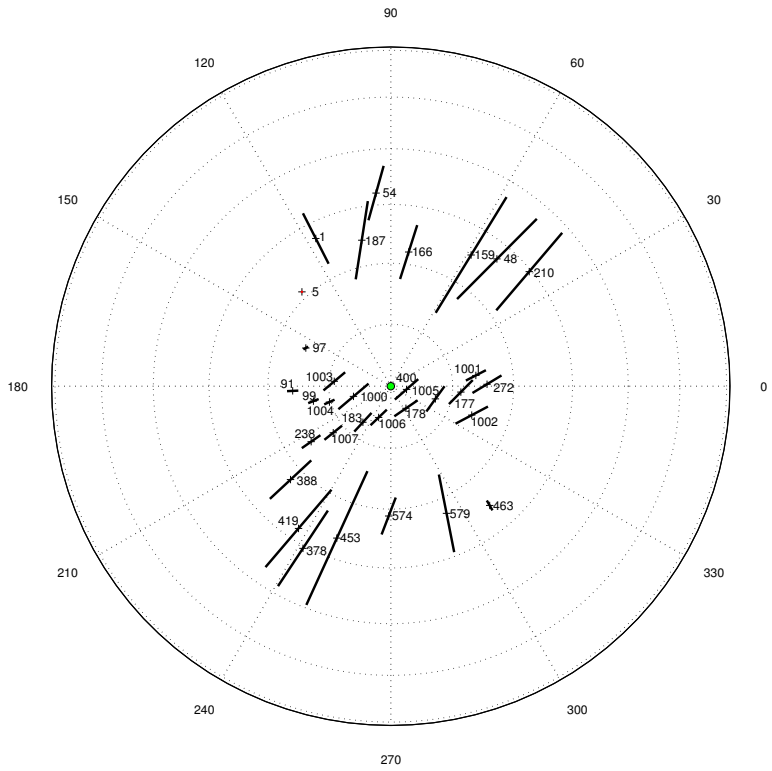

Figure 7.6: Equal area projection of measured S1 polarization and time delay in the reservoir (below 4000 ft). The orientation of the lines is the azimuth of the S1 polarization, whereas the length of the lines is proportional to the time delay between the split shear waves. Each line is labelled with the source number. For instance, the time delay for source 238 is 2 ms, while for source 48 it is 10 ms. Near-offset data (incidence angles $< 30^o$) show a consistent polarization azimuth of the leading shear wave with an average of N55^{o}E and small time delays. For far offsets the S1 polarization is nearly radial and time delays are large. At far-offset locations 5 and 463 northwest and southeast of the well the S1 polarization is still radial, but the time delay remains nearly constant in the reservoir.

7.5 Interpretation of the results

The main characteristics of the shear-wave splitting signature, which I have found in the entire data set, are summarized schematically in Fig. 7.7. The shear-wave behaviour observed from near-offset source locations shows effects of azimuthal anisotropy for the interval between the shallowest receiver and the top of the Lewis shale at 2500 ft, as well as for the reservoir sandstones below 4000 ft. In the reservoir the HTI effect is very weak, even for near-vertical propagation of the shear waves. In the shallower interval, however, azimuthal anisotropy is larger, and there is also considerable lateral variability in measured time delays. The

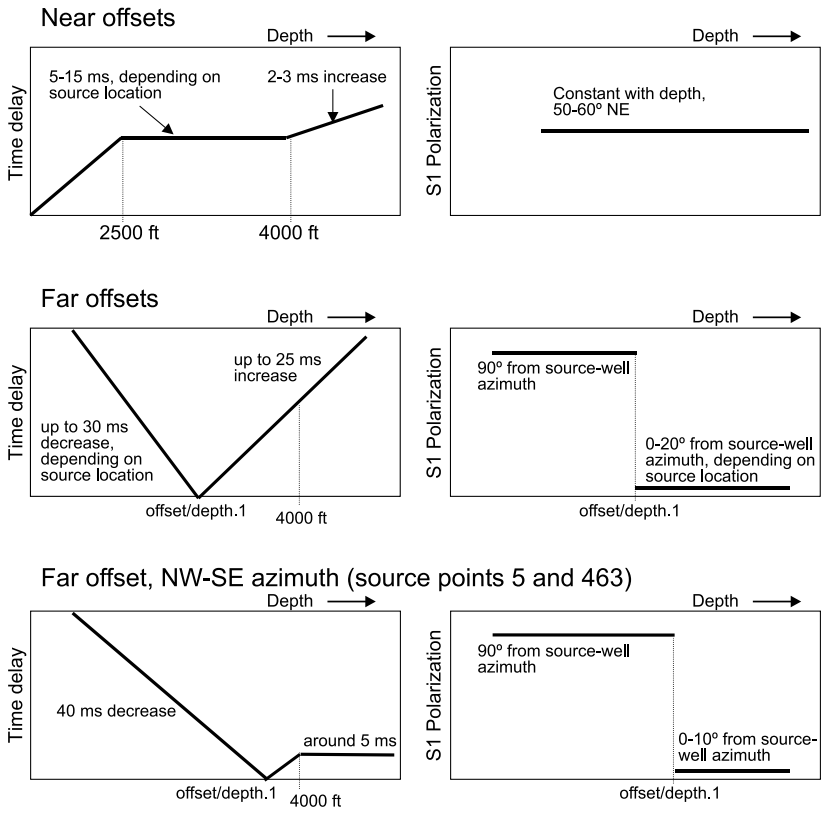

Figure 7.7: Sketches that summarize the measured shear-wave splitting patterns as a function of depth for groups of source locations, in which the shear-wave behaviour is similar. Near-offset data show an HTI effect above 2500 ft and below 4000 ft, while far-offset data indicate VTI anisotropy with clear evidence of a shear-wave singularity at offset/depth ≈ 1.

average fast direction in both intervals is N55^{o}E. In the Lewis shale between 2500 ft and 4000 ft there appears to be no shear-wave splitting for near offsets, so that the time delay remains constant. I can therefore interprete this interval as azimuthally isotropic.

In the far-offset VSP data effects of VTI symmetry are apparent for the interval of the Lewis shale between 2500 ft and 4000 ft. A line singularity is observed around an offset-to-depth ratio of one, where at all azimuths the time delay between the split shear waves reaches zero, and the polarization of the fast shear wave flips by 90^o from transverse at larger incidence angles (shallower receivers) to radial at smaller incidence angles (deeper receivers). The results indicate the presence of polar anisotropy also for the reservoir and the formations above the Lewis shale. The S1-polarization shows a consistent behaviour over the entire depth range.

The time delay has very high values (30-40 ms) at the shallowest receivers, which means that there must be an effect of VTI anisotropy in the overburden above the first receiver. Then it decreases more or less continuously until the shear-wave singularity is reached (*see* also Figs. 7.9 and 7.10). This suggests that polar anisotropy is also present in the interval between the shallowest receiver and the top of the Lewis shale. Except for the two sources northwest and southeast of the well, the time delay continues to increase significantly in the Mesaverde Group for all far-offset source locations, and the polarization of the fast shear wave is close to radial. This indicates that in the reservoir the shear-wave behaviour is affected by thin-layer anisotropy as well. The small component of azimuthal anisotropy in the reservoir is not obvious from the far-offset data.

7.5.1 Synthetic modelling

In order to support the findings and interpretations discussed above I perform full-wave synthetic modelling. The objective is not to derive exact elastic constants, but to understand the overall characteristics of the anisotropy that can reproduce the shear-wave splitting patterns observed in the data. These characteristics are important to consider in the subsequent analysis of the shear-wave anisotropy as a function of frequency.

As discussed in the previous section, the data suggest the presence of VTI symmetry for all receiver depths. In addition, the near-offset data show weak azimuthal anisotropy for two intervals: between the shallowest receiver and the top of the Lewis shale, as well as in the Mesaverde Group below 4000 ft. The combination of the two effects in these intervals yields orthorhombic symmetry as the simplest model to explain the observations.

I build a four-layer model with the parameters given in Tables 7.1 and 7.2. Average vertical velocities shown in Table 7.1 are chosen from the velocity model of Fig. 7.2 and densities are obtained from well log data. The orthorhombic layers contain vertical fractures striking N55^{o}E. Elastic constants are computed using the model of Hudson (1981). The fractures in the reservoir and the shallow orthorhombic layer are gas-saturated. The fracture-induced anisotropy is rather small compared to the VTI effect with fracture densities being only 1.5% in the reservoir and 2% in the overburden layer.

Layer	Depth (ft)	v_P (m/s)	v_S (m/s)	ρ (kg/m^3)	Symmetry
1	1150	3300	1700	2300	VTI
2	2500	3300	1700	2300	Orthorhombic; fracture density = 0.02
3	4000	3900	2000	2500	VTI
4	Halfspace	4100	2300	2600	Orthorhombic; fracture density = 0.015

Table 7.1: Vertical velocities, densities and anisotropic symmetry systems of the model used in the synthetic study.

Layer	c_{11}	c_{33}	c_{13}	c_{44}	c_{66}	S-wave anisotropy
1	27.80	25.05	12.73	6.65	7.86	16%
2	27.80	25.05	12.73	6.65	7.86	16%
3	46.47	38.03	17.64	10.00	13.64	26%
4	46.33	43.71	14.86	13.75	14.72	7%

Table 7.2: Elastic constants of the VTI materials in GPa. For the two orthorhombic layers vertical aligned fractures are inserted into the VTI medium following the model of Hudson (1981). The shear-wave anisotropy is defined as $(c_{66} - c_{44})/c_{66}$.

Figs. 7.8 to 7.10 show the shear-wave splitting data obtained from the synthetic VSPs compared to the real data results for near- and far-offset sources. Source 178 (Fig. 7.8) is located at an offset of 476 ft from the well and an azimuth of N145^{o}E, the offset for source 159 (Fig. 7.9) is 3260 ft at N32^{o}E and for source 5 it is 2590 ft at N43^{o}W.

The general patterns of S1-polarization and time delay as a function of depth are well matched by the synthetic data. The modelling reproduces the shear-wave line singularity observed in the Lewis shale for far-offset VSPs, preceded by a continuous steep decrease in time delay from very high values at the shallowest receivers. Furthermore, the difference in time delay signature at the reservoir level for far offsets northwest or southeast of the well compared to all other azimuths is reproduced in the synthetic data.

For near offsets, the modelled shear-wave behaviour shows the same general features as observed in the real data. However, it is difficult to explain the significant variability in measured time delays with source location above the Lewis shale with a single model. This may suggest that there is lateral heterogeneity in the rock properties that are causing azimuthal anisotropy in

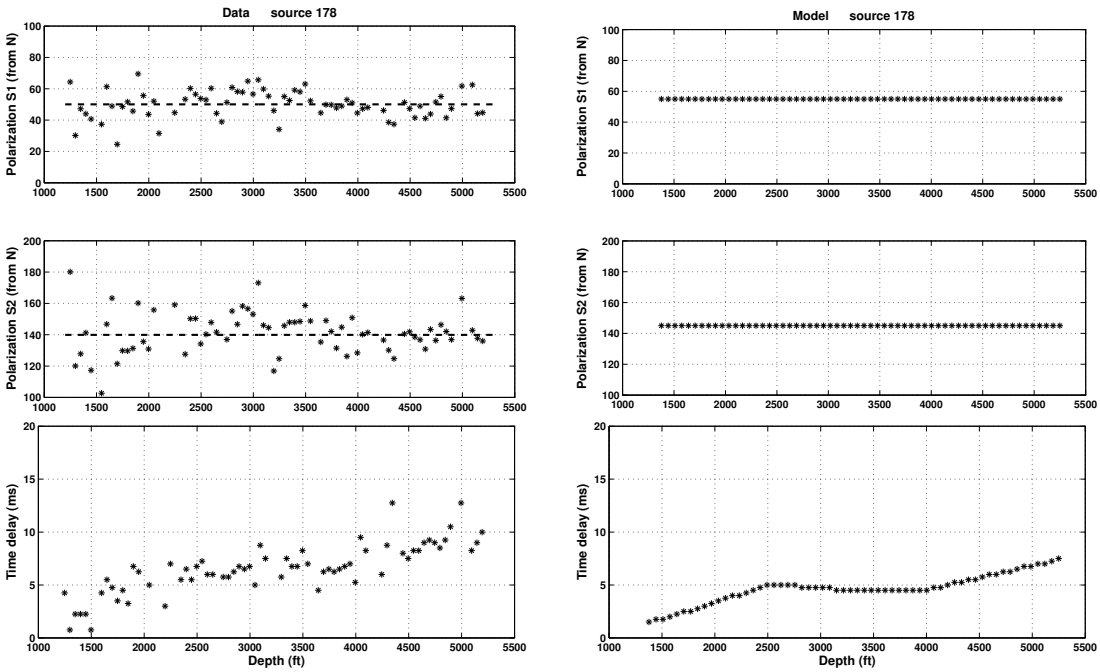

Figure 7.8: Shear-wave splitting data from near-offset source 178 in comparison with synthetic modelling results. The main features of constant S1 polarization with depth around N55^{o}E, constant time delay in the Lewis shale (2500 ft to 4000 ft), and increase in time delay above and below are well matched.

these shallow intervals.

The vertical transverse isotropy in the Lewis shale is well constrained by the shear-wave singularity. Since it is a line singularity that is radially symmetric about the vertical axis, the symmetry cannot be orthorhombic as in that case point singularities at specific propagation directions would occur (Wild and Crampin, 1991). In the reservoir the VTI effect is required to explain the change in S1-polarization from N55^{o}E at near offsets to approximately radial at far offsets. In addition, the shear-wave splitting pattern measured in near-offset data cannot be explained without the fracture-induced anisotropy in the reservoir and above the Lewis shale. The VTI effect in the intervals above the Lewis shale is needed to model the high values in time delay at the shallowest receivers followed by the steep continuous decrease down to zero.

Overall, the findings of the shear-wave splitting analysis are consistent with FMI data from the reservoir zone that revealed fine layering in the Mesaverde Group and only few open fractures striking NE (*see* Section 7.2). Furthermore, this direction agrees with the orientation of the NMO ellipse derived from 3D seismic

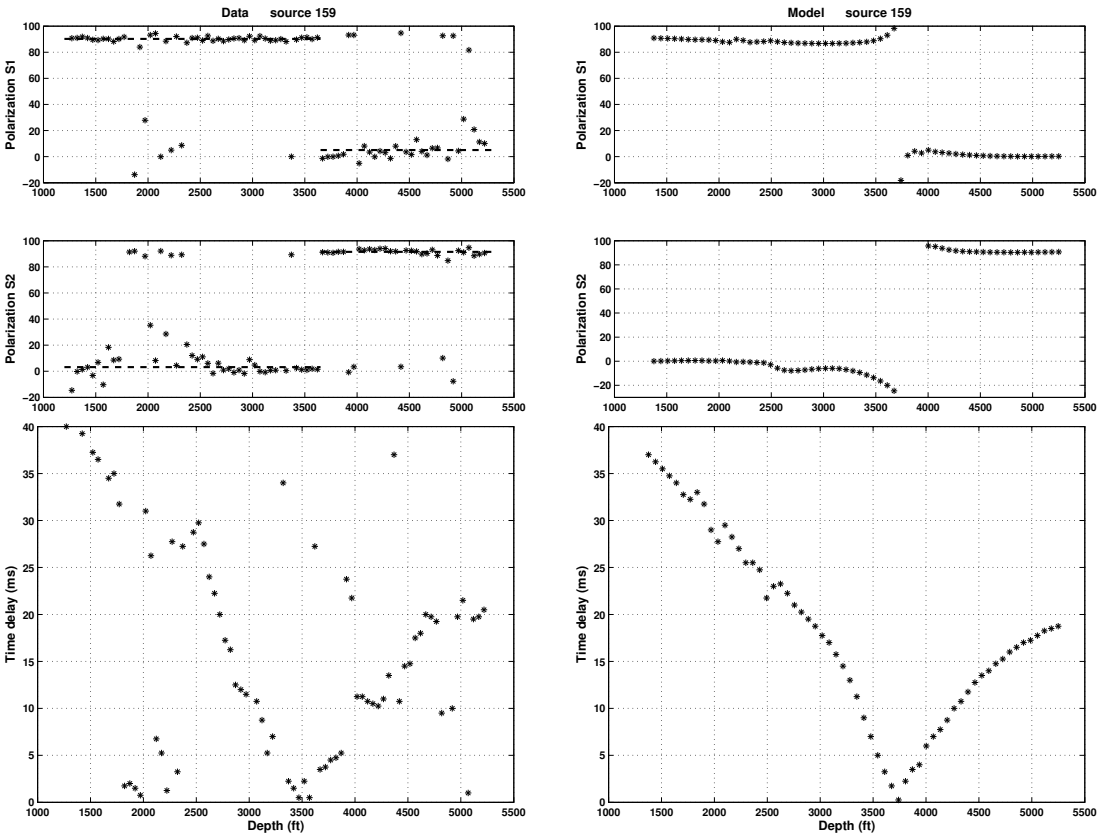

Figure 7.9: Far-offset data and modelling example from source location 159. Both real and synthetic data clearly show the effect of a shear-wave singularity where the S1 polarization flips by 90^o from normal to parallel to the source-well azimuth, and the time delay reaches zero. The magnitude of decrease in time delay above and of the increase below the singularity are well matched by the model.

data (Majer *et al.*, 2002). The results are consistent with the general tectonic framework discussed by Lorenz and Cooper (2003) that relates fracturing in the sandstone reservoirs to horizontal compressive stresses oriented NNE and NE during various stages of the Laramide orogeny.

Nevertheless, the original objective of acquiring a 3D VSP in the San Juan basin was to obtain a more detailed characterization of the fracture pattern around the well. Considering the dominance of the VTI effect over azimuthal anisotropy, the question arises whether in principle more information about fracturing can be confidently extracted from these data. Therefore, I repeat the synthetic study for a second model, where the symmetry in the reservoir is decreased by inserting a second fracture set. The angle between the strike of the first and second set is 60^o, which would be consistent with the fault pattern mapped from 3D reflection

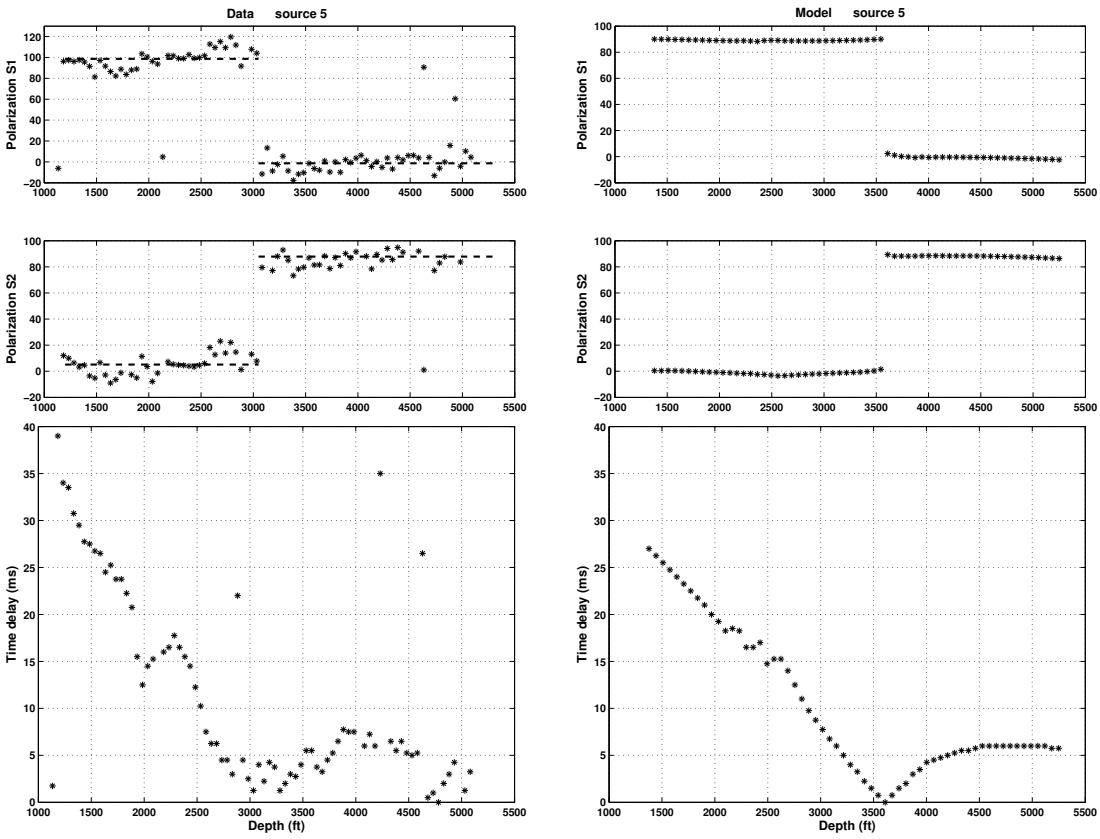

Figure 7.10: Results of shear-wave splitting analysis from real and synthetic data for far-offset source 5 northwest of the well. The shear-wave singularity is still clearly observable. However, as depth increases the time delay reaches a constant level, which is reproduced by the synthetic model.

seismic data in the study area (Majer *et al.*, 2002). The fracture density of the first set is increased to 0.02, while the second set has a fracture density of 0.01. For near-vertical propagation the polarization of the leading shear wave in this medium will be the density-weighted average of the two fracture orientations (Liu *et al.*, 1993a). To obtain an average of N55^{o}E I set the strike of the first set to N35^{o}E, while the second set strikes N95^{o}E.

The shear-wave splitting analysis for this second model yields results that are very similar to the previous ones. The differences in S1-polarization and time delay lie within the scatter that is present in the real data. Polarization errors, for instance, reach up to $\pm 10^o$. Fig. 7.11 compares equal area projections of S1 polarizations and time delay contours for the reservoir layer of the two models. The results of the real data from Fig. 7.6 are overlain on the plots. It is obvious from Fig. 7.11

that there is only a small range of propagation directions (close to horizontal at certain azimuths), where the polarization of the fast shear wave is significantly different between the two models. This is consistent with the findings of Liu *et al.* (1993a) who modelled shear-wave behaviour in media containing two fracture sets. The authors concluded that it would be difficult to distinguish between the effects of a single set and two sets of fractures from field data acquired within a limited range of offsets and azimuths. Here, there is an additional complication due to the fact that the VTI effect is dominant over the fracture-induced anisotropy. Therefore, the far-offset data do not provide additional constraints that could be used to characterize fractures in the reservoir. An interpretation relating the observations to the presence of a small number of fractures with one dominant orientation is equally possible as an interpretation in terms of several fracture sets with different orientations.

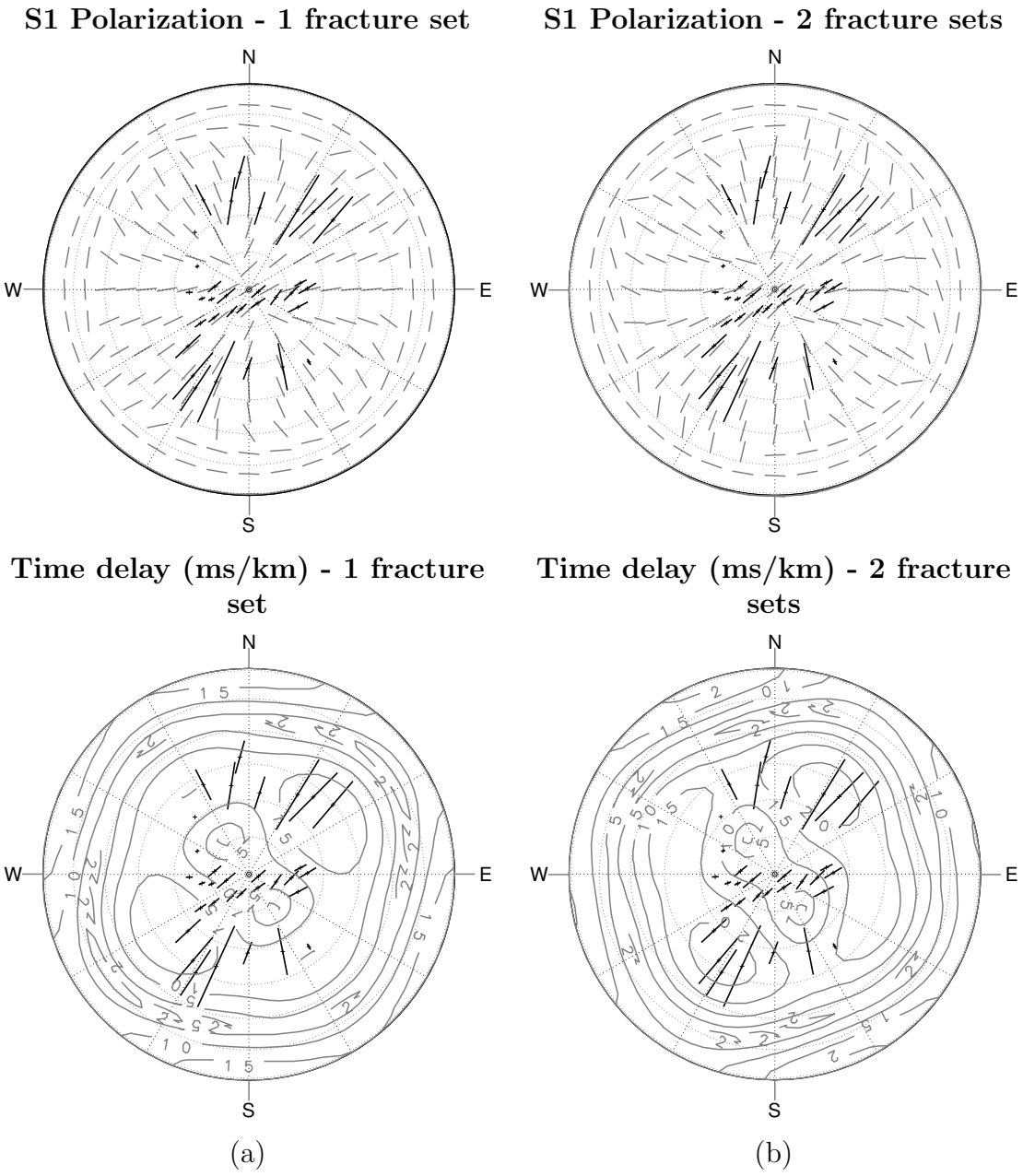

Figure 7.11: Equal area projections of S1-polarization and time delay for models of the reservoir layer. a) One fracture set striking N55^{o}E, fracture density 0.015; b) two fracture sets striking N35^{o}E and N95^{o}E, fracture densities 0.02 and 0.01. The data, which are overlain on the graphs do not provide sufficient constraints to distinguish between the two models.

7.6 Analysis of shear-wave splitting in different frequency bands

The analyses in the previous section have shown that the dominance of polar anisotropy poses a problem for an interpretation of the weak effect of azimuthal anisotropy in this data set in terms of fracturing in the reservoir. It is therefore unlikely that in this case an analysis of shear-wave splitting in different frequency bands improves the characterization of fracture-induced anisotropy. In the previous chapter I mentioned that theoretical studies also predict the frequency dependence of anisotropy in thinly layered media (e.g. Shapiro and Hubral, 1995). If such an effect is present in the VSP from the San Juan basin, it should be apparent in data from far-offset source locations. I now investigate these issues in more detail.

I apply the same technique as in the previous chapter, where I filter the data into different frequency bands and then perform an Alford rotation to measure shear-wave splitting parameters. The energy of the shear-wave arrivals in the VSP data is concentrated between 5 Hz and 35 Hz. As in Chapter 6 I use zero-phase cosine tapered bandpass filters with a passband of 10 Hz and a taper length of 5 Hz. Fig. 7.12 shows the time delay in the reservoir interval measured for different frequency bands at two of the near-offset source locations. As demonstrated by the linear fit also displayed in the diagrams, no systematic variation in the

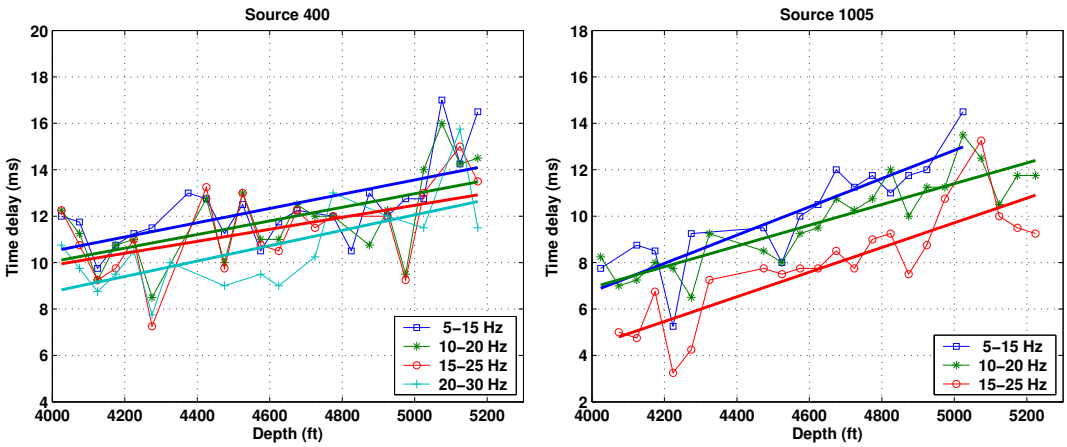

Figure 7.12: Examples of time delay in the reservoir measured for different frequency bands from near-offset data. There is no systematic change in the time delay gradient with frequency, and the values show considerable scatter.

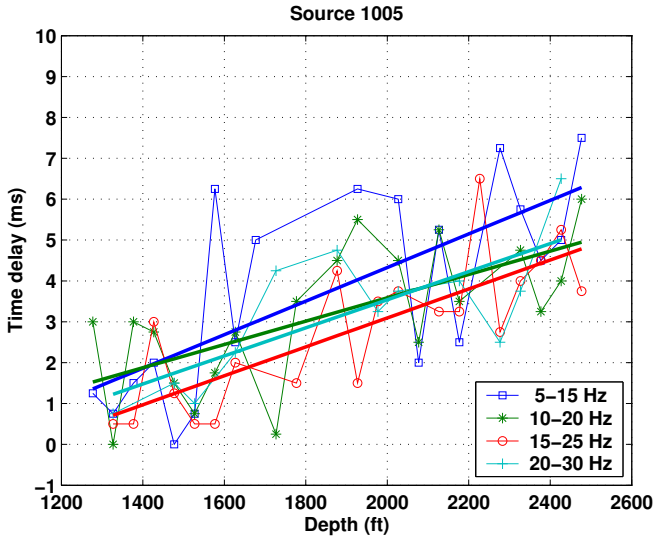

Figure 7.13: Time delay in the overburden for different frequency bands. Again, there is no systematic dependence of the gradient of time delays on frequency, and considerable noise is present in the data.

increase in time delay over the depth interval with frequency can be observed. Due to the small absolute values of time delay accumulated over the reservoir section the measurements are very susceptible to noise in the seismograms. This results in considerable scatter in the estimated values. The slopes of the fitted lines are therefore hugely dependent on which data points are included in the linear regression and which ones are regarded as outliers. The noise level in the data from many other near-offset source locations is even higher than for the examples given in Fig. 7.12.

I find that the same difficulties occur for the interval above the Lewis shale where azimuthal anisotropy was observed. Fig. 7.13 shows the corresponding time delay data measured for source location 1005. As in the reservoir, the gradients do not show any systematic variation with frequency. Again, the chosen example suffers less from effects of noise than other VSPs of the data set. Nevertheless, the time delay measurements do not appear to be robust enough to detect variations with frequency, even if they were present in the data.

I now investigate shear-wave splitting in the far-offset data for different frequency bands. Here, the shear-wave behaviour observed in the unfiltered data reflects mainly the effect of polar anisotropy. Examples of time delays measured in different frequency bands for two of the far-offset source locations are displayed in

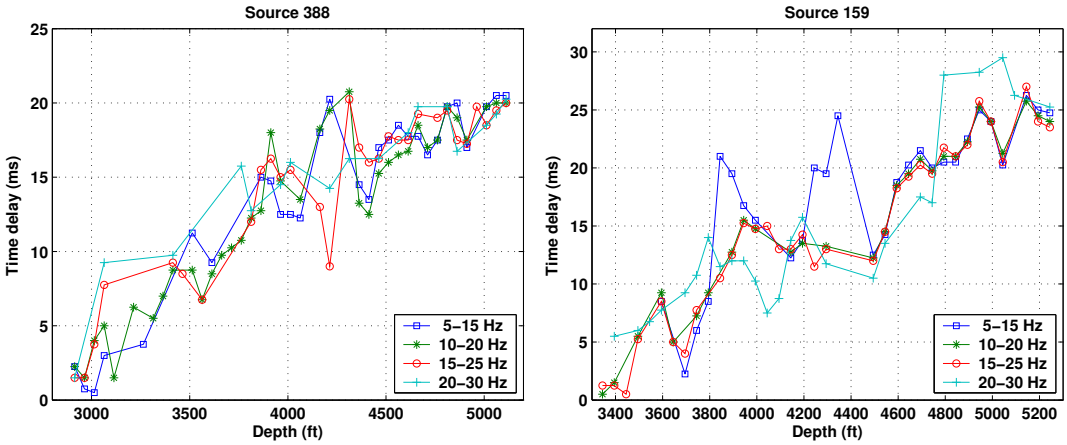

Figure 7.14: Examples of time delay measured for different frequency bands from far-offset data. As for near-offset sources no systematic change in the time delay curves with frequency can be observed.

Fig. 7.14. I focus on the depth range below the recording level where the shear-wave singularity is observed. Again, no systematic variation of the time delay curves with frequency is apparent. Due to the large time delays in the reservoir interval one would expect the analysis in this case to be more robust than for the near-offset data, so that frequency dependence may be detected if it occurred.
For both the thin-layer scattering and the fracture-related squirt-flow mechanism, the theories predict a decrease in the magnitude of shear-wave anisotropy with increasing frequency. The time delay data of the San Juan VSP do not reveal such an effect. However, the question remains whether in principle frequency-dependent azimuthal anisotropy could be detected in data if strong polar anisotropy is present. I now look at this issue in more detail.

7.6.1 Synthetic modelling

In this section I perform synthetic modelling to investigate how dominant polar anisotropy affects the signature of frequency-dependent azimuthal anisotropy. I build a simple model that consists of 400 m of an isotropic material above a halfspace of a frequency-dependent orthorhombic medium that contains vertical fractures in a VTI background material. The frequency-dependent halfspace has the same properties as the orthorhombic material defined in Tables 7.1 and 7.2 for the reservoir (Layer 4). The only difference is that I now compute the effect

of fracturing according to the model of Chapman (2003). The P-wave and S-wave velocities of the isotropic overburden are the vertical velocities of the same material (*see* Table 7.1).

I derive the elastic constants of the orthorhombic halfspace by adding compliances following the approach of Schoenberg (1980) and Schoenberg and Douma (1988) (*see* Section 3.2 of Chapter 3). Supposing the compliance tensor $\mathbf{s}^{\mathrm{VTI}}$ of the VTI medium is given by

$$\mathbf{s}^{\mathrm{VTI}} = \mathbf{s}_{iso}^{\mathrm{VTI}} + \mathbf{s}_{l}^{\mathrm{VTI}}, \tag{7.1}$$

where $\mathbf{s}_{iso}^{\mathrm{VTI}}$ is the compliance tensor of the isotropic background material and $\mathbf{s}_{l}^{\mathrm{VTI}}$ is an excess compliance describing the effect of thin layering. Equally, we can write the compliance tensor $\mathbf{s}^{\mathrm{HTI}}$ of the frequency-dependent fracture medium as

$$\mathbf{s}^{\mathrm{HTI}} = \mathbf{s}_{iso}^{\mathrm{HTI}} + \mathbf{s}_{f}^{\mathrm{HTI}}. \tag{7.2}$$

Again, $\mathbf{s}_{iso}^{\mathrm{HTI}}$ is the compliance tensor of the isotropic background material, whereas the excess compliance $\mathbf{s}_{f}^{\mathrm{HTI}}$ accounts for the effect of vertical aligned fractures. I then compute the compliance tensor $\mathbf{s}$ of the combined orthorhombic medium as:

$$\mathbf{s} = \mathbf{s}_{iso}^{\mathrm{HTI}} + \mathbf{s}_{f}^{\mathrm{HTI}} + \mathbf{s}_{l}^{\mathrm{VTI}}. \tag{7.3}$$

This is not an exact extension of the Chapman (2003) model for orthorhombic media, since the excess compliance $\mathbf{s}_{l}^{\mathrm{VTI}}$ does not depend on parameters such as porosity and frequency. Nevertheless, it serves as a reasonable approximation to study the main effects of combining polar anisotropy with frequency-dependent fracture-induced anisotropy.

The properties of the frequency-dependent fractured component of the material are given in Table 7.3. I choose τ_m and a_f, so that $\omega\tau_f = 1$ at a peak frequency of 25 Hz of the seismic pulse. This simulates a measurement in the frequency range where maximum dispersion occurs. The fractures in the model strike N30^{o}E. The source offset is 400 m along East, and 20 geophones are placed at depths of 450 m to 925 m with a 25 m spacing. This yields incidence angles roughly between 45^o and 25^o.

I process the four-component synthetic shear-wave data in the same way as the real data by applying bandpass filters followed by an Alford rotation. Fig. 7.15

ε_f	0.015
a_f	1 m
r	0.0001
Φ_p	10%
τ_m	8 μs
k_f	25 MPa

Table 7.3: Parameters of the frequency-dependent HTI component of the orthorhombic material.

shows the measured S1 polarization azimuths and time delays for four different frequency bands. The S1 polarization is nearly constant with frequency and rotates towards the direction of the fracture strike as depth increases. The time delays show some separation in frequency at shallow recording levels, but it vanishes as receiver depth increases. The shape of the time delay curve is dominated by the VTI effect, which causes a gradual decrease in slope of the curve as incidence angles become smaller. Even at the deepest recording levels, where the magnitude of fracture-related shear-wave anisotropy becomes larger, the time delays do not reveal the HTI effect. It would therefore be very difficult to derive the decrease in magnitude of azimuthal anisotropy with increasing frequency, which is present in the model, from these measurements.

Fig. 7.16 displays the time delays obtained for the same model, but without the VTI component in the fractured material. In this case a steeper increase in time

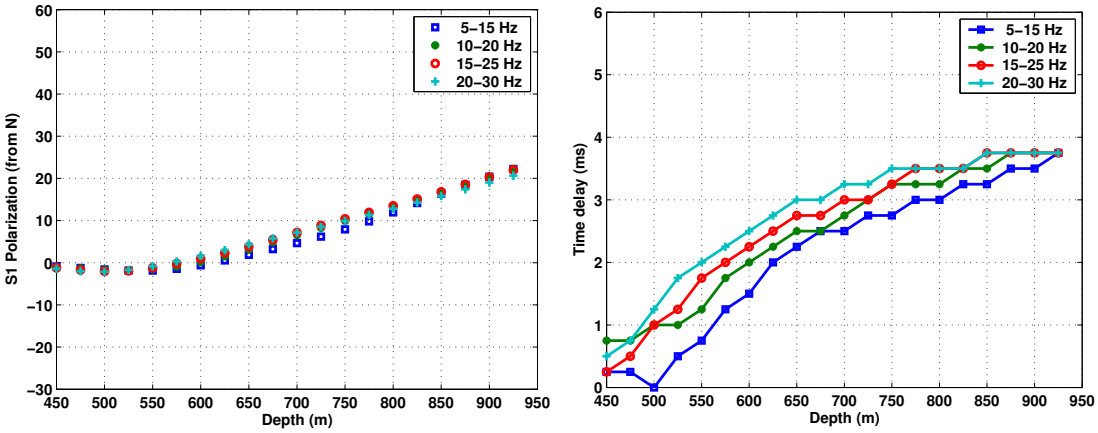

Figure 7.15: S1 polarization and time delays measured for four different frequency bands from the synthetic data. The fracture-induced anisotropy is frequency dependent, but it is dominated by polar anisotropy, which makes it difficult to measure the effect from the data.

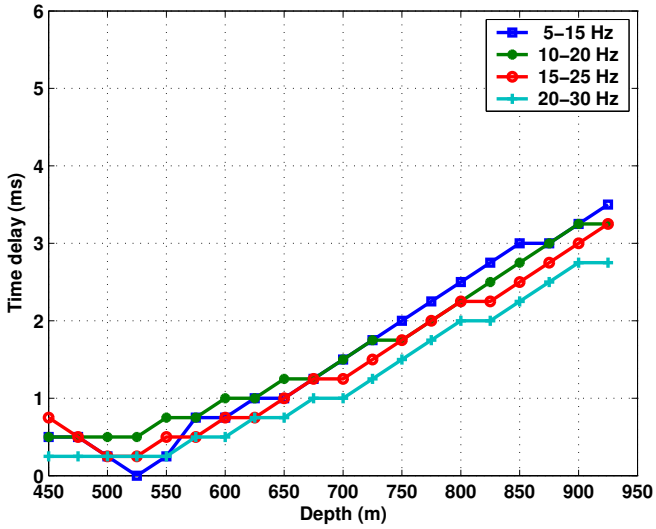

Figure 7.16: Time delays measured for different frequency bands if only the fracture-induced anisotropy is present. Now the frequency dependence can be recognized, although the effect is still very weak.

delays with depth can be observed for low frequencies than for high frequencies. The differences, however, are still very small due to the low magnitude of fracture-induced anisotropy and the narrow bandwidth of the data.

7.7 Discussion and conclusions

In the San Juan VSP data, seismic anisotropy is clearly evident and can be described by analysing shear-wave splitting parameters as shown in Sections 7.4 and 7.5. However, there is no evidence of frequency dependence of the anisotropy in the seismic frequency band. As demonstrated with synthetic modelling, a fracture-related frequency-dependent effect, if present, would not be detectable due to the dominant influence of polar anisotropy in the data. The azimuthal anisotropy is very weak resulting in small time delays, so that frequency-dependent measurements are not robust. This is in contrast to the VSP data from the Bluebell-Altamont field analysed in Chapter 6, where the absolute values of the time delays were above 30 ms. Furthermore, the noise level in the seismograms of the San Juan VSP is significantly higher than in the Bluebell VSP data. Over the narrow frequency bandwidth of the data it would therefore be generally impossible to detect frequency-dependent azimuthal anisotropy. This

also means that, in such a case, the availability of data from many offsets and azimuths does not help to constrain an interpretation of the observed anisotropy in terms of fracture and fluid properties. For the large time delays caused by the VTI effect at far offsets, a dependence on frequency could not be detected either. Here, the analysis is more robust due to the larger magnitude of anisotropy.
Frequency-dependent anisotropy as described by theoretical models only occurs in a limited frequency range, regardless of the mechanism that is causing dispersion. The frequency range where the effect would be observed depends on the model parameters. It is therefore plausible that frequency-dependent anisotropy is observed in some datasets, but not in every case where the data show effects of seismic anisotropy. The analysis and modelling presented in this chapter also demonstrate that the ability to detect frequency-dependent anisotropy in seismic data has limitations depending on data quality and the magnitude of anisotropy.

Chapter 8

Frequency-dependent anisotropy in P- and S-wave VSP data from the Rangely oil field

8.1 Introduction

In Chapters 5 and 6 I have shown that frequency-dependent azimuthal anisotropy can be found in VSP data in the form of P-wave attenuation anisotropy and the frequency dependence of the time delay between split shear waves. In Chapter 5 I discussed the analysis of P-wave attenuation from multi-azimuth VSP data recorded at a constant depth, whereas in Chapter 6 I measured frequency-dependent shear-wave splitting from near-offset VSP data recorded over a large depth interval. In this chapter I analyse a data set from the Rangely oil field that comprises both a walkaround VSP with receivers at one depth level in the reservoir and an offset VSP recorded over a range of depths in the well. Therefore it provides an opportunity to analyse both the P-wave and the shear-wave attributes that I have used throughout this thesis to detect and characterize frequency-dependent anisotropy. However, the data are acquired only with a P-wave source, so that converted waves have to be used to investigate shear-wave properties. This poses new challenges for the techniques applied in the previous chapters. The data set is also of interest, because the reservoir in the Rangely field is known to be fractured, and azimuthal anisotropy has previously

been measured in the VSP data showing good agreement with *a priori* fracture information (Horne *et al.*, 2002; Thompson *et al.*, 2002).

8.2 Location and VSP geometry

The Rangely oil field is located in northwest Colorado at the eastern edge of the Uinta basin and the northwestern margin of the Piceance basin. Its structure is a large doubly-plunging asymmetrical anticline with gentle dips of less than 4^o (Heffner and Barrow, 1992). The main reservoir in the field is the 200 m thick Weber formation, which is an aeolian fine-grained sandstone interbedded with fluvial and alluvial facies. The reservoir top is at a depth of 5600 ft (1700 m) (Thompson *et al.*, 2002). The overburden consists of shale and sandstone units, some of which contain naturally fractured tight gas reservoirs in the Piceance, Uinta and the nearby San Juan basin (Kruuskraa *et al.*, 1997, *see* Chapters 6 and 7).

The Weber sandstone in the Rangely field has an average porosity of 11%, and permeability values lie around 10 mD (Horne *et al.*, 2002). It has been recognized that natural fractures partly control production in the field (Ortega *et al.*, 2001; Horne *et al.*, 2002; Sassi *et al.*, 2003). However, studies to characterize fracture systems in the region have been predominantly focused on the shallower tight gas reservoirs in the surrounding sedimentary basins. Geological data mainly from outcrops in the area indicate the presence of a dominant regional fracture system striking N80^o-97^oE that is also beleived to be an important hydrocarbon migration pathway throughout the Piceance basin (Grout and Verbeek, 1985; Kruuskraa *et al.*, 1997; Thompson *et al.*, 2002; Robertson, 2004).

The VSP data were acquired to assess whether insight into fracturing at reservoir depths of the Rangely oil field can be gained through the use of seismic anisotropy (Horne *et al.*, 2002). A plan view of the VSP acquisition geometry is given in Fig. 8.1. The data set consists of a walkaround VSP, an offset VSP and a zero-offset VSP. For the walkaround VSP vertical vibroseis sources were located on a circle around the well at an offset of 4500 ft (1370 m). 16 source points were equally distributed between azimuths of -180^o and 45^o from North, so that the increment in azimuth is 15^o. The number of receivers alternated between two and four

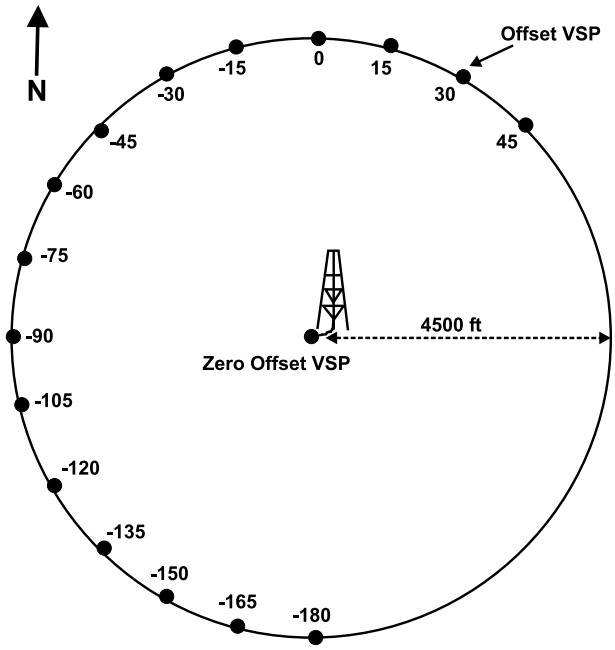

Figure 8.1: Location of source points relative to the well.

depending on the source location. The three-component receivers were placed in the reservoir interval between depths of 5915 ft (1800 m) and 6215 ft (1890 m). The offset VSP was acquired using the source location at N30^{o}E and 40 receivers in the well at depths of 4330 ft (1320 m) to 6280 ft (1915 m) with a spacing of 50 ft. The deepest thirteen receivers span the Weber sandstone interval. The sample rate in both data sets is 2 ms, and the trace length is 2.1 s.

The source offset had been chosen according to modelling results of Horne *et al.* (2002), so that maximum downgoing converted-wave energy would be excited at the reservoir top. The authors analysed converted-wave splitting from the walkaround VSP data using the transverse-to-radial amplitude ratio as a function of azimuth and the non-linearity of the particle motion in the horizontal plane. They found significant shear-wave splitting in the reservoir with a consistent S1 polarization direction of N85^{o}E and time delays measured from the offset VSP data reaching up to 7 ms at the base of the Weber formation. A crossed-dipole shear-wave log (DSI), that had been acquired in the same well, showed a fast shear-wave polarization of N75^{o}E to N85^{o}E in good agreement with the VSP data (Horne *et al.*, 2002).

Thompson *et al.* (2002) present additional geological data that were assembled to characterize fracturing in the reservoir. Analyses of cores from 15 wells in the field revealed the presence of near-vertical fractures with a dominant strike of N80^{o}E. The maximum horizontal stress and rapid well-to-well communication have also been observed to follow an E-W to NE-SW direction. Thus, there is good agreement between geological evidence and studies of seismic anisotropy in the field.

In the subsequent analyses I assess the spectral signature of the direct P-wave arrivals in the walkaround VSP data and of the converted-wave arrivals in the offset VSP data to investigate whether they show effects of frequency-dependent anisotropy.

8.3 Walkaround VSP: Spectral signature of P-wave arrivals

Fig. 8.2 shows the traces of the walkaround VSP after rotation of the P-wave first-arrival energy onto one component. From inspection of the first arrivals it is obvious that there are large differences in amplitude and wavelet shape between source locations. However, these changes are not gradual as the source azimuth varies and appear to be random rather than systematic. In general, it is possible that not only intrinsic properties of the rock are causing variations in recorded waveforms, but also acquisition-related issues such as differences in source coupling. Since the azimuths are closely spaced in the walkaround VSP, any spatial changes in attenuation properties of the rock section, through which the waves propagate, would be expected to produce smooth variations in waveforms between adjacent source locations. The abrupt changes seen in the data of Fig. 8.2 are therefore more likely to reflect variations in the source wavelet. Since the source wavelet is unknown it is impossible to separate the effects of source instability from potential attenuation effects in the rock. Measuring attenuation between receiver depths would partially circumvent the problem. However, an attempt of such an analysis failed, because the depth interval spanned by the receivers is only of the order of a wavelength and therefore not sufficiently large. Nevertheless, it may still be possible to identify qualitatively a general pattern

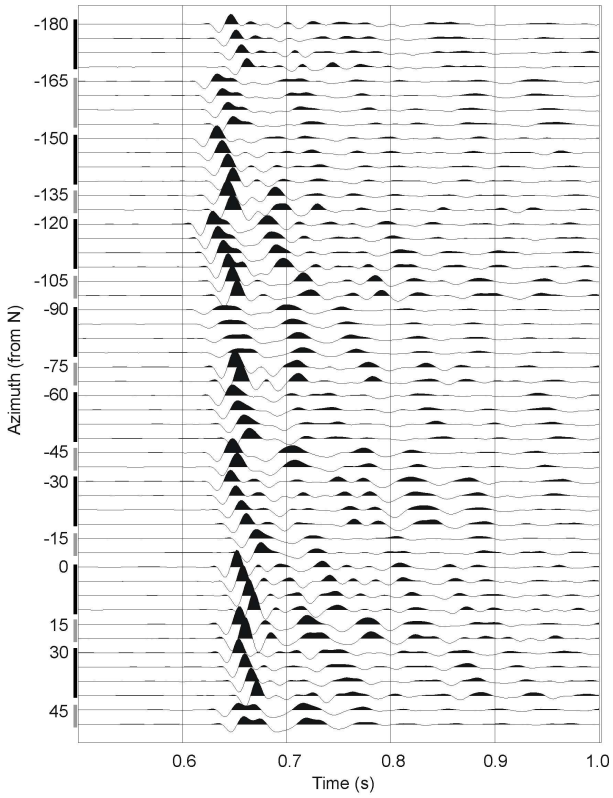

Figure 8.2: Walkaround traces after rotation onto one component. The wavelet changes significantly between adjacent source locations (e.g. compare azimuths of 30^o and 45^o or -105^o, -90^o and -75^o).

of spatial changes in attenuation properties of the rock, if they exist, such as the symmetry of azimuthal attenuation anisotropy. I investigate this issue further by analysing different spectral attributes, which I have used throughout this thesis. Fig. 8.3 gives examples of the windowed direct P-wave arrivals, amplitude spectra, and spectral ratios between different source azimuths and a reference azimuth. The reference pulse is shown in green in the graphs of the time series, its amplitude spectrum is plotted in red. At each azimuth I have averaged the spectra over all receivers. The large variation in waveforms between azimuths seen in the seismograms is also apparent in the amplitude spectra. Since the general shape of the spectra changes considerably with source azimuth it is difficult to identify any consistent trend in the spectral ratios. I therefore attempt to measure a change in attenuation between azimuths with the instantaneous frequency method described in Chapter 4, which is less sensitive to the particular shape of the spectra (Dasios

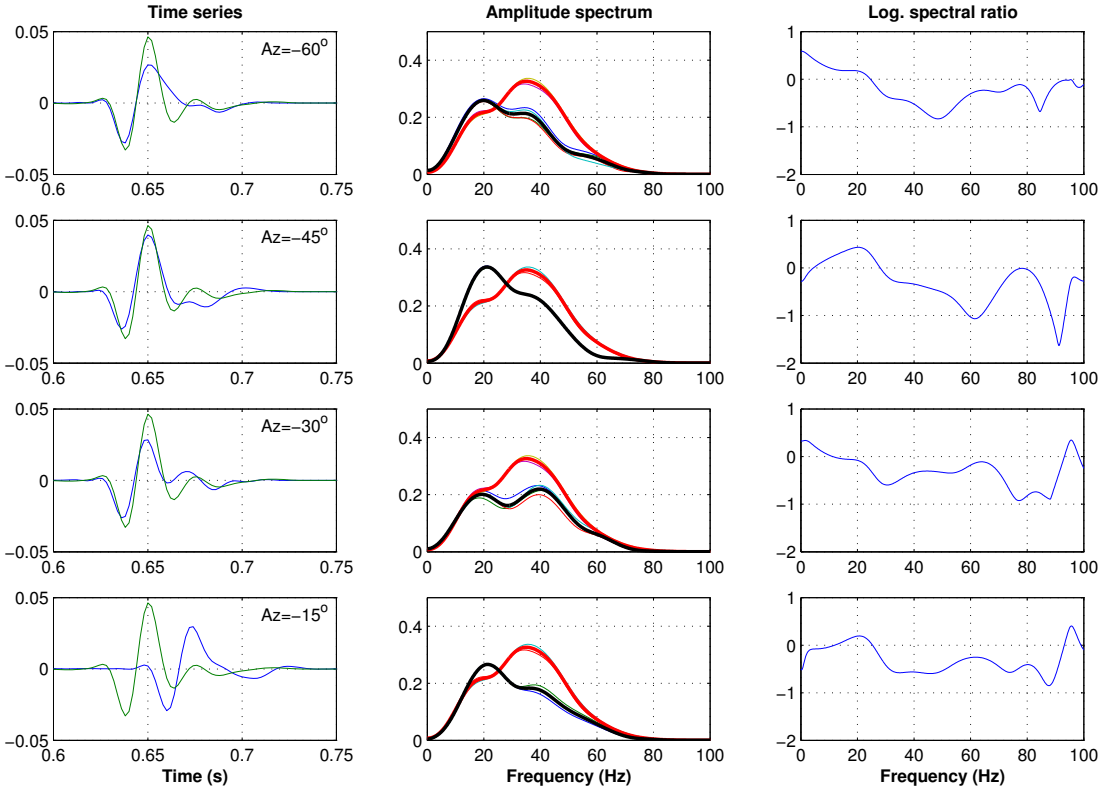

Figure 8.3: Example of the windowed first arrivals, spectra and spectral ratios. The trace data are shown for the deepest receiver at 6215 ft. The amplitude spectra averaged over all receivers are displayed as thick lines, whereas the thin lines are the spectra corresponding to the individual receivers. Because of the large difference in the shape of the spectra it is difficult to see any clear trend in the spectral ratios.

et al., 2001).

Fig. 8.4a displays the instantaneous frequencies computed at the peak of the amplitude envelope of the direct P-wave arrival as a function of azimuth. The values do not show any obvious systematic variation with azimuth, and there are large differences between data from adjacent source azimuths. The derived change in attenuation $\Delta 1/Q$ relative to the data from the source south of the well is displayed in Fig. 8.4b. Even without the obvious outlier at -90^o the values appear to be very scattered and there is no clear systematic variation with azimuth. A least-squares fit with the $\cos 2\varphi$-function of Eq. 4.8 yields values of $C_2 = 0.003 \pm 0.0015$ and $\varphi_0 = 18^o \pm 17^o$ measured clockwise from N. The inverted azimuth is not consistent with the symmetry directions of the fractured reservoir that were identified previously and yielded a fracture strike of N75$-$85^{o}E

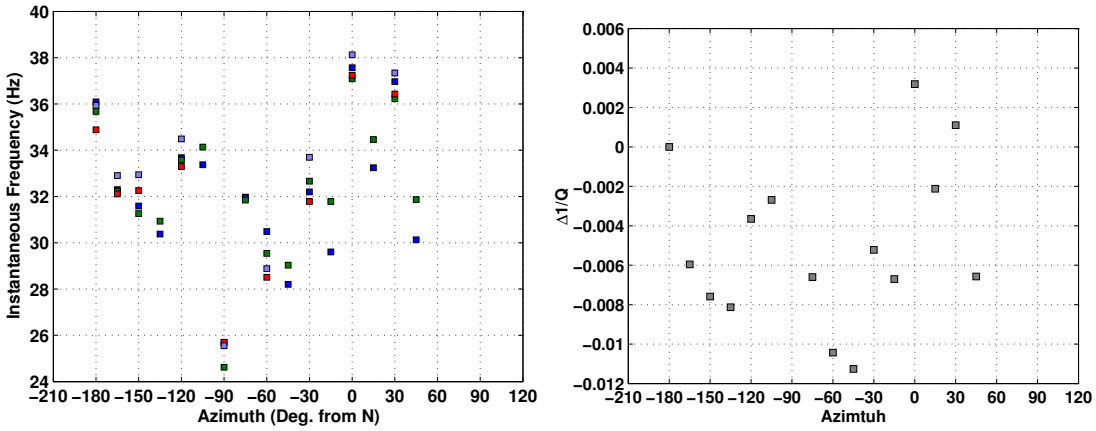

(a) (b)

Figure 8.4: Instantaneous frequency and $\Delta 1/Q$ as a function of azimuth. The data do not reveal any obvious systematic azimuthal variation.

(Horne *et al.*, 2002). Any systematic azimuthal variation in attenuation that is an intrinsic property of the subsurface would be expected to yield a spatially consistent attenuation signature over a certain area, whereas the effects of source instability change with location. In principle, this can be investigated if data acquired at different offsets are available, as it was the case for the Clair VSP analysed in Chapter 5. However, the walkaround VSP data of the Rangely field are only acquired at one offset and therefore do not provide a means to investigate this issue. Since the instability of the source wavelet is likely to have a strong influence on the measured attenuation values I do not consider these quantitative results to provide conclusive arguments for attenuation properties of the subsurface.

I now investigate whether the S-transform and the spectral colour attributes introduced in Chapter 4 give any more insight as to whether the azimuthal anisotropy observed in this data set by Horne *et al.* (2002) changes with frequency. For each source azimuth I compute the S-transform of the time series. Examples of the resulting time-frequency distributions for four different azimuths are given in Fig. 8.5. Again the issue of source instability is very obvious. The amplitude distributions in the time-frequency plane change significantly between azimuths, but not in a systematic way as for the synthetic example given in Appendix B. The frequency ranges where energy is well localized in time also vary between

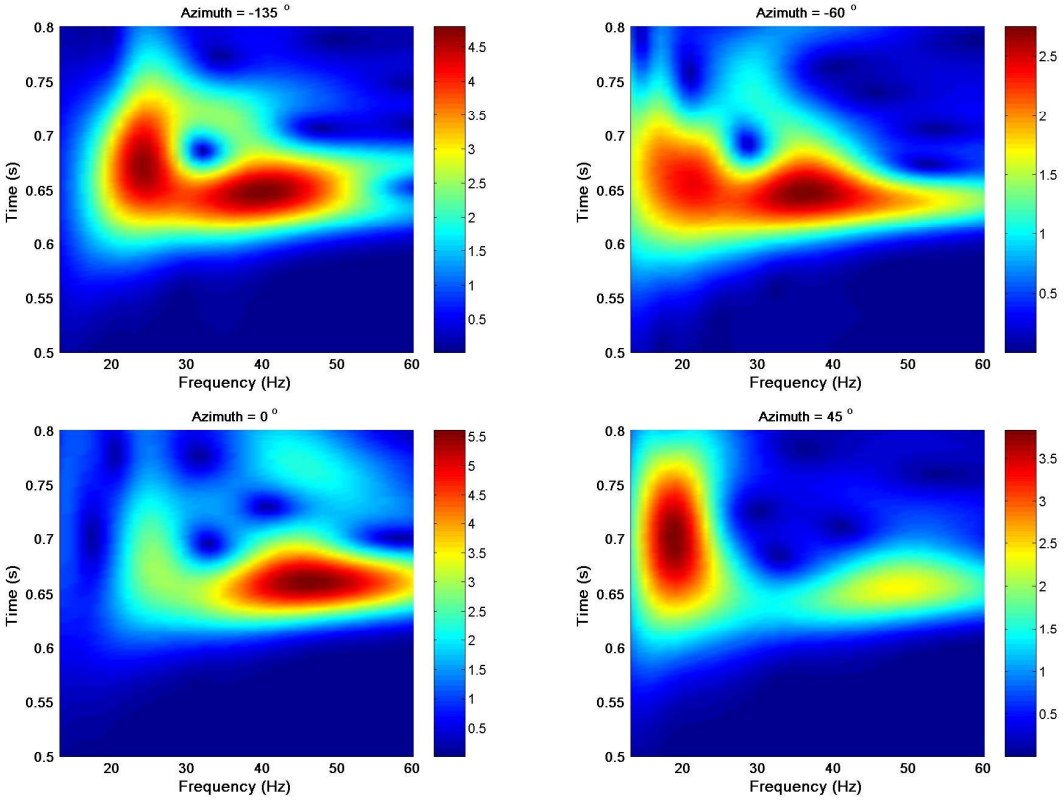

Figure 8.5: Time-frequency plots obtained with the S-transform of the data for different source azimuths. The distribution of amplitudes in the time-frequency plane varies strongly between source locations.

azimuths, and particularly at lower frequencies interference with energy from other arrivals becomes apparent.

In Appendix B I demonstrate with synthetic data how velocity dispersion and frequency-dependent traveltime anisotropy can be measured from the time picks of the maximum amplitudes of the S-transform in the time-frequency plane. For this real data case, however, I do not expect the technique to be robust enough to detect effects of anisotropic velocity dispersion if they were present in the data. This is demonstrated in Fig. 8.6, which shows the results of fitting the $\cos(2\varphi)$-function of Eq. 2.10 at each frequency to the azimuthal variation of the time picks obtained from the S-transform of the data. The inverted parameters C_1 and C_2, which would indicate velocity dispersion and the frequency dependence of azimuthal traveltime anisotropy, do not show any systematic variation with frequency. There is, however, significant azimuthal traveltime anisotropy at all frequencies with a consistent slow direction (i.e. direction of maximum

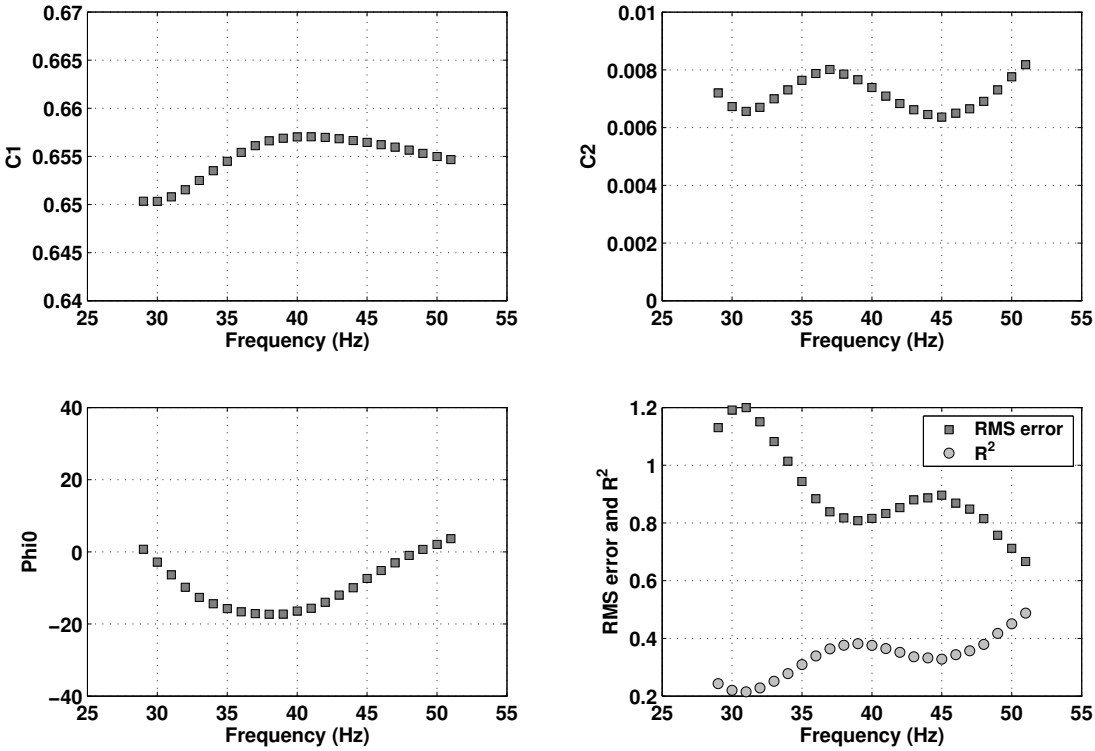

Figure 8.6: Results of fitting a $\cos(2\varphi)$-function to the traveltimes as a function of azimuth at each frequency.

traveltimes) between azimuths of -20^o and 0^o and an average traveltime difference of 14 ms between the symmetry directions. The mean of the traveltime data

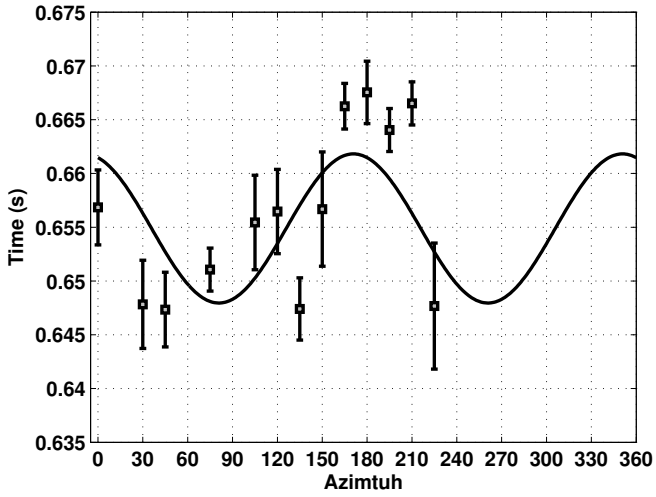

Figure 8.7: Mean of the traveltimes for all frequencies as a function of azimuth and fitted curve.

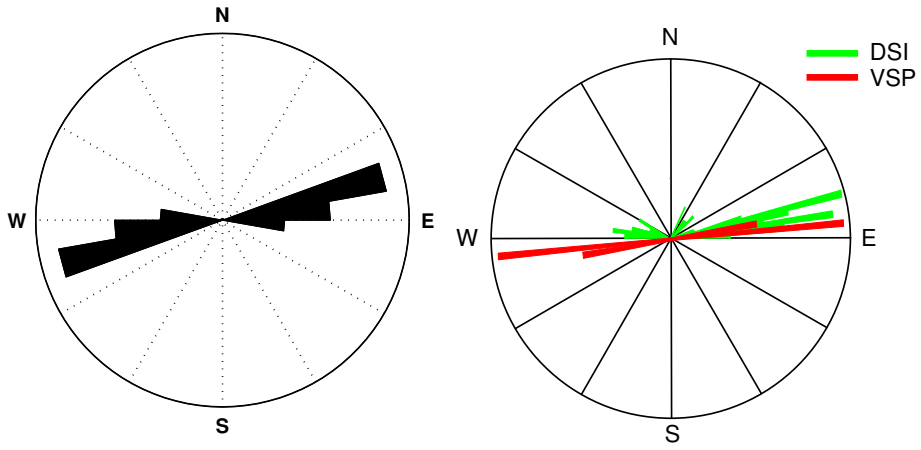

Figure 8.8: Comparison of the fast direction obtained from the azimuthal traveltime analysis (a) with the results from DSI data and converted-wave energy of Horne *et al.* (2002) (b).

computed over all frequencies together with the fitted function are shown in Fig. 8.7. The standard deviations are displayed as error bars.

Fig. 8.8 shows a rose diagram of the inverted azimuths of the fast direction in comparison with the converted-wave splitting and DSI data results of Horne *et al.* (2002). There is excellent agreement between the derived symmetry azimuths, which indicate a fracture strike of N75^o-85^{o}E if the anisotropy is interpreted to be fracture induced. This direction is parallel to the fracture strike reported by Thompson *et al.* (2002) from core measurements.

I now compute a spectral colour image from the S-transform of the data as described in Chapter 4. Since the spectral colour attributes represent average properties of the amplitude spectra, they are less sensitive to the particular shape of the spectra. The spectral colour image of the walkaround data is displayed in Fig. 8.9. The traces are projected onto the horizontal plane along their corresponding source azimuths with time increasing radially from the centre of the image. The display clearly shows that the first-arrival time forms an ellipse in the horizontal plane with the long axis of the ellipse oriented NNW. This again confirms the azimuthal traveltime anisotropy shown in Fig. 8.7. Apart from that, however, it is difficult to see any systematic azimuthal pattern in the image. The

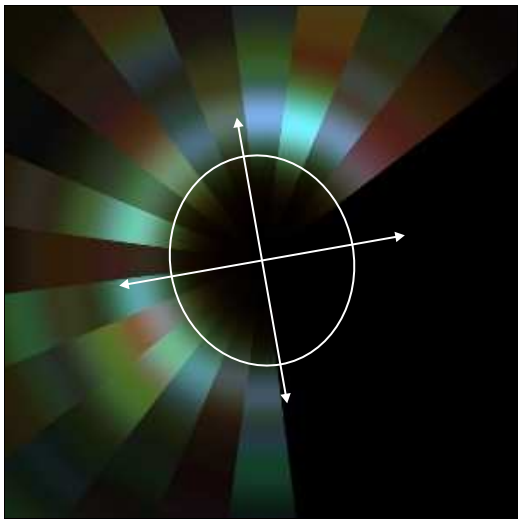

Figure 8.9: Spectral colour display of the walkaround data. The white ellipse indicates the traveltime anisotropy.

colour of the direct-arrival energy changes abruptly from one source azimuth to the other.

An inspection of the spectral colour attributes hue, luminosity and saturation reveals that a separation into these attributes may be more useful in this particular case than the combined image. Fig. 8.10 shows a contour plot of the luminosity of the image and the spectral colour display with hue and saturation set to a

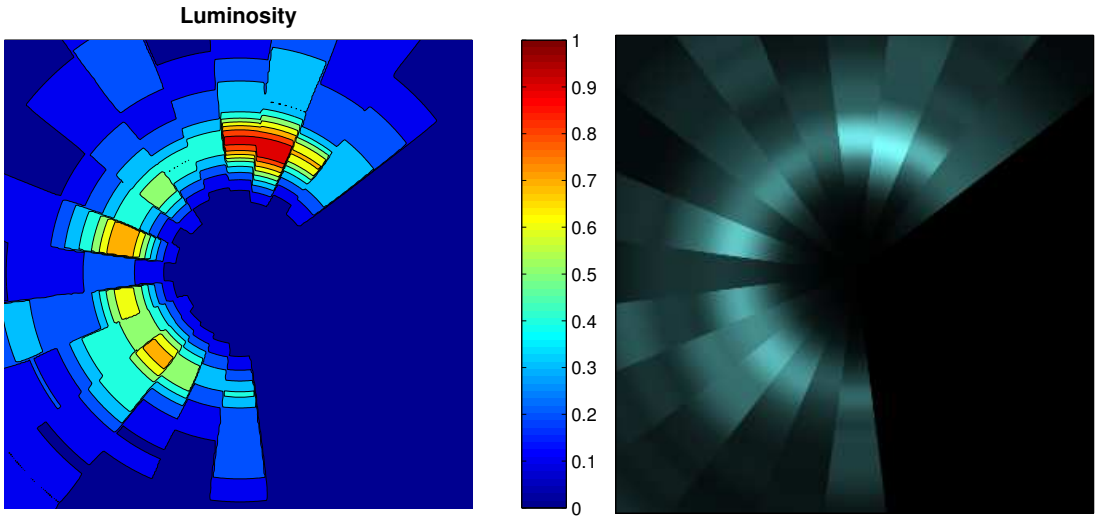

Figure 8.10: Contour plot of the luminosity of the image and the spctral colour display with constant hue and saturation.

constant value. Discarding the anomalous low-amplitude trace at an azimuth of -90^o, the plots indicate that there is some dimming of amplitudes around the direction of maximum traveltimes. The azimuthal variation of the luminosity appears to be less random than any of the other attributes analysed in this section. Nevertheless, the changes between adjacent azimuths are still not gradual across the entire dataset, and the absence of data between the NE and NS directions make it difficult to determine whether the pattern is truly symmetric.

The analyses presented in this section demonstrate that the spectral signature of the direct P-wave arrivals in the walkaround VSP data is severely affected by the instability of the source wavelet. From these data alone it is not possible to draw definite conclusions as to whether the azimuthal anisotropy measured in the traveltimes changes with frequency. In the following section I will investigate whether the converted-wave arrivals in the offset VSP data show any effects of frequency-dependent anisotropy.

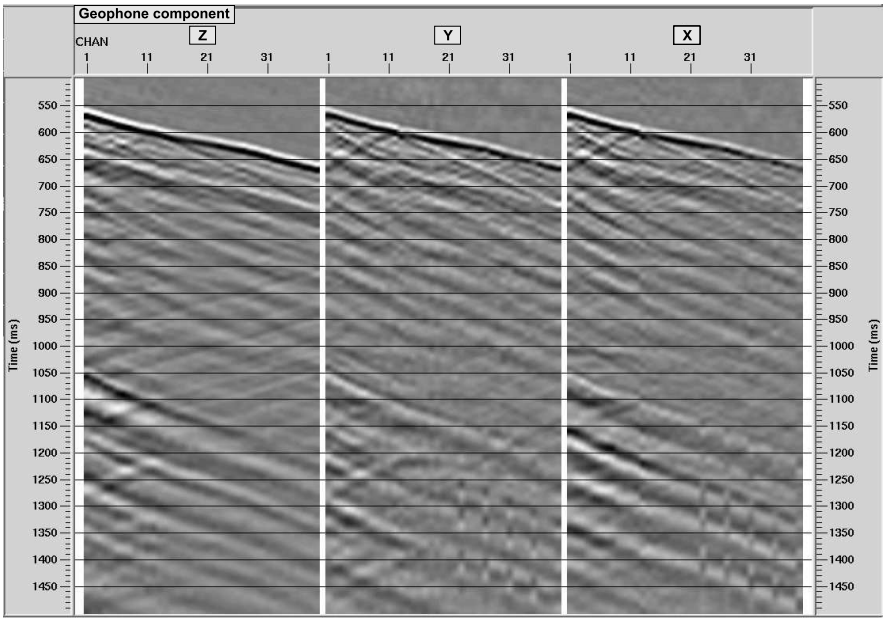

Figure 8.11: Raw three-component data.

8.4 Offset VSP: Spectral signature of converted waves and converted-wave splitting

Fig. 8.11 shows the raw three-component data of the offset VSP. I separate the up- and downgoing wavefields using a dip filter. The downgoing wavefield is displayed in Fig. 8.12. As indicated by the red arrows there are prominent downgoing converted-wave arrivals. The event that arrives at about 730 ms at the lowest receiver is continuous from the depth on where the shear wave is excited ($\sim$ 4800 ft) and only interferes with a P-wave multiple at the deepest receivers. The second converted-wave arrival marked in Fig. 8.12 is less continuous over the logged depth interval and interferes strongly with P-wave energy between depths of 4780 ft and 5530 ft (geophones 10 to 25). A mode conversion from the top of the Weber sandstone, indicated by the green arrow, is also visible, but it is comparatively weak and not clearly separated in time from the direct P-wave arrival. From Fig. 8.11 it is apparent that the upgoing converted-wave energy from reflectors below the reservoir is very weak. I therefore only discuss the analysis of the downgoing wavefield.

I analyse converted-wave splitting using the first converted-wave arrival marked in Fig. 8.12 at the lower 20 geophones in order to confirm the results of Horne

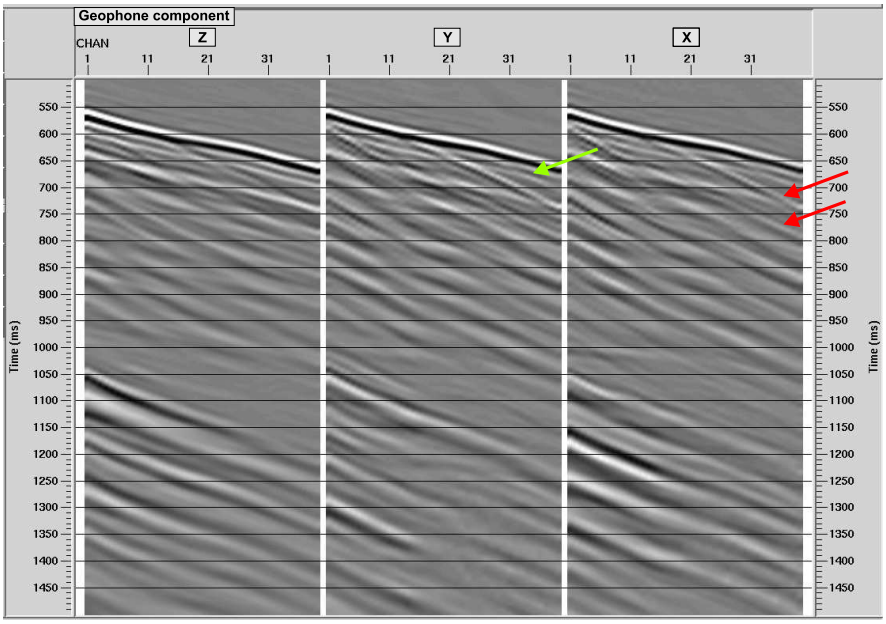

Figure 8.12: Downgoing wavefield. The arrows indicate converted-wave arrivals.

et al. (2002). I use the algorithm of Zeng and MacBeth (1993) discussed in Section 2.4 of Chapter 2 that approximately determines the azimuths of the S1 and S2 polarizations for the case of a single source polarization. The resulting S1 polarization azimuths and time delays are displayed as a function of depth in Fig. 8.13. In good agreement with the findings of Horne *et al.* (2002) the time delay

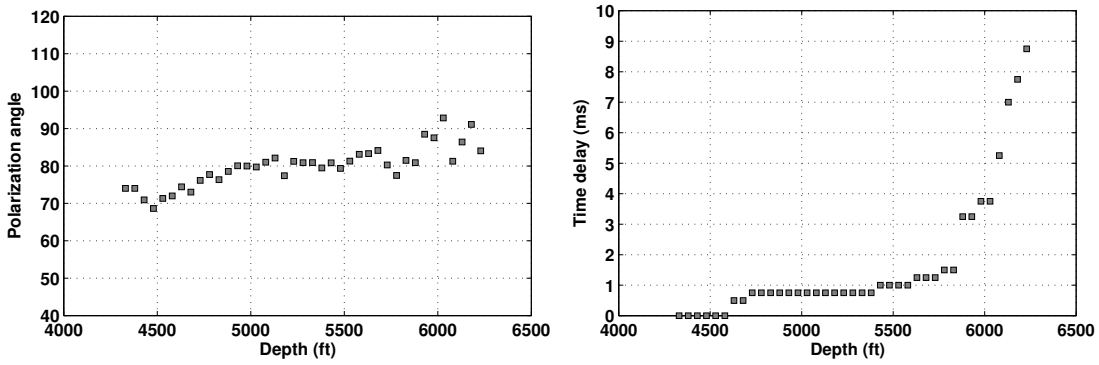

(a) (b)

Figure 8.13: S1 polarization azimuth and time delay between the split converted waves. The time delay shows a steep increase in the reservoir, where the average S1 polarization is N85^{o}E.

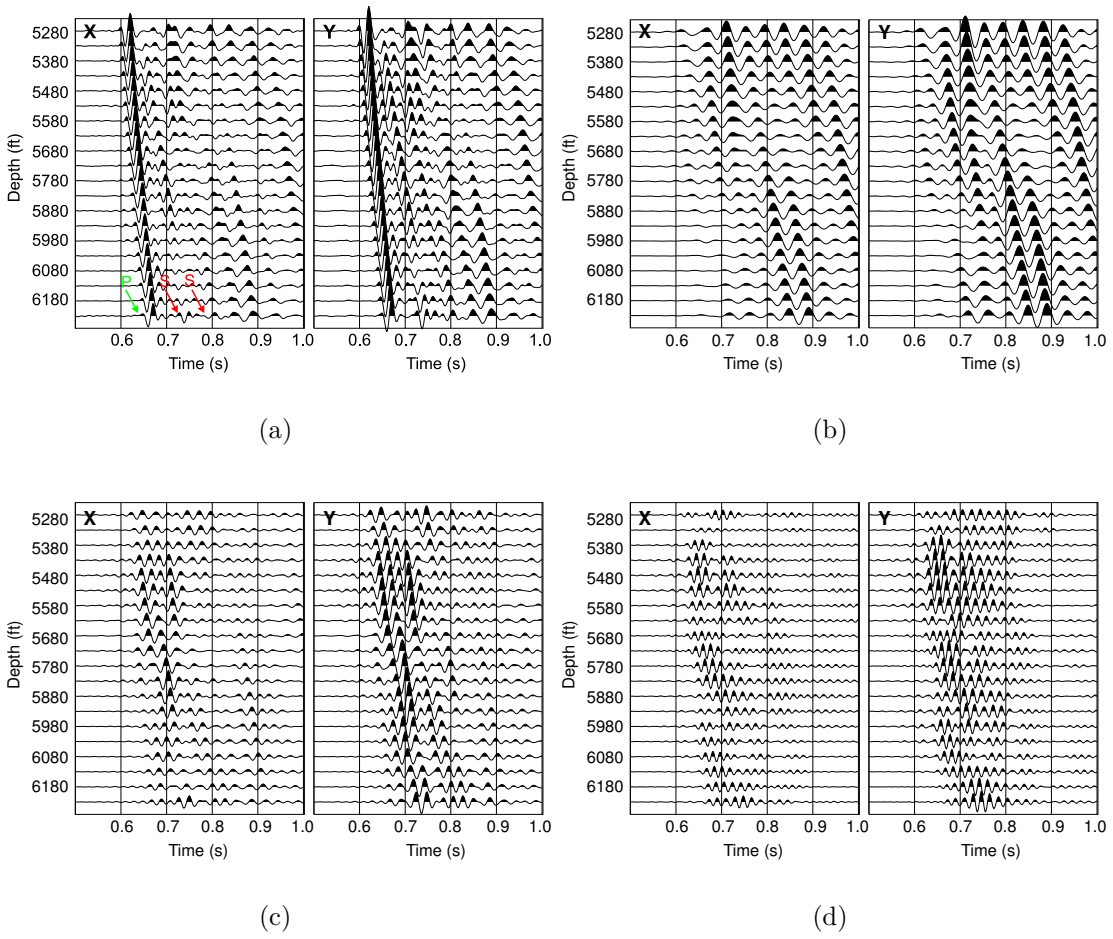

Figure 8.14: Horizontal components of the data of the lower 20 receivers after rotation into the fast (X) and slow (Y) directions and filtering into different frequency bands. a) Full bandwidth; b) 10-30 Hz; c) 30-50 Hz; d) 50-70 Hz.

starts to increase sharply in the reservoir from about 150 ft below the top of the Weber sandstone down to the lowest geophone level at the base of the reservoir. The values are very small above the Weber formation and reach only 1 ms at the reservoir top. The average polarization angle of the fast shear wave in the reservoir is N85^{o}E, which matches the results of shear-wave splitting analysis in the walkaround VSP data from Horne *et al.* (2002) and the fast direction I have derived from P-wave traveltimes in the previous section.

In Chapter 6 I presented an analysis of frequency-dependent shear-wave splitting by measuring the time delay between split shear waves from the rotated data that have been filtered into different frequency bands. I now investigate whether

the same technique can be applied to the converted-wave arrivals in this data set. Fig. 8.14a shows the data of the two horizontal geophone components of the 20 deepest receivers after rotation into the fast (X) and slow (Y) directions at N85^{o}E and N5^{o}W, respectively. It is apparent that at the deepest receiver the first converted-wave arrival is separated in time by only about half a cycle from the direct P-wave and the following converted-wave arrival. The latter is closely followed by another, low-frequency converted-wave event that arrives at around 850 ms at the deepest receiver. The close spacing of arrivals in time with the converted-wave events all containing similar energy poses a problem for the time delay measurements if the data are bandpass filtered. Figs. 8.14 b to d show the X- and Y-components of the data filtered into frequency bands of 10-30 Hz, 30-50 Hz, and 50-70 Hz, respectively. The traces have been windowed, so that the dominant energy of the direct P-wave arrival is attenuated. As discussed in Appendix A the decrease in frequency bandwidth leads to a loss in time resolution. This effect can be seen very clearly in Fig. 8.14: After bandpass filtering the traces show strong ringing and the spread of the energy in time leads to interference between the different arrivals. As a result it is very difficult to locate the converted-wave events seen in the unfiltered data, and in some of the traces the interference effects cause the shear-wave energy to be severely attenuated. In this case, it is therefore not possible to measure accurate time delays as a function of frequency from the bandpass filtered data.

I now compute the S-transform of the X- and Y-component data to investigate whether this approach resolves spectral components of the converted-wave events better in time than the bandpass filtering. Two examples of the resulting amplitude distribution in the time-frequency plane are given in Fig. 8.15. In Appendix A I explain how time-frequency transforms aim to localize signal components well in time and in frequency, but that simultaneous resolution in both domains is always limited by the Heisenberg uncertainty principle. Fig. 8.15 demonstrates that for this particular dataset the S-transform does not completely overcome the time resolution problems of the bandpass filtering discussed above. In Fig. 8.15a, which is the S-transform of the data from the lowest receiver, there are only two distinct areas of energy concentration in the time-frequency plane: One around the first converted-wave arrival, and a low frequency event around the third converted-wave arrival at approximately 850 ms. They both, however, in-

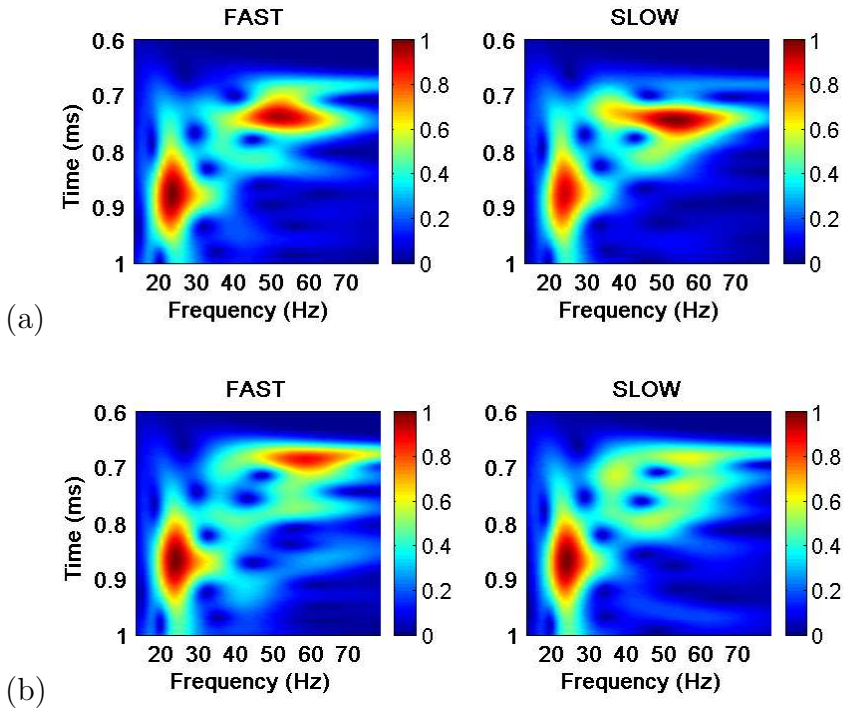

Figure 8.15: Examples of the S-transform of the fast and slow components for two traces recorded in the reservoir. The different converted-wave events are still not clearly separated in time.

terfere with the converted-wave arrival in between, which does not appear as a separate event in the figure. Fig. 8.15b shows the corresponding time-frequency distributions of the traces from the receiver at 6180 ft, which is 100 ft above the lowest geophone. Here it becomes more obvious that there are several arrivals between 700 and 800 ms, but the events are still not fully separated in time. The lack of time resolution in most of the data does not allow a reliable measurement of frequency-dependent differences in arrival times in the time-frequency plane.

Since in this data set I cannot use the change in time delay with frequency as a shear-wave attribute to detect frequency-dependent anisotropy, I analyse the spectral content of the fast and slow converted-wave arrivals. Models describing a squirt-flow mechanism between aligned fractures and matrix porosity predict only velocity dispersion and attenuation of the quasi-shear wave (*see* Chapter 3). The pure shear wave, which is always polarized in the fracture plane, is not affected. If such an effect occurs at seismic frequencies and is present in field data, one would expect to find differential attenuation between the fast and slow

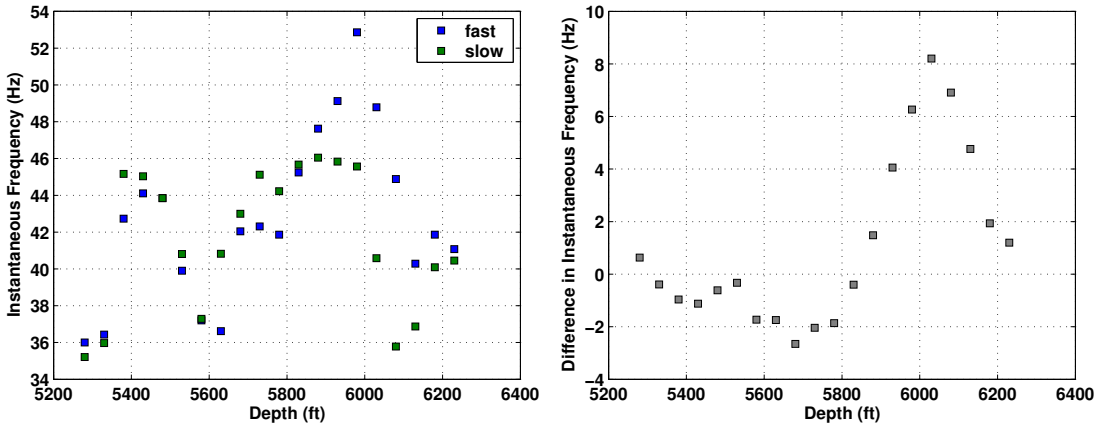

(a) (b)

Figure 8.16: a) Instantaneous frequencies of the fast and slow converted-wave components; b) their difference. Values for the slow converted arrival are lower in the reservoir than the values of the fast one, indicating that it is more attenuated.

shear-wave arrivals with the slow shear-wave energy being more attenuated than the fast one. Whether the Rangely offset VSP shows such an effect is studied in the remainder of the chapter.

I compute the instantaneous frequencies for X- and Y-components at the peak of the amplitude envelope of the first converted-wave arrival at the lower 20 receivers marked in Fig. 8.12. The computed values are displayed in Fig. 8.16a. Fig. 8.16b shows the difference in instantaneous frequencies between the fast and the slow component. The data reveal that in the reservoir from the depth on where the time delay between the split shear waves begins to increase their instantaneous frequencies separate. The slow converted-wave arrival has lower instantaneous frequencies than the fast one, which means that it is attenuated compared to the fast component. The separation in instantaneous frequencies first increases with depth, but then becomes very small again at the deepest receivers, which are close to the base of the reservoir. The effect does not decrease or even disappear if I rotate the data away from the directions of N85^{o}E and N5^{o}W. It is therefore not caused by inaccuracies of separating the fast and slow components through rotation into the symmetry directions.

I seek to confirm with synthetic modelling that fracture-related frequency dependent anisotropy described by a squirt-flow model can produce such a separation

Depth (ft)	Thickness (m)	v_{P} (m/s)	v_{S} (m/s)	ρ (kg/m^3)
950	290	2653	1474	2300
2800	564	3411	1692	2300
4080	390	3603	2002	2300
4950	265	4132	2500	2300
5612	202	4845	3095	2300
5784	52	4482	3033	2400
halfspace	-	4180	2790	2300

Table 8.1: Model parameters used for the synthetic modelling of the VSP data.

of instantaneous frequencies between the fast and slow converted-wave components. I create a synthetic model based on well log data from Horne *et al.* (2002) and velocities derived from the zero-offset VSP. The model parameters are given in Table 8.1. I insert fractures into the halfspace and the layer above according to the model of Chapman (2003). The additional parameters of the fractured dispersive materials are given in Table 8.2. The values for fracture radius a_f and relaxation time τ_m are chosen, so that $\omega\tau_f = 1$. The fractures strike N85^{o}E and are oil-filled. The VSP geometry is the same as in the real data. As a source wavelet I use a Ricker wavelet with a peak frequency of 50 Hz. As in the real data the sample rate is 2 ms.

Fig. 8.17 shows the synthetic traces of the horizontal geophone components after rotation into the fast and slow directions. There are strong converted-wave arrivals at similar times to the real data. The mode conversion at the top of the Weber formation has larger amplitudes than in the real data, and the different converted-wave arrivals are more clearly separated in time in these noise-free

f	50 Hz
ϵ_c	0
ϵ_f	0.08
a_f	1 m
r	0.0001
Φ_p	0.11
k_f	1.41 GPa
τ_m	4 μs

Table 8.2: Parameters of the frequency-dependent fractured materials.

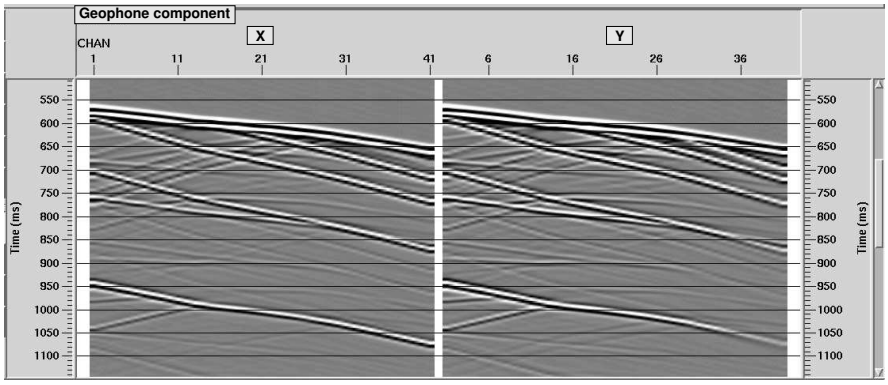

Figure 8.17: X- and Y-component of the synthetic data after rotation into the fast and slow direction, respectively.

synthetic traces. I compute the instantaneous frequencies for the X- and Y-components of the same converted-wave event that I have analysed in the real data. The results are shown in Fig. 8.18. Below the top of the frequency-dependent fractured layer, which is at a depth of 5612 ft, the instantaneous frequencies of the fast and slow components begin to separate, showing that the slow shear wave is attenuated compared to the fast shear wave. The difference in instantaneous frequencies increases steeply with depth over the first 200 ft but then levels off. This result of differential attenuation between the fast and slow shear-wave components is similar to the findings in the real data. The syn-

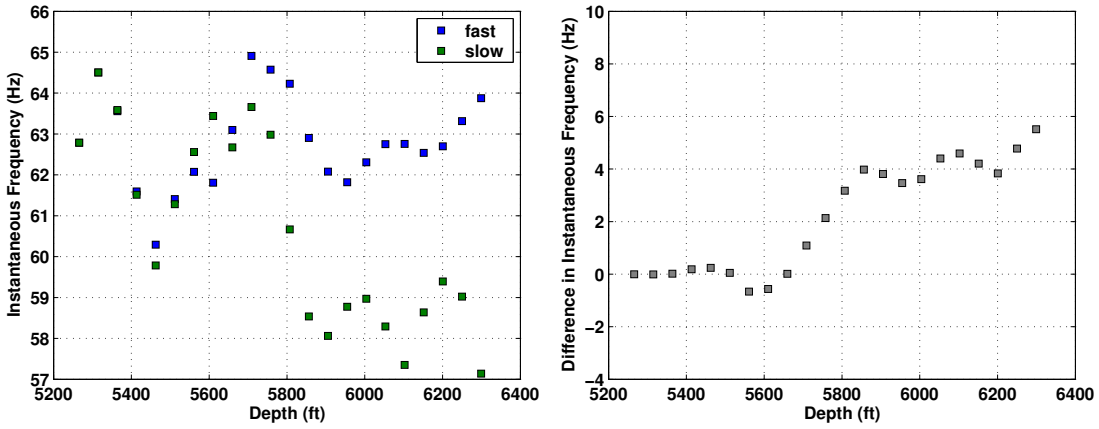

(a) (b)

Figure 8.18: Instantaneous frequencies of the fast and slow converted-wave arrivals of the synthetic data.

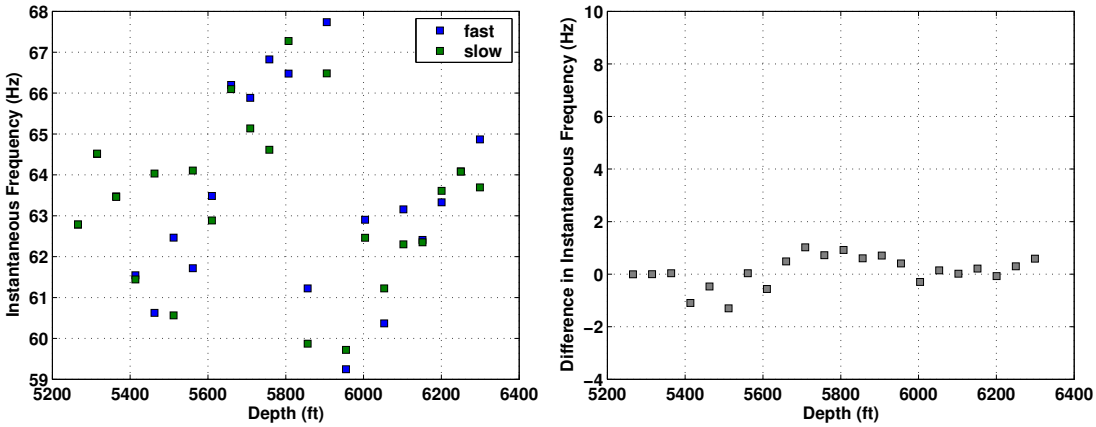

(a) (b)

Figure 8.19: Measured instantaneous frequencies of the fast and slow converted-wave components for a model with a stack of frequency-independent fractured thin layers. There is no difference in instantaneous frequencies between the two components.

thetic modelling also demonstrates that the actual values of the instantaneous frequencies can be quite complicated functions of depth due to local interference with other arrivals. In the real data case we can see from Fig. 8.12 that at the deepest few receivers, where the difference in instantaneous frequencies becomes small again, the converted-wave arrival strongly interferes with a P-wave multiple. These data points are therefore not reliable estimates of the spectral properties of the converted-wave components.

In principle, attenuation of the shear-wave energy could also be caused by multiple scattering from thin layers (e.g. O'Doherty and Anstey, 1971; Schoenberger and Levin, 1978; Marion *et al.*, 1994; Shapiro and Hubral, 1995). I modify the model given in Table 8.1 by replacing the 200 m thick reservoir interval with a stack of thin layers. The thickness of the layers varies between 10 m and 19 m, which is of the order of a quarter of a wavelength. Their properties alternate between the ones of the halfspace given in Table 8.1 and the ones of the layer above. Fractures are inserted in each individual layer according to the model of Hudson (1981), so that the elastic constants are frequency-independent. The results of analysing instantaneous frequencies of the fast and slow converted-wave components from this synthetic data set are displayed in Fig. 8.19. The graphs demonstrate that in this case there is no significant differential attenuation between the split shear

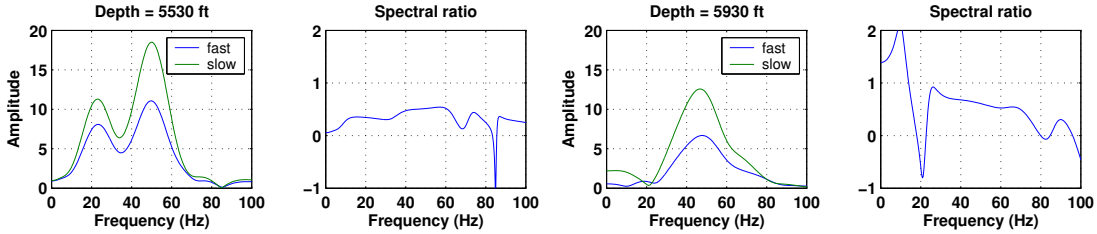

(a) (b)

Figure 8.20: Amplitude spectra of the fast and slow converted-wave components and spectral ratios. a) Above the reservoir; b) within the reservoir.

waves.

The real data result can be further confirmed by computing spectral ratios between the slow and the fast converted-wave components as shown for two receiver levels in Fig. 8.20. The data in Fig. 8.20a are recorded above the reservoir and show that the spectral ratio is more or less flat over the bandwidth of the data. In contrast, for a receiver within the reservoir as shown in Fig. 8.20b, the spectral ratios clearly decrease with increasing frequency, indicating attenuation between the two components. I compute the difference in attenuation $\Delta 1/Q$ between the fast and the slow converted-wave arrivals from the slopes of the spectral ratios. The resulting values are displayed in Fig. 8.21. As the instantaneous frequency

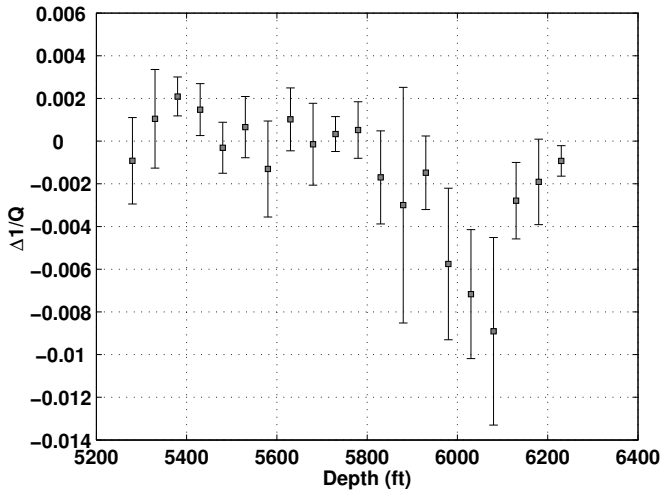

Figure 8.21: Change in attenuation $\Delta 1/Q$ between the fast and the slow shear-wave components measured from the slopes of the spectral ratios.

showed, the slow converted-wave arrival is increasingly more attenuated than the fast one in the reservoir, coinciding with the increase in time delay shown in Fig. 8.13b. Again the differential attenuation becomes small at the deepest receivers where the converted wave interferes with a P-wave multiple.

8.5 Discussion and conclusions

I have measured azimuthal anisotropy in the Weber sandstone reservoir of the Rangely oil field using P-wave traveltimes and shear-wave splitting from a walkaround and an offset VSP. Other data presented in the literature strongly suggest that the anisotropy is fracture-induced. The inferred fast direction matches geological evidence of the dominant fracture orientation in the field (Thompson *et al.*, 2002) and is in excellent agreement with results of Horne *et al.* (2002) of analysing different shear-wave attributes and a DSI log acquired in the same well. The fast direction also agrees with flow corridors in the field determined by rapid well-to-well communication (Thompson *et al.*, 2002) and with the strike of a regional fracture system in the area (Grout and Verbeek, 1985; Kruuskraa *et al.*, 1997; Robertson, 2004).

I have applied several different techniques to analyse the spectral characteristics of P- and converted-wave arrivals in the walkaround and offset VSP data to investigate whether the azimuthal anisotropy shows effects of frequency dependence. The P-wave analysis in the walkaround VSP suffers severely from the instability of the source wavelet, so that definite conclusions as to whether there is any systematic azimuthal variation in attenuation properties in the subsurface cannot be drawn. Quantitative techniques that measure the change in $1/Q$ as a function of azimuth show a large scatter in the derived values, which seems to reflect strong variations in the shape of the spectra due to source instability. Only the spectral colour attributes, which represent average spectral properties, indicate qualitatively that a systematic azimuthal pattern may also be contained in the data. In particular, the luminosity, which measures the average spectral power, shows that amplitudes are somewhat dimmed towards the azimuth of maximum traveltimes, which is normal to the strike of fractures measured from cores in the reservoir.

The analysis of converted-wave arrivals in the offset VSP data provides more in-

sight into the question as to whether there is evidence of frequency-dependent anisotropy. Although the measurement of time delays between split converted waves from the bandpass filtered data fails due to the loss in time resolution, interesting results are obtained by investigating the spectral content of the fast and the slow arrivals. Using two independent methods I find that in the reservoir the slow converted wave is attenuated compared to the fast one, which also coincides with an increase in time delay between the split converted waves.

I demonstrate with synthetic modelling that the effect can be explained by squirt flow between aligned fractures and the matrix porosity. I have also modelled the reservoir as a stack of frequency-independent fractured thin layers, which produced no differential attenuation between the split converted waves. Nevertheless, it remains an open question whether a different choice of layers would cause such an effect. The frequency-independent modelling also demonstrates that the measured differential attenuation is not processing induced.

Although in this particular data set the attenuation of the slow shear wave compared to the fast one is the only useful attribute to detect frequency-dependent anisotropy due to the reasons discussed throughout the chapter, it is another phenomenon that can be related theoretically to anisotropic P-wave attenuation and frequency-dependent shear-wave splitting.

Chapter 9

Conclusions

In this thesis I have analysed a number of VSP data sets from different sedimentary basins with the objective of studying the potential dependence of anisotropy on frequency. The analyses have shown that frequency-dependent anisotropy exists and can be detected in real data. I have found the effect in both P-wave and shear-wave attributes. These are anisotropy of P-wave attenuation, the frequency dependence of the time delay between split shear waves, and attenuation of the slow shear wave compared to the fast one. The three attributes can be theoretically linked, so that the results are consistent with a common theoretical framework and the recognition of each effect supports the observations of the other attributes.

In addition to the real data analyses I have performed forward modelling and reproduced the measurements of frequency-dependent P-wave and S-wave anisotropy on synthetic VSP data. A potential bias of the real data results due to processing effects is a difficult problem to address theoretically. I have therefore used the tests on synthetic data as a pragmatic approach to verify that the techniques I have developed and applied to the field data measure physical effects rather than processing artefacts.

The field data sets studied in this thesis have been acquired over different naturally fractured oil and gas reservoirs. In all cases the symmetry directions I have inferred from the analysis of frequency-dependent anisotropy are consistent with geological evidence of the dominant fracture orientation in the subsurface. Furthermore, they agree with the symmetry directions derived from conventional frequency-independent analyses of seismic anisotropy. The results therefore sug-

gest that the frequency-dependent anisotropic effects are fracture related.
The principal directions of P-wave attenuation anisotropy observed in the walkaround VSP data from the Railroad Gap oilfield are consistent with shear-wave splitting data from the same well, such that the azimuth of minimum attenuation agrees with the polarization direction of the fast shear wave.
For the multi-azimuth walkaway VSP data from the Clair field I have found that P-wave attenuation anisotropy is present in the fractured reservoir but not in the overburden, which is considered to be essentially unfractured. The azimuth of minimum attenuation correlates with the fast direction derived from P-wave traveltimes and polarizations. Moreover, it closely matches the strike of open fractures in the reservoir measured from cores and FMI data in a nearby well. The analyses of the Clair VSP data also revealed that the magnitude of attenuation is significantly higher in the reservoir than in the overburden.
In the near-offset VSP data from the Bluebell-Altamont field, which contains a tight gas reservoir, I have found that the time delay between split shear waves depends on frequency. I have measured a systematic decrease in magnitude of shear-wave anisotropy with increasing frequency in the reservoir section. The S1 polarization is parallel to the strike of fractures in the reservoir as inferred from geological and borehole data as well as surface seismic measurements. The results of the shear-wave splitting analysis indicate that the same effect also occurs in the near surface. However, rock and fluid type in this interval are unknown, so that an interpretation of the near-surface effect is not possible.
The analysis of walkaround and offset VSP data from the Rangely oil field has revealed that there is a difference in spectral signature between split converted waves in the reservoir, such that the slow shear-wave arrivals are attenuated compared to the fast ones. The azimuthal variation of average spectral properties of the P-wave arrivals indicate qualitatively that P-wave attenuation anisotropy might also be present in the data. Again, there is a priori information from previous work and geological data that highlights the correlation of azimuthal anisotropy with the dominant fracture orientation in the reservoir. The same symmetry directions are reflected in the frequency-dependent attributes, which I have analysed in this thesis.
In the 3D VSP data from the San Juan basin I have not found any systematic variation of anisotropy with frequency. However, there is clear evidence of a strong

VTI effect in the data, whereas the fracture-induced azimuthal anisotropy is only weak. Therefore, the results do not contradict an interpretation that relates the frequency-dependent azimuthal anisotropy observed in the other data sets to the presence of vertical aligned fractures, which cause a strong HTI effect rather than VTI symmetry. Nevertheless, the results do not exclude the possibility that in a different case layering-induced polar anisotropy could be found to depend on frequency as well.

In principle, different possible approaches exist that aim to describe frequency-dependent anisotropy with theoretical models. These are based on wave-induced fluid motion in fractured rock (Hudson *et al.*, 1996; van der Kolk *et al.*, 2001; Chapman, 2003; Gurevich *et al.*, 2003) or scattering from ordered heterogeneities (Shapiro and Hubral, 1995; Chesnokov *et al.*, 2001). Since wave propagation in the complex heterogeneous and fluid-saturated media of the Earth's crust cannot be treated exactly, there is no right or wrong approach and a somewhat simplified representation of the subsurface is always required. Significant magnitudes of velocity dispersion and attenuation due to scattering occur if the scale associated with the heterogeneities is of the order of the seismic wavelength. For heterogeneities much smaller than the seismic wavelength equivalent medium theory applies, and large magnitudes of velocity dispersion and attenuation may be explained by wave-induced fluid motion in the porous rock. The fluid and the scattering effect are not truly separate and can be expected to occur simultaneously. Different scales of heterogeneities, such as cracks and fractures, will normally be present in the subsurface and will have an influence on both effects. Furthermore, both the fluid-flow related dispersion as well as the scattering response are sensitive to the type of the saturating fluid. A distinction between the two effects should therefore not be overemphasized, and an approach that attempts to discriminate one from the other may not be helpful. I have rather chosen to follow an approach that emphasises testing the predictive power of one particular theory.

Throughout my thesis I confront an equivalent medium theory, which models dispersion due to squirt flow in fractured porous rock, with the evidence of frequency-dependent anisotropy from the field data sets. The philosophy is essentially based on an interpretation of laboratory results where squirt flow has been recognized to be the dominant mechanism for velocity dispersion and attenuation. The hy-

pothesis is that field data can be interpreted with the same ideas. Considering the squirt-flow effect for seismic field measurements, where fractures that are much larger than the rock samples studied in the laboratory constitute part of the pore space, is therefore a logical extension. Furthermore, the effects can be described by a comparatively simple theory, which allows the evaluation of real data measurements in relation to synthetic modelling results. Studies of the scattering response, in contrast, are currently largely based on numerical forward modelling due to the lack of a theoretical model that can explain fracture-related anisotropic dispersion in the seismic frequency band with realistic parameters (Daley *et al.*, 2002; Nihei *et al.*, 2002; Liu *et al.*, 2004; Willis *et al.*, 2004). The development of a concise, constrainable equivalent medium style model entirely based on the scattering effect poses a significant challenge for theoreticians.

Through the synthetic studies performed in this thesis I have found that the squirt-flow model is consistent with the observations of frequency-dependent anisotropy from the real VSP data sets. It can explain the measured anisotropy in P-wave attenuation, the decrease in magnitude of shear-wave anisotropy with increasing frequency, and the attenuation of the slow shear wave compared to the fast one. Except for the VSP data from the Railroad Gap oil field, the modelling of squirt flow between vertical aligned fractures and the matrix porosity also reproduces the magnitudes of anisotropic dispersion observed in the field data. Furthermore, I found that the sensitivity of the modelled response to fracture scale and fluid type yields results that are consistent with the real data observations. For the Bluebell VSP data, the measured frequency dependence of shear-wave anisotropy could be modelled for fracture lengths of the order of a few metres. The presence of metre-scale fractures in the reservoir is confirmed by geological evidence. For the VSPs from the Clair field, the Bluebell field and the Rangely field frequency-dependent anisotropy always occurs in the gas- or oil-saturated reservoirs. Moreover, the analyses of the Clair field data have shown that regardless of the propagation direction attenuation is much higher in the reservoir than in the overburden. This is consistent with the squirt-flow model in the sense that the theory predicts higher magnitudes of dispersion for the fluid bulk moduli of gas and oil than for water or brine. However, the observations do not represent direct evidence of the fluid effect, which would require measurements from the same rock type that is saturated with different fluids.

The analyses of frequency-dependent anisotropy from the VSP data sets presented in this thesis allow some conclusions to be drawn in terms of of applied techniques and data requirements. If the dispersive effect is small and the noise level in the data high, systematic variations with frequency over the narrow bandwidth of seismic measurements may not exceed the scatter in the data. The technique of estimating frequency-dependent time delays as a linear function of depth, from which the magnitude of anisotropy is inferred, relies on a simple model of an HTI medium. If the data indicate lower symmetry, however, the time delays may be more complicated functions of depth, so that an estimation of the magnitude of anisotropy is not straightforward. The San Juan VSP data represent a case where these complications occur, so that fracture-related frequency-dependent anisotropy, if it was present in the data, could not be detected.

For the P-wave analysis a dense and regular coverage in azimuth is more beneficial than an acquisition geometry with a large number of offsets. The technique relies on the stability of the source wavelet, and lateral homogeneity has to be assumed over the area covered by the source locations. The estimation of frequency-dependent shear-wave parameters is most robust if direct arrivals from orthogonal shear-wave sources are available. The use of converted-wave arrivals, although in principle possible, may be compromised by interference with other events. For measurements of velocity dispersion it is generally more accurate to determine relative shifts in time using a cross-correlation technique rather than picking absolute arrival times. This is independent of whether the changes with frequency are evaluated by bandpass filtering or by applying a time-frequency transform. Similarly, measurements of attenuation anisotropy are more reliable if relative changes in attenuation with propagation direction are determined instead of estimating absolute values of Q. As discussed in this thesis, attenuation measurements may be very inaccurate due to multiple scattering in a layered medium. Relative changes in attenuation as a function of azimuth, however, will be less sensitive to this effect if the medium can be considered to be laterally homogeneous.

Although I have developed a number of different methods throughout this thesis to measure effects of frequency-dependent anisotropy, it is not a comprehensive study of the merits and limitations of possible techniques. In particular, the use of time-frequency transforms is a broad field that could be the subject of

further investigations. In my thesis I have used the S-transform to compute spectral colour attributes, which served as a simple and robust approach to detect frequency-dependent anisotropy and describe it qualitatively. The potential quantitative use of the spectral colour attributes and the S-transform, as well as the performance of other time-frequency transforms for the purpose of analysing frequency-dependent anisotropy would be interesting areas of future work. It is also open to question as to whether in this analysis time-frequency transforms are generally superior to techniques involving the Fourier transform, such as estimating anisotropy from bandpass filtered data. Similarly, the methods of measuring attenuation can possibly be refined. Various approaches have been proposed in the literature to improve spectral ratio estimates, such as the multitaper technique (Park *et al.*, 1987; Neep, 1995; Wang, 2003) or the estimation of Q from the minimum phase equivalent of a given wavelet (Taner and Treitel, 2003). Furthermore, both real data and synthetic studies could be complemented by sensitivity analyses. These include the sensitivity of the relaxation time to variations in parameters used in its derivation, the resulting uncertainties of inverted fracture sizes and fracture densities, the sensitivity of derived attenuation values to errors in measured instantaneous frequencies, and uncertainties in estimated shear-wave splitting parameters.

The fact that I have found frequency-dependent anisotropy in several VSP data sets that can be related to fracturing in subsurface reservoirs and modelled with a consistent theory suggests that it is worthwhile to extend the work to the analysis of surface seismic data. This would require a modification of the techniques I have applied in this thesis according to different acquisition geometries of reflection seismic data and a thorough investigation of possible processing effects. Of particular interest for the study of frequency-dependent anisotropy in surface seismic data would be the analysis of the reflected wavefield and AVO signatures (Chapman and Liu, 2004; Chapman *et al.*, 2005).

It may be worthwhile to compare forward modelling results of the scattering response in more detail to the modelled effects of wave-induced fluid motion. The spatial pattern of attenuation, for example, may be different and offer possibilities to discriminate between the two effects. Furthermore, time lapse data acquired over fractured reservoirs could provide means to study the effects of changes in the saturating fluid on the frequency dependence of anisotropy. If frequency-

dependent anisotropy can be identified as a time lapse attribute and related to the fluid effect, it may also serve as a predictive tool to differentiate between pressure and fluid changes in subsurface reservoirs.

References

Aki, K. and Richards, P.G., 2002. *Quantitative Seismology*. University Science Books, 2nd edn.

Alford, R.M., 1986. Shear data in the presence of azimuthal anisotropy. In *56th Ann. Internat. Mtg., Expanded Abstracts*, 476–479, Soc. of Expl. Geophys.

Allen, P.A. and Mange-Rajetzky, M.A., 1992. Devonian-Carboniferous sedimentary evolution of the Clair area, offshore northwestern UK: Impact of changing provenance. *Marine and Petroleum Geology*, **9**, 29–52.

Backus, M., 1962. Long-wave elastic anisotropy produced by horizontal layering. *Journal of Geophysical Research*, **67**, 4427–4440.

Bakulin, A., Grechka, V. and Tsvankin, I., 2000a. Estimation of fracture parameters from reflection seismic data - Part I: HTI model due to a single fracture set. *Geophysics*, **65**, 1788–1802.

Bakulin, A., Grechka, V. and Tsvankin, I., 2000b. Estimation of fracture parameters from reflection seismic data - Part II: Fractured models with orthorhombic symmetry. *Geophysics*, **65**, 1803–1817.

Bakulin, A., Grechka, V. and Tsvankin, I., 2000c. Estimation of fracture parameters from reflection seismic data - Part III: Fractured models with monoclinic symmetry. *Geophysics*, **65**, 1818–1830.

Barnes, A.E., 1991. Instantaneous frequency and amplitude at the envelope peak of a constant-phase wavelet. *Geophysics*, **56**, 1058–1060.

Barnes, A.E., 1993. When the concepts of spectral frequency and instantaneous frequency converge. *The Leading Edge*, **12**, 1020–1023.

Bates, C.R., Lynn, H.B., Hoekstra, P., Simone, M.K. and Phillips, D.R., 1995. Fracture detection, mapping, and analysis of naturally fractured gas reservoirs using seismic technology. Tech. Rep. Contract No. DE-AC21-92MC28135, US Department of Energy.

Bath, M., 1974. *Spectral Analysis in Geophysics*. Elsevier, Amsterdam.

Berryman, J.G., 1979. Long-wave elastic anisotropy in transversely isotropic media. *Geophysics*, **44**, 896–917.

Berryman, J.G., 1980. Long-wavelength propagation in composite elastic media. *Journal of the Acoustical Society of America*, **68**, 1809–1831.

Biot, M.A., 1956. Theory of propagation of elastic waves in a fluid-saturated porous solid. I. low frequency range and II. higher frequency range. *Journal of the Acoustical Society of America*, **28**, 168–191.

Bird, P., 1998. Kinematic history of the Laramide orogeny in latitudes 35^o-49^oN, western United States. *Tectonics*, **17**, 780–801.

Bourbié, T., Coussy, O. and Zinszner, B., 1987. *Acoustics of Porous Media*. Gulf Publishing Co., Houston.

Bracewell, R., 1965. *The Fourier transform and its applications*. McGraw-Hill Book Co., New York.

Brown, R. and Korringa, J., 1975. On the dependence of the elastic properties of a porous rock on the compressibility of the pore fluid. *Geophysics*, **40**, 608–616.

Brown, R.L. and Seifert, D., 1997. Velocity dispersion: A tool for characterizing reservoir rocks. *Geophysics*, **62**, 477–486.

Brown, R.L., Wiggins, M. and Gupta, A., 2000. Fracture roughness: The key to relating seismic velocities, seismic attenuation and permeability to reservoir pressure and saturation. In *70th Ann. Internat. Mtg., Expanded Abstracts*, Soc. of Explor. Geophys.

Bush, I. and Crampin, S., 1991. Paris Basin VSPs: Case history establishing combinations of fine-layer (or lithologic) anisotropy and crack anisotropy from modelling shear wavefields near point singularities. *Geophysical Journal International*, **107**, 433–447.

Buttkus, B., 1991. *Spektralanalyse und Filtertheorie*. Springer Verlag, Berlin.

Chapman, M., 2001. *Modelling the wide-band laboratory response of rock samples to fluid and pressure changes*. Ph.D. thesis, University of Edinburgh.

Chapman, M., 2003. Frequency dependent anisotropy due to meso-scale fractures in the presence of equant porosity. *Geophysical Prospecting*, **51**, 369–379.

Chapman, M. and Liu, E., 2003. The frequency dependent azimuthal AVO response of fractured rock. In *73rd Ann. Internat. Mtg., Expanded Abstracts*, 105–108, Soc. of Explor. Geophys.

Chapman, M. and Liu, E., 2004. Frequency dependent azimuthal amplitude variations in reflections from a fractured layer. In *74th Ann. Internat. Mtg., Expanded Abstracts*, Soc. of Explor. Geophys.

Chapman, M., Zatsepin, S.V. and Crampin, S., 2002. Derivation of a microstructural poroelastic model. *Geophysical Journal International*, **151**, 427–451.

Chapman, M., Maultzsch, S., Liu, E. and Li, X.Y., 2003. The effect of fluid saturation in an anisotropic multi-scale equant porosity model. *Journal of Applied Geophysics*, **54**, 191–202.

Chapman, M., Liu, E. and Li, X.Y., 2005. Modelling the effect of frequency dependent anisotropy on azimuthal AVO analysis. In *67th Ann. Internat. Mtg., Expanded Abstracts*, submitted, Eur. Assn. Geosci. Eng.

Chen, W., 1995. *AVO in azimuthally anisotropic media. Fracture detection using P-wave data and a seismic study of naturally fractured tight gas reservoirs*. Ph.D. thesis, Stanford University.

Cheng, H.C., Toksöz, M.N. and Willis, M.E., 1982. Determination of in situ attenuation from full waveform acoustic logs. *Journal of Geophysical Research*, **87**, 5477–5484.

Chesnokov, E., Queen, J., Vichorev, A., Lynn, H., Hooper, J., Bayuk, I., Castagna, J. and Roy, B., 2001. Frequency dependent anisotropy. In *71st Ann. Internat. Mtg., Expanded Abstracts*, 2120–2123, Soc. of Expl. Geophys.

Chu, P., 1996. The S-transform for obtaining localized spectra. *MTS Journal*, **4**, 28–38.

Clark, R.A., Carter, A.J., Nevill, C., P. and Benson, P.M., 2001. Attenuation measurements from surface seismic data: azimuthal variation and time-lapse case studies. In *63rd Ann. Internat. Mtg., Expanded Abstracts*, L–28, Eur. Assn. Geosci. Eng.

Coney, D., Fyfe, T.B., Retail, P. and Smith, P.J., 1993. Clair appraisal: the benefits of a co-operative approach. In *Petroleum Geology of Northwest Europe: Proceedings of the 4th Conference*, 1409–1420, The Geological Society, London.

Cosgrove, J.W., 1998. The role of structural geology in reservoir characterization. In M.P. Coward, T.S. Daltaban and H. Johnson, eds., *Structural Geology in Reservoir Characterization*, vol. 127, 1–13, Geol. Soc. Spec. Publ.

Coyner, K. and Cheng, C.H., 1984. New laboratory measurements of seismic velocities in porous rocks. In *54th Ann. Internat. Mtg., Expanded Abstracts*, Session: RP.6, Soc. of Explor. Geophys.

Crampin, S., 1981. A review of wave motion in anisotropic and cracked elastic media. *Wave Motion*, **3**, 343–391.

Crampin, S., 1985. Evaluation of anisotropy by shear-wave splitting. *Geophysics*, **50**, 142–152.

Crampin, S., 1987. Geological and industrial applications of extensive dilatancy anisotropy. *Nature*, **328**, 491–496.

Crampin, S., 1991. Effects of singularities on shear-wave propagation in sedimentary basins. *Geophysical Journal International*, **107**, 531–543.

Crampin, S. and Lovell, J., 1991. A decade of shear-wave splitting in the Earth's crust: What does it mean? What use can we make of it? And what should we do next? *Geophysical Journal International*, **107**, 387–407.

Daley, T., Myer, L., Queen, J., Fortuna, M., Murphy, J., Coates, R., Nihei, K. and Majer, E., 2002. Numerical modeling of scattering from discrete fracture zones in a San Juan Basin gas reservoir. In *72nd Ann. Internat. Mtg., Expanded Abstracts*, 109–112, Soc. of Expl. Geophys.

Dasgupta, R. and Clark, R.A., 1998. Estimation of Q from surface seismic reflection data. *Geophysics*, **63**, 2120–2128.

Dasios, A., Astin, T.R. and McCann, C., 2001. Compressional-wave Q estimation from full-waveform sonic data. *Geophysical Prospecting*, **49**, 353–373.

De, G.S., Winterstein, D.F. and Meadows, M.A., 1994. Comparison of P- and S-wave velocities and Q's from VSP and sonic log data. *Geophysics*, **59**, 1512–1529.

Dellinger, J.A., Nolte, B. and Etgen, J.T., 2001. Alford rotation, ray theory, and crossed-dipole geometry. *Geophysics*, **66**, 637–647.

Dvorkin, J. and Nur, A., 1993. Dynamic poroelasticity: A unified model with the squirt and the Biot mechanisms. *Geophysics*, **58**, 524–533.

Dvorkin, J., Mavko, G. and Nur, A., 1995. Squirt flow in fully saturated rocks. *Geophysics*, **60**, 97–107.

Endres, A.L. and Knight, R.J., 1997. Incorporating pore geometry and fluid pressure communication into modeling the elastic behavior of porous rocks. *Geophysics*, **62**, 106–117.

Engelhard, L., 1986. Determination of the attenuation of seismic waves from actual field data, as well as considerations to fundamental questions from model and laboratory measurements. In H. Burkhardt, J. Paffenholz and R. Schütt, eds., *Absorption Seismischer Wellen, DGMK Forschungsbericht 254*, pp. 83–119, Deutsche Wiss. Gesellschaft für Erdöl, Erdgas und Kohle, Hamburg.

Engelhard, L., 1996. Determination of seismic-wave attenuation by complex trace analysis. *Geophysical Journal International*, **125**, 608–622.

Engelhard, L., Gross, T. and Neupert, F., 1984. Determination of in-situ attenuation from full waveform acoustic logs - comment. *Journal of Geophysical Research*, **89**, 3400–3402.

Eshelby, J.D., 1957. The determination of the elastic field of an ellipsoidal inclusion, and related problems. *Proceedings of the Royal Society of London*, **A241**, 376–396.

Gabor, D., 1946. Theory of communications. *J. Inst. Elec. Eng.*, **93**, 429–457.

Gaiser, J., 2000. 3D PS-wave data - unraveling shearwave birefringence for fracture detection. In *62nd Ann. Internat. Mtg., Expanded Abstracts*, Session: C0015, Eur. Assn. Geosci. Eng.

Gardner, G.H.F., Wyllie, M.R.J. and Droschak, D.M., 1964. Effects of pressure and fluid saturation on the attenuation of elastic waves in sands. *Journal of Petroleum Technology*, **16**, 189–198.

Gassmann, F., 1951. Über die Elastizität poröser Medien. *Vierteljahresschr. der Naturforsch. Ges. Zürich*, **96**, 1–21.

Geertsma, J., 1961. Velocity-log interpretation: The effect of rock bulk compressibility. *Journal of the Society of Petroleum Engineers*, **1**, 235–248.

Goldberg, D., Moos, D. and Anderson, R.J., 1985. Attenuation changes due to diagenesis in marine sediments. In *26th Ann. Logging Symp.*, paper: KK, Soc. Prof. Well Log Analysts.

Gray, D. and Head, K., 2000. Fracture detection in Manderson field: A 3-D AVAZ case history. *The Leading Edge*, **19**, 1214–1221.

Grechka, V. and Tsvankin, I., 1998. 3-D description of normal moveout in anisotropic inhomogeneous media. *Geophysics*, **63**, 1079–1092.

Grout, M.A. and Verbeek, E.R., 1985. Fracture history of the Plateau Creek and adjacent Colorado River valleys, southern Piceance Creek basin - Implications for predicting joint patterns at depth. Open File Report 85-744, US Department of Energy.

Gurevich, B., Brajanovki, M. and Brown, L., 2003. Theory for fluid substitution in porous fractured reservoirs. In *Proceedings of the 6th SEGJ International Symposium*, 1–8, SEGJ.

Hackert, C.L., Parra, J.O., Brown, R.L. and Collier, H.A., 2001. Characterization of dispersion, attenuation and anisotropy at the Buena Vista Hills field, California. *Geophysics*, **66**, 90–96.

Hall, S.A. and Kendall, J.M., 2003. Fracture characterization at Valhall: Application of P-wave amplitude variation with offset and azimuth AVOA analysis to a 3D ocean-bottom data set. *Geophysics*, **68**, 1150–1160.

Hamilton, E.L., 1972. Compressional wave attenuation in marine sediments. *Geophysics*, **37**, 620–646.

Han, D.H., 1986. *Effects of Porosity and Clay Content on Acoustic Properties of Sandstones and Unconsolidated Sediments*. Ph.D. thesis, Stanford University.

Hauge, P.S., 1981. Measurements of attenuation from vertical seismic profiles. *Geophysics*, **46**, 1548–1558.

Heffner, T.A. and Barrow, K.T., 1992. *Giant Oil and Gas Fields, Structural Traps VII*, chap. Rangely Field - U.S.A., Uinta / Piceance Basins, Colorado, pp. 29–56. AAPG Treatise on Petroleum Geology.

Helbig, K., 1984. Kinds of anisotropy and possible causes. In *54th Ann. Internat. Mtg., Expanded Abstracts*, Session: W4.2, Soc. of Expl. Geophys.

Helbig, K., 1994. *Foundations of elastic anisotropy in exploration seismics*. Handbook of Geophysical Exploration, Seismic Exploration, Pergamon Press.

Horne, S. and MacBeth, C., 1997. AVA observations in walkaround VSPs. In *67th Ann. Internat. Mtg., Expanded Abstracts*, 290–293, Soc. of Expl. Geophys.

Horne, S.A., 2003. Fracture characterization from walkaround VSPs. *Geophysical Prospecting*, **51**, 493–499.

Horne, S.A., McGarrity, J.P., Sayers, C.M., Smith, R.L. and Wijnands, F., 1998. Fractured reservoir characterization using multi-azimuthal walkaway VSPs. In *68th Ann. Internat. Mtg., Expanded Abstracts*, 1640–1643, Soc. of Expl. Geophys.

Horne, S.A., Thompson, C., Moran, R., Walsh, J., Hyde, J. and Liu, E., 2002. Planning, acquiring and processing a walkaround VSP for fracture induced anisotropy. In *64th Ann. Internat. Mtg., Expanded Abstracts*, B028, Eur. Assn. Geosci. Eng.

Hudson, J.A., 1981. Wave speeds and attenuation of elastic waves in material containing cracks. *Geophysical Journal of the Royal Astronomical Society*, **64**, 133–150.

Hudson, J.A., 1994. Overall properties of materials with inclusions or cavities. *Geophysical Journal International*, **117**, 555–561.

Hudson, J.A. and Crampin, S., 2003. Comment on: 'The 3D shear experiment over the Natih field in Oman: The effect of fracture-filling fluids on shear propagation' by C.M. van der Kolk, W.S. Guest and J.H.H.M. Potters. *Geophysical Prospecting*, **51**, 365–368.

Hudson, J.A., Liu, E. and Crampin, S., 1996. The mechanical properties of materials with interconnected cracks and pores. *Geophysical Journal International*, **124**, 105–112.

Hudson, J.A., Pointer, T. and Liu, E., 2001. Effective medium theories for fluid saturated materials with aligned cracks. *Geophysical Prospecting*, **49**, 509–522.

Ikelle, L.T., 1997. Parameterization of AVAZ (Amplitude variation with AZimuth) inversion. *Journal of Seismic Exploration*, **6**, 19–34.

Johnston, D.H., 1981. Attenuation: A state-of-the-art summary. In M.N. Toksöz and D.H. Johnston, eds., *Seismic Wave Attenuation*, Geophysics reprint series, 123–135, Soc. of Expl. Geophys.

Johnston, D.H. and Toksöz, M.N., 1980. Ultrasonic P and S wave attenuation in dry and saturated rocks under pressure. *Journal of Geophysical Research*, **85**, 925–936.

Johnston, D.H., Toksöz, M.N. and Timur, A., 1979. Attenuation of waves in dry and saturated rocks: II. Mechanisms. *Geophysics*, **44**, 691–711.

Jones, D.J., 1986. Pore fluids and frequency-dependent wave propagation in rocks. *Geophysics*, **51**, 1939–1953.

Kan, T.K., Batzle, M.L. and Gaiser, J.E., 1983. Attenuation measured from VSP: Evidence of frequency-dependent Q. In *Expanded Abstracts*, Session S23.2, SEG.

Kelder, O. and Smeulders, D.M.J., 1997. Observation of the Biot slow wave in water-saturated Nievelsteiner sandstone. *Geophysics*, **62**, 1794–1796.

King, M.S., 1966. Wave velocities in rocks as a function of changes in overburden pressure and pore fluid saturants. *Geophysics*, **31**, 50–73.

Klimentos, T. and McCann, C., 1988. Why is the Biot slow wave not observed in real rocks? *Geophysics*, **53**, 1605–1609.

Knopoff, L., 1964. Q. *Reviews of Geophysics*, **2**, 625–660.

Kruuskraa, V., Decker, D. and Squires, S., 1997. Naturally fractured tight gas reservoir detection optimization. Summary Report prepared by Advanced Resources International Inc., DOE Contract No. DE-AC21-93MC30086, US Department of Energy, Morgantown Energy Technology Center.

Lefeuvre, F. and Mandal, B., 1991. Fracture evaluation using a 3-D propagator matrix method. In *61th Ann. Internat. Mtg., Expanded Abstracts*, 1628–1632, Soc. of Expl. Geophys.

Li, X.Y., 1999. Fracture detection using azimuthal variation of P-wave moveout from orthogonal seismic survey lines. *Geophysics*, **64**, 1193–1201.

Li, X.Y. and Crampin, S., 1993. Linear-transform techniques for processing shear-wave anisotropy in four-component seismic data. *Geophysics*, **58**, 240–256.

Li, X.Y., Wei, X., Maultzsch, S., Liu, E., Chapman, M. and Fowler, S., 2004. An integrated study of Clair 4C and VSP data for fracture detection. Annual research report Volume 11, EAP, pp. C1:1-30.

Liu, E., Crampin, S., Queen, J.H. and Rizer, W.D., 1993a. Behaviour of shear waves in rocks with two sets of parallel cracks. *Geophysical Journal International*, **113**, 509–517.

Liu, E., Crampin, S., Queen, J.H. and Rizer, W.D., 1993b. Velocity and attenuation anisotropy caused by microcracks and macrofractures in a multiazimuth reverse VSP. *Canadian Journal of Exploration Geophysics*, **29**, 177–188.

Liu, E., Hudson, J.A. and Pointer, T., 2000. Equivalent medium representation of fractured rock. *Journal of Geophysical Research*, **105**, 2981–3000.

Liu, E., Queen, J.H., Li, X.Y., Chapman, M., Maultzsch, S., Lynn, H.B. and Chesnokov, E.M., 2003. Observation and analysis of frequency-dependent anisotropy from a multicomponent VSP at Bluebell-Altamont Field, Utah. *Journal of Applied Geophysics*, **54**, 319–333.

Liu, E., Vlastos, S., Li, X.Y., Main, I.G. and Schoenberg, M., 2004. Modelling seismic wave propagation during fluid injection in a fractured network: Effects of pore fluid pressure on time-lapse seismic signatures. *The Leading Edge*, **23**, 778–783.

Liu, Y.J., 2003. *Analysis of P-wave Seismic Reflection Data for Azimuthal Anisotropy*. Ph.D. thesis, University of Edinburgh.

Lockner, D., Walsh, J.B. and Byerlee, J., 1977. Changes in seismic velocity and attenuation during deformation of granite. *Journal of Geophysical Research*, **82**, 5374–5378.

Lorenz, J.C. and Cooper, S.P., 2003. Tectonic setting and characteristics of natural fractures in Mesaverde and Dakota reservoirs of the San Juan Basin. *New Mexico Geology*, **25**, 3–14.

Lorenz, J.C., Warpinski, N.R. and Teufel, L.W., 1996. Natural fracture characteristics and effects. *The Leading Edge*, **15**, 909–911.

Lucet, N. and Zinszner, B., 1992. Effects of heterogeneities and anisotropy on sonic and ultrasonic attenuation in rocks. *Geophysics*, **57**, 1018–1026.

Lynn, H.B., 1996. A geophysicist's view on seismic anisotropy. In J.S. Rathore, ed., *Seismic Anisotropy*, 1–14, Soc. of Explor. Geophys.

Lynn, H.B., 2004. The winds of change: Anisotropic rocks - their preferred direction of fluid flow and their associated seismic signatures - Part II. *The Leading Edge*, **23**, 1258–1268.

Lynn, H.B., Beckham, W.E., Simon, K.M., Bates, C.R., Layman, M. and Jones, M., 1999. P-wave and S-wave azimuthal anisotropy at a naturally fractured gas reservoir, Bluebell-Altamont field, Utah. *Geophysics*, **64**, 1312–1328.

MacBeth, C., 1999. Azimuthal variation in P-wave signatures due to fluid flow. *Geophysics*, **64**, 1181–1192.

Majer, E.L., Queen, J.H., Daley, T.M., Murphy, J., Fortuna, M., Lynn, H., Coates, R., Eike, P., Sinton, J., Cox, D., Myer, L., Nihei, K. and Nakagowa, S., 2002. Scaling between logs, single well, VSP and surface seismic for fracture quantification in naturally fractured gas reservoirs. In *72nd Ann. Internat. Mtg., Expanded Abstracts*, 2381–2384, Soc. of Expl. Geophys.

Mallat, S., 1999. *A wavelet tour of signal processing*. Academic Press, 2nd edn.

Marion, D., Mukerji, T. and Mavko, G., 1994. Scale effects on velocity dispersion: From ray to effective medium theories in stratified media. *Geophysics*, **59**, 1613–1619.

Mason, W.P., Marfurt, K.J., Beshers, D.N. and Kuo, J.T., 1978. Internal friction in rocks. *Journal of the Acoustical Society of America*, **63**, 1596–1603.

Maultzsch, S., Chapman, M., Liu, E. and Li, X.Y., 2003a. Modelling frequency-dependent seismic anisotropy in fluid-saturated rock with aligned fractures: implication of fracture size estimation from anisotropic measurements. *Geophysical Prospecting*, **51**, 381–392.

Maultzsch, S., Horne, S., Archer, S. and Burkhardt, H., 2003b. Effects of an anisotropic overburden on azimuthal amplitude analysis in horizontal transverse isotropic media. *Geophysical Prospecting*, **51**, 61–72.

Mavko, G. and Jizba, D., 1991. Estimating grain-scale fluid effects on velocity dispersion in rocks. *Geophysics*, **56**, 1940–1949.

Mavko, G. and Mukerji, T., 1995. Seismic pore space compressibility and Gassmann's relation. *Geophysics*, **60**, 1743–1749.

Mavko, G. and Nur, A., 1997. The effect of a percolation threshold in the Kozeny-Carman relation. *Geophysics*, **62**, 1480–1482.

Mavko, G., Mukerji, T. and Dvorkin, J., 1998. *The Rock Physics Handbook*. Cambridge University Press.

McDonald, F.J., Angona, F.A., Mills, R.L., Sengbush, R.L., van Nostrand, R.G. and White, J.E., 1958. Attenuation of shear and compressional waves in Pierre shale. *Geophysics*, **23**, 421–439.

McWilliams, M., 2001. Using flue gas huff'n puff technology and surfactants to increase oil production from the Antelope Shale formation of the Railroad Gap oil field. Technical Report DOE/BC/16248-1, US Department of Energy.

Miller, D.E., Leaney, S. and Borland, W., 2000. An in-situ estimation of anisotropic elastic muduli for a submarine shale. In C. MacBeth and H.B. Lynn, eds., *Applied seismic anisotropy: Theory, background, and field studies*, vol. 20 of *Geophysics Reprint Series*, 538–542, Soc. of Explor. Geophys.

Montgomery, S.L. and Morea, M.F., 2001. Antelope shale (Monterey Formation), Buena Vista Hills field: Advanced reservoir characterization to evaluate CO_2 injection for enhanced oil recovery. *AAPG Bulletin*, **85**, 561–585.

Montgomery, S.L. and Morgan, C.D., 1998. Bluebell field, Uinta basin: Reservoir characterization for improved well completion and oil recovery. *AAPG Bulletin*, **82**, 1113–1132.

Mukerji, T. and Mavko, G., 1994. Pore fluid effects on seismic velocity in anisotropic rocks. *Geophysics*, **59**, 233–244.

Murphy, W.F., 1984. Acoustic measures of partial gas saturation in tight sandstones. *Journal of Geophysical Research*, **89**, 11549–11559.

Murphy, W.F., 1985. Sonic and ultrasonic velocities: Theory versus experiment. *Geophysical Research Letters*, **12**, 85–88.

Musgrave, M.J.P., 1970. *Crystal Acoustics*. Holden Day.

Narr, W.N. and Currie, J.B., 1982. Origin of fracture porosity - example from the Altamont field, Utah. *AAPG Bulletin*, **66**, 1231–1247.

Neep, J., 1995. Robust estimation of P-wave attenuation from full waveform sonic data. *Journal of Seismic Exploration*, **4**, 329–344.

Newman, P.J. and Worthington, M.H., 1982. In-situ investigation of seismic body wave attenuation in heterogeneous media. *Geophysical Prospecting*, **30**, 337–400.

Nicoletis, L., Client, C. and Lefeuvre, F., 1988. Shear-wave splitting measurements from multishot VSP data. In *58th Ann. Internat. Mtg., Expanded Abstracts*, 527–430, Soc. of Expl. Geophys.

Nihei, K.T., Nakagawa, S., Myer, L. and Majer, E., 2002. Finite difference modeling of seismic wave interactions with discrete, finite length fractures. In *72nd Ann. Internat. Mtg., Expanded Abstracts*, 1963–1966, Soc. of Expl. Geophys.

Nishizawa, O., 1982. Seismic velocity anisotropy in a medium containing oriented cracks–transversely isotropic case. *Journal Phys. Earth*, **30**, 331–347.

Nolen-Hoeksema, R.C., 2000. Modulus-porosity relations, Gassmann's equations and the low-frequency elastic-wave response to fluids. *Geophysics*, **65**, 1355–1363.

Nur, A. and Winkler, K., 1980. The role of friction and fluid flow in wave attenuation in rocks. *Geophysics*, **45**, 591–592.

O'Connell, R.J. and Budiansky, B., 1974. Seismic velocities in dry and saturated cracked solids. *Journal of Geophysical Research*, **79**, 5412–5426.

O'Connell, R.J. and Budiansky, B., 1977. Viscoelastic properties of fluid-saturated cracked solids. *Journal of Geophysical Research*, **82**, 5719–5736.

O'Doherty, R.F. and Anstey, N.A., 1971. Reflections on amplitudes. *Geophysical Prospecting*, **19**, 430–458.

Ortega, O.J., Randall, M., Laubach, S.E., Milliken, K.L., Olson, J. and Reed, R., 2001. Outcrop analogs for fractured reservoir characterization: Rangely field, Colorado. In *AAPG Ann. Mtg., Technical Program*, Am. Assn. of Petr. Geol.

Park, J., Lindberg, C.R. and Vernon, F.L., 1987. Multitaper spectral analysis of high frequency seismograms. *Journal of Geophysical Research*, **92**, 12675–12684.

Parra, J.O., Hackert, C.L. and Xu, P.C., 2002. Characterization of fractured low Q zones at the Buena Vista Hills reservoir, California. *Geophysics*, **67**, 1061–1070.

Pérez, M.A., Gibson, R.L. and Toksöz, M.N., 1999. Detection of fracture orientation using azimuthal variation of P-wave AVO responses. *Geophysics*, **64**, 1253–1265.

Plona, T., 1980. Observation of a second bulk compressional wave in a porous medium at ultrasonic frequencies. *Appl. Phys. Lett.*, **36**, 259–261.

Pointer, T., Liu, E. and Hudson, J.A., 2000. Seismic wave propagation in cracked porous media. *Geophysical Journal International*, **142**, 199–231.

Pujol, J. and Smithson, S., 1991. Seismic wave attenuation in volcanic rocks from VSP experiments. *Geophysics*, **56**, 1441–1455.

Queen, J.H. and Rizer, W.D., 1990. An integrated study of seismic anisotropy and the natural fracture system at the Conoco borehole test facility Kay county, Oklahoma. *Journal of Geophysical Research*, **95**, 11225–11273.

Raikes, S.A. and White, R.E., 1984. Measurements of earth attenuation from downhole and surface seismic recordings. *Geophysical Prospecting*, **32**, 892–919.

Rathore, J.S., Fjaer, E., Holt, R.M. and Renlie, L., 1995. P- and S-wave anisotropy of a synthetic sandstone with controlled crack geometry. *Geophysical Prospecting*, **43**, 711–728.

Reid, F.J.L., Nguyen, P.H., MacBeth, C., Clark, R.A. and Magnus, I., 2001. Q estimates from North Sea VSPs. In *71th Ann. Internat. Mtg., Expanded Abstracts*, 440–443, Soc. of Expl. Geophys.

Robertson, R.D., 2004. Fletcher Gulch prospect, Rio Blanco County, Colorado. Geological report, Great Northern Gas Company.

Rüger, A. and Tsvankin, I., 1997. Using AVO for fracture detection: Analytical basis and practical solutions. *The Leading Edge*, **16**, 1429–1434.

Saha, J.G., 1987. Relationship between Fourier and instantaneous frequency. In *57th Ann. Internat. Mtg., Expanded Abstracts*, 591–594, Soc. of Expl. Geophys.

Sams, M. and Goldberg, D., 1990. The validity of Q estimates from borehole data using spectral ratios. *Geophysics*, **55**, 97–101.

Sams, M.S., Neep, J.P., Worthington, M.H. and King, M.S., 1997. The measurement of velocity dispersion and frequency-dependent intrinsic attenuation in sedimentary rocks. *Geophysics*, **62**, 1456–1464.

Sassi, W., Guiton, M.L.E., Daniel, J.M., Faure, J.L., Mengus, J.M., Schmidtz, J., Delisle, S., Leroy, Y.M. and Massot, J., 2003. Technical reconstruction of fracture development in Weber sandstone formation, Split Mountain, Utah. In *AAPG Ann. Mtg., Technical Program*, Am. Assn. of Petr. Geol.

Sayers, C.M., 2002. Fluid-dependent shear-wave splitting in fractured media. *Geophysical Prospecting*, **50**, 393–401.

Sayers, C.M. and Kachanov, M., 1991. A simple technique for finding effective elastic constants of cracked solids for arbitrary crack orientation statistics. *International Journal of Solids and Structures*, **27**, 671–680.

Schoenberg, M., 1980. Elastic wave behaviour across linear slip interfaces. *Journal of the Acoustical Society of America*, **68**, 1516–1521.

Schoenberg, M. and Douma, J., 1988. Elastic wave propagation in media with parallel fractures and aligned cracks. *Geophysical Prospecting*, **36**, 571–590.

Schoenberg, M. and Helbig, K., 1997. Orthorhombic media: Modeling elastic wave behavior in a vertically fractured earth. *Geophysics*, **62**, 1954–1974.

Schoenberg, M. and Sayers, C., 1995. Seismic anisotropy of fractured rock. *Geophysics*, **60**, 204–211.

Schoenberger, M. and Levin, F.K., 1974. Apparent attenuation due to intrabed multiples. *Geophysics*, **39**, 278–291.

Schoenberger, M. and Levin, F.K., 1978. Apparent attenuation due to intrabed multiples, II. *Geophysics*, **43**, 730–737.

Shapiro, S.A. and Hubral, P., 1995. Frequency-dependent shear-wave splitting and velocity anisotropy due to elastic multilayering. *Journal of Seismic Exploration*, **4**, 151–168.

Slater, C., Crampin, S., Brodov, L.Y. and Kruznetsov, V.M., 1993. Observations of anisotropic cusps in transversely isotropic clay. *J. Can. Soc. Expl. Geophys.*, **29**, 216–226.

Smith, R.L. and McGarrity, J.P., 2001. Cracking the fractures - seismic anisotropy in an offshore reservoir. *The Leading Edge*, **20**, 18–26.

Snedecor, G.W. and Cochran, W.G., 1989. *Statistical Methods*. Iowa State University Press, 8th edn.

Sothcott, J., McCann, C. and O'Hara, S., 2000. The influence of two pore fluids on the acoustic properties of reservoir sandstones at sonic and ultrasonic frequencies. In *70th Ann. Internat. Meeting, Expanded Abstracts*, 1883–1886, Soc. of Expl. Geophys.

Spencer, J.W., 1981. Stress relaxation at low frequencies in fluid-saturated rocks: Attenuation and modulus dispersion. *Journal of Geophysical Research*, **86**, 1803–1812.

Spencer, T.W., Sonnad, J.R. and Butler, T.M., 1982. Seismic Q - Stratigraphy or dissipation. *Geophysics*, **47**, 16–24.

Stainsby, S.D. and Worthington, M.H., 1985. Q estimation from vertical seismic profile data and anomalous variations in the central North Sea. *Geophysics*, **49**, 1153–1168.

Stewart, R.R., Huddleston, P.D. and Kan, T.K., 1984. Seismic versus sonic velocities: A vertical seismic profiling study. *Geophysics*, **49**, 1153–1168.

Stockwell, R.G., Mansinha, L. and Lowe, R.P., 1996. Localization of the complex spectrum: The S transform. *IEEE Transactions on Signal Processing*, **44**, 998–1001.

Taner, M.T. and Treitel, S., 2003. A robust method for Q estimation. In *73rd Ann. Internat. Mtg., Expanded Abstracts*, 710–713, Soc. of Explor. Geophys.

Taylor, D., 2001. *ANISEIS v5.2 Manual*. Applied Geophysical Software Inc., Houston.

Teufel, L.W., Warpinski, N.R. and Lorenz, J.C., 1984. A model for fracture genesis; application to Mesaverde Group, Piceance Creek basin, Colorado. *AAPG Bulletin*, **68**, 534.

Theophanis, S. and Queen, J.H., 2000. Color display of the localized spectrum. *Geophysics*, **65**, 1330–1340.

Thompson, C., Moran, R., Horne, S.A., Walsh, J. and Fairborn, J., 2002. Seismic fracture characterization of a sandstone reservoir - Rangely Field, Colorado. In *72nd Ann. Internat. Mtg., Expanded Abstracts*, 1049–1052, Soc. of Expl. Geophys.

Thomsen, L., 1986. Weak elastic anisotropy. *Geophysics*, **51**, 1954–1966.

Thomsen, L., 1988. Reflection seismology over azimuthally anisotropic media. *Geophysics*, **53**, 304–313.

Thomsen, L., 1995. Elastic anisotropy due to aligned cracks in porous rock. *Geophysical Prospecting*, **43**, 805–829.

Thomsen, L., 2002. *Understanding Seismic Anisotropy in Exploration and Exploitation*. No. 5 in Distinguished Instructor Series, Soc. of Expl. Geophys.

Tittmann, B.R., Nadler, H., Clark, V.A., A., A.L. and Spencer, T.W., 1981. Frequency dependence of seismic dissipation in saturated rocks. *Geophysical Research Letters*, **8**, 36–38.

Tod, S.R. and Liu, E., 2002. Frequency-dependent anisotropy due to fluid flow in bed limited cracks. *Geophysical Research Letters*, **29**, 10.1029/2002GL015369.

Toksöz, M.N. and Johnston, D.H., eds., 1981. *Seismic Wave Attenuation*. Geophysics reprint series, Soc. of Expl. Geophys.

Toksöz, M.N., Johnston, D.H. and Timur, A., 1979. Attenuation of seismic waves in dry and saturated rocks: I. Laboratory measurements. *Geophysics*, **44**, 681–690.

Tonn, R., 1991. The determination of seismic quality factor Q from vsp data: A comparison of different computational methods. *Geophysical Prospecting*, **39**, 1–27.

Tsvankin, I., 2001. *Seismic Signatures and Analysis of Reflection Data in Anisotropic Media*, vol. 29 of *Handbook of Geophysical Exploration, Seismic Exploration*. Pergamon, Elsevier Science.

Tullos, F.N. and Reid, C., 1969. Seismic attenuation of Gulf Coast sediments. *Geophysics*, **34**, 516–528.

van der Kolk, C.M., Guest, W.S. and Potters, J.H.H.M., 2001. The 3D shear experiment over the Natih field in Oman: The effect of fracture-filling fluids on shear propagation. *Geophysical Prospecting*, **49**, 179–197.

Wang, Y., 2003. Quantifying the effectiveness of stabilized inverse Q filtering. *Geophysics*, **68**, 337–345.

Wang, Z., 1992. The Gassmann equation revisited: Comparing laboratory data with Gassmann's predictions. In Z. Wang and A. Nur, eds., *Seismic and Acoustic Velocities in Reservoir Rocks*, vol. 3 of *Geophysics reprint series*, 8–23, Soc. of Expl. Geophys.

Wang, Z., 2002. Seismic anisotropy in sedimentary rocks, part 2: Laboratory data. *Geophysics*, **67**, 1423–1440.

Wang, Z. and Nur, A., 1990. Dispersion analysis of acoustic velocities in rocks. *Journal of the Acoustical Society of America*, **87**, 2384–2395.

Wang, Z. and Nur, A., 1992. Elastic-wave velocities in porous media: A theoretical recipe. In Z. Wang and A. Nur, eds., *Seismic and Acoustic Velocities in Reservoir Rocks, 2 - Theoretical and model studies*, vol. 3 of *Geophysics reprint series*, 1–35, Soc. of Expl. Geophys.

Werner, U. and Shapiro, S.A., 1999. Frequency-dependent shear-wave splitting in thinly layered media with intrinsic anisotropy. *Geophysics*, **51**, 604–608.

White, J.E., Nicoletis, L. and Monash, C., 1983. Measured anisotropy in Pierre Shale. *Geophysical Prospecting*, **31**, 709–725.

White, R.E., 1992. The accuracy of estimating Q from seismic data. *Geophysics*, **57**, 1508–1511.

Whitehead, N.H., 1993. *Atlas of major Rocky Mountain gas reservoirs*, chap. San Juan Basin Plays, pp. 118–132. New Mexico Bureau of Mines and Mineral Resources.

Wijnands, F., 1997. Walkaway Vertical Seismic Profile WVSP. Borehole Seismic Processing Report BP-GAPS-91082, BP.

Wild, P. and Crampin, S., 1991. The range of effects of azimuthal isotropy and EDA anisotropy in sedimentary basins. *Geophysical Journal International*, **107**, 513–529.

Willis, M.E., Pearce, F., Burns, D.R., Byun, J. and Minsley, B., 2004. Reservoir fracture orientation and density from reflected and scattered seismic energy. In *66th Ann. Internat. Mtg., Expanded Abstracts*, C043, Eur. Assn. Geosci. Eng.

Winkler, K.W., 1985. Dispersion analysis of velocity and attenuation in Berea sandstone. *Journal of Geophysical Research*, **90**, 3793–6800.

Winkler, K.W., 1986. Estimates of velocity dispersion between seismic and ultrasonic frequencies. *Geophysics*, **51**, 183–189.

Winkler, K.W. and Nur, A., 1979. Pore fluids and seismic attenuation in rocks. *Geophysical Research Letters*, **6**, 1–4.

Winkler, K.W., Nur, A. and Gladwin, M., 1979. Friction and seismic attenuation in rocks. *Nature*, **227**, 528–531.

Winterstein, D.F. and Meadows, M.A., 1991. changes in shear-wave polarization azimuth with depth in Cymric and Railroad Gap oil fields. *Geophysics*, **56**, 1349–1364.

Winterstein, D.F., De, G.S. and Meadows, M.A., 2001. Twelve years of vertical birefringence in nine-component VSP data. *Geophysics*, **66**, 582–597.

Yale, E.P., Strubhar, M.K. and El Rabaa, A.W., 1993. Determination of hydraulic fracture direction, San Juan basin. In *Production Operations Symposium, Oklahoma City*, paper no. SPE 25466, Soc. of Petr. Eng.

Yilmaz, Ö., 2001. *Seismic data analysis*. Soc. of Expl. Geophys., 2nd edn.

Zatsepin, S.V. and Crampin, S., 1997. Modelling the compliance of crustal rock - I. response of shear-wave splitting to differential stress. *Geophysical Journal International*, **129**, 477–494.

Zeng, X. and MacBeth, C., 1993. Algebraic processing techniques for estimating shear-wave splitting in near-offset VSP data: Theory. *Geophysical Prospecting*, **41**, 1033–1066.

Zimmerman, R.W., 1991. *Compressibility of sandstones*. Elsevier Science.

Zoback, M.D., Zoback, M.L., Mount, V.S., Suppe, J., Eaton, J.P., Healy, J.H., Oppenheimer, D., Reasenberg, P., Jones, L., Raleigh, C.B., Wong, I.G., Scotti, O. and Wentworth, C., 1987. New evidence on the state of stress of the San Andreas fault system. *Science*, **238**, 1105–1111.

Appendix A

Fourier transform, instantaneous attributes and wavelet transform

In this appendix I summarize aspects of the Fourier transform, the Hilbert transform and the wavelet transform that are relevant for this thesis.

A.1 Fourier transform

The Fourier transform is the decomposition of a function $f(t)$ into sinosoidal waves $e^{i\omega t}$ where ω is the angular frequency. The transform is defined as (Bracewell, 1965)

$$F(\omega) = \int_{-\infty}^{\infty} f(t) e^{-i\omega t} dt. \tag{A.1}$$

Its inverse transform is given by

$$f(t) = \frac{1}{2\pi} \int_{-\infty}^{\infty} F(\omega) e^{i\omega t} d\omega. \tag{A.2}$$

The Fourier transform is particularly useful in time-invariant linear signal processing, because $e^{i\omega t}$ are eigenvectors of a time-invariant linear system (Buttkus, 1991). The time invariance of a linear operator L means that if its input $f(t)$ is delayed by τ, then its output $g(t)$ will also be delayed by τ, i.e.:

$$\text{If} \quad g(t) = Lf(t), \qquad \text{then} \quad g(t-\tau) = Lf(t-\tau). \tag{A.3}$$

The time-invariant linear operator L is characterized by its impulse response $h(t)$, which is its response to a Dirac impulse $\delta(t)$:

$$h(t) = L\delta(t). \tag{A.4}$$

Because of the time invariance of the filter L, $h(t-\tau) = L\delta(t-\tau)$. $f(t)$ can be obtained through integration against a Dirac impulse:

$$f(t) = \int_{-\infty}^{\infty} f(\tau)\delta(t-\tau)d\tau.$$

It then follows that the time-invariant linear filter L applied to a function $f(t)$ is equivalent to convolving $f(t)$ with the filter's impulse response:

$$\begin{aligned} Lf(t) &= \int_{-\infty}^{\infty} f(\tau)L\delta(t-\tau)d\tau = \int_{-\infty}^{\infty} f(\tau)h(t-\tau)d\tau \\ &= f(t) * h(t) = h(t) * f(t). \end{aligned} \tag{A.5}$$

A linear system is causal if its output $g(t)$ does not depend on any future input values $f(\tau)$ for $\tau > t$, i.e. if $f(t) = 0$ for $t < 0$ then $g(t) = 0$ for $t < 0$. From Eq. A.5 it becomes clear that causality requires $h(\tau) = 0$ for $\tau < 0$.
We can now see that $e^{i\omega t}$ are indeed eigenvectors of time-invariant linear systems L:

$$Le^{i\omega t} = \int_{-\infty}^{\infty} h(\tau)e^{i\omega(t-\tau)}d\tau = e^{i\omega t}\int_{-\infty}^{\infty} h(\tau)e^{-i\omega\tau}d\tau = H(\omega)e^{i\omega t}. \tag{A.6}$$

The eigenvalues $H(\omega)$ are the Fourier transform of $h(t)$ (*see* Eq. A.1). This is also expressed in the convolution theorem, which is the basis of many signal processing applications and thus one of the most important properties of the Fourier transform (Buttkus, 1991). If $f(t)$ has the Fourier transform $F(\omega)$ and $h(t)$ has the Fourier transform $H(\omega)$, then the Fourier transform of the convolution $g(t) = h(t) * f(t)$ is

$$G(\omega) = H(\omega) \cdot F(\omega). \tag{A.7}$$

Conversely, the inverse Fourier transform of $\frac{1}{2\pi}H(\omega) * F(\omega)$ is $h(t) \cdot f(t)$. We can therefore write the response of a linear time-invariant system $g(t) = Lf(t)$ as an

inverse Fourier transform:

$$g(t) = Lf(t) = \frac{1}{2\pi} \int_{-\infty}^{\infty} H(\omega)F(\omega)e^{i\omega t}d\omega. \tag{A.8}$$

This illustrates why the term *filter* is used as a synonym for time-invariant linear systems: Each frequency component $e^{i\omega t}$ of f that has amplitude $F(\omega)$ is attenuated or amplified by $H(\omega)$. $H(\omega)$ is also referred to as the transfer function of the filter L.

Another important property of the Fourier transform is that inner products are conserved up to a factor of 2π, which is known as the Parseval theorem (Bracewell, 1965). The inner product $\langle f, h\rangle$ of functions $f(t)$ and $h(t)$ is defined as:

$$\langle f, h\rangle = \int_{-\infty}^{\infty} f(t)h^*(t)dt. \tag{A.9}$$

The Parseval theorem relates the inner product of the time series to the inner product of their Fourier transforms:

$$\int_{-\infty}^{\infty} f(t)h^*(t)dt = \frac{1}{2\pi} \int_{-\infty}^{\infty} F(\omega)H^*(\omega)d\omega. \tag{A.10}$$

For the special case that $h(t) = f(t)$ this gives:

$$\|f\|^2 = \int_{-\infty}^{\infty} |f(t)|^2 dt = \frac{1}{2\pi} \int_{-\infty}^{\infty} |F(\omega)|^2 d\omega, \tag{A.11}$$

which means that the energy of the signal $f(t)$ is equal to its spectral energy.

From the definition of the Fourier transform in Eqs. A.1 and A.2 it is apparent that each Fourier coefficient $F(\omega)$ depends on the values of $f(t)$ for all times, and equally each value of $f(t)$ depends on $F(\omega)$ for all frequencies. The better a signal is localized in time, the wider is its energy spread in the frequency domain, and vice versa. The Fourier transform of the Dirac impulse $\delta(t)$, which is perfectly localized in time, is 1, so that its energy is spread equally over all frequencies. Similarly, the inverse Fourier transform of a Dirac in the frequency domain has its energy distributed equally over all times. This trade-off between time and

frequency localization is expressed in the Heisenberg uncertainty principle (Bath, 1974). It states that the simultaneous concentration of energy in time and in frequency cannot be arbitrarily small. The average locations u and ξ of a signal f in time and in frequency are given by (Mallat, 1999):

$$u = \frac{1}{\|f\|^2} \int_{-\infty}^{\infty} t|f(t)|^2 dt \quad \text{and} \quad \xi = \frac{1}{\|F\|^2} \int_{-\infty}^{\infty} \omega|F(\omega)|^2 d\omega. \tag{A.12}$$

The variances σ_t^2 and σ_ω^2 around these averages are then:

$$\sigma_t^2 = \frac{1}{\|f\|^2} \int_{-\infty}^{\infty} (t-u)^2|f(t)|^2 dt, \tag{A.13}$$

$$\sigma_\omega^2 = \frac{1}{\|F\|^2} \int_{-\infty}^{\infty} (\omega-\xi)^2|F(\omega)|^2 d\omega. \tag{A.14}$$

The Heisenberg uncertainty theorem proves that the product of the variances cannot be arbitrarily small:

$$\sigma_t^2 \sigma_\omega^2 \geq \frac{1}{4}. \tag{A.15}$$

This fundamentally restricts simultaneous localization in time and in frequency. A further property of the Fourier transform is that $F(\omega)$ cannot have compact support for any function $f(t)$ with compact support and vice versa (Mallat, 1999). These restrictions become important if one is interested in the transient nature of a signal, such as the frequency spectrum of a particular arrival along a seismic trace or the change in the local frequency content with time. Other transforms, such as the windowed Fourier transform and the wavelet transform, have been developed to address these issues. They will be discussed in section A.3.

If $f(t)$ is represented by a discrete time series and is uniformly sampled at intervals Δt, then it can be recovered exactly as long as the support of its Fourier transform does not exceed the Nyquist frequency $|f_N| = 1/(2\Delta t)$. The reconstruction of $f(t)$ from its discrete representation is given by the sampling theorem: If the support of $F(\omega)$ is included in $\left[-\frac{\pi}{\Delta t}, \frac{\pi}{\Delta t}\right]$, then $f(t)$ can be recovered from the discrete

values $f(n\Delta t)$ by

$$f(t) = \sum_{n=-\infty}^{+\infty} f(n\Delta t)\,\mathrm{sinc}\left(\frac{t}{\Delta t}\right) \qquad \text{(A.16)}$$

$$\text{with} \qquad \mathrm{sinc}(t) = \frac{\sin(\pi t)}{\pi t}.$$

This means that each frequency component of $f(t)$ has to be represented by at least two uniformly spaced samples per period to describe $f(t)$ accurately with a discrete time series.

A.2 Hilbert transform and instantaneous attributes

Let $f(t)$ be a causal function, so that $f(t) = 0$ for $t < 0$. It thus can be written as

$$f(t) \cdot h(t) \quad \text{with} \quad h(t) = \begin{cases} 0\,, & t < 0 \\ 1\,, & t \geq 0 \end{cases}.$$

Multiplication in the time domain is equivalent to a convolution in the frequency domain, so that

$$\begin{aligned} F(\omega) &= \frac{1}{2\pi} F(\omega) * H(\omega) = \frac{1}{2\pi} F(\omega) * \left[\pi\delta(\omega) + \frac{1}{i\omega}\right] \\ &= \frac{1}{2} F(\omega) + \frac{1}{2\pi} \int_{-\infty}^{\infty} \frac{F(u)}{i(\omega - u)} du. \\ &= \frac{1}{i\pi} \int_{-\infty}^{\infty} \frac{F(u)}{(\omega - u)} du. \end{aligned} \qquad \text{(A.17)}$$

With $F(\omega) = R(\omega) + iI(\omega)$ it follows that

$$R(\omega) + iI(\omega) = \frac{1}{\pi} \int_{-\infty}^{\infty} \frac{I(u)}{\omega - u} du - \frac{i}{\pi} \int_{-\infty}^{\infty} \frac{R(u)}{\omega - u} du. \qquad \text{(A.18)}$$

The Hilbert transform $\hat{f}(x)$ of the function $f(x)$ is defined as (Bracewell, 1965):

$$\hat{f}(x) = \frac{1}{\pi x} * f(x) = \frac{1}{\pi} \int_{-\infty}^{\infty} \frac{f(y)}{x-y} dy, \tag{A.19}$$

and its inverse as:

$$f(x) = -\hat{\hat{f}}(x) = -\frac{1}{\pi x} * \hat{f}(x) = -\frac{1}{\pi} \int_{-\infty}^{\infty} \frac{\hat{f}(y)}{x-y} dy. \tag{A.20}$$

From Eq. A.18 it therefore follows that the real and imaginary parts of the Fourier transform of causal functions are Hilbert transform pairs. This is an important property of causal linear systems. Their transfer functions have real and imaginary parts that are not independent, but related through the Hilbert transform. For wave propagation in anelastic media, for example, this leads to a specific relationship between velocity dispersion and attenuation.
An analog in the frequency domain for causal functions is a Fourier transform $F_a(\omega)$ that is zero for negative frequencies:

$$F_a(\omega) = 0 \quad \text{if } \omega < 0.$$

The corresponding complex time function $f_a(t)$ is referred to as the analytic signal, and its real and imaginary parts are Hilbert transform pairs (Bracewell, 1965):

$$f_a(t) = f(t) + i\hat{f}(t). \tag{A.21}$$

The Fourier transform of $f_a(t)$ is then

$$F_a(\omega) = \begin{cases} 2F(\omega)\,, & \omega \geq 0 \\ 0 \qquad\;\; , & \omega < 0 \end{cases}, \tag{A.22}$$

and is thus completely defined by the real part of $f_a(t)$. $f_a(t)$ can be written as

$$f_a(t) = |f_a(t)|\, e^{i\Phi(t)}. \tag{A.23}$$

$|f_a(t)|$ is called the envelope of the signal, $\Phi(t)$ is the instantaneous phase, and $\Phi'(t) = d\Phi(t)/dt$ is the instantaneous frequency. These instantaneous attributes

are often used for the interpretation of seismic sections (Yilmaz, 2001). The envelope is a measure of the energy along a signal, the instantaneous phase measures the local phase of the signal at every point in time, and the instantaneous frequency gives an average frequency at each time sample. Since the attributes describe local signal properties in time, they are useful for the interpretation of transient signals, where these properties change as a function of time. However, the instantaneous frequency is an average of all frequency components contained in the signal. Let, for example, $f(t)$ be the sum of two cosine waves: $f(t) = a[\cos(\omega_1 t) + \cos(\omega_2 t)]$. It has the analytic signal

$$f_a(t) = a\left[e^{i\omega_1 t} + e^{i\omega_2 t}\right] = a\cos\left[\frac{1}{2}(\omega_1 - \omega_2)t\right] e^{\frac{i}{2}(\omega_1+\omega_2)t}.$$

The instantaneous frequency is therefore $\Phi'(t) = \frac{\omega_1+\omega_2}{2}$, which is the average of the two frequencies. In order to separate instantaneous frequencies of several spectral components contained in a signal, a windowed Fourier transform or wavelet transform can be used. This is explained in the following section.

A.3 Windowed Fourier and Wavelet transform

Windowed Fourier and wavelet transforms aim to reveal local spectral characteristics of transient signals by decomposing a signal over elementary functions that have their energy well concentrated in time and in frequency. These elementary functions are also called 'time-frequency atoms'. A linear time-frequency transform is defined by the correlation of a signal with a family of time-frequency atoms (Mallat, 1999). The windowed Fourier and the wavelet transform are particular types of linear time-frequency transforms.

The windowed Fourier transform was introduced by Gabor (1946). Its atoms are constructed from a real symmetric time window $g(t)$ that is translated in time by u and modulated by frequency ξ:

$$g_{u,\xi}(t) = g(t-u)e^{i\xi t}. \tag{A.24}$$

It's Fourier transform $G(\omega)$ is therefore translated by ξ:

$$G_{u,\xi}(\omega) = G(\omega - \xi)e^{-iu(\omega-\xi)}. \tag{A.25}$$

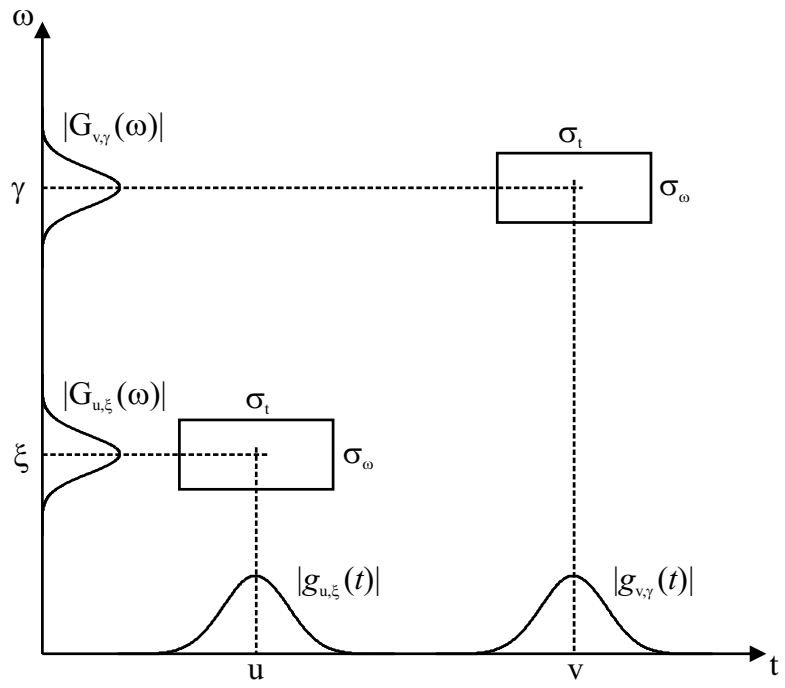

Figure A.1: The Heisenberg boxes of the windowed Fourier transform have constant sizes across the time-frequency plane. (*After* Mallat (1999).)

The window is normalized, so that $\|g_{u,\xi}\| = 1$ independent of u and ξ. The corresponding time-frequency transform is then defined as:

$$Pf(u,\xi) = \langle f, g_{u,\xi} \rangle = \int_{-\infty}^{\infty} f(t)\, g(t-u)\, e^{-i\xi t} dt. \tag{A.26}$$

The windowed Fourier atoms are centred at u in time and at ξ in frequency. Their energy spreads are measured with the variances defined in Eqs. A.14 and A.13, and they are independent of u and ξ (Mallat, 1999):

$$\sigma_t^2 = \int_{-\infty}^{\infty} t^2 |g(t)|^2 dt \quad \text{and} \quad \sigma_\omega^2 = \frac{1}{2\pi} \int_{-\infty}^{\infty} \omega^2 |G(\omega)|^2 d\omega. \tag{A.27}$$

A windowed Fourier transform therefore has constant resolution across the time-frequency plane. This can be illustrated by so-called Heisenberg boxes of widths σ_t and σ_ω that are translated across the time-frequency plane as shown in Fig. A.1. The Heisenberg uncertainty principle states that the area of these boxes, $\sigma_t\, \sigma_\omega$, cannot be smaller than 1/2. It can be shown that the area is equal to 1/2,

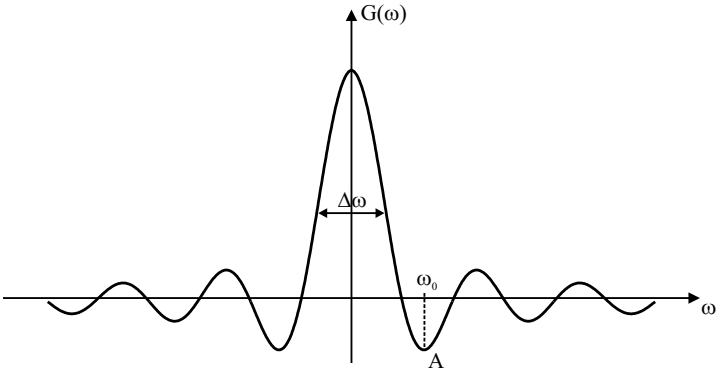

Figure A.2: Fourier transform of a time window with finite support. It has infinite support in the frequency domain with a main lobe at $\omega = 0$ and asymptotically decaying side lobes causing spectral leakage.

if and only if $g(t)$ is a Gaussian window function (Mallat, 1999). $g_{u,\xi}$ are then called Gabor atoms.

The window function $g(t)$ can be delated or compressed, such that the area of its Heisenberg box remains constant. Indeed, for $g_s(t) = 1/\sqrt{s}\, g(t/s)$ the width of the Heisenberg box in time and in frequency, respectively, is $s \cdot \sigma_t$ and σ_ω / s. This demonstrates again the trade-off between time and frequency resolution.

The resolution of the transform also depends on the type of window function that is used. For any numerical application the time window $g(t)$ must have finite support. As discussed in the previous section, its Fourier transform $G(\omega)$ must then have infinite support. As shown in Fig. A.2 it has a main lobe at $\omega = 0$ and side lobes decaying with increasing absolute values of ω. There are three common parameters that are used to describe the frequency resolution of a window function (Mallat, 1999):

- The bandwidth $\Delta\omega$, which is defined as follows:

$$\frac{|G(\Delta\omega/2)|^2}{|G(0)|^2} = \frac{1}{2}.$$

- The maximum amplitude A at the first side lobe (in decibels):

$$A = 10 \log_{10} \frac{|G(\omega_0)|^2}{|G(0)|^2}.$$

Window	$g(t)$	$\Delta\omega$	A	p
Rectangle	1	0.89	-13 db	0
Hamming	$0.54 + 0.46\cos(2\pi t)$	1.36	-43 db	0
Gaussian	$\exp[-18t^2]$	1.55	-55 db	0
Hanning	$\cos^2(\pi t)$	1.44	-32 db	2
Blackman	$0.42 + 0.5\cos(2\pi t)$ $+0.08\cos(4\pi t)$	1.68	-58 db	2

Table A.1: Parameters of the frequency resolution of different window functions.

- The exponent p describing the asymptotic decay of $G(\omega)$:

$$|G(\omega)| = O(\omega^{-p-1}).$$

If $\Delta\omega$ is small, the energy of a single frequency component of a signal will be concentrated more closely around that particular frequency. The sidelobes, however, create 'shadows' at other frequencies, which is also called spectral leakage (Bath, 1974). This effect depends on the amplitudes of the side lobes. If $|G(\omega)|$ decays rapidly with increasing frequency, the window can better separate different frequency components of a signal. Table A.1 lists these parameters for various commonly used window functions. They all have their support restricted to $\left[-\frac{1}{2}, \frac{1}{2}\right]$ and are normalized, so that $g(0) = 1$. The Blackman window, which I use in this thesis to compute local spectra of first arrivals, has a larger bandwidth than other windows, but the amplitude of the first side lobe is small and $|G(\omega)|$ is decaying rapidly, so that spectral leakage is reduced.
The finite support of a time window $g(t)$ determines the frequency spacing of independent values of the Fourier transform of a windowed signal due to the limited resolution of $G(\omega)$. Only the number of samples included in the time window give independent samples in the frequency domain spread between the Nyquist frequencies $\left[-\frac{\pi}{\Delta t}, \frac{\pi}{\Delta t}\right]$. Any zeros added at either end of the time window do not add information in the frequency domain. It can be proved that a signal f is recoverable from its windowed Fourier transform and that energy is conserved by the transform (Mallat, 1999):

$$f(t) = \frac{1}{2\pi} \int_{-\infty}^{\infty} \int_{-\infty}^{\infty} Pf(u, \xi) g(t-u) e^{i\xi t} d\xi \, du, \tag{A.28}$$

and

$$\int_{-\infty}^{\infty} |f(t)|^2 dt = \frac{1}{2\pi} \int_{-\infty}^{\infty} \int_{-\infty}^{\infty} |Pf(u,\xi)|^2 d\xi \, du. \tag{A.29}$$

$|Pf(u,\xi)|^2$ can therefore be interpreted as an energy density in the time-frequency plane.

Since the size of the window in the windowed Fourier transform is fixed, its resolution is optimized for a signal structure of particular width in time. However, signals often contain structures of different sizes, such as high and low frequency events along a seismic trace. The wavelet transform addresses this issue by using time-frequency atoms of varying sizes. It decomposes a signal over dilated and translated wavelets. A wavelet ψ is defined as a function of zero mean (Mallat, 1999):

$$\int_{-\infty}^{\infty} \psi(t) \, dt = 0. \tag{A.30}$$

It is centred around $t = 0$ and normalized, so that $\|\psi\| = 1$. A wavelet can be real or complex. The corresponding time-frequency atoms are obtained by scaling the wavelet by a constant s and translating it by u:

$$\psi_{u,s}(t) = \frac{1}{\sqrt{s}} \psi \left(\frac{t-u}{s} \right). \tag{A.31}$$

The wavelet transform is defined as the correlation of a function $f(t)$ with a wavelet atom (Mallat, 1999):

$$Wf(u,s) = \langle f, \psi_{u,s} \rangle = \int_{-\infty}^{\infty} f(t) \frac{1}{\sqrt{s}} \psi^* \left(\frac{t-u}{s} \right) dt. \tag{A.32}$$

This can also be written as a convolution:

$$Wf(u,s) = f * \tilde{\psi}_s(u) \quad \text{with} \quad \tilde{\psi}_s(t) = \frac{1}{\sqrt{s}} \psi^* \left(\frac{-t}{s} \right). \tag{A.33}$$

The convolution is equivalent to a multiplication of the Fourier transforms in the frequency domain. The Fourier transform of $\tilde{\psi}_s(t)$ is $\tilde{\Psi}_s(\omega) = \sqrt{s}\Psi^*(s\omega)$. Since the wavelet has zero mean, $\Psi(0) = 0$, and Ψ can therefore be regarded as the

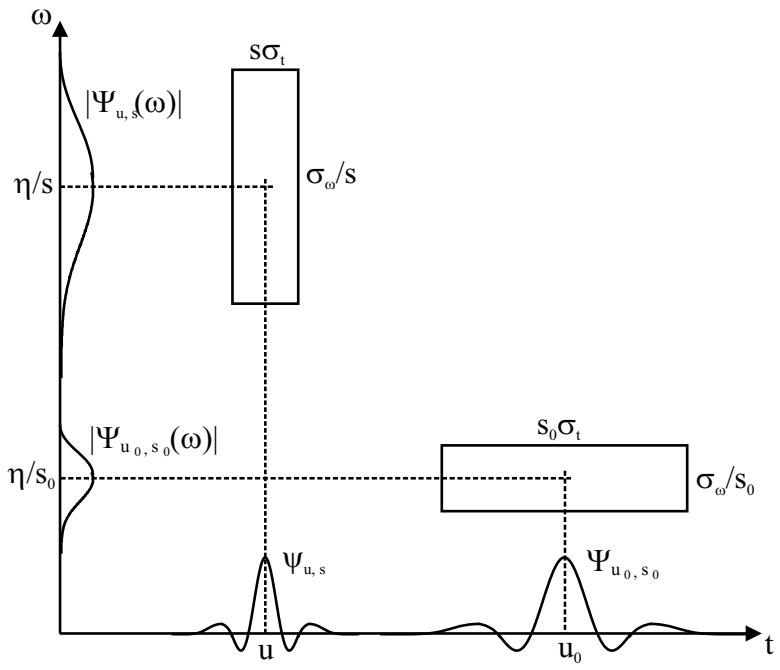

Figure A.3: Heisenberg boxes illustrating the time and frequency resolution of the wavelet transform. At low frequencies the Heisenberg box is stretched in time and compressed in frequency, whereas at high frequencies it is compressed in time and stretched in frequency.

transfer function of a bandpass filter. The wavelet transform as written in Eq. A.33 can then be understood as an application of dilated bandpass filters.
Applying the Parseval theorem to Eq. A.32 gives:

$$Wf(u,s) = \int_{-\infty}^{\infty} f(t)\psi^*_{u,s}(t)dt = \frac{1}{2\pi}\int_{-\infty}^{\infty} F(\omega)\Psi^*_{u,s}(\omega)d\omega, \tag{A.34}$$

with

$$\Psi^*_{u,s}(\omega) = e^{-iut}\sqrt{s}\Psi(s\omega).$$

The wavelet coefficients $Wf(u,s)$ therefore depend on $f(t)$ and $F(\omega)$ in the region of the time-frequency plane defined by the energy spreads of $\psi_{u,s}$ and $\Psi_{u,s}$. These can again be illustrated by Heisenberg boxes, as shown in Fig. A.3. $\Psi_{u,s}(t)$ is centred at u and its energy spread is proportional to s. If $\Psi(\omega)$ is centred at η, then $\Psi_{u,s}(\omega)$ is centred at η/s and the frequency width of the Heisenberg box is scaled by $1/s$. This means that for larger scales in time the energy spread along the frequency axis is decreased and shifted to lower frequency values. The wavelet transform therefore tries to adapt resolution to different scales contained

in a signal.

It can be shown that the instantaneous frequency $\Phi'(t)$ of a signal $f(t)$ is approximately obtained from the location of the maxima of $|Pf(u,\xi)|^2$ or $\frac{1}{s}|Wf(u,s)|^2$, which are also referred to as ridge points (Mallat, 1999). For signals that are sums of several spectral components each with a particular instantaneous frequency as a function of time, this approach can separate the different instantaneous frequencies in the time-frequency plane. The instantaneous frequency obtained from the analytic signal as defined in Eq. A.21, in contrast, yields average frequency values of all spectral components.

For the windowed Fourier transform the approximation of the instantaneous frequency as location of the ridge points requires that $\Phi'(t)$ has small variations over intervals of size s, which is the width of the support of g, and that $\Phi'(t) \geq \Delta\omega/s$, where $\Delta\omega$ is the bandwidth of $G(\omega)$. Different spectral components can be separated if the difference in their instantaneous frequencies exceeds $\Delta\omega/s$, which is the bandwidth of $G(s\omega)$. Here it is particularly important that the amplitudes of the side lobes of $G(\omega)$ are negligible (Mallat, 1999).

In the case of the wavelet transform the approximation requires $\Phi'(t)$ to vary slowly over the support of $\psi_{s,u}$ at small instantaneous frequencies, but it may vary much more rapidly at high values. The ability to separate spectral components with different instantaneous frequencies depends on the parameter η (Mallat, 1999). In general it depends on the characteristics of a particular signal, which transform is best suited to separate the instantaneous frequencies in the time-frequency plane.

Another time-frequency representation that contains elements of both the windowed Fourier and the wavelet transform is the S-transform introduced in Section 4.5 of Chapter 4. It is defined as (Stockwell *et al.*, 1996):

$$S(u,\omega) = \frac{1}{2\pi} \int_{-\infty}^{\infty} f(t) \, \frac{|\omega|}{\sqrt{2\pi}} \, e^{-\frac{(u-t)^2\omega^2}{8\pi^2}} e^{-i\omega t} dt. \tag{A.35}$$

It resembles a windowed Fourier transform in that a Gaussian window is translated across a signal and a local spectrum is computed. However, the window size is not fixed, but a function of frequency itself. Like the wavelet transform, the S-transform contains the element of different scales in the time-frequency plane. High frequencies have good time resolution but poor frequency resolution, while

low frequencies have poor time resolution and good frequency resolution. The S-transform is, however, not a wavelet transform, because its time-frequency atoms are not functions of zero mean.
An integration of the S-transform of a signal over time gives the Fourier transform of the signal (Stockwell *et al.*, 1996):

$$\int_{-\infty}^{\infty} S(u,\omega)du = F(\omega). \tag{A.36}$$

This shows that the S-transform is indeed a representation of the local spectrum, and $f(t)$ can be exactly recovered from $S(u,\omega)$:

$$f(t) = \frac{1}{2\pi}\int_{-\infty}^{\infty}\left\{\int_{-\infty}^{\infty} S(u,\omega)du\right\}e^{i\omega t}d\omega. \tag{A.37}$$

Writing the S-transform as an operation on the Fourier spectrum of $f(t)$ gives:

$$S(u,\omega) = \frac{1}{2\pi}\int_{-\infty}^{\infty} F(\alpha+\omega)e^{-\frac{2\pi^2\alpha^2}{\omega^2}}e^{i\alpha u}d\alpha, \quad \omega \neq 0. \tag{A.38}$$

For each frequency ω_0 the Fourier spectrum is shifted by that frequency and then filtered with a Gaussian window function of width ω_0. In fact, negative frequencies are removed from the spectrum, which means that for any ω_0 the S-transform can be understood as a bandpass filtered version of the analytic signal of $f(t)$. The instantaneous frequency defined by the S-transform in the time-frequency plane is then given by (Stockwell *et al.*, 1996):

$$\Phi'(u,\omega_0) = \frac{\partial}{\partial u}\left\{\omega_0 u + \tilde{\Phi}(u,\omega_0)\right\}, \tag{A.39}$$

where $\tilde{\Phi}(u,\omega_0)$ is the phase of $S(u,\omega_0)$.
All these different time-frequency representations vary in their ability of separating signal components in the time-frequency plane, depending on the particular structure of a signal. The best suitable transform for a given analysis will therefore depend on the objective of the analysis and the type of signal that is analysed. Common to all time-frequency transforms, however, is the fundamental trade-off between time and frequency resolution, which is expressed in the Heisenberg

uncertainty principle. Any windowing in the time domain decreases frequency resolution, and conversely, any window applied in the frequency domain, such as a bandpass filter, decreases resolution in time. This principle is independent of the particular design of a time-frequency transform.

Appendix B

S-transform of synthetic VSP data

In this appendix I demonstrate the application of the S-transform to the synthetic VSP data of model 1 from Chapter 4. I show how effects of the frequency-dependent anisotropy described by the model of Chapman (2003) can be revealed by the time-frequency representation.

Fig. B.1 displays the time-frequency panels obtained by the S-transform of the synthetic traces at azimuths of 0^o, 45^o and 90^o from the fracture strike, which is N-S. The white dots show the arrival time of the maximum amplitude at each frequency. The plots clearly demonstrate the dependence of time resolution on frequency, which is caused by scaling the Gaussian window in Eq. 4.13 with the inverse of frequency. By comparing the different azimuths we can see that the centre frequency of the spectrum shifts to lower values towards the azimuth normal to the fracture strike. The maximum amplitude also decreases towards this direction. Moreover, the arrival times are increased at lower frequencies compared to higher frequencies for azimuths of 45^o and 90^o. These are the effects of attenuation and velocity dispersion, which change with azimuth and are largest in the direction normal to the fractures.

The analysis of attenuation anisotropy is described in Chapter 4. Here I show an analysis of the frequency-dependent traveltime anisotropy. At each frequency I use the time picks of the maximum amplitudes from the S-transform of the data (white dots in Fig. B.1) as a function of azimuth and fit the $\cos(2\varphi)$-function of Eq. 2.10 to the data points. An example of the azimuthal fit is given in Fig. B.2. Fig. B.3 shows the resulting inverted parameters and errors as a function of

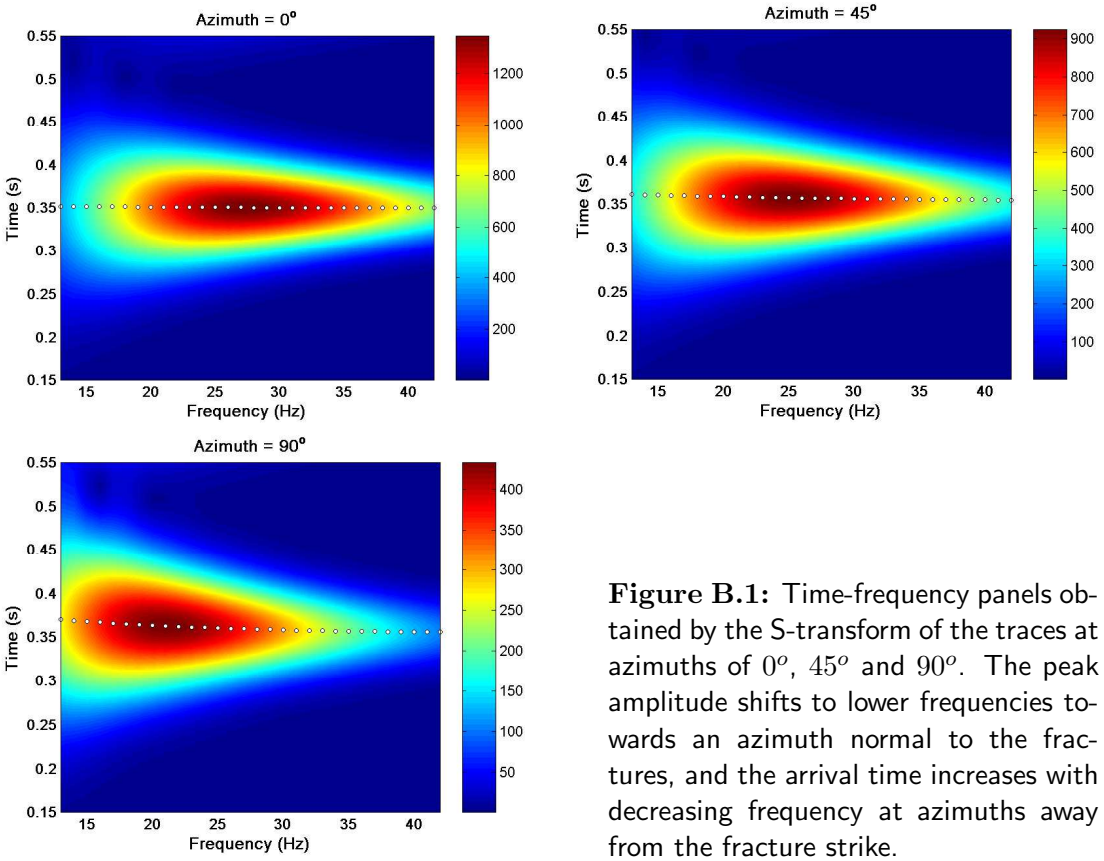

Figure B.1: Time-frequency panels obtained by the S-transform of the traces at azimuths of 0^o, 45^o and 90^o. The peak amplitude shifts to lower frequencies towards an azimuth normal to the fractures, and the arrival time increases with decreasing frequency at azimuths away from the fracture strike.

frequency. C_1, which is the average traveltime of all azimuths, decreases with increasing frequency, indicating the effect of velocity dispersion. The magnitude of traveltime anisotropy, which is measured by C_2, also decreases with increasing frequency. The azimuth of maximum traveltime, or the 'slow' direction, is constant at 90^o, which is the azimuth normal to the fracture strike. Errors are generally small, but they increase slightly towards higher frequencies where the azimuthal traveltime variation is smaller.

For this noise-free synthetic data set where no other arrivals interfere with the direct P-wave arrivals, the S-transform clearly reveals the velocity dispersion and frequency dependence of traveltime anisotropy. However, this may not be the case for field data. If signal components are not well separated in the time-frequency plane, picking the arrival times of maximum amplitudes in that plane is not a robust technique to measure traveltime anisotropy as a function of frequency. In such a case an analysis of the change of average spectral properties with propagation direction is a more appropriate approach to characterize frequency-dependent anisotropy.

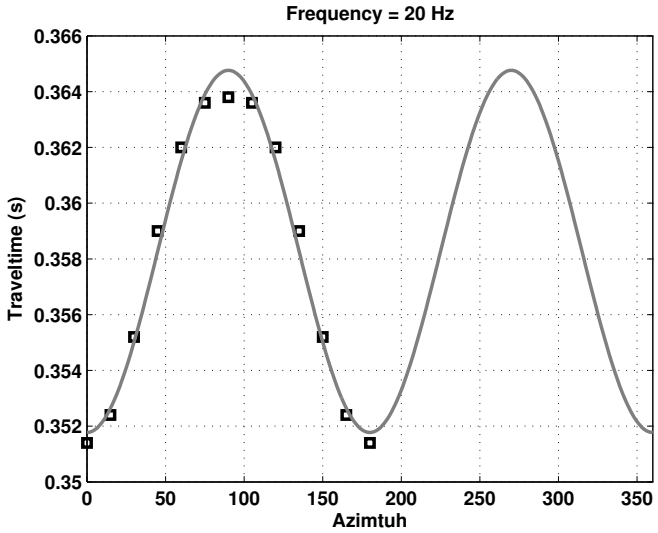

Figure B.2: Example of picked traveltimes and azimuthal fit at a frequency of 20 Hz.

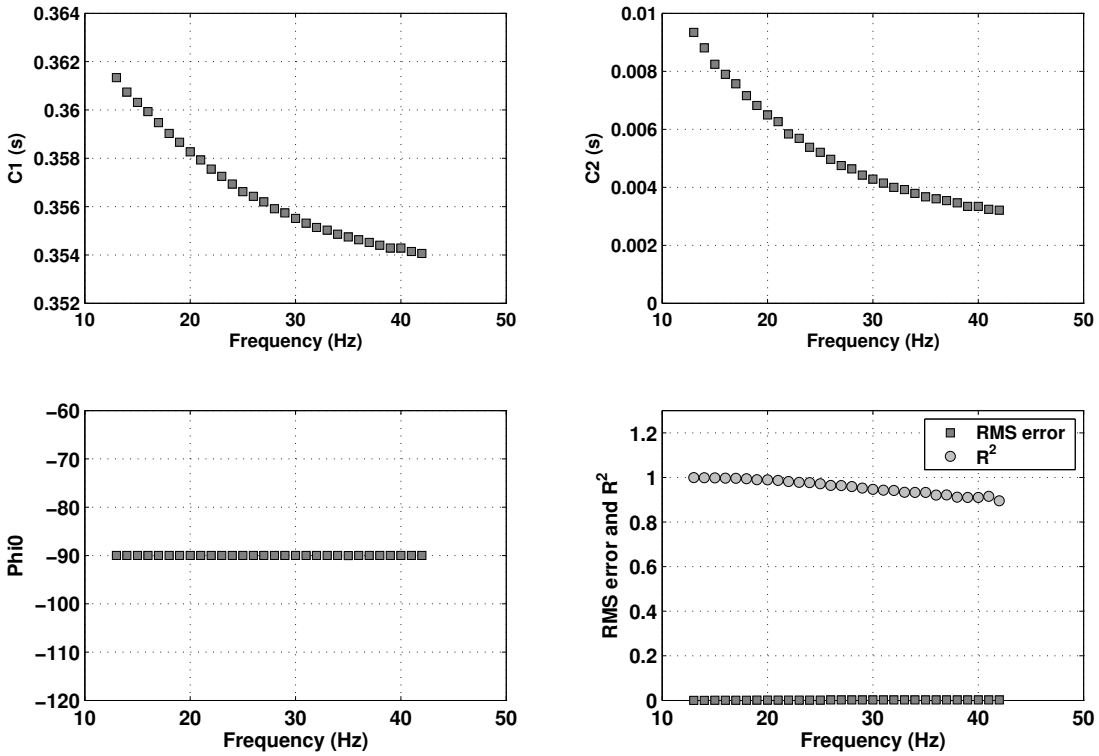

Figure B.3: Inverted parameters as a function of frequency from the $\cos(2\varphi)$-fit to the traveltimes.

Appendix C

Publications

Maultzsch, S., Chapman, M., Liu, E. and Li, X.-Y., 2003. Modelling frequency-dependent seismic anisotropy in fluid-saturated rock with aligned fractures: implication of fracture size estimation from anisotropic measurements. *Geophysical Prospecting*, **51**, 381-392.

Geophysical Prospecting, 2003, **51**, 381–392

Modelling frequency-dependent seismic anisotropy in fluid-saturated rock with aligned fractures: implication of fracture size estimation from anisotropic measurements

Sonja Maultzsch, Mark Chapman, Enru Liu* and Xiang Yang Li

British Geological Survey, Murchison House, West Mains Road, Edinburgh EH9 3LA, UK

Received July 2002, revision accepted April 2003

ABSTRACT

Measurements of seismic anisotropy in fractured rock are used at present to deduce information about the fracture orientation and the spatial distribution of fracture intensity. Analysis of the data is based upon equivalent-medium theories that describe the elastic response of a rock containing cracks or fractures in the long-wavelength limit. Conventional models assume frequency independence and cannot distinguish between microcracks and macrofractures. The latter, however, control the fluid flow in many subsurface reservoirs. Therefore, the fracture size is essential information for reservoir engineers. In this study we apply a new equivalent-medium theory that models frequency-dependent anisotropy and is sensitive to the length scale of fractures. The model considers velocity dispersion and attenuation due to a squirt-flow mechanism at two different scales: the grain scale (microcracks and equant matrix porosity) and formation-scale fractures. The theory is first tested and calibrated against published laboratory data. Then we present the analysis and modelling of frequency-dependent shear-wave splitting in multicomponent VSP data from a tight gas reservoir. We invert for fracture density and fracture size from the frequency dependence of the time delay between split shear waves. The derived fracture length matches independent observations from borehole data.

INTRODUCTION

Fractures are common geological features in the subsurface of the earth's crust, and they control much of the mechanical strength and transport properties of the solid structure. Fracture systems are also crucial for hydrocarbon production, control and manipulation of water supplies, and dispersal of pollutants. Much of our knowledge about the earth's crust is obtained from seismic waves. One of the most successful methods for the detection and characterization of fractures and the prediction of fluid-flow directions is the use of seismic shear waves (Crampin 1985; Queen and Rizer 1990; Li 1997). The success of seismic anisotropy is its ability to provide subsurface fracture orientations as derived from the polarization of fast shear waves, and spatial distribution of fracture intensity inferred from time delays between fast and slow shear waves. However, the reservoir engineers' reluctance to accept seismic anisotropy as a routine technique for fracture characterization is partially because of its failure to provide information about sizes and volume of fractures. So far the terms 'crack' and 'fracture' have been used as synonyms in geophysics and we do not distinguish between microcracks and macrofractures. Although it has been thought that both micro-scale (grain-scale) cracks and/or macro-scale (metre-scale) fractures can be considered the dominant causes of observed anisotropy in hydrocarbon reservoirs (Liu *et al*. 1993), reservoir engineers are more interested in the latter as fluid flow in reservoirs is believed to be dominated by large-scale fluid units (Queen, Rizer and DeMartini 1992). Therefore, a quantitative

*E-mail: e.liu@bgs.ac.uk

characterization of natural fracture systems in the subsurface from seismic data would potentially provide essential information for the prediction of permeability and flow patterns within reservoirs.

In the long-wavelength limit, the elastic response of a fractured rock is described by equivalent-medium theories. Various theories have been developed (e.g. Schoenberg 1980; Hudson 1981; Nishizawa 1982; Thomsen 1995). These models predict frequency-independent behaviour and are in that sense static equivalent-medium theories. There is agreement between the models for dry rock, but considerable differences occur in the case of fluid fill and fluid flow between cracks and pores (Liu, Hudson and Pointer 2000).

For applications to seismic data, the Thomsen equant porosity model (Thomsen 1995) and the Hudson model (Hudson 1981) are most widely used. Thomsen's model assumes perfect pressure equalization between cracks and equant pores in the surrounding rock matrix. It is therefore limited to low frequencies, where the period of the wave is much longer than the time it takes for the pressure to equalize. The flow of fluid from cracks into equant pores can significantly increase the anisotropy (Thomsen 1995). In contrast, Hudson's model (Hudson 1981) assumes that cracks are isolated and that there is no fluid communication between elements of pore space. It can thus be regarded as a high-frequency theory, bearing in mind that it is still only valid when wavelengths are much longer than the length scale associated with the cracks.

A common parameter in all theories, which is related to the magnitude of anisotropy, is the crack density ε. It is defined as the number density γ of cracks multiplied by the crack radius a cubed: $\varepsilon = \gamma a^3$. The crack density can be estimated from the time delay of split shear waves (Crampin 1985; Mueller 1992; Li 1997; Potters *et al*. 1999). However, a material with only a few large fractures can have the same crack density as a material with many small cracks, which is schematically illustrated in Fig. 1. Thus, conventional equivalent-medium theory cannot determine whether the anisotropy is caused by microcracks or by macrofractures that would potentially enhance fluid flow in hydrocarbon reservoirs.

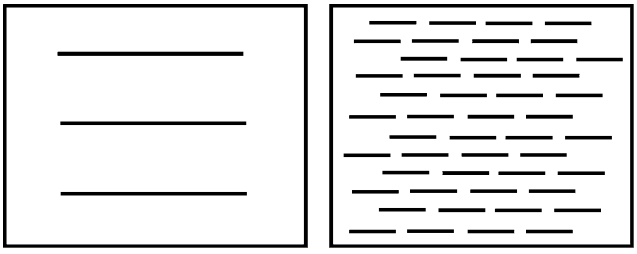

Figure 1 The same crack density can be caused by a few large fractures as shown on the left or many small cracks as shown on the right.

Some results obtained from data cannot be explained by static equivalent-medium theory and demand the use of more complicated models. Van der Kolk, Guest and Potters (2001) found that a region with a large increase in shear-wave splitting and attenuation of high frequencies coincided with the gas/oil contact in a fractured carbonate reservoir. Furthermore, there is evidence that anisotropy can depend on frequency: Marson-Pidgeon and Savage (1997) and Liu *et al*. (2001) observed a decrease in time delay between split shear waves with increasing frequency in earthquake data.

Dynamic equivalent-medium theories have been proposed by Hudson, Liu and Crampin (1996; interconnected crack model and equant porosity model) and van der Kolk *et al*. (2001; BOSK model). Tod (2001) considered the Hudson interconnected crack model in the case of nearly aligned cracks. For application purposes these models have limitations. It is not possible to remove the fractures from the models and then calibrate them against laboratory data. Furthermore, the explanation of observed effects in the seismic frequency range can be problematic.

In this study, we use a poroelastic model recently proposed by Chapman (2003). The model considers two different length scales: a grain scale with microcracks and equant pores and a scale larger than that with aligned fractures. It describes frequency-dependent anisotropy with the length of the fractures being one of the key parameters. The model is first tested and calibrated against published laboratory data. Then we apply the calibrated theory to model frequency-dependent anisotropy that has been observed in multicomponent VSP data. The measured change in time delay between split shear waves with frequency is used to invert for fracture density and fracture size. We test the results with synthetic modelling. Finally, the derived fracture length is compared with independent borehole data.

THEORETICAL MODEL

The poroelastic model of Chapman (2003) is based on a squirt-flow mechanism in fractured porous rock. It considers an isotropic collection of spherical pores and ellipsoidal microcracks, the size of which is identified with the grain scale, and the presence of aligned fractures, which can be larger than the grain scale. Thus, the theory accounts for two different length scales. The resulting medium is transversely isotropic.

The model agrees with the results of Brown and Korringa (1975) and Hudson (1981) in the low- and high-frequency

limits, respectively. In the absence of fractures it returns to the earlier squirt-flow model of Chapman, Zatsepin and Crampin (2002). Tests of this earlier model against laboratory measurements are discussed by Chapman (2000).

The expressions for the elements of the effective stiffness tensor are given by Chapman (2003). The stiffness tensor is of the form:

$$C_{ijkl} = C^0_{ijkl} - \Phi_p C^1_{ijkl} - \varepsilon_c C^2_{ijkl} - \varepsilon_f C^3_{ijkl}, \quad (1)$$

where $\mathbf{C}^0$ is the isotropic elastic tensor of the matrix with Lamé parameters λ and μ; $\mathbf{C}^1$, $\mathbf{C}^2$ and $\mathbf{C}^3$ are the additional contributions from pores, microcracks and fractures, respectively, multiplied by the porosity Φ_p, the crack density ε_c, and the fracture density ε_f. The corrections are functions of the Lamé parameters, fluid and fracture properties, frequency, and a time-scale parameter τ, which is related to the squirt flow.

Since the calculation of the elastic constants followed the interaction energy approach of Eshelby (1957), the model in its original form is restricted to very low porosity. To circumvent the problem, we use a slightly modified version as described by Chapman *et al*. (2003). The method is similar to the self-consistent scheme. We suggest using Lamé parameters λ^o and μ^o for the corrections that are derived from the velocities V_p^o and V_s^o of the unfractured porous rock. Additionally, we require $\mathbf{C}^0(\Lambda, M)$ to be defined in such a way that the measured isotropic velocities are obtained by applying the crack and pore correction at a certain frequency f_0. Therefore, we must have

$$\Lambda = \lambda^o + \Phi_{c,p}(\lambda^o, \mu^o, f_0), \; M = \mu^o + \Phi_{c,p}(\lambda^o, \mu^o, f_0), \quad (2)$$

with $\lambda^o = \rho\,(V_p^o)^2 - 2\mu^o$; $\mu^o = \rho (V_s^o)^2$.

Equation (1) is then written as

$$C_{ijkl}(\omega) = C^0_{ijkl}(\Lambda, M, \omega) - \Phi_p C^1_{ijkl}(\lambda^o, \mu^o, \omega) - \varepsilon_c C^2_{ijkl}(\lambda^o, \mu^o, \omega) - \varepsilon_f C^3_{ijkl}(\lambda^o, \mu^o, \omega). \quad (3)$$

Now the corrections for pores, microcracks and fractures, which describe the frequency dependence and anisotropy of the material, will be calculated with physical properties obtained from measured velocities instead of being fitted to the data.

Chapman *et al*. (2003) have shown that in cases of high porosity the model can be further simplified by setting the microcrack density ε_c to zero. The influence of the parameter is negligible for modelling the effect of fractures, if the spherical porosity is significantly larger than the crack porosity. This will be the case for most practical applications, and therefore the number of variables can be further reduced.

The fact that fluid flow in the model takes place at two scales, the grain scale (microcracks and pores) and the fracture scale, leads to the existence of two characteristic frequencies and associated relaxation times. The grain-scale fluid flow is related to the traditional squirt-flow frequency (or relaxation time τ_m), which experiments suggest lie somewhere between the sonic and ultrasonic range (Murphy 1985; Winkler 1986; Lucet and Zinszner 1992; Thomsen 1995). The flow in and out of fractures is associated with a lower characteristic frequency or larger time-scale constant τ_f, which depends on the size of the fractures. With increasing fracture radius, the ratio of surface area to volume decreases. Therefore, more volume of fluid has to move through an element of surface area to equalize the pressure, which requires more time. The two time-scale parameters are related to each other by the expression,

$$\tau_f = \frac{a_f}{\varsigma}\tau_m, \quad (4)$$

where a_f is the fracture radius and ς is the grain size. τ_m is given by

$$\tau_m = \frac{c_v \eta (1 + K_c)}{\sigma_c k \varsigma c_1}, \quad (5)$$

where c_v is the volume of an individual crack and c_1 is the number of connections to other elements of pore space. $\sigma_c = \pi\mu r/[2(1-\nu)]$ is the critical stress or, equivalently, the inverse of the crack space compressibility, and $K_c = \sigma_c/k_f$, where r is the aspect ratio of the cracks, ν is Poisson's ratio and k_f is the fluid bulk modulus.

The theory models velocity dispersion and velocity anisotropy. Thus, the anisotropy is frequency dependent. The effect is also sensitive to the fracture size. In Fig. 2, we see the change in shear-wave anisotropy with frequency as a function of fracture radius. For any given fracture size the anisotropy decreases as frequency increases. This behaviour is consistent with observations from earthquake data (Marson-Pidgeon and Savage 1997; Liu *et al*. 2001). The larger the size of the fractures, the lower the frequency range where velocity dispersion and frequency dependence of anisotropy occurs. The effect has also been observed in VSP data (Chesnokov *et al*. 2001; Liu *et al*. 2003) and will be used to invert for fracture size. Furthermore, the model can explain a large change in anisotropy due to fluid substitution for frequencies other than the static limit (Chapman *et al*. 2003). Such an effect has been found by van der Kolk *et al*. (2001) in shear-wave data from a fractured carbonate reservoir.

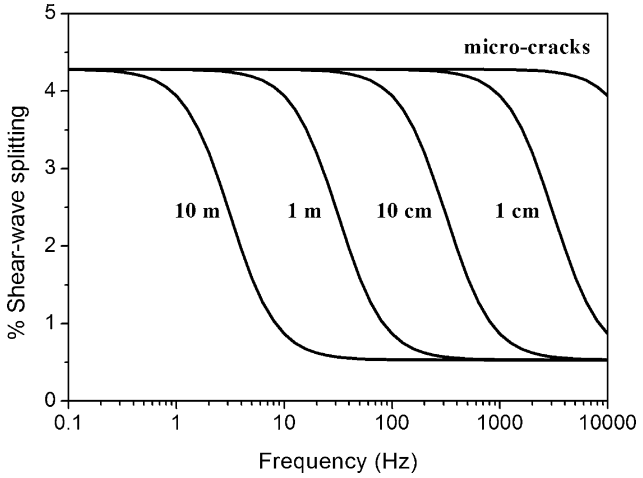

Figure 2 Percentage of shear-wave anisotropy as a function of frequency for different fracture sizes. The waves are propagating at an angle of 60° measured from the fracture normal. For a given fracture size there is a characteristic frequency range, where anisotropy decreases with increasing frequency. For smaller fractures the change in anisotropy occurs at higher frequencies.

CALIBRATION OF THE MODEL

Effective-medium theories for materials containing cracks or fractures can only be tested and validated by comparison with laboratory measurements. Rathore *et al.* (1995) performed measurements on synthetic sandstone samples that contained cracks of known geometry and orientation. The samples were manufactured by embedding thin metal discs into a sand-epoxy matrix, which were chemically leached out later on. P- and S-wave velocities were measured as a function of angle from the crack normal at a frequency of 100 kHz.

The data were used to test the model of Thomsen (1995) and the models of Hudson (1981) and Hudson *et al.* (1996) and to discuss their differences (Rathore *et al.* 1995; Thomsen 1995; Hudson, Pointer and Liu 2001). Rathore *et al.* (1995) and Thomsen (1995) found that for fluid-saturated samples the data are better matched by the Thomsen equant porosity model, where pressure is always equalized between cracks and equant pores, and anisotropy is therefore increased. While the Hudson (1981) model for isolated cracks gives a poor fit, the data were satisfactorily matched with the Hudson *et al.* (1996) equant porosity model, if the matrix wave speeds were also taken as fitting parameters (Hudson *et al.* 2001).

We now test the Chapman model against the data. All relevant parameters are given in Table 1. The only free variable in the modelling is the relaxation time τ_m. We seek the value of τ_m that minimizes the misfit between data and model.

Table 1 Rock and fluid parameters used in the experiment of Rathore *et al.* (1995)

V_p	2678 m/s
V_s	1384 m/s
ρ	1712 kg/m^3
Φ_p	34.6%
k_f	2.16 GPa
f_0	100 kHz
Fracture density	0.1
Fracture radius	2.75 mm
Aspect ratio	0.0036

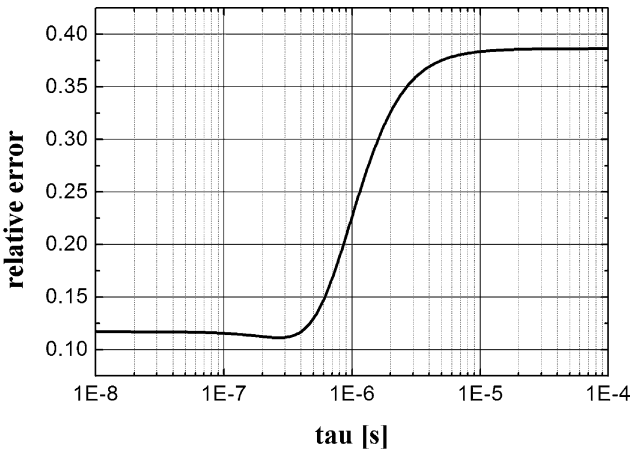

Figure 3 Relative error between measured and modelled velocities as a function of τ_m. There is a minimum at $\tau_m = 0.27$ μs. The curve also shows that the data are much better matched by a low-frequency model than a high-frequency model.

Figure 3 shows the error curve as a function of τ_m. There is a minimum at $\tau_m = 0.27$ μs. This value is used to compute P- and S-wave velocities as a function of angle, and these are displayed together with the data points from Rathore *et al.* (1995) in Fig. 4. There is a good match between data and model. Figure 3 demonstrates that a low-frequency model (left side of the plot), which assumes equalized pressure throughout the pore space, fits the data much better than a high-frequency model (right side of the plot), where the cracks are effectively isolated.

The misfit for the optimal τ_m value of 0.27 μs is not significantly smaller than for the low-frequency limit. Therefore, we also attempt to model the attenuation data, which was reported by Thomsen (1995). Figures 5 and 6 show the corresponding error curve and the best-fitting model values compared with the data points. In this case the error function has a distinct minimum, which is near the optimum value obtained for the velocity modelling. Thus, we have constrained

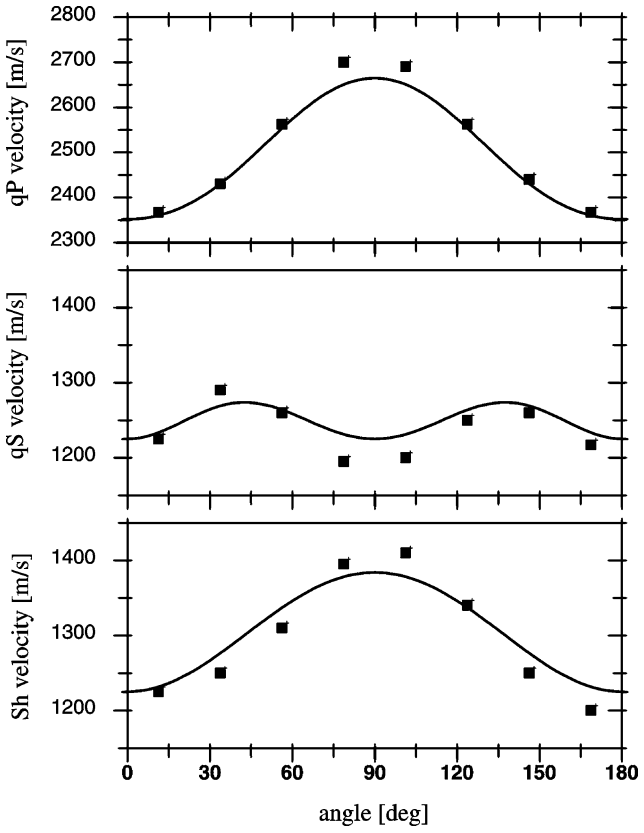

Figure 4 Comparison of the Rathore *et al.* (1995) data (squares) for saturated synthetic sandstone with the best-fitting model. Measured and modelled velocities agree very well.

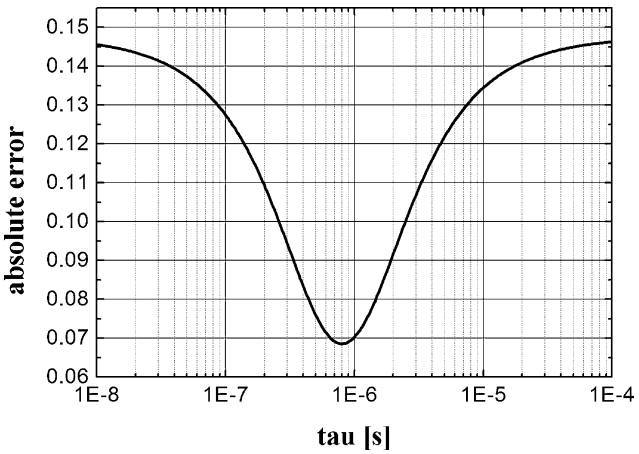

Figure 5 Misfit between measured and modelled qP-wave attenuation as a function of τ_m. There is a distinct minimum in a position similar to that in Fig. 3. This result constrains τ_m against lower values.

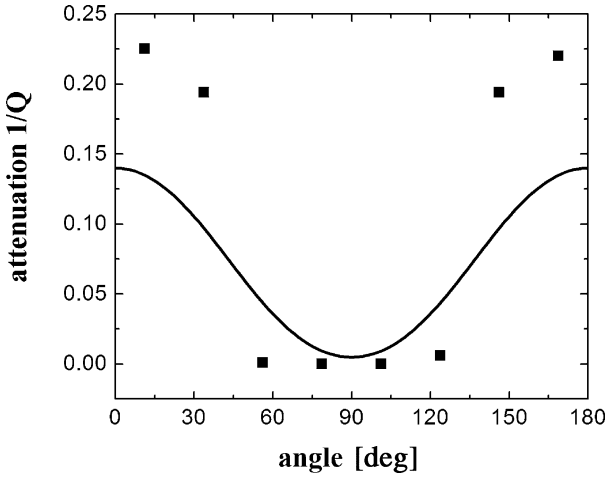

Figure 6 Attenuation data with the best-fitting model.

τ_m against the lower-frequency limit as well. We cannot expect a perfect numerical match with the attenuation data, since scattering effects are also expected to contribute to the measured values (Hudson *et al.* 2001). The model is now tested and calibrated, and we can proceed to apply it to field data.

APPLICATION TO FIELD DATA

We model frequency-dependent anisotropy in nine-component VSP data from the Bluebell-Altamont Field in the Uinta Basin, Utah. The aim is to estimate fracture density and fracture size from the data. The field contains a fractured gas reservoir, the Green River Formation. It is a sandstone with generally low porosity and permeability. Production from the reservoir is believed to be primarily controlled by size, orientation and concentration of natural fractures (Lynn *et al.* 1999). Therefore, estimates of these parameters from seismic data are vital information for reservoir engineers.

Fracture orientations measured from seismic data, boreholes, outcrops and cores show a fracture strike between N30°W and N45°W. Observed fractures are vertical to subvertical. The VSP is a near-offset VSP with the source located 550 ft west of the well. Three-component receivers were placed at depths from 2800 ft to 8650 ft with a 50 ft spacing. The reservoir (Green River Formation) is located at depths of 6687 ft to 8591 ft. A P-wave and two orthogonal S-wave sources were used, yielding a nine-component data set.

Shear-wave splitting has been observed in the VSP data and analysed from direct arrivals. The polarization angles of the fast shear waves are found to be consistent at N43°W throughout all receiver depths. This direction is identified with the fracture strike. The time delay between the fast and the slow shear waves shows a sharp increase with depth at the reservoir level, indicating the presence of fractures.

We now analyse the data from the Green River Formation for frequency-dependent shear-wave splitting as described by Chesnokov *et al*. (2001) and Liu *et al*. (2003). Following Liu *et al*. (2003), the data are first filtered into several frequency bands. Then we perform an Alford rotation to determine the polarization angles of the fast shear-wave component. The time delays are obtained by cross-correlating the rotated traces. The processing technique has been tested on synthetic data for both frequency-dependent and frequency-independent anisotropic materials to ensure that the effects described below are not related to processing issues (Liu *et al*. 2003).

Figures 7 and 8 show the results. The polarization angles are consistent at around 43° for all frequency bands. The time delays, in contrast, show a systematic variation with frequency: as frequency increases, the change in time delay with depth decreases, i.e. the magnitude of anisotropy decreases. This behaviour will be used to invert for fracture density and fracture radius.

Before we can proceed to the inversion, we have to correct the τ_m value obtained from the calibration to laboratory measurements in order to match the rock and fluid properties of the Green River Formation. The latter are given in Table 2. The Rathore *et al*. (1995) experiment was performed on water-saturated high-porosity sandstone, while the Green River Formation is a gas-saturated sandstone of low porosity. From (5) we can see that τ_m is proportional to the fluid viscosity η, multiplied by the term $(1/\sigma_c + 1/k_f)$. There is a large change in viscosity and fluid bulk modulus going from water to natural gas. Since all relevant parameters are known, we can calculate the corresponding change in τ_m.

Also, τ_m is inversely proportional to the permeability. Since we do not know the permeability values for either case, we suggest inferring the change in permeability from the change in porosity. For that purpose we use an extended form of the Kozeny–Carman relationship given by Mavko and Nur (1997), which considers the existence of a percolation threshold. As a result we obtain a decrease in permeability and therefore an increase in τ_m of a factor of 123. Combining all corrections yields a τ_m value of 6 μs, which can now be used for modelling the elastic response of the Green River sandstone.

From the polarization angles obtained from the field data we infer an average fracture strike of N43°W, which is input

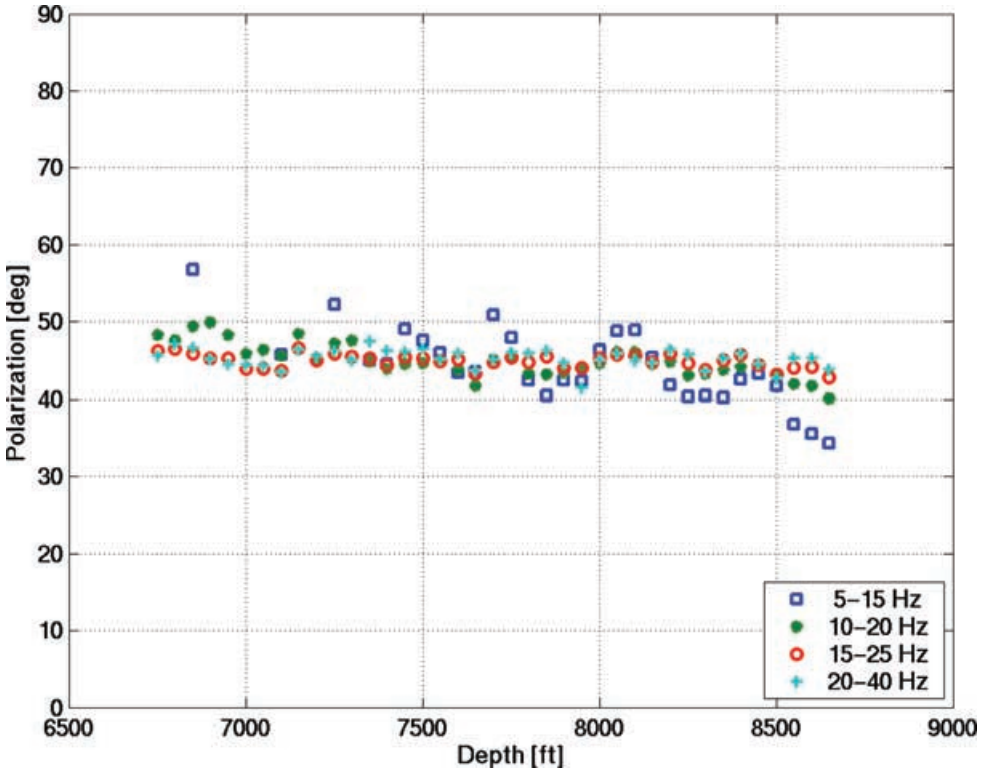

Figure 7 Polarization angles of the fast shear wave for different frequency bands. The values are consistent around 43°, which agrees with the fracture strike in the reservoir.

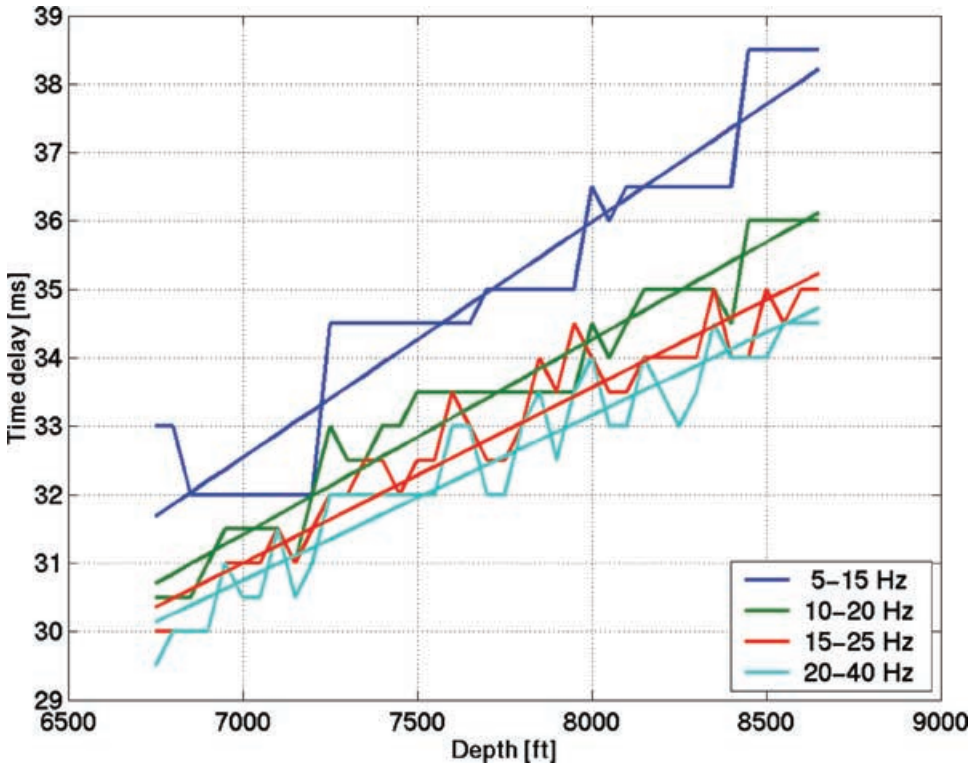

Figure 8 The time delays over the reservoir depth interval show a systematic decrease with increasing frequency.

Table 2 Rock properties of the Green River Formation in the Bluebell-Altamont Field

V_p	4877 m/s
V_s	2575 m/s
ρ	2600 kg/m^3
Φ_p	9.4%
k_f	25 MPa

into the model. The aspect ratio is chosen to be very small with a value of 0.0001, so that its exact value has no influence on the resulting elastic constants. The value is supported by observations from borehole images and cores (Lynn *et al.* 1995). We tilt the fractures by 20° from the vertical in order to model propagation directions of the waves, where frequency-dependent effects would occur. In reality there would be a distribution of orientations around a certain angle that would produce the effect. Slightly tilted fractures have also been observed in the field (Lynn *et al.* 1995).

Now the only unknowns in the model are fracture density and fracture radius. We estimate these parameters by matching the change in time delay with frequency, which was observed in the data. For each pair of fracture density and fracture radius we compute the RMS error between the measured and the predicted increases in time delay with depth as a function of frequency.

Figure 9 displays the error function. There is a well-defined minimum at a fracture radius of about 3 m and a fracture density of approximately 3.5%. It is interesting to observe the bottom and top sections of the diagram. They represent what would be obtained using the Thomsen (1995) and Hudson (1981) models, respectively. As stated earlier, neither of the models is sensitive to the fracture size, which can be clearly seen in Fig. 9. Furthermore, we would infer a fracture density of 5% from the data by using Hudson's model, while the model of Thomsen yields a value of about 2.5%. However, by incorporating the frequency-dependent effects and modelling the data with Chapman's (2003) model, we obtain a more tightly constrained estimate of the fracture density, and we can also deduce a fracture size from the data.

The two fracture parameters (i.e. fracture radius and fracture density) are used to carry out forward modelling. We create a simple four-layer model that matches the main formations in the field. The model parameters are given in Table 3. Synthetic seismograms are computed using the reflectivity method, which has been modified to handle

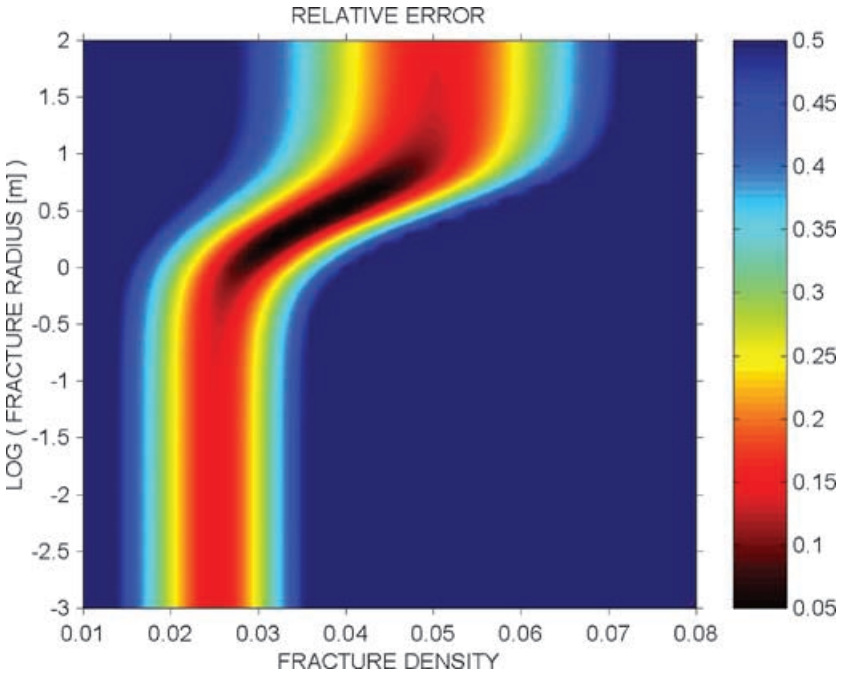

Figure 9 Relative error between measured and computed time delays as a function of frequency for a wide range of fracture densities and fracture sizes. There is a clear minimum at a fracture density of 0.035 and a fracture radius of about 3 m.

Table 3 Parameters of the model that are used to generate synthetic seismograms

Depth (ft)	ρ (kg/m^3)	V_p (m/s)	V_s (m/s)	
2800	2200	2963	1363	Anisotropic
6687	2450	4000	2128	Isotropic
8591	2600	4877	2575	Anisotropic, frequency-dependent
Half-space	2500	4382	2583	Isotropic

frequency-dependent anisotropic elastic constants. The four-component shear-wave data are shown in Fig. 10 before and after an Alford rotation and can be compared with the synthetics in Fig. 11. We process the synthetic data in the same way as the real data. The polarization angles of the fast shear wave are plotted in Fig. 12 for different frequency bands. They are invariant to frequency and plotted at a constant value of 43°, which is the fracture strike that was input into the model. From the measured time delays we can compute the percentage of anisotropy. Figure 13 shows the modelled percentage of anisotropy as a function of frequency compared with the real data results. There is good agreement between the two curves. The error bars represent the error between measured time delays as a function of depth and the best-fitting straight line.

Finally, we compare our deduced fracture radius of about 3 m (or fracture length of 6 m) with independent borehole data. There is evidence from borehole images and cores that lengths of fractures in the reservoir lie in the range of 2–3 m (Lynn *et al*. 1995). Our inferred average length matches these independent observations quite closely.

DISCUSSION

Conventional static equivalent-medium theories can be used to infer an average fracture density and orientation from measurements of seismic anisotropy. However, the models fail to provide any information on the fracture size. Moreover, there is evidence of frequency-dependent anisotropy from field data that cannot be satisfactorily explained by static equivalent-medium theories.

Heterogeneous and fractured porous rock may be characterized by observations in different critical wavelength ranges, each reflecting different physical mechanisms. The scale length associated with the heterogeneities or the fracturing has to be much smaller than the seismic wavelength to cause effective anisotropy instead of scattering.

Scattering of seismic waves due to aligned heterogeneities has long been recognized to be frequency dependent (e.g. Shapiro and Hubral 1995; Werner and Shapiro 1999). Shapiro and Hubral (1995) have shown that in finely layered media velocity dispersion and frequency-dependent anisotropy in the seismic frequency band can be produced by scattering, if there is a specific ratio between wavelength and

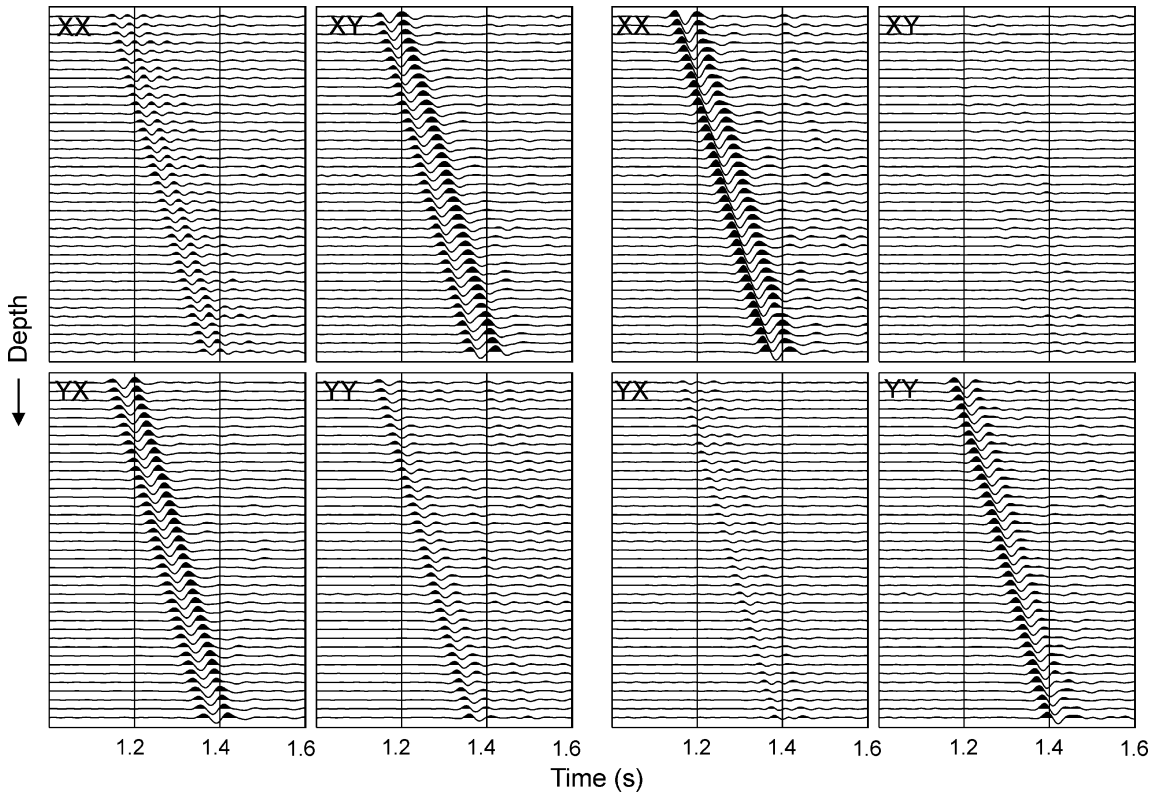

Figure 10 Four-component shear-wave data before (left) and after (right) Alford rotation. The strong energy in the cross-diagonal components before rotation indicates shear-wave splitting.

correlation length. They predict significant frequency-dependent shear-wave splitting at far offsets. The data set investigated in this study, however, is a near-offset VSP with nearly vertical incidence. The effect of layering does not cause shear-wave splitting at normal incidence and therefore cannot explain the observed shear-wave behaviour.

The model of Chapman (2003) as used here predicts frequency-dependent anisotropy due to squirt flow in fractured porous rock. The fractures can be much larger than the cracks and pores, but are much smaller than the wavelength. The explicit dependence on fracture size is in contrast to the earlier models of Hudson *et al*. (1996) and Thomsen (1995). Tod and Liu (2002) modelled frequency-dependent anisotropy in earthquake and VSP data using a layer-bounded fracture model based on Hudson *et al*. (1996). Nevertheless, it appears that in this study rather high values of the permeability had to be assumed, and it remains an open question as to whether these values are reasonable.

In the model of Chapman (2003), coupled fluid-flow motion occurs on two scales: the grain scale and the scale of the fractures. As a consequence the form of the predicted frequency dependence of anisotropy is directly related to the fracture size. Previous estimates of the squirt-flow frequency have given high values, typically between the sonic and ultrasonic bands, which leads to the suggestion that at seismic frequencies there should be little dispersion (Thomsen 1995). In the presence of larger-scale fractures, however, substantial frequency dependence can be expected in the seismic frequency ranges, and therefore it is not safe to treat seismic frequency as a low-frequency limit.

Our study has an important implication for the characterization of natural fractures in that fracture sizes, which control the fluid flow, may potentially be predicted from seismic anisotropic measurement. This goes beyond applications of static equivalent-medium theories that are limited to extracting information about fracture orientation and fracture density.

CONCLUSIONS

We have presented results demonstrating the dependence of seismic anisotropic parameters on frequency using a recently

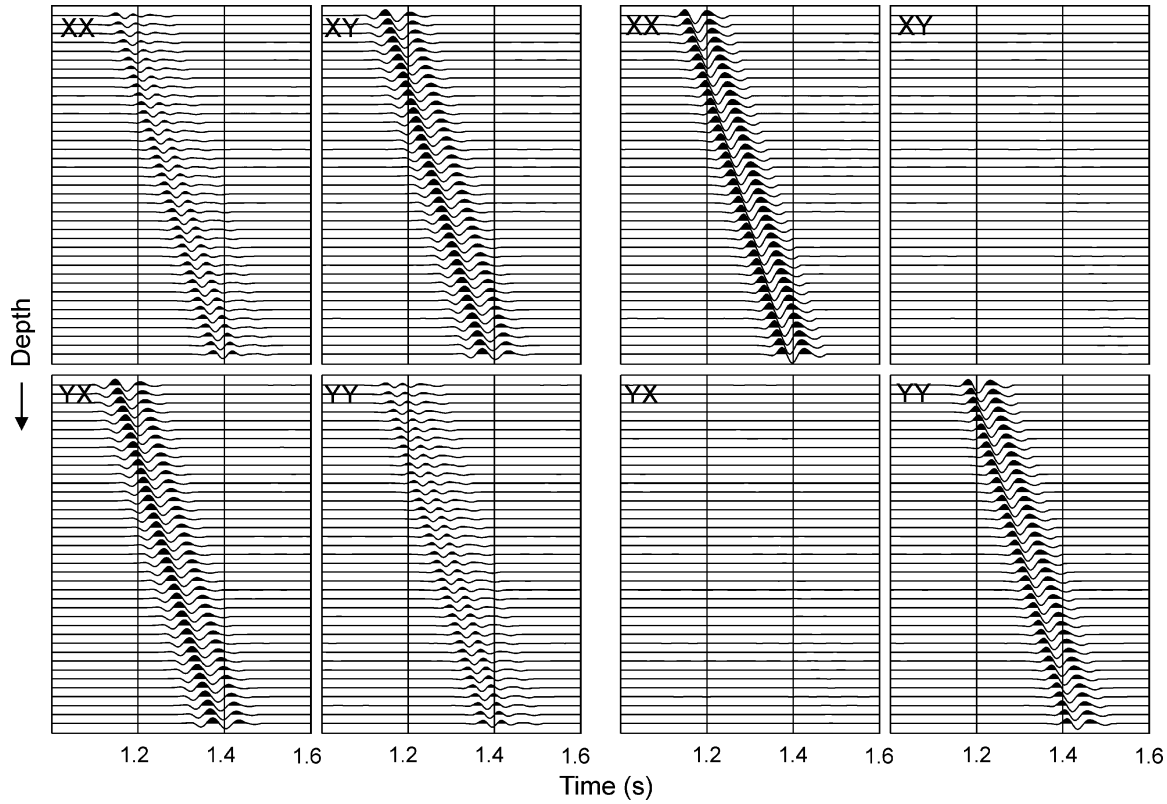

Figure 11 Four-component synthetics before and after Alford rotation. They agree well with the real data.

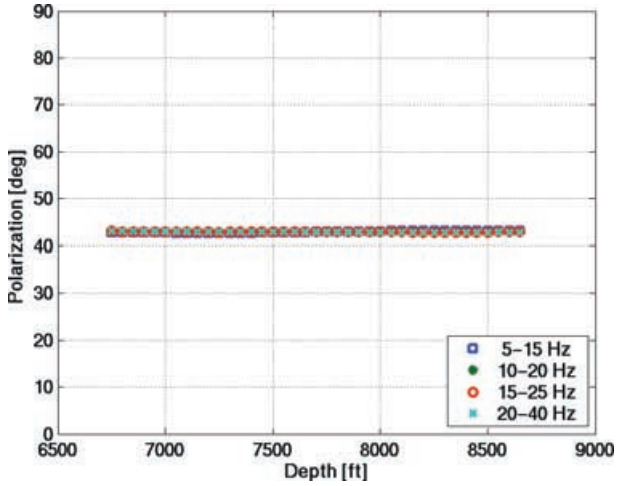

Figure 12 Polarization angles measured from the synthetic data for different frequency bands. The values are constant at 43° for all frequencies, which corresponds to the fracture strike in the reservoir layer.

developed dynamic equivalent-medium theory by Chapman (2003) and Chapman *et al*. (2003). This model is based on a squirt-flow mechanism and suggests that frequency dependence of anisotropy is sensitive to the length scale of fractures. We have tested and calibrated the model against published laboratory data. This provides the basis for application to field data. We developed a methodology for using the model to invert for fracture density and fracture size from frequency-dependent shear-wave splitting in a near-offset VSP. The derived average fracture length matches geological evidence very well.

Since the analysed data set is a near-offset VSP with nearly vertical incidence, scattering due to thin layers can be excluded as a cause of the observed shear-wave behaviour. If the measured frequency-dependent anisotropy was caused by scattering at fractures, then the dominant length scales associated with the fracturing would have to be of the order of seismic wavelengths, i.e. several tens to hundreds of metres. We believe that the squirt-flow mechanism is more likely to be the dominant cause, which is supported by the good match between inferred fracture length and independent geological data. Moreover, there is evidence from field and laboratory data that fluid plays a significant role with regard to velocity dispersion and attenuation (Spencer 1981; van der Kolk *et al*. 2001; Parra, Hackert and Xu 2002).

The study demonstrates that the frequency dependence of shear-wave splitting can be extracted from seismic data and

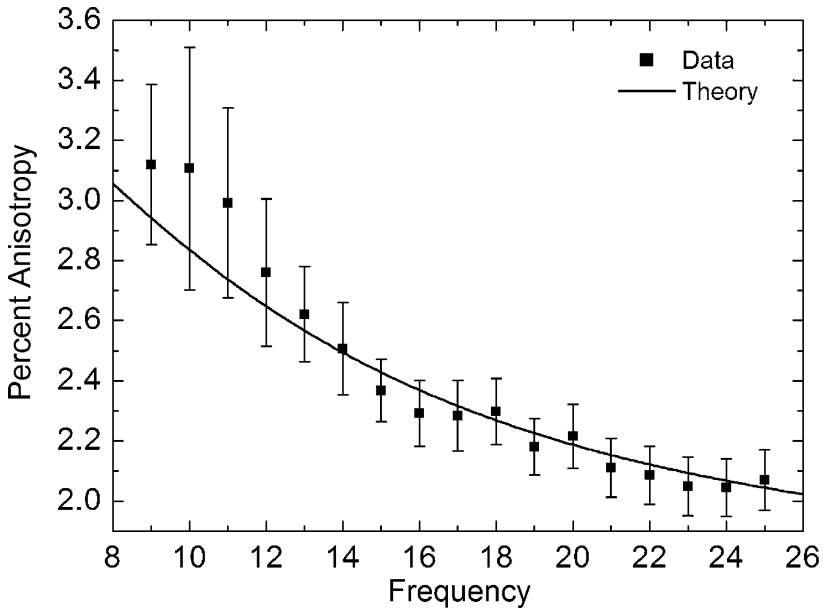

Figure 13 Percentage anisotropy as a function of frequency measured from the VSP data, compared with the modelled results.

interpreted in terms of an average length scale of fractures. The most important result is the successful discrimination between the effect of microcracks at the grain or millimetre scale and the effect of formation-scale fractures. Fluid flow and permeability in a reservoir are believed to be much more strongly controlled by formation-scale fractures than by microcracks.

Our study indicates that there is great potential in using frequency-dependent seismic anisotropy to estimate average fracture sizes, which are ultimately needed in reservoir simulation. It is the aim of future work to extend our approach to the use of other attributes, such as amplitudes and attenuation, and to understand better the effects of multiscale fractures on amplitudes versus offsets and frequency variation with offset as used by Lynn *et al*. (1999). With further validation of the model there is potential for an improved and more quantitative fracture characterization from seismic data compared with previous approaches using static theory.

ACKNOWLEDGEMENTS

We thank John Queen (ConocoPhillips) and Heloise Lynn (Lynn Inc.) for useful discussions and for providing the field VSP data (by H.L.). We also thank Simon Tod (formerly at BGS, now at BP) and John Hudson (Cambridge University) for many discussions about the fracture modelling and for comments on this work. We are very grateful to David Taylor (Edinburgh University) for his help with the computation of synthetic seismograms (using a modified ANISEIS package). This work is supported by the Natural Environment Research Council (UK) as part of the 'Thematic micro-to-Macro Programme' (Project No. GST22305), and by the sponsors of the Edinburgh Anisotropy Project (EAP). This paper is published with the approval of the Executive Director of the British Geological Survey (NERC) and the EAP sponsors: ENI-Agip, BP, BG Group, ChevronTexaco, CNPC, ConocoPhillips, ExxonMobil, Norsk Hydro, KerrMcGee, Marathon, PetroChina, PGS, Schlumberger, Total, Trade Partners UK and Veritas DGC.

REFERENCES

Brown R. and Korringa J. 1975. On the dependence of the elastic properties of a porous rock on the compressibility of the pore fluid. *Geophysics* **40**, 608–616.

Chapman M. 2000. *Modelling the wide-band laboratory response of rock samples to fluid and pressure changes*. PhD thesis, University of Edinburgh.

Chapman M. 2003. Frequency-dependent anisotropy due to mesoscale fractures in the presence of equant porosity. *Geophysical Prospecting* **51**, 369–379.

Chapman M., Maultzsch S., Liu E. and Li X.Y. 2003. The effect of fluid saturation in an anisotropic, multi-scale equant porosity model. *Journal of Applied Geophysics*, in press (10IWSA Proceedings).

Chapman M., Zatsepin S.V. and Crampin S. 2002. Derivation of a microstructural poroelastic model. *Geophysical Journal International* **151**, 427–451.

Chesnokov E.M., Queen J.H., Vichorev A., Lynn H.B., Hooper J., Bayuk I., Castagna J. and Roy B. 2001. Frequency dependent anisotropy. 71st SEG Meeting, San Antonio, Texas, USA, Expanded Abstracts, 2120–2123.

Crampin S. 1985. Evaluation of anisotropy by shear-wave splitting. *Geophysics* **50**, 142–152.

Eshelby J.D. 1957. The determination of the elastic field of an ellipsoidal inclusion and related problems. *Proceedings of the Royal Society of London* **A241**, 376–396.

Hudson J.A. 1981. Wave speeds and attenuation of elastic waves in material containing cracks. *Geophysical Journal of the Royal Astronomical Society* **64**, 133–150.

Hudson J.A., Liu E. and Crampin S. 1996. The mechanical properties of materials with interconnected cracks and pores. *Geophysical Journal International* **124**, 105–112.

Hudson J.A., Pointer T. and Liu E. 2001. Effective-medium theories for fluid-saturated materials with aligned cracks. *Geophysical Prospecting* **49**, 509–522.

van der Kolk C.M., Guest W.S. and Potters J.H.H.M. 2001. The 3D shear experiment over the Natih field in Oman: the effect of fracture-filling fluids on shear propagation. *Geophysical Prospecting* **49**, 179–197.

Li X.Y. 1997. Fractured reservoir delineation using multicomponent seismic data. *Geophysical Prospecting* **45**, 39–64.

Liu E., Crampin S., Queen J.H. and Rizer W.D. 1993. Velocity and attenuation anisotropy caused by microcracks and macrofractures in a multiazimuthal reverse VSP. *Canadian Journal of Exploration Geophysics* **29**, 177–188.

Liu E., Hudson J.A. and Pointer T. 2000. Equivalent medium representation of fractured rock. *Journal of Geophysical Research* **105**(B2), 2981–3000.

Liu E., Queen J.H., Li X.Y., Chapman M., Maultzsch S., Lynn H.B. and Chesnokov E.M. 2003. Observation and analysis of frequency-dependent anisotropy from a multicomponent VSP at Bluebell-Altamont Field, Utah. *Journal of Applied Geophysics*, in press (10IWSA Proceedings).

Liu K., Zhang Z., Hu J. and Teng J. 2001. Frequency band-dependence of S-wave splitting in China mainland and its implications. *Science in China (Series D)* **44**(7), 659–665.

Lucet N. and Zinszner B. 1992. Effects of heterogeneities and anisotropy on sonic and ultrasonic attenuation in rocks. *Geophysics* **57**, 1018–1026.

Lynn H.B., Bates C.R., Hoekstra P., Simone M.K. and Phillips D.R. 1995. *Fracture Detection, Mapping, and Analysis of Naturally Fractured Gas Reservoirs using Seismic Technology*. Report to the US Department of Energy.

Lynn H.B., Beckham W.E., Simon K.M., Bates C.R., Layman M. and Jones M. 1999. P-wave and S-wave azimuthal anisotropy at a naturally fractured gas reservoir, Bluebell-Altamont field, Utah. *Geophysics* **64**, 1312–1328.

Marson-Pidgeon K. and Savage M.K. 1997. Frequency-dependent anisotropy in Wellington, New Zealand. *Geophysical Research Letters* **24**, 3297–3300.

Mavko G. and Nur A. 1997. The effect of a percolation threshold in the Kozeny–Carman relation. *Geophysics* **62**, 1480–1482.

Mueller M.C. 1992. Using shear waves to predict lateral variability in vertical fracture intensity. *The Leading Edge* **11**(2), 29–35.

Murphy W.F. 1985. Sonic and ultrasonic velocities: Theory versus experiment. *Geophysical Research Letters* **12**, 85–88.

Nishizawa O. 1982. Seismic velocity anisotropy in a medium containing oriented cracks – transversely isotropic case. *Journal of Physics of the Earth* **30**, 331–347.

Parra J.O., Hackert C.L. and Xu P.C. 2002. Characterization of fractured low Q zones at the Buena Vista Hills reservoir, California. *Geophysics* **67**, 1061–1070.

Potters J.H.H.M., Groenendaal H.J.J., Oates S.J., Hake J.H. and Kalden A.B. 1999. The 3D shear experiment over the Natih field in Oman: Reservoir geology, data acquisition and anisotropy analysis. *Geophysical Prospecting* **47**, 637–662.

Queen J.H. and Rizer W.D. 1990. An integrated study of seismic anisotropy and the natural fracture systems at the Conoco Borehole Test Facility, Kay County, Oklahoma. *Journal of Geophysical Research* **95**, 11255–11273.

Queen J.H., Rizer W.D. and DeMartini D. 1992. Geophysical methods of fracture detection and estimation. *The Leading Edge* **11**, 19–21.

Rathore J.S., Fjaer E., Holt R.M. and Renlie L. 1995. P- and S- wave anisotropy of a synthetic sandstone with controlled crack geometry. *Geophysical Prospecting* **43**, 711–728.

Schoenberg M. 1980. Elastic wave behaviour across linear slip interfaces. *Journal of the Acoustical Society of America* **68**, 1516–1521.

Shapiro S.A. and Hubral P. 1995. Frequency-dependent shear-wave splitting and velocity anisotropy due to elastic multilayering. *Journal of Seismic Exploration* **4**, 151–168.

Spencer J.W. 1981. Stress relaxation at low frequencies in fluid-saturated rocks: Attenuation and modulus dispersion. *Journal of Geophysical Research* **86**, 1803–1812.

Thomsen L. 1995. Elastic anisotropy due to aligned cracks in porous rock. *Geophysical Prospecting* **43**, 805–829.

Tod S.R. 2001. The effects on seismic waves of interconnected nearly aligned cracks. *Geophysical Journal International* **146**, 249–263.

Tod S.R. and Liu E. 2002. Frequency-dependent anisotropy due to fluid flow in bed limited cracks. *Geophysical Research Letters* **29**(15), 39-1–39-4. Paper no. 10.1029/2002GL015369.

Werner U. and Shapiro S.A. 1999. Frequency-dependent shear-wave splitting in thinly layered media with intrinsic anisotropy. *Geophysics* **64**, 604–608.

Winkler K.W. 1986. Estimates of velocity dispersion between seismic and ultrasonic frequencies. *Geophysics* **51**, 183–189.